Section 5

Blast Experience Models

5.1 Blast Experience Model Names

Short Name	Description
Blast 1	NTS source and NTS attenuation
Blast 2	NTS attenuation with Sadigh 1993 spectral shape
Blast 3	Little Skull Mtn spectral shape and Sadigh magnitude scaling

5.2 Description of the Blast Experience Models

8.0 Explosion-Based Empirical Modeling Results

8.1 Background and Method Development

As noted above, the explosion-based empirical modeling approach described in this section is fundamentally different from the physical modeling methods used by the other investigators to predict ground motion for the scenario earthquakes at the Yucca Mountain site. In developing an empirical basis for predicting strong ground motion from earthquakes at a site like Yucca Mountain, the ideal would be to have recorded ground motion in the site vicinity covering a range of earthquake magnitudes which might be expected and covering distances at which such events might affect the site. However, as is the case with most engineering projects, such information is generally not available for the Yucca Mountain site. What we do have for Yucca Mountain are the records of strong ground motion made in the same general region as the site for a fairly large earthquake (viz. the 1992 Little Skull Mountain event) and for a large number of seismic events (viz. underground nuclear explosion tests) covering a range of strong motion levels and distances similar to those which are of interest for earthquake-resistant design at the Yucca Mountain site. These data provide information on region-specific attenuation, site response, and the uncertainties associated with these elements of the ground motion prediction problem. One objective of this project has been to identify procedures which permit us to utilize this region-specific knowledge of strong-ground motion to make reasonable inferences about seismic motions from large scenario earthquakes which might be postulated for the Yucca Mountain site. Our investigations under this element of the program have focused on utilization of the nuclear explosion experience base and the strong motion records from the Little Skull Mountain earthquake.

From the late 1950's until just recently, hundreds of underground nuclear explosions have been conducted at NTS. The yields of these explosions have ranged from less than 1 kiloton (kt) to 1200 kt, and the ground motions produced by these events were recorded at ranges from less than 1 km out to more than 100 km (cf. ERC, 1974; Bennett and Murphy, 1993). More than 1300 strong motion observations from this large explosion database were analyzed by ERC (1974) and used to develop prediction relations for the region surrounding NTS. These ERC prediction relations took the form of a power law model

$$A = A_0 W^B R^C \qquad (8.1.1)$$

where A is either a peak time-domain ground motion measure or the spectral response at some frequency, W is explosion yield in kilotons, and R is range. The coefficient term, A_0, and the exponential terms, B and C, were derived from standard regression and covariance analyses of the explosion data. Similar power law models and regression analyses have subsequently been used by other authors to further analyze NTS explosion observations and to predict ground motions for the Yucca Mountain site (cf. Vortman, 1986; Phillips, 1991; Bennett and Murphy, 1993) from potential future NTS nuclear explosion tests. For the spectral response, which is the main focus of the studies presented in this section, A is a function of frequency and the coefficient and exponential terms are frequency dependent and determined by the regression analysis for each frequency. The response spectra predicted by these empirical relations have been found to be quite reliable for analyzing ground motion and building response from explosions at sites throughout the region.

The procedures used to extend this model to predict earthquake ground motions have been developed over the relatively short term of this project. Three distinct schemes based on the NTS explosion knowledge base have been identified and implemented to predict earthquake ground motions for the vicinity of the Yucca Mountain site. These three models are characterized as follows:

- Equivalent explosion with NTS attenuation relationship
- Geomatrix/ATC spectral shape with NTS attenuation relationship

- Little Skull Mountain earthquake spectral shape with NTS attenuation relationship and Geomatrix/ATC magnitude scaling

For the first of these models, we have attempted to use empirical relationships between magnitude and yield to identify an explosion source which is approximately equivalent to the postulated earthquake scenario. The scenario earthquakes are specified in terms of moment magnitude, M_W, while the most reliable relationship between magnitude and yield for underground nuclear explosions uses the body-wave magnitude, m_b. Lacking reliable empirical relationships between moment magnitude and yield for explosions, we resorted to an indirect approach. It is well known from seismic discrimination studies (e.g. Bolt, 1976; OTA, 1988) that nuclear explosions and earthquakes are generally different with respect to their relative excitation of long-period versus short-period seismic waves and this produces differences in surface-wave magnitude, M_S, with respect to m_b between the two source types. Similar differences are also implied for M_W versus m_b for the two source types. If we assume that seismic events with the same M_W have approximately equal M_S, then, based on experience with worldwide earthquakes (cf. Richter, 1957) and with NTS explosions (cf. Marshall et al., 1971; Murphy, 1977; Bache, 1982; OTA, 1988), for the same M_W we can infer

$$m_b \text{ (Explosion)} = m_b \text{ (Earthquake)} + 0.60 \qquad (8.1.2)$$

at magnitude levels of interest here. Finally, using empirical relations based on NTS experience between m_b and yield for explosions and the results of Houston and Kanamori (1986) for the empirical relationship between m_b and M_W for worldwide earthquakes, we have after some simplification

$$\log W \text{ (Equivalent Explosion)} = 0.654\, M_W \text{ (Earthquake)} - 0.780 \qquad (8.1.3)$$

where W is the yield in kilotons for the explosion equivalent to the earthquake with moment magnitude of M_W. To arrive at the ground motion predictions for this model, we used this approximate relationship to estimate yields for the equivalent explosions corresponding to the M_W's for the scenario earthquakes and simply applied the NTS explosion prediction relationship to obtain the 5-% damped PSRV response spectra. Figure 8.1 shows a comparison of 5-% damped PSRV spectra based on this equivalent explosion model for a fixed reference distance (viz. 10 km) and corresponding to a set of moment magnitudes, M_W, in the general range of interest. It should be noted for this and subsequent predictions derived from the NTS explosion experience that the period band for the spectra are somwhat more limited, mainly due to response of the recording systems

The second explosion-based empirical model involves a modification of the Geomatrix/ATC response spectra empirical model, as defined by Geomatrix (1992) and Sadigh et al. (1995), to include the region-specific attenuation information from the explosion experience appropriate to the vicinity of NTS and the Yucca Mountain site. The original Geomatrix model was based on analyses of the large empirical database of earthquake strong motion records principally from the California region. In our modified model we use the Geomatrix model to develop 5-% damped PSRV response spectra for the horizontal rock motions at a reference distance of 10 km for each of the postulated scenario earthquakes. Thus, the Geomatrix model establishes the level and the shape of the response spectrum at this reference distance. We then use the attenuation relationship from the power law model, derived from the experience with NTS explosions, to scale the spectrum at the reference distance to nearer or farther ranges. It is clear from this procedure that the calculated response spectra will generally match the standard Geomatrix model at distances near the reference distance and that departures away from that distance should be indicative of attenuation differences between the NTS region and the average for the Geomatrix data sample. Figure 8.2 shows that the somewhat stronger attenuation in the NTS

model causes the modified Geomatrix/ATC spectrum to lie above the standard spectrum at ranges less than 10 km and fall below the standard spectrum at farther ranges.

The third empirical model which we developed uses a reference response spectrum derived from the 1992 Little Skull Mountain earthquake which has been modified using the attenuation information from NTS explosion experience and scaled for magnitude based on the Geomatrix/ATC model, described above. In developing this model we used the 5-% damped PSRV spectra computed at eight strong motion sites for the 5.68 M_W Little Skull Mountain earthquake to determine a power law spectral model based on those observed data alone. We next derived a spectrum at a reference distance of 36 km, the average distance of the eight stations. This reference spectral shape was then scaled to nearer and farther distances corresponding to postulated scenario earthquakes using the NTS explosion-based attenuation exponents. After determining the spectrum for the appropriate distance, we scaled the ground motion up to the appropriate magnitude using the same magnitude dependence which is built into the Geomatrix/ATC empirical model. As will be shown in the following section, this model does a very good job in predicting the observed response spectra for the Little Skull Mountain earthquake, as would be expected since the ground motion attenuation observed from the Little Skull Mountain earthquake is not greatly different from that based on NTS explosion experience and no magnitude scaling is required.

8.2 Comparison of Predictions to 1992 Little Skull Mountain Earthquake Observations

The 1992 Little Skull Mountain earthquake is clearly important in seismic design consideration for the Yucca Mountain site because it represents a fairly large earthquake in a similar tectonic and propagation environment like that for several of the postulated scenario earthquakes. The main shock with magnitude 5.68 M_W was recorded at several surrounding strong motion stations at ranges between 12.9 km and 99.1 km from the fault. These strong motion records provide an excellent data sample to analyze characteristics of the ground motion from earthquakes in the vicinity of Yucca Mountain and to test modeling and prediction capability for such motions. As part of this project, we performed analyses of the attenuation characteristics of the PSRV spectra observed at the eight strong motion sites which recorded the Little Skull Mountain earthquake and attempted to test the explosion-based empirical prediction techniques described in the preceding section using the observed response spectra.

To analyze the attenuation of the strong motion observations from the main shock, we applied a power law model similar to that described above in equation 8.1.1. Because we were concerned with attenuation from a single event, there was no dependence on magnitude and the model reduced to

$$L(f) = L_0(f)\ R^{n(f)} \qquad (8.2.1)$$

for the PSRV spectra. Comparison of the N-S and E-W components of the PSRV spectra revealed insignificant (less than a factor of two) differences between the two observations at most stations and frequencies. We, therefore, performed the regression analyses on the combined data set with both horizontal components included as separate observations at each frequency. The attenuation exponent, n(f) in equation 8.2.1, was determined for each frequency as the slope of the least-squares linear fit to the response spectra measurements in log-log space. The attenuation exponents determined from the analysis of the Little Skull Mountain earthquake observations are compared to the attenuation exponents from the NTS explosion experience in Figure 8.3. The attenuation exponents from the NTS experience are seen to lie within the 95-% confidence limits bounding the mean values determined for the Little Skull Mountain earthquake at all periods in the left-hand figure. However, on the right the attenuation exponents for the Little Skull Mountain earthquake are seen to lie slightly above the rather narrow confidence bounds about the average NTS experience in a period band from about 0.2 to 2.0 seconds. Thus, over this band the Little Skull Mountain earthquake appears to show somewhat greater attenuation than that based on

average NTS explosion experience; but the differences are well within the statistical uncertainty in both estimates. The insignificance of the attenuation differences was further demonstrated by comparing the observed Little Skull Mountain response spectra at the eight strong motion sites with spectral predictions (1) based on the power law model derived directly from the Little Skull Mountain earthquake data and (2) based on the Little Skull Mountain earthquake spectral shape from a fixed reference distance scaled to other distance ranges using the NTS explosion attenuation exponents. There was little discernible difference found in the fits to the observations using these two approaches; the predictions for both approaches were generally within a factor of two of the observations at all stations and periods, and residuals for the two approaches were seen to have similar trends.

Figure 8.4 shows the 5-% damped PSRV spectrum derived from the power law model applied to the Little Skull Mountain earthquake observations. The figure compares the spectrum from the model at the average distance of the strong motion sites (viz. 35.7 km) with response spectra predicted for three other models: (1) the standard Geomatrix/ATC empirical model, (2) the modified Geomatrix/ATC model including NTS attenuation, and (3) the equivalent explosion model. At short periods (up to nearly 1 second) the three models show reasonable agreement among themselves and with the spectrum derived from the Little Skull Mountain earthquake observations. The standard Geomatrix/ATC empirical model actually appears to provide a somewhat better fit to the observed Little Skull Mountain earthquake spectrum over the period band from about 0.05 to 0.3 seconds. This is a little surprising considering that within this period range the attenuation derived from the Little Skull Mountain earthquake observations agreed quite well with NTS explosion experience, and this region-specific attenuation would be expected then to provide a better fit. Nevertheless, we find the agreement (within a factor of two) between the models within the short period band, up to almost 1-second period, is quite remarkable, particularly considering the simplicity of the assumptions used to develop some of the models, like the equivalent explosion model. It is only at long periods that we see divergence, with the three predictions all overestimating the observed response. One explanation for the differences seen here might be relatively poor excitation of longer-period surface waves or higher modes by the Little Skull Mountain earthquake because of a somewhat deeper than normal focal depth. We would certainly expect this to be the case for the equivalent explosion model because of the shallow explosion sources that contribute to the spectral shape there, but predictions based on the Geomatrix/ATC spectral shape are also significantly enhanced relative to the observations at periods from about 1 to 3 seconds. As described above, we have used the spectral estimate at the reference distance shown here for the Little Skull Mountain earthquake observations as the basis for our third ground motion prediction scheme. Thus, the PSRV spectrum labeled "LSM Observed" in Figure 8.4 serves as the reference spectral shape which we adjust for distance using NTS attenuation and scale with magnitude where necessary to provide our predictions.

We used the three explosion-based empirical models to compute 5-% damped PSRV spectral predictions for each of the eight strong motion sites from the Little Skull Mountain earthquake. For these calculations we used the magnitude of 5.68 M_W and the ranges to the stations measured from the surface projection of the fault - i.e. ranges between 12.9 km and 99.1 km. Figure 8.5 shows the spectra determined for the three modeling schemes at 12.9 km, the distance to the nearest station. The figure presents comparisons between the model predictions and the horizontal-component PSRV response spectra observed for the Little Skull Mountain earthquake at the Lathrop Wells site. The predictions all match the observations fairly well at periods up to about 1 second. At periods less than 0.1 seconds the predictions are tightly grouped and agree with the observations within a factor of about 1.4. Between periods of 0.1 and 1 second, there is somewhat more variability in the observations, but the predictions are generally within about a factor of 2. The best fit appears to be that provided by the Little Skull Mountain earthquake spectral shape scaled using the NTS attenuation, which provides a good fit to the two horizontal-component observations over nearly the entire period band shown, including longer periods. The other prediction schemes again tend to overestimate the observations at longer periods; the largest divergence from the observations is seen in the equivalent explosion prediction

which overestimates by about a factor of 4 at periods near 2 seconds. Similar results were found for comparisons between the explosion-based empirical model predictions and observations for the Little Skull Mountain earthquake spectra at other strong motion sites. These test cases for the Little Skull Mountain earthquake appear to provide some confirmation that the explosion-based empirical modeling schemes defined here, or some variant of those schemes, can provide a useful supplement to the alternative ground motion prediction methods based on physical models.

8.3 Ground Motion Predictions for Earthquake Scenarios at the Yucca Mountain Site

The earthquake hazard to the Yucca Mountain site can be defined in terms of a number of scenario earthquakes associated with faults in the general vicinity of the site. For this project six faults were considered: Bow Ridge, Paintbrush Canyon, Solitario Canyon, Bare Mountain, Rock Valley, and Furnace Creek. For the first four faults the scenario earthquakes have normal-slip mechanisms, based on the dominant sense of displacement observed for the fault, and are assumed to be represented by a moment magnitude of 6.4 M_W. For the Rock Valley and Furnace Creek faults the scenario earthquakes have strike-slip mechanisms, again based on the dominant sense of displacement, and are assumed to be represented by moment magnitudes of 6.71 M_W and 7.04 M_W respectively. For each of these scenario earthquakes, we used the explosion-based empirical models to predict 5-% damped PSRV spectra.

In specifying the distance to use in the ground motion calculations, we assumed hypocenters located at two different focal depths (viz. 6 km and 9 km) on the faults to provide some range of depth within the crust for the earthquake sources. Because our models essentially represent simple point sources with no effect of radiation pattern, the only effect of the focal depth differences is to alter the hypocentral distances used in the calculations. It should be noted in this regard that small differences in the assumed hypocentral distance produce relatively insignificant perturbations for the response spectra considering the other uncertainties associated with the predictions. For the normal fault scenarios, the faults were assumed to have a common dip of 57.5° with dip direction measured from field observations. The distances were then measured from the site to the hypocenter at the appropriate focal depth on each of the dipping faults. With these assumptions the hypocentral distances used for the base case normal fault scenario predictions ranged from 6.0 km to 13.3 km. For the strike-slip scenarios, the faults were assumed to be vertical; and the distances were again determined from the site to the appropriate hypocenter at each assumed focal depth on the fault. Because these faults are at fairly large horizontal distances from the Yucca Mountain site, the differences between the two assumed focal depths for the scenario earthquakes have little effect on the hypocentral distances. As a result, hypocentral distances for the Rock Valley fault scenario earthquakes are 26 km and 27 km, and hypocentral distances for the Furnace Creek fault scenario earthquakes are 51 km and 52 km.

For each of the scenario earthquakes, we calculated the PSRV spectral responses for the three empirical models described in Section 8.1 above. Thus, we generated a total of 36 response spectra for the 12 earthquake scenarios (i.e. two focal depths for each of the six faults). Figure 8.6 shows a representative prediction for the base case normal fault scenario with a magnitude of 6.4 Mw and a range of 9.1 km. This prediction corresponds to the Paintbrush Canyon fault scenario earthquake with a focal depth of 9 km. In Figure 8.6 we show comparisons of the predictions for each of the explosion-based empirical models with the prediction determined for the same scenario earthquake using the standard Geomatrix/ATC empirical model. The plot on the left shows fairly close agreement between the prediction for the equivalent explosion model and the standard Geomatrix/ATC model. At short periods, 0.05 to 0.1 seconds, and again at long periods, 0.9 to 3 seconds, the equivalent explosion model prediction lies slightly (about a factor of 1.5) above the standard Geomatrix/ATC model prediction; while at intermediate periods, 0.1 to 0.9 seconds, the two predictions overlap. The middle plot compares the standard Geomatrix/ATC empirical model prediction with the prediction using the Geomatrix/ATC model spectrum modified based on NTS explosion attenuation experience. The distance range is not much different from the reference distance used for the latter model, and as a result the two predictions are quite close. The modified

Geomatrix/ATC model prediction lies slightly above the standard model because of somewhat greater attenuation in the modified model, as discussed above. The plot on the right illustrates the steps in the process of scaling the Little Skull Mountain earthquake spectrum to the appropriate range and magnitude. Comparing the final predictions we note that the prediction based on the scaled Little Skull Mountain earthquake spectrum lies above the standard Geomatrix/ATC model prediction (by about a factor of 1.5 to 2) over the short period band, 0.05 to 0.3 seconds; while above 0.6 seconds the scaled Little Skull Mountain spectrum falls below the standard model predictions.

Figure 8.7 presents a similar set of predictions for the Furnace Creek fault scenario earthquake with a magnitude of 7.04 M_W and range of 52 km (9 km focal depth). The equivalent explosion spectrum generally agrees quite well with the standard Geomatrix/ATC spectral prediction over nearly the entire period band; maximum differences are less than a factor of about 1.5. For the modified Geomatrix/ATC model, we see in the middle plot that the predicted spectrum falls consistently below the standard model prediction by about a factor of 2. The differences are again apparently due to the stronger attenuation based on the NTS explosion experience; such differences tend to appear enhanced at the relatively large range for this scenario. Finally, the plot on the right in Figure 8.7 compares the scaled Little Skull Mountain earthquake spectrum with the standard Geomatrix/ATC model spectrum. The two predictions match very closely at short periods, 0.05 to 0.5 seconds. However, the spectral shapes are quite different; so that the scaled Little Skull Mountain prediction falls below the standard model spectrum by up to a factor of 3 at longer periods, above about 0.5 seconds.

As described elsewhere in this report, a number of physical fault rupture models were also used to provide strong ground motion predictions for the scenario earthquakes associated with the faults in the vicinity of the Yucca Mountain site. In Figure 8.8 we show a few examples of comparisons between those physical model results and the predictions developed for the explosion-based empirical models. The physical model spectra shown in each of these comparisons correspond to the median values determined from the spectral estimates derived from multiple realizations of four different physical models for each scenario. The four physical models contributing to the estimates shown here were (1) the barrier source model implemented by the University of Southern California, (2) the composite fractal source method used by the University of Nevada - Reno, (3) the stochastic method with subevents used by Pacific Engineering and Analysis, and (4) the broadband Green's function method used by Woodward-Clyde Consultants. As noted, the spectrum shown in each plot for these physical models is a median value and variations in the estimates, attributable to methodological differences and uncertainty in source parameter specification and attenuation, may be quite large, as evidenced by scatter between realizations.

The plot on the left in Figure 8.8 compares the explosion-based empirical model predictions determined for an earthquake with magnitude of 6.4 M_W at a range of 6.0 km with the prediction from the physical model. This prediction corresponds to the Paintbrush Canyon fault scenario earthquake for which we assumed a focal depth of 6 km. It should be noted that the plots in this figure correspond to 5-% damped acceleration response spectra in g's. Somewhat surprisingly the match between the spectra determined using our simple explosion-based empirical models and the median for the physical model spectrum is remarkably good. This is particularly notable considering that the estimates are for a close range site where the physical models would be expected to do a better job of accounting for near-source effects like radiation pattern which are disregarded in the explosion-based empirical models. At most periods the differences seen in the plot on the left amount to less than a factor of 2. Both the equivalent explosion and the scaled Little Skull Mountain earthquake spectra agree quite closely with the physical model prediction at short periods, 0.05 up to 0.2 seconds. Differences at longer periods are somewhat greater, particularly for the scaled Little Skull Mountain spectral prediction. However, even there it would appear that the uncertainty bounds about the median for the physical models probably envelope the explosion-based model predictions.

The middle and right-hand plots in Figure 8.8 correspond to the two strike-slip scenario earthquakes associated with the Rock Valley (6.71 M_W) and Furnace Creek (7.04 M_W) faults respectively. For these two scenarios there is more variation in the spectral prediction between our explosion-based models, and the difference between the spectra for those models and the median of the physical models is greater. The biggest differences seem to be those in the middle plot (i.e. Rock Valley scenario). There the equivalent explosion and scaled Little Skull Mountain earthquake spectrum fall below the physical model median by about a factor of 2 to 3 over a fairly broad period band, while the modified Geomatrix/ATC predictions are up to a factor of 4 lower than the physical model median. The predictions are more in agreement for the Furnace Creek scenario earthquake (shown in the right-hand figure), where maximum differences between the physical model median spectrum and the equivalent explosion and scaled Little Skull Mountain predictions are again low but only by about a factor of 2 at short periods, less than 1 second. We would suggest that the larger differences between the explosion-based and physical model predictions for the two strike-slip scenario earthquakes may be largely attributable to attenuation differences, which appear enhanced at the larger distances for these events. As noted above, the NTS explosion experience appears to indicate stronger attenuation in this region than for California. The prediction comparisons here seem to indicate that the stronger attenuation in the NTS region is not being adequately accounted for in the physical models.

8.4 Summary and Conclusions Regarding the Explosion-Based Empirical Modeling Procedures

Our objective in this element of the project has been to identify how the extensive experience with strong ground motion from NTS underground nuclear explosions might be used to assist in assessing earthquake ground motion predictions for use in design at the Yucca Mountain site. As part of these investigations, we analyzed strong ground motion observations from the 1992 Little Skull Mountain earthquake and compared those to the NTS explosion experience. Three explosion-based empirical models which take advantage of the NTS explosion experience as well as ground motion characteristics observed from the Little Skull Mountain earthquake were developed. We have applied these explosion-based empirical models to predict ground motions for the Little Skull Mountain earthquake and compared the results to observations as a test of the modeling procedures. The same models were then used to predict ground motions for several postulated scenario earthquakes which are being considered in assessing seismic design for the Yucca Mountain site.

In general, we find that the explosion-based empirical models do a fairly good job of predicting earthquake strong ground motion response spectra when compared to the Little Skull Mountain earthquake observations and to the alternative empirical and physical model predictions. With regard to specific model performance, we found that spectral predictions developed for our simple equivalent explosion model agreed surprisingly well with other prediction methods. Predictions based on the Little Skull Mountain earthquake spectral shape were generally found to be anomalously low at long periods compared to the other empirical prediction methods and to the physical model predictions; this might be associated with anomalous source depth. However, at periods below about 1 second, all three explosion-based models agree fairly well among themselves, with other empirical earthquake models, and with observations from the Little Skull Mountain earthquake, particularly at the nearer recording sites. Analyses of the 1992 Little Skull Mountain earthquake strong motion records indicate that the observed attenuation is not significantly different from that based on NTS explosion experience, so we would conclude that the explosion experience should play a role in assessing strong motion attenuation from postulated earthquakes in the region. This might be important considering that stronger attenuation in the NTS region does not appear to be properly accounted for in the physical models, particularly for more distant scenarios.

References

Bache, T. C. (1982). "Estimating the Yield of Underground Nuclear Explosions," Bull. Seism. Soc. Am. 72, pp. S131-S168.

Bennett, T. J., and J. R. Murphy (1993). "Estimation of Near-Regional Seismic Ground Motion from Underground Nuclear Explosion Tests," in Dynamic Analysis and Design Considerations for High-Level Nuclear Waste Repositories, edited by Q. A. Hossain, ASCE, New York, pp. 191-205.

Bolt, B. A. (1976). Nuclear Explosions and Earthquakes - The Parted Veil, W. H. Freeman and Company, San Francisco, CA.

Environmental Research Corporation (1974). "Prediction of Ground Motion Characteristics of Underground Nuclear Detonations," U.S. Atomic Energy Commission Nevada Operations Office Report NVO-1163-239, Las Vegas, NV.

Geomatrix (1992). "Seismic Ground Motion Studies for Major Northern California Bridges," Studies conducted in association with International Civil Engineering Consultants for Caltrans, Division of Structures, Sacramento, CA.

Houston, H., and H. Kanamori (1986). "Source Spectra of Great Earthquakes: Teleseismic Constraints on Rupture Process and Strong Motion," Bull. Seism. Soc. Am. 76, pp. 19-42.

Marshall, P. D., A. Douglas, and J. A. Hudson (1971). "Surface Waves from Underground Nuclear Explosions," Nature 234, pp. 8-9.

Murphy, J. R. (1977). "Seismic Source Functions and Magnitude Determinations for Underground Nuclear Detonations," Bull. Seism. Soc. Am. 67, pp. 135-158.

Office of Technology Assessment (1988). Seismic Verification of Nuclear Testing Treaties, OTA-ISC-361, Washington, D.C.

Phillips, J. S. (1991). "Prediction of Pseudo Relative Velocity Response Spectra at Yucca Mountain for Underground Nuclear Explosions Conducted in the Pahute Mesa Testing Area at the Nevada Test Site," Sandia Report Sand88-3032, Albuquerque, NM.

Richter, C. F. (1957). Elementary Seismology, W. H. Freeman and Company, San Francisco, CA.

Sadigh, K., C.-Y. Chang, N. A. Abrahamson, S. J. Chiou, and M. S. Power (1995). "Specification of Long-Period Ground Motions: Updated Attenuation Relationships for Rock Site Conditions and Adjustment Factors for Near-Fault Effects," in Technical Papers on Seismic Isolation, ATC-17.1, pp. 59-68.

Vortman, L. J. (1986). "Ground Motion Produced at Yucca Mountain from Pahute Mesa Underground Nuclear Explosions," Sandia Report Sand86-7006, Albuquerque, NM.

Figure Captions

Figure 8.1 Comparison of 5-% damped PSRV spectra predictions at a range of 10 km for the NTS equivalent explosion model for different moment magnitudes in the range of interest.

Figure 8.2 Comparison of standard Geomatrix/ATC 5-% damped PSRV spectral predictions with predictions produced using the Geomatrix/ATC spectral shape at 10 km scaled with distance using NTS explosion attenuation experience. Note the two predictions coincide at the nominal reference distance of 10 km.

Figure 8.3 Comparison of distance attenuation exponents and their 95-% confidence limits for NTS explosion experience and Little Skull Mountain (LSM) earthquake observations. NTS experience falls within the larger confidence limits about the LSM average (left), while LSM attenuation falls within or just above the smaller confidence limits surrounding average NTS experience (right).

Figure 8.4 Comparison of 5-% damped PSRV spectral predictions for three models with the spectrum at R = 35.7 km derived from the power law model applied to the Little Skull Mountain earthquake observations.

Figure 8.5 Comparison of 5-% damped PSRV spectral predictions for the three explosion-based empirical models with the spectra observed at the Lathrop Wells site (R = 12.9 km) for the Little Skull Mountain earthquake.

Figure 8.6 Comparison of 5-% damped PSRV spectral predictions for the base case normal scenario earthquake (Mw = 6.4) for the Yucca Mountain site at a range of 9.1 km for the equivalent explosion model (left), modified Geomatrix/ATC model (center), and Little Skull Mountain earthquake spectral shape scaled with NTS attenuation and Geomatrix/ATC magnitude dependence (right). For reference the model results are compared to similar spectral predictions based on the standard Geomatrix/ATC empirical model.

Figure 8.7 Comparison of 5-% damped PSRV spectral predictions for the Furnace Creek fault strike-slip scenario earthquake (Mw = 7.04) for the Yucca Mountain site at a range of 52 km for the equivalent explosion model (left), modified Geomatrix/ATC model (center), and Little Skull Mountain earthquake spectral shape scaled with NTS attenuation and Geomatrix/ATC magnitude dependence (right). For reference the model results are compared to similar spectral predictions based on the standard Geomatrix/ATC empirical model.

Figure 8.8 Comparison of 5-% damped acceleration response spectral predictions for the three explosion-based empirical models with the median of the spectral predictions determined from four physical models for the Solitario Canyon fault scenario earthquake (left), the Rock Valley fault scenario earthquake (center), and the Furnace Creek fault scenario earthquake (right).

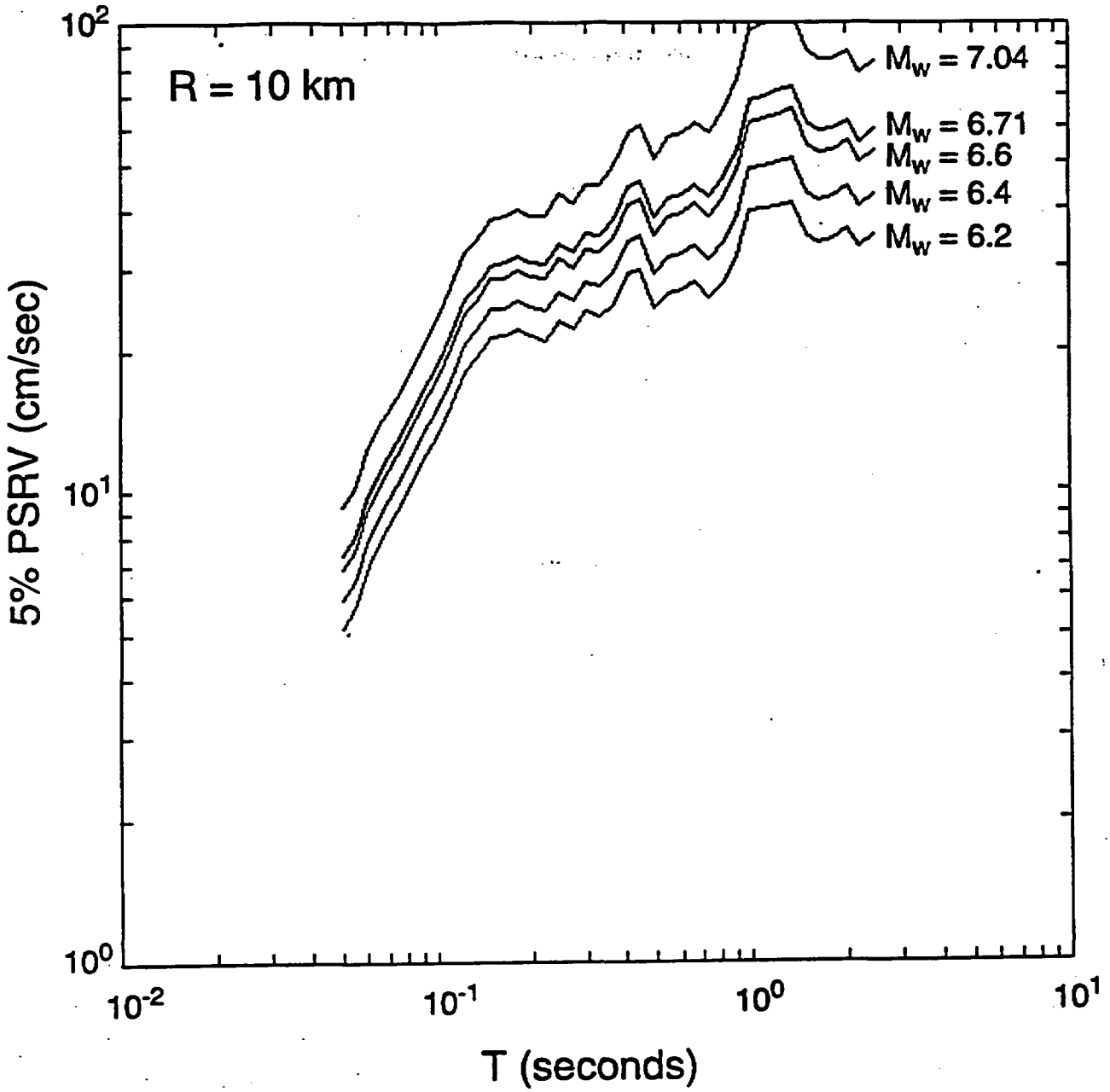
R = 10 km
M_w = 7.04
M_w = 6.71
M_w = 6.6
M_w = 6.4
M_w = 6.2
5% PSRV (cm/sec)
T (seconds)
10^2
10^1
10^0
10^{-2}
10^{-1}
10^0
10^1

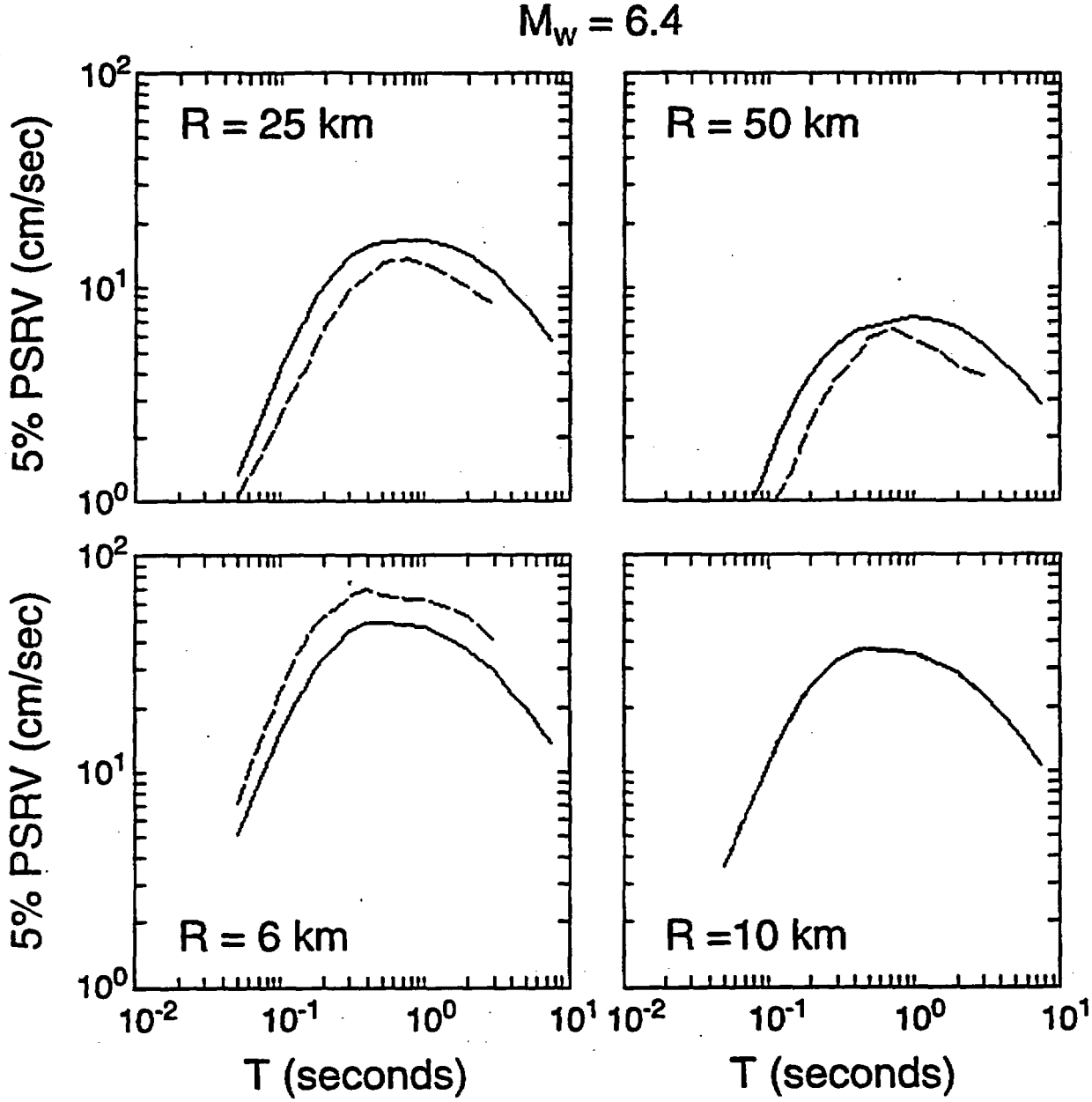
$M_W = 6.4$
R = 25 km
R = 50 km
R = 6 km
R =10 km
5% PSRV (cm/sec)
5% PSRV (cm/sec)
10^2
10^1
10^0
10^{-2}
10^{-1}
10^0
10^1
T (seconds)
T (seconds)

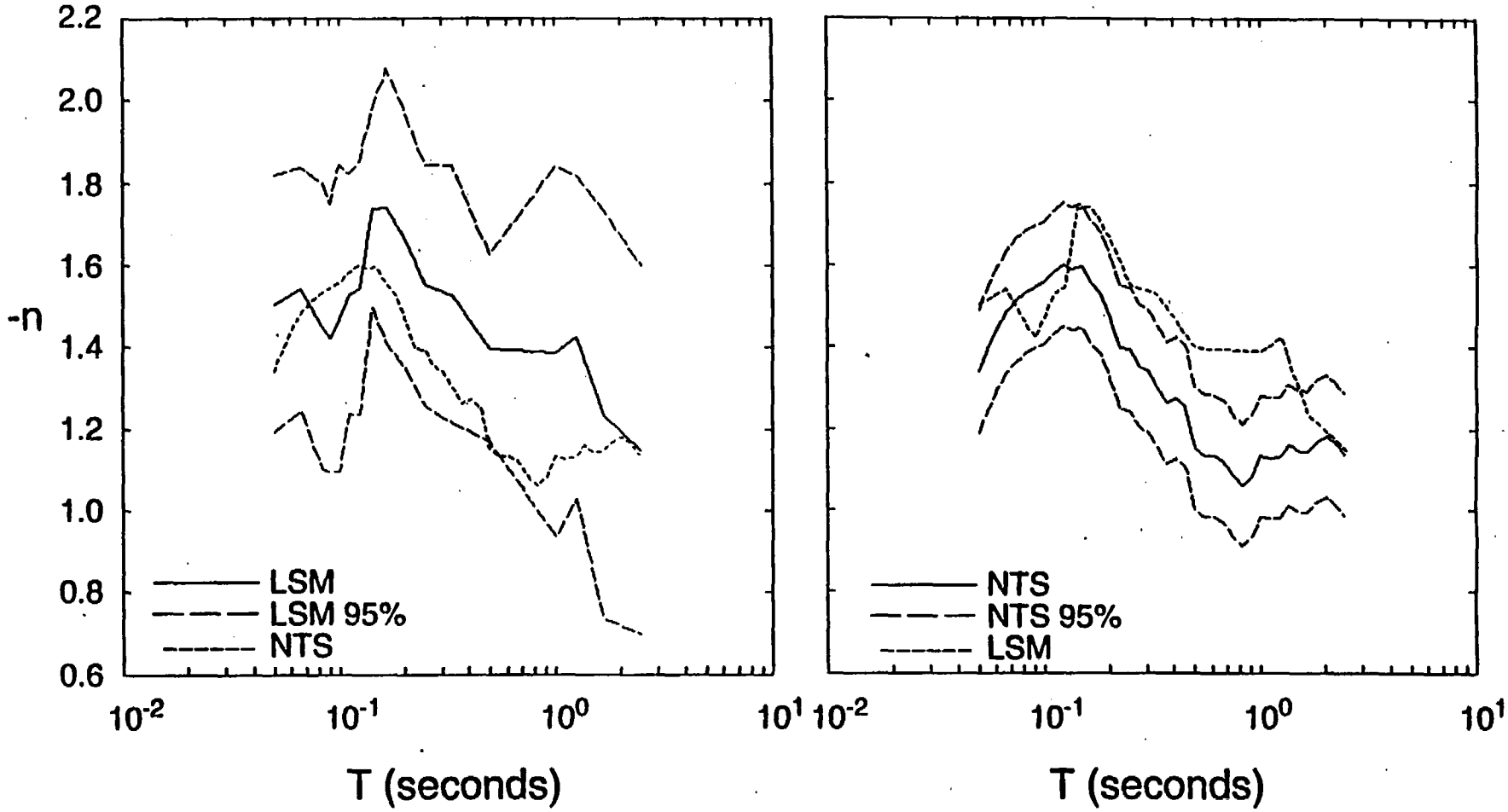
2.2
2.0
1.8
1.6
1.4
1.2
1.0
0.8
0.6
-n
LSM
LSM 95%
NTS
10^{-2}
10^{-1}
10^{0}
10^{1}
T (seconds)
NTS
NTS 95%
LSM
10^{-2}
10^{-1}
10^{0}
10^{1}
T (seconds)

5.2-13

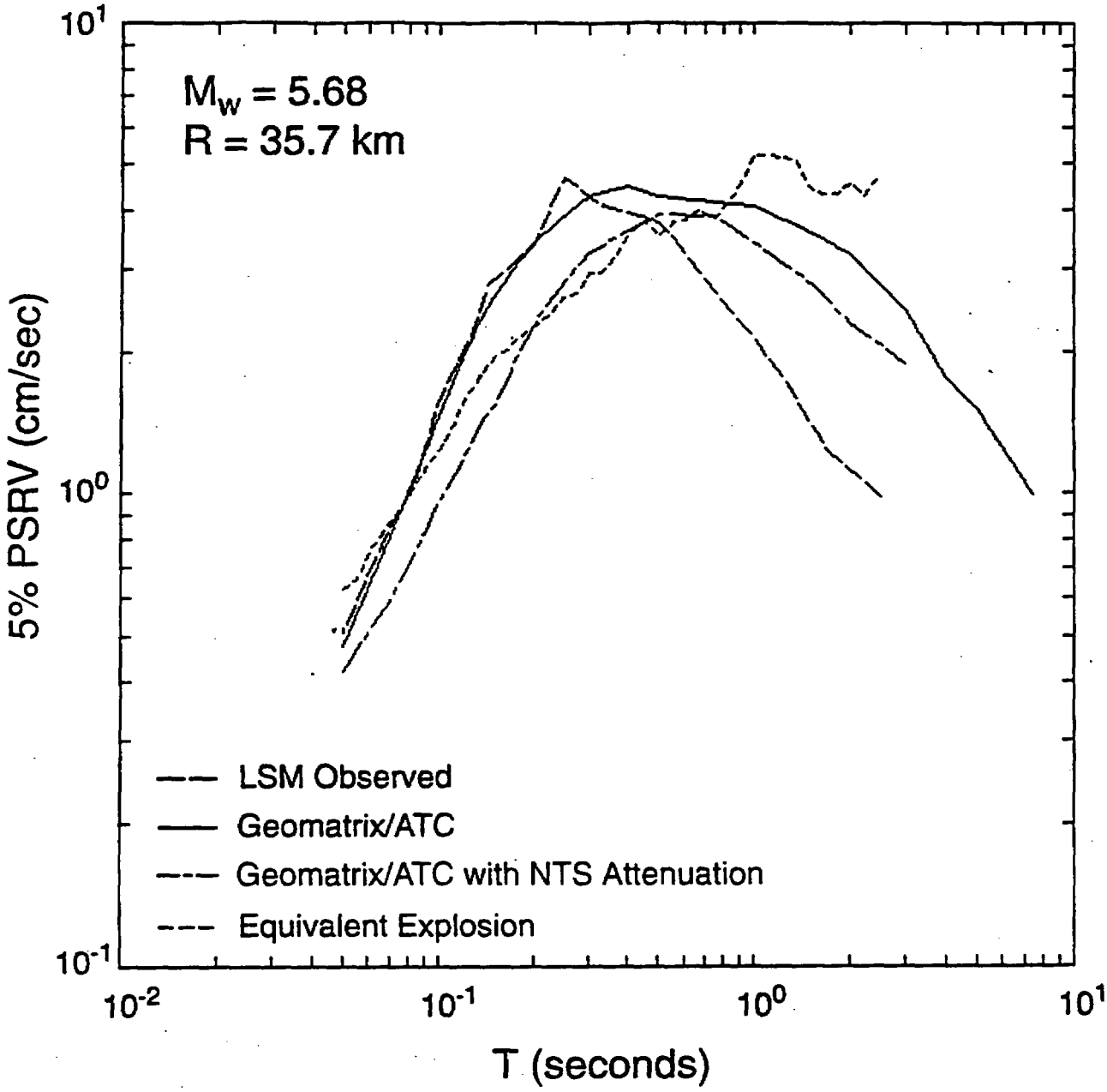
M_w = 5.68
R = 35.7 km
5% PSRV (cm/sec)
T (seconds)
LSM Observed
Geomatrix/ATC
Geomatrix/ATC with NTS Attenuation
Equivalent Explosion
10^1
10^0
10^{-1}
10^{-2}
10^{-1}
10^0
10^1

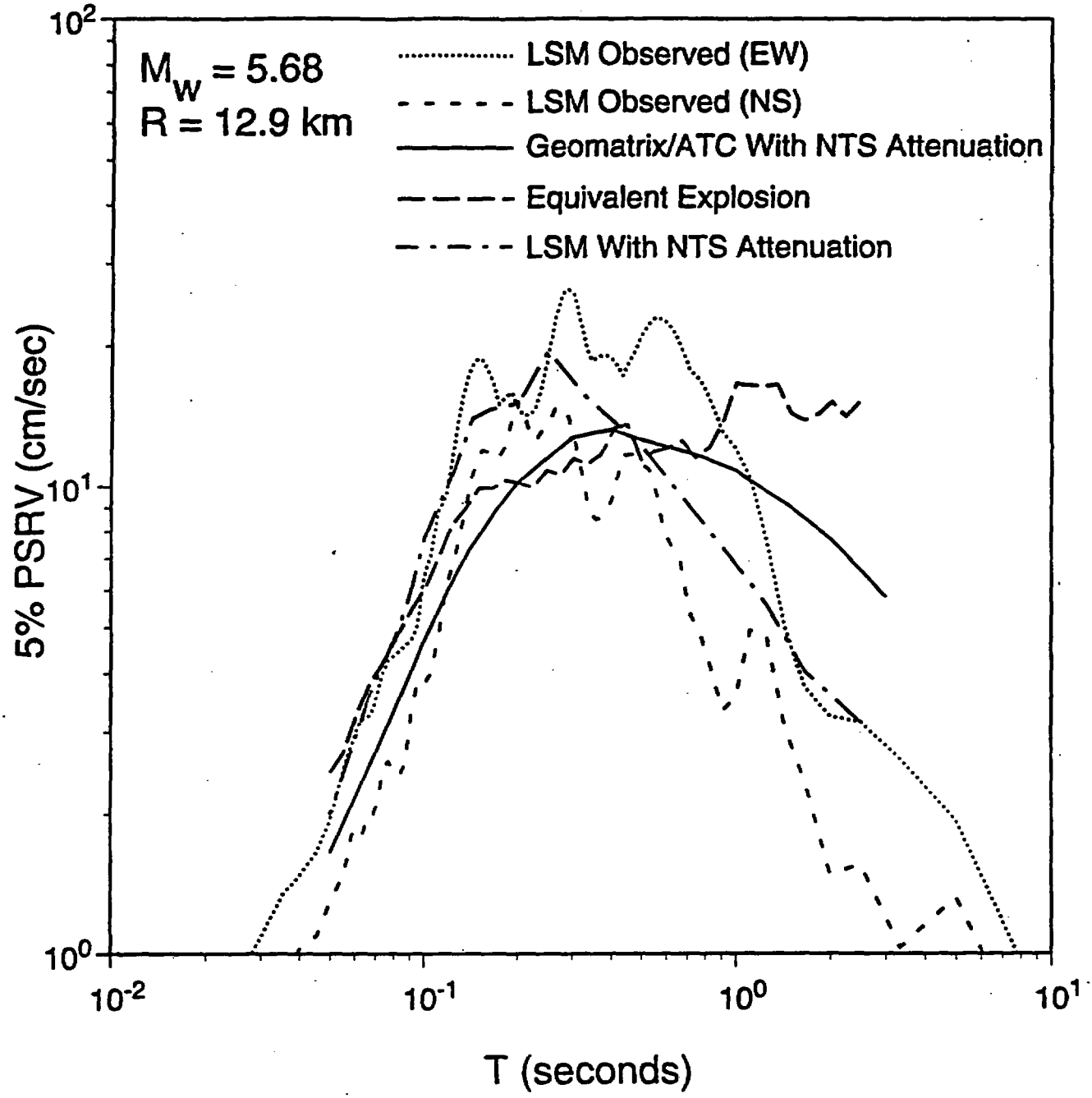
M_w = 5.68
R = 12.9 km
LSM Observed (EW)
LSM Observed (NS)
Geomatrix/ATC With NTS Attenuation
Equivalent Explosion
LSM With NTS Attenuation
5% PSRV (cm/sec)
10^2
10^1
10^0
10^{-2}
10^{-1}
10^0
10^1
T (seconds)

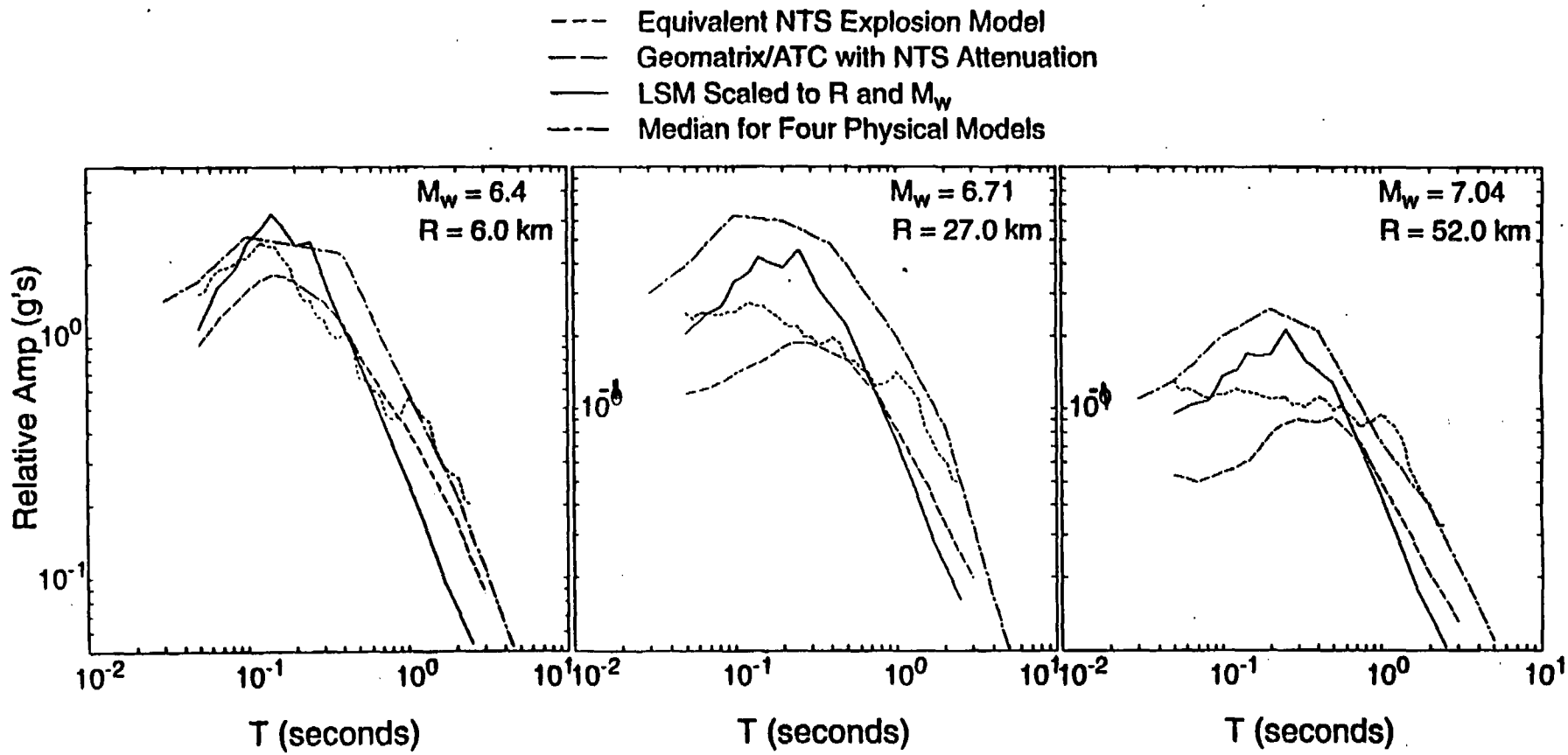
Equivalent NTS Explosion Model
Geomatrix/ATC with NTS Attenuation
LSM Scaled to R and M_W
Median for Four Physical Models
M_W = 6.4
R = 6.0 km
M_W = 6.71
R = 27.0 km
M_W = 7.04
R = 52.0 km
Relative Amp (g's)
10^0
10^{-1}
10^{-2}
10^1
T (seconds)

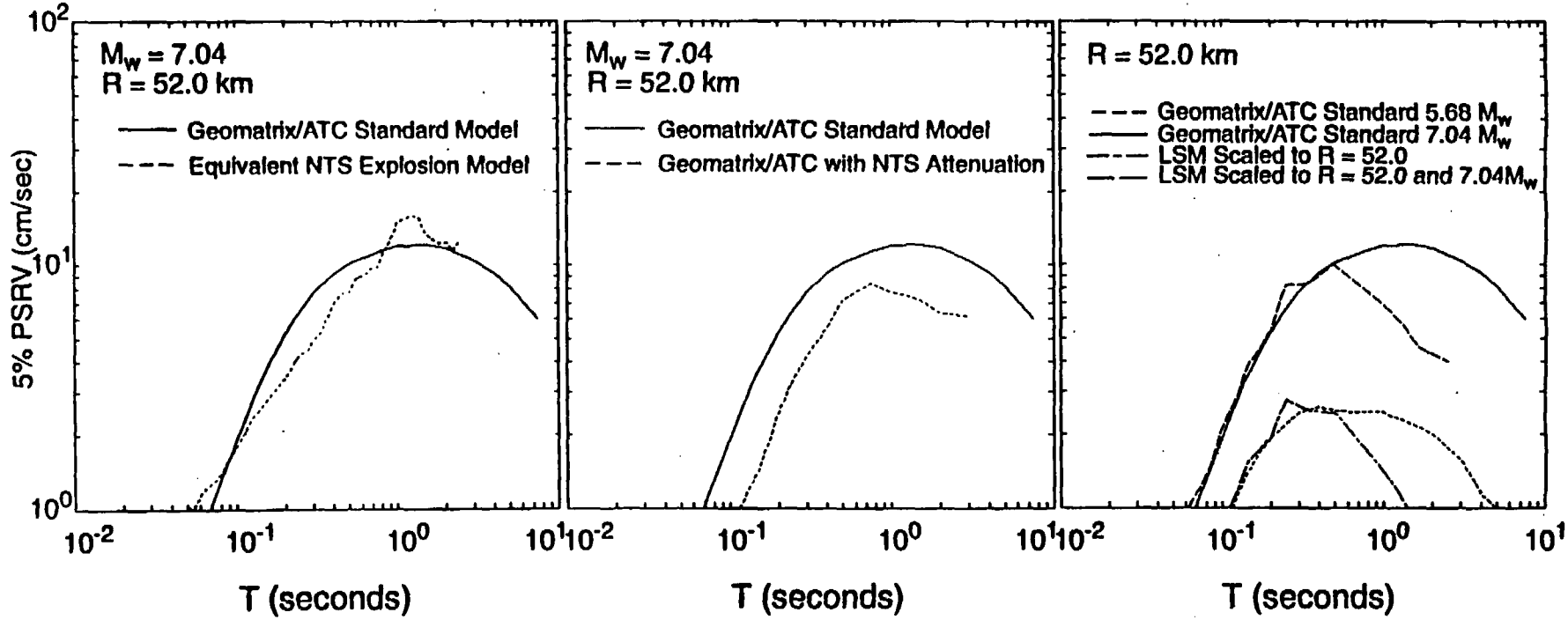
M_w = 7.04
R = 52.0 km
Geomatrix/ATC Standard Model
Equivalent NTS Explosion Model
M_w = 7.04
R = 52.0 km
Geomatrix/ATC Standard Model
Geomatrix/ATC with NTS Attenuation
R = 52.0 km
Geomatrix/ATC Standard 5.68 M_w
Geomatrix/ATC Standard 7.04 M_w
LSM Scaled to R = 52.0
LSM Scaled to R = 52.0 and 7.04M_w
5% PSRV (cm/sec)
10^2
10^1
10^0
10^{-2}
10^{-1}
10^0
10^1
T (seconds)

S.2-12

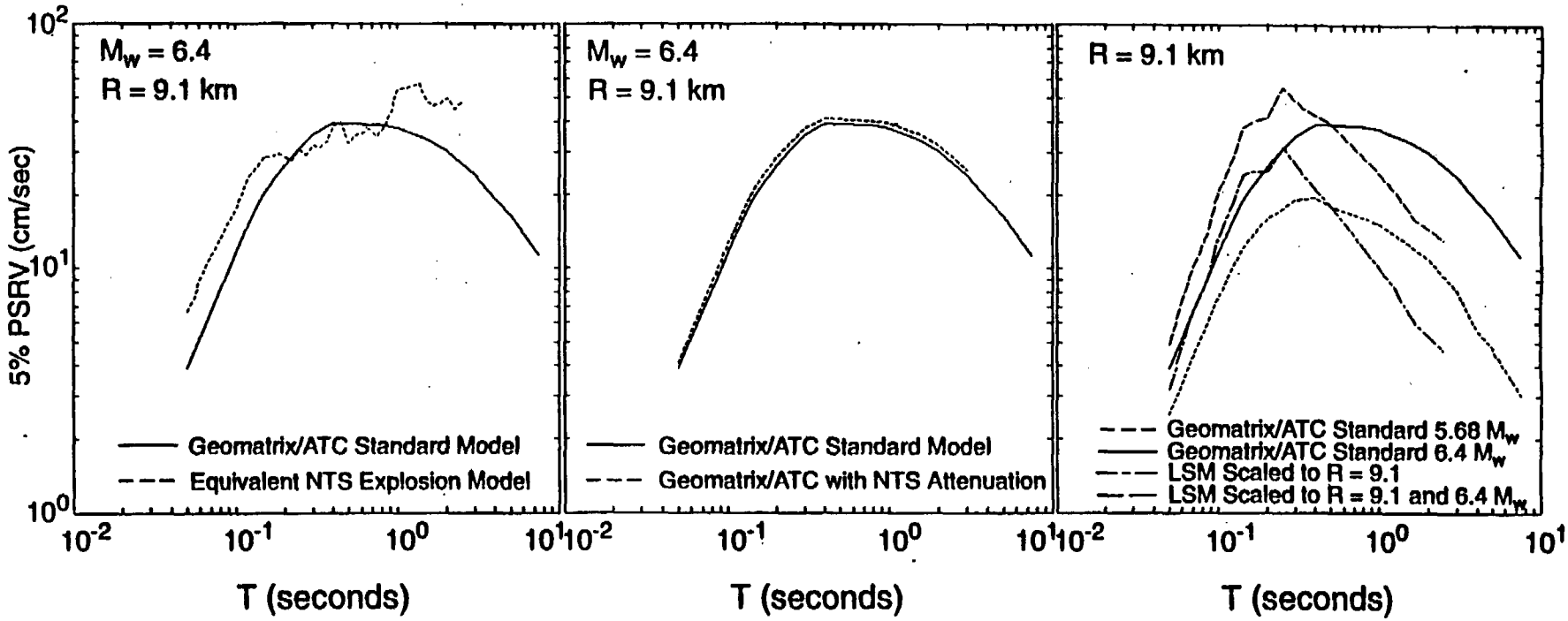
10^2
10^1
10^0
5% PSRV (cm/sec)
M_w = 6.4
R = 9.1 km
Geomatrix/ATC Standard Model
Equivalent NTS Explosion Model
M_w = 6.4
R = 9.1 km
Geomatrix/ATC Standard Model
Geomatrix/ATC with NTS Attenuation
R = 9.1 km
Geomatrix/ATC Standard 5.68 M_w
Geomatrix/ATC Standard 6.4 M_w
LSM Scaled to R = 9.1
LSM Scaled to R = 9.1 and 6.4 M_w
10^{-2}
10^{-1}
10^0
10^1
T (seconds)

5.3 Excerts from Prediction of ground motion characteristics of underground nuclear explosions

NVO-1163-239

NVO-1163-239
UC-11

PREDICTION OF GROUND MOTION CHARACTERISTICS OF UNDERGROUND NUCLEAR DETONATIONS

ENVIRONMENTAL RESEARCH CORPORATION
2769 South Highland Drive
Las Vegas, Nevada 89109

March 1974

PREPARED FOR THE U. S. ATOMIC ENERGY COMMISSION
NEVADA OPERATIONS OFFICE
UNDER CONTRACT NO. AT(29-2)-1163

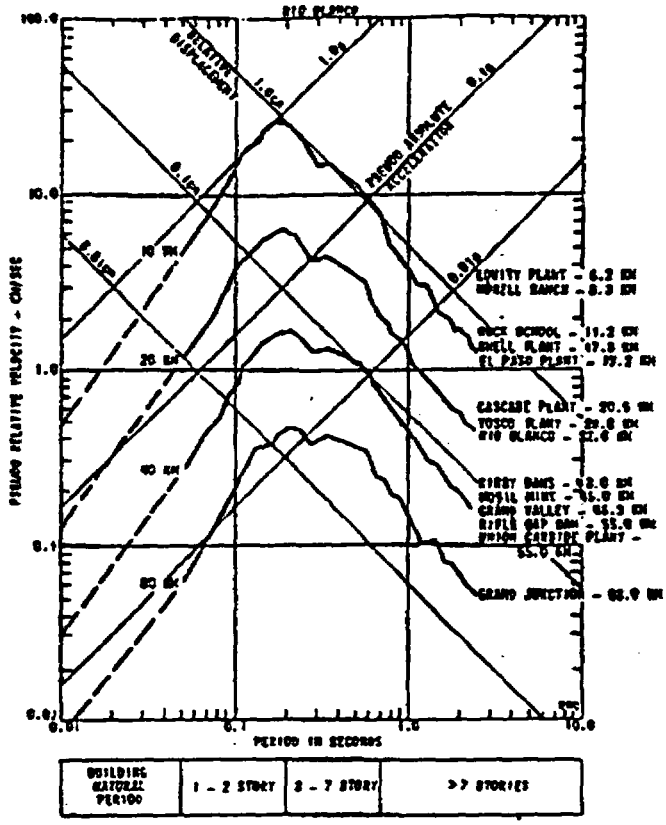

Figure 2.18. Example of Family of Predicted Mean 5% Damped PSRV Spectra, Rio Blanco Event

2.13 PREDICTION EQUATIONS

The functional relationship between mean ground motion, $\hat{M}$ (peak amplitude or spectral value at a single period) and the independent variables yield, W, and distance, R, is a power law of the form

$$\hat{M}(W, R) = A W^{B_1} R^{B_2} \quad .$$

This general equation describes the trend of the ground motion parameter with individual observations distributed in a random manner about the mean value. The distribution about the geometric mean is approximately log-normal and is characterized by the geometric standard error of estimate, σ. The amplitude coefficient, A, and the yield (B_1) and distance (B_2) scaling exponents are derived by standard statistical analyses of ground motion data.

2.13.1.3 Equation Group 3: Regression Equations for Peak Vector Motions, Pahute Mesa (Whipple and O'Brien, 1970a)

Event Area and Type of Motion	Equations: $\hat{M} = AW^{B_1} R^{B_2}$	Number of Data Points	Standard Error of Estimate
PAHUTE MESA: Acceleration: (g)	$a = 2.49 \times 10^{-1} W^{0.464} R^{-1.34}$	401	2.30
PAHUTE MESA: Velocity: (cm/sec)	$u = 6.64 \times 10^{0} W^{0.622} R^{-1.34}$	221	1.95
PAHUTE MESA: Displacement: (cm)	$d = 4.41 \times 10^{-1} W^{0.775} R^{-1.17}$	380	2.12

2.13.1.4 Equation Group 4: Average Ratio of Peak Horizontal to Resultant Vector Accelerations, Pahute Mesa Detonations

STATION	RATIO	STATION	RATIO
Mercury (Q25)	0.8	Las Vegas (SE-6)	0.7
Tonopah Church	0.6	Las Vegas (SQP)	0.9
Tonopah Motel	0.9	E-MAD	0.8
Beatty Hardrock	0.8	NRDS-1	0.8
Beatty Alluvium	0.9	Alamo Alluvium	0.8

These are applied by multiplying the appropriate equations in Groups 1, 2, 3 or 5

2.13.1.6 Equation Group 6: Regression Equations to Predict 5% Damped PSRV Spectra, Pahute Mesa Detonations (From Lynch, 1969)

Period	Amplitude Coefficient A	Yield Exponent B_1	Distance Exponent B_2	Standard Error of Estimate σ
.050	2.69E+00	.491	-1.340	3.06
.055	3.69E+00	.479	-1.395	2.87
.061	5.00E+00	.483	-1.447	2.85
.067	6.76E+00	.474	-1.486	2.84
.075	8.87E+00	.463	-1.515	2.88
.082	1.08E+01	.457	-1.533	2.85
.091	1.18E+01	.468	-1.546	2.98
.101	1.29E+01	.475	-1.558	2.96
.111	1.53E+01	.480	-1.582	2.97
.123	1.89E+01	.480	-1.600	2.98
.136	2.18E+01	.468	-1.591	3.02
.150	2.48E+01	.466	-1.597	2.98
.166	2.06E+01	.478	-1.555	2.87
.183	2.01E+01	.479	-1.533	2.84
.203	1.67E+01	.480	-1.469	2.82
.224	1.21E+01	.498	-1.399	2.82
.248	1.21E+01	.509	-1.395	2.72
.274	1.10E+01	.504	-1.354	2.65
.302	1.13E+01	.508	-1.342	2.62
.334	8.65E+00	.528	-1.303	2.66
.369	6.82E+00	.555	-1.263	2.62
.408	7.15E+00	.572	-1.276	2.62
.451	6.40E+00	.583	-1.255	2.49
.499	3.63E+00	.601	-1.150	2.54
.551	2.96E+00	.632	-1.134	2.54
.609	2.93E+00	.636	-1.134	2.59
.673	2.76E+00	.645	-1.121	2.55
.744	2.02E+00	.665	-1.085	2.54
.822	1.59E+00	.698	-1.060	2.52
.908	1.72E+00	.713	-1.083	2.54
1.004	2.08E+00	.732	-1.133	2.62
1.110	1.83E+00	.748	-1.128	2.69
1.226	1.56E+00	.771	-1.129	2.75
1.355	1.66E+00	.775	-1.160	2.74
1.498	1.61E+00	.753	-1.145	2.74
1.655	1.59E+00	.749	-1.143	2.78
1.829	1.96E+00	.732	-1.168	2.76
2.022	2.35E+00	.719	-1.181	2.72
2.234	2.37E+00	.701	-1.165	2.72
2.469	2.40E+00	.699	-1.137	2.72

Sample: 260 PSRV spectra from 11 Pahute Mesa detonations; yield range 20 to 1200 kt; distance range 4.4 to 551 km. Mean yield ~200 kt; mean distance ~100 km.

Section 6

Hybrid Empirical Model

DOCUMENTATION OF EXCEL 5.0 SPREADSHEETS FOR DEVELOPING HYBRID EMPIRICAL GROUND-MOTION ESTIMATES

Kenneth W. Campbell

EQE International, Inc.
Evergreen, Colorado

INTRODUCTION

I have developed several EXCEL 5.0 spreadsheets for calculating the various distance measures and empirical ground-motion estimates for application of the Hybrid Empirical Ground Motion Model, hereafter referred to as the Hybrid Model. These spreadsheets allow the user to add distances and ground-motion parameters for which the estimates are to be made as well as change the weights assigned to the various relationships and adjustment factors. A brief description of the spreadsheets are given below.

DESCRIPTION OF SPREADSHEETS

1. DIST_SH.XLS and DIST_DP.XLS

These spreadsheets calculate the three fault-distance measures required to estimate empirical ground motions using contemporary empirical strong-motion attenuation relationships for both shallow-focus (DIST_SH.XLS) and deep-focus (DIST_DP.XLS) earthquakes. Each spreadsheet contains three worksheets for fault dips of 90, 60, and 30 degrees. Distances for other fault dips can be calculated by simply changing the value of the fault dip on any of the worksheets or by copying an existing worksheet to a new worksheet and changing the fault dip to the desired value. Significant parameters in these spreadsheets are defined below. Only those parameters that are required to use the spreadsheets are described. All depths, widths, and distances have units of kilometers.

alpha. The dip of the fault plane measured from a horizontal plane in degrees. The dips of 90 and 60 degrees were specified by the methodology team. The dip of 30 degrees is included because there is a possibility that faults with this dip will be considered sometime in the future.

d. Depth to the center of the fault-rupture plane. This parameter is only used for shallow-focus earthquakes for which this depth is held constant for all rupture scenarios. This depth (5 km) was specified by the methodology team.

dmax. Maximum depth of fault rupture. This depth (14 km) was specified by the methodology team. For deep-focus earthquakes, the fault rupture was constrained to propagate to this depth for all earthquake scenarios, as specified by the methodology team.

dseis. Depth to the top of the seismogenic portion of the fault. The seismogenic zone of rupture is not allowed to propagate to depths shallower than this value. This

depth should be selected by the user. The value of 3 km is the minimum value recommended by Campbell (1997).

Magnitude. Moment magnitude, Mw. The values of Mw were provided by the methodology team.

Fault Width. The median estimate of the fault rupture width for the given value of moment magnitude (Mw). This width is calculated using a relationship between rupture width and magnitude developed by Wells and Coppersmith (1994), as specified by the methodology team.

Horizontal Distance. The horizontal distance from the site to the surface trace of the fault. The values of these distances were provided by the methodology team.

Rjb. The shortest distance from the site to the projection of the fault rupture plane on the surface of the earth. This is the distance measure proposed by Joyner and Boore. See Abrahamson and Shedlock (1997) for a brief description of this distance measure.

Rrup. The shortest distance from the site to the fault rupture plane. See Abrahamson and Shedlock (1997) for a brief description of this distance measure.

Rseis. The shortest distance from the site to the seismogenic part of the fault rupture plane. This is the distance measure proposed by Campbell. See Abrahamson and Shedlock (1997) for a brief description of this distance measure.

2. HYBRD_SH.XLS and HYBRD_DP.XLS

These spreadsheets calculate hybrid empirical ground-motion parameters for both shallow-focus (HYBRD_SH.XLS) and deep-focus (HYBRD_DP.XLS) earthquakes using contemporary empirical strong-motion attenuation relationships for California (except for Spudich et al., 1997) and adjustment factors for applying the California ground-motion estimates to Yucca Mountain. The adjustment factors were calculated using the band-limited white noise (BLWN) point-source stochastic simulation model with PSA, PGA, and PGV estimated from random vibration theory (RVT). A single estimate of these parameters were developed for California for each magnitude and distance of interest using model parameters developed by Walt Silva (personal communication), which he developed by calibrating these parameters to give ground-motion estimates consistent with the empirical attenuation relationship developed by Abrahamson and Silva (1997). Multiple estimates were developed for Yucca Mountain taking into account uncertainty in the median estimates of crustal attenuation (both Q_0 and (), site amplification (characterized by shear-wave velocity and density as a function of depth), and site attenuation (($_0$).

Each spreadsheet contains five worksheets. The first three worksheets give empirical estimates of ground motion for the specified ground-motion parameters, magnitudes, and horizontal distances for fault dips of 90 and 60 degrees, the latter for both the hanging wall and the foot wall of the fault plane (not the rupture plane). The fourth worksheet (Factors) gives the calculated adjustment factors and their standard deviations for the same set of ground-motion parameters, magnitudes, and distances: The fifth worksheet (Hybrid

Estimates) gives an example of the calculation of ground motions using the Hybrid Model for a single ground-motion parameter (5%-damped pseudo-absolute acceleration at 0.5 Hz) and a single value of moment magnitude ($M_W = 5.0$). The user can add additional ground-motion parameters, magnitudes, and distances by extending the table with the existing entries and changing the references in the cells to the appropriate cells in the other worksheets.

Significant parameters in these spreadsheets are defined below. Only those parameters that are required to use the spreadsheets are described. Parameters common to more than one worksheet are defined only once.

Empirical Estimates Worksheets (Dip=90; Dip=60, Hanging Wall; Dip=60, Foot Wall)

Attenuation Relationships. Identification of the attenuation relationships used to develop the empirical ground-motion estimates. The user can add additional relationships if desired.

Dip. The dip of the fault plane measured from a horizontal plane in degrees.

Style of Faulting (F). The style of faulting parameter F used in the attenuation relationships. The default value of 0 corresponds to strike-slip faulting. Most relationships do not include many normal-faulting earthquakes, but the authors generally recommend that F = 0 be used for normal-faulting earthquakes. This parameter should be selected by the user based on his or her opinion as to what value is appropriate for Yucca Mountain faults.

Depth to Hard Rock (D). The depth to basement (hard) rock defined by Campbell. This parameter was selected as the depth to the Yucca Mountain stratum with an S-wave velocity (V_S) of 2.9 km/sec and a P-wave velocity (V_P) of 5.0 km/sec, generally consistent with the recommendations provided by Campbell (1997), minus the depth to the stratum at which the ground-motion estimates are calculated (i.e., the stratum with $V_S = 1.9$ km/sec and $V_P = 3.2$ km/sec). This parameter is site-dependent and can be adjusted by the user as appropriate.

Mw. Moment magnitude.

Rhor. Horizontal distance to the surface trace of the fault plane. The values of these distances were specified by the methodology team.

Rjb, Rrup, Rseis. The fault-distance measures defined above. The values are those calculated in the DIST_SH.XLS and DIST_DP.XLS spreadsheets for the specified values of *Mw* and *Rhor*.

PSA. The random horizontal component of 5%-damped pseudo-absolute acceleration in g for oscillator frequencies of 0.5, 1.0, 2.0, 5.0, 10.0, and 20 Hz.

PGA. The random horizontal component of peak ground acceleration in g.

PGV. The random horizontal component of peak ground velocity in cm/sec.

Median Ground Motion Estimates. The median estimates of PSA, PGA, and PGV from the selected attenuation relationships. Only Campbell (1997) and Joyner and Boore (1988) developed attenuation relationships for PGV. Other estimates were developed by applying the median ratio of PGV to PGA from these two relationships to the median estimates of PGA from the other relationships.

Standard Errors. The standard errors (i.e., aleatory uncertainty) associated with the empirical estimates of PSA, PGA, and PGV, increased to represent the random horizontal component, if necessary, using the horizontal inter-component standard deviation calculated by Boore et al. (1997).

Subjective Weights. The weights assigned to each of the attenuation relationships. These weights must add up to 1, but can be 0 for those attenuation relationships which are not used. Equal weights were assumed for demonstration purposes only. The user should select these weights according to his or her belief that the relationship is appropriate for the specific magnitude and distance for which the estimate is being developed. Changing the weights will automatically adjust the weighted estimates in the spreadsheet.

Weighted Median. There are two sets of weighted medians, each weighted by the subjective weights assigned to the attenuation relationships: (1) the weighted median of the median ground-motion estimates, with weights applied to the logarithm of the ground-motion parameters assuming a lognormal distribution of the medians; and (2) the weighted median of the standard errors, with weights applied to the standard errors assuming a normal distribution of the standard errors.

Weighted (. There are two sets of weighted (s, each weighted by the subjective weights assigned to the attenuation relationships: (1) the weighted standard deviation of the median ground-motion estimates (i.e., epistemic modeling uncertainty), and (2) the weighted standard deviation of the standard errors. The weights are applied to the square of the standard deviations (i.e., to the variances), which is consistent with the definition of the weighted standard error in weighted regression analyses.

Adjustment Factors Worksheet (Factors)

((. Stress drop in bars. Calculations were done for a suite of stress drops so that the user can select which stress drop to use in developing the adjustment factors.

Adjustment Factors. The multiplicative adjustment factors for estimating ground-motion parameters for Yucca Mountain from those parameters estimated for California. These factors were developed using the BLWN-RVT stochastic simulation model as described above. The median represents the median of the factors calculated from the proposed Yucca Mountain models. The (represents the standard deviation of the factors calculated from the distribution of the proposed Yucca Mountain model parameters (i.e., epistemic parametric uncertainty), assuming no uncertainty in the California model parameters. This latter assumption should be evaluated by the user. The reasons for not including any uncertainty in the California model estimates are: (1) the model parameters were

constrained by calibrating the model to the Abrahamson and Silva (1997) attenuation relationship, so modeling uncertainty that would result from calibrating these parameters to other attenuation relationships is already accounted for in the modeling uncertainty of the empirical estimates from these attenuation relationships (note that there may be a bias between the ground-motion estimates from this attenuation relationship and the weighted median of all of the attenuation relationships which has not been included); (2) the set of California parameters cannot be replaced with independent assessments of these parameters because of inter-parameter correlation, and (3) the same model is applied in both California and the Yucca Mountain regions, so presumably uncertainty in the appropriateness of the stochastic simulation model does not contribute significantly to the modeling uncertainty in the calculated adjustment factors.

Subjective Weights. The weights assigned to each of the stress drops. These weights must add up to 1, but can be 0 for those stress drops which are not used. The given weighting scheme is for demonstration purposes only. The user should select these weights according to his or her belief that the stress drop is appropriate for earthquakes in the Yucca Mountain region. Note that the stress drop used for California earthquakes in the development of the adjustment factors was 59 bars, so appropriate median stress drops for earthquakes in the Yucca Mountain region should be selected relative to this value (i.e., whether the median stress drop is higher or lower than the median stress drop for California earthquakes). Changing the weights will automatically adjust the weighted estimates in the spreadsheet.

Weighted Median. There are two sets of weighted medians, each weighted by the subjective weights assigned to the stress drops: (1) the weighted median of the median adjustment factors, with weights applied to the logarithm of the ground-motion parameters assuming a lognormal distribution of the medians; and (2) the weighted median of the standard deviation of the adjustment factors, with weights applied to the standard deviations assuming a normal distribution of the standard deviations.

Weighted (. There are two sets of weighted (s, each weighted by the subjective weights assigned to the stress drops: (1) the weighted standard deviation of the median adjustment factors (i.e., epistemic parametric uncertainty), and (2) the weighted standard deviation of the standard deviations of the adjustment factors. The weights are applied to the square of the standard deviations (i.e., to the variances), which is consistent with the definition of the weighted standard error in weighted regression analyses. If the user believes that epistemic modeling uncertainty should be included in the California BLWN-RVT estimates, this uncertainty should be included in the estimate of the standard deviation of the median adjustment factors.

Example Hybrid Estimates Worksheet (Hybrid Estimates)

Median. The weighted median empirical ground-motion estimate times the weighted median adjustment factor for the given ground-motion parameter, magnitude, and horizontal distance. Estimates for only one ground-motion parameter and magnitude are given as an example. The user should extend this table to include all other ground-motion parameters, magnitudes, and horizontal distances of interest.

(. The standard deviations of the empirical ground-motion estimates (aleatory uncertainty), of the hybrid empirical estimates (epistemic uncertainty), and of the aleatory and epistemic standard deviations (() for the given ground-motion parameter, magnitude, and horizontal distance. All of the standard deviations are given in terms of the natural logarithm (log base e). The epistemic uncertainty includes modeling uncertainty in the median estimates of the empirical ground motions from the attenuation relationships, parametric uncertainty in the median stress drop for the Yucca Mountain region, and parametric uncertainty in the median adjustment factors for a given stress drop. The standard deviation of (includes the standard deviations of the weighted standard deviations of the empirical ground-motion estimates from the attenuation relationships and of the adjustment factors.

Section 7

Stochatic Point Model

POINT SOURCE SIMULATIONS			
M	$\Delta\sigma$ (bars)	Depth (km)	Kappa (sec)
5.0	25	5	0.01
5.5	50	10	0.02
6.0	100	15	0.03
6.5	200		0.04
7.0			
7.5			
8.0			

D(km): 1, 3, 5, 10, 20, 50, 75, 100, 150, 200

$Q(f) = 250\ f^{0.4}$

Crustal Model: Regional plus local near surface

Geometrical Attenuation: $1/R$; $1/\sqrt{R}$, $R>64$ km

Duration: $1/f_c + 0.05\ R$ ($R \geq 10$ km)

PGA Range: 10.25g - 0.0005g

yucca97\prca\point

Regression Coefficients Yucca Point Source (YM300)

2/17/97

Freq	C1	C2	C3	C4	C5	C6	C7	C8	C9	C10	C11	Sigma
0.200	-3.63228	1.58005	-0.41240	-0.97361	0.51359	-0.01987	-0.00196	0.30084	0.22458	-0.55511	-46.08318	0.12928
0.400	-2.79799	1.12663	-0.36340	-0.98898	0.47583	-0.00555	-0.00277	0.42082	0.20394	-1.20843	-41.48531	0.12891
0.500	-2.58313	1.01088	-0.33059	-0.99805	0.46618	0.00128	-0.00309	0.46191	0.18808	-1.54027	-38.64104	0.12846
1.000	-2.12866	0.75427	-0.21629	-1.03132	0.45610	0.02539	-0.00435	0.58068	0.12836	-3.15556	-24.59208	0.10486
2.000	-1.80900	0.65354	-0.12724	-1.06735	0.47585	0.04879	-0.00613	0.66938	0.06837	-6.05627	-5.41158	0.06392
5.000	-1.48361	0.70145	-0.07424	-1.12538	0.44421	0.07267	-0.00867	0.73956	0.00000	-13.75716	26.11159	0.07272
10.000	-1.18658	0.59687	-0.06690	-1.22965	0.36632	0.09462	-0.00916	0.74655	0.00000	-23.36904	98.78373	0.10245
20.000	-1.15425	0.54235	-0.07363	-1.33956	0.46074	0.11416	-0.00825	0.74367	0.00000	-31.82678	378.66663	0.17990
pga	-1.90460	0.58370	-0.08343	-1.25685	0.46449	0.11210	-0.00663	0.73581	0.00000	-18.63800	301.22351	0.13007
pgv	2.85071	0.64839	-0.17083	-1.16113	0.44881	0.11702	-0.00337	0.57511	0.09720	-4.43697	32.67279	0.07802

For $R < r_c$:

$$\ln Y = C_1 + C_2 (M-6) + C_3 (M-6)^2 + (C_4 + C_6 (M-6)) \ln (R) + C_7 R + (C_8 + C_9 (M-6)) \ln (\Delta\sigma) + C_{10}(K-0.025) + C_{11}(K-0.025)^2$$

For $R > r_c$:

$$\ln Y = C_1 + C_2 (M-6) + C_3 (M-6)^2 + (C_4 + C_6 (M-6)) \ln (R) + C_5(\ln(R) - \ln (r_c)) + C_7 R + (C_8 + C_9 (M-6)) \ln (\Delta\sigma) + C_{10}(K-0.025) + C_{11}(K-0.025)^2$$

Point Source (Silva) (Model 6) Uncertainty					
Frequency (hz)	Modeling Aleatory		Modeling Aleatory	Parametric Aleatory SE(ln $\Delta\sigma$) x (C8 + C9(m-6))	
	Point Source	Equation fit	total	C8	C9
.5	.86	.13	0.87	.46	.19
1	.66	.10	0.67	.58	.13
2	.59	.06	0.59	.67	.07
5	.52	.07	0.52	.74	0.0
10	.50	.10	0.51	.75	0.0
20	.48	.18	0.51	.74	0.0
PGA	.48	.13	0.50	.74	0.0
PGV	.66*	.08	.66	.58	.10

Notes: The parametric aleatory uncertainty depends on the assumed variability of the stress drop. Here the C8 and C9(m-6) factors (from the regression model) are multiplied by the standard error of the natural logarithm of stress drop. The expert must specify the standard deviation of natural log of stress drop.

The modeling aleatory has two parts. The "point source" part is from comparisons of the point source predictions to data. The "equation fit" part is the standard error of Abrahamson's fit of an equation to the point source values.

The total modeling aleatory uncertainty is computed by combining these two terms (square root of sum of squares)

* recommended by Silva. Use T=1.0 seconds σ for PGV

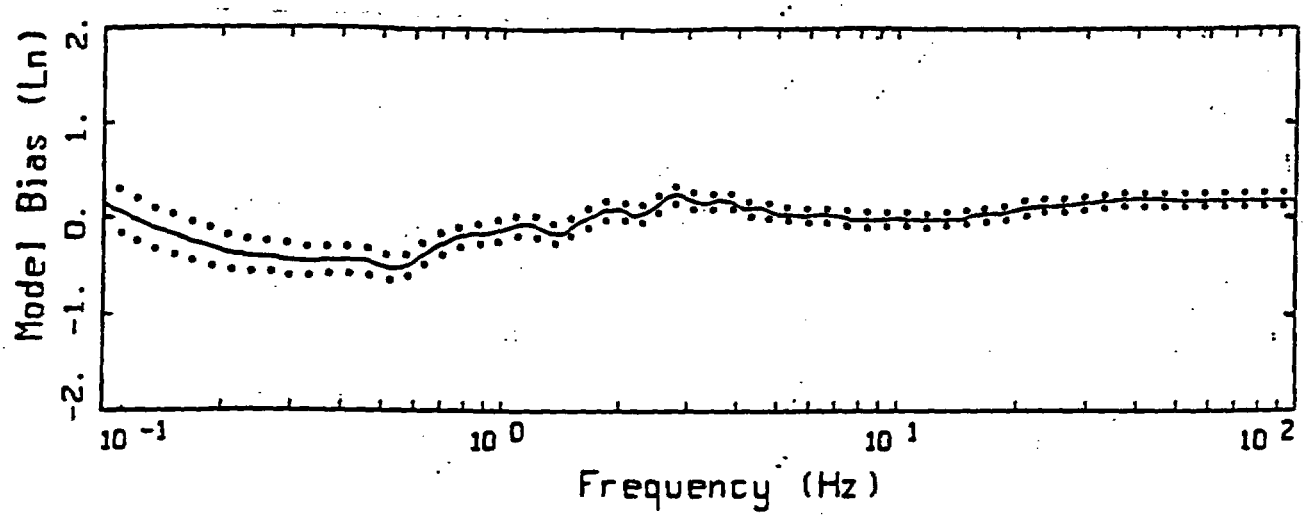

LEGEND
MODELING BIAS
90% CONFIDENCE INTERVAL OF MODELING BIAS
90% CONFIDENCE INTERVAL OF MODELING BIAS

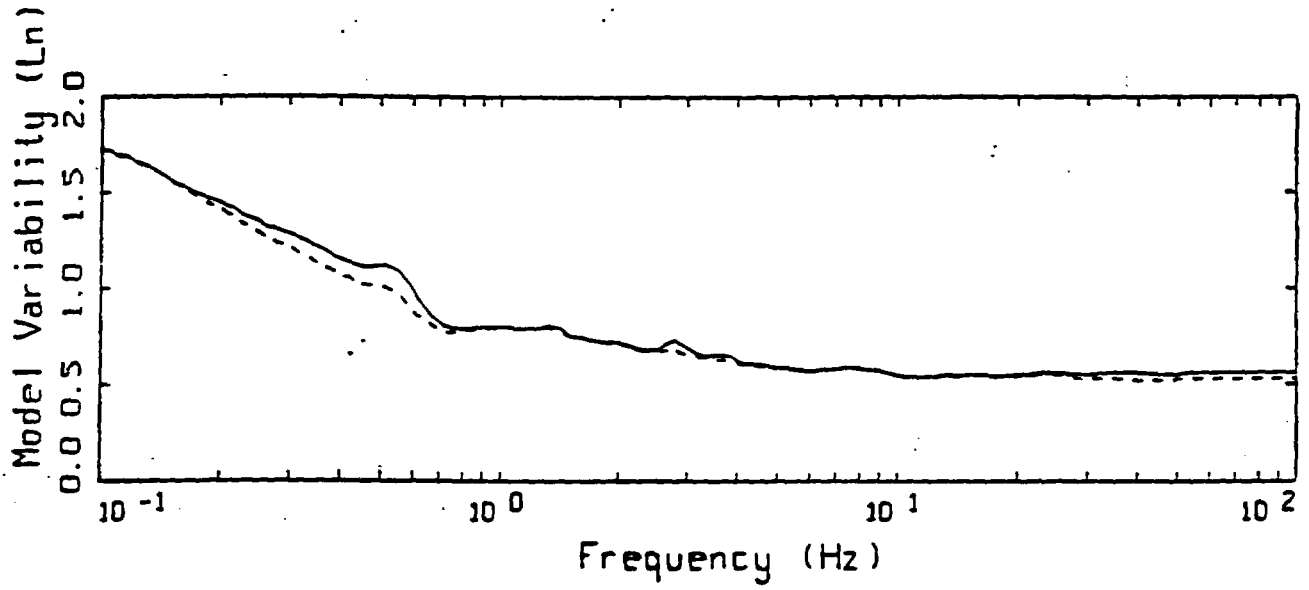

LEGEND
MEAN=0.0
BIAS CORRECTED

16 EARTHQUAKES POINT-SOURCE
NONLINEAR, ALL 159 ROCK SITES

Figure 5.154

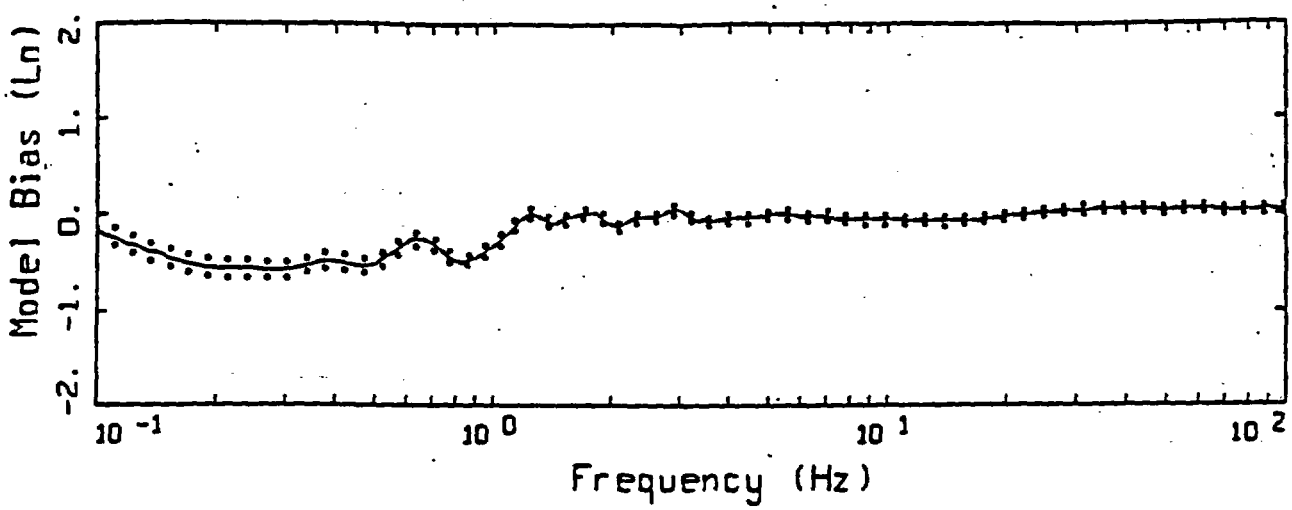

LEGEND
——— MODELING BIAS
..... 90% CONFIDENCE INTERVAL OF MODELING BIAS
..... 90% CONFIDENCE INTERVAL OF MODELING BIAS

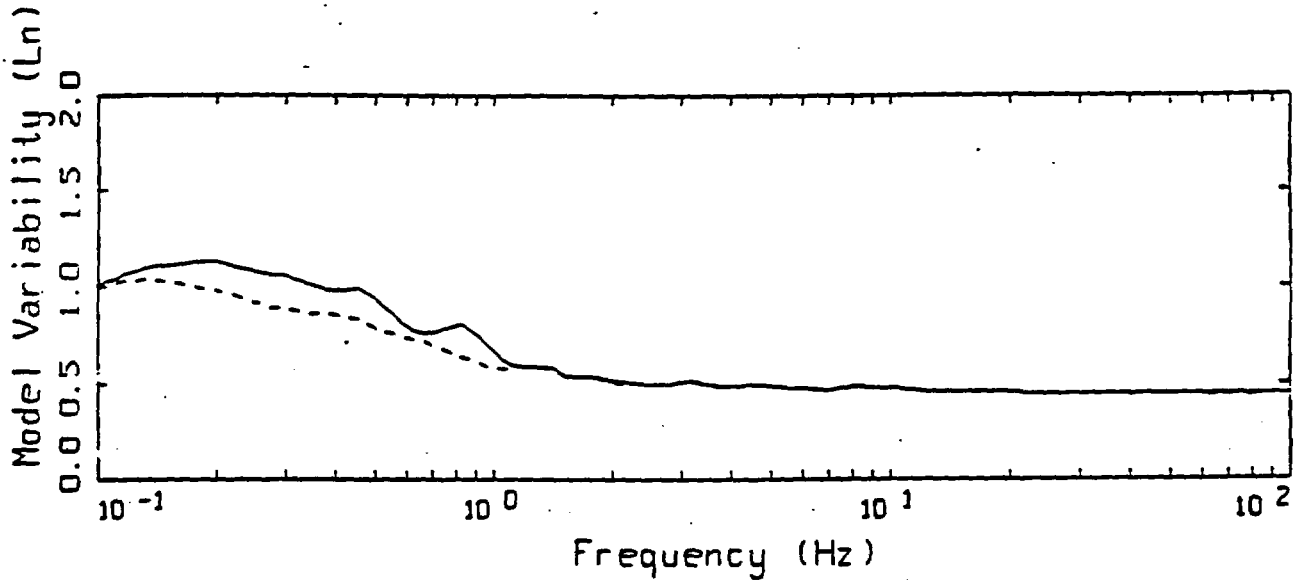

LEGEND
——— MEAN=0.0
------ BIAS CORRECTED

16 EARTHQUAKES POINT-SOURCE
NONLINEAR, ALL 344 SOIL SITES

Figure 5.153

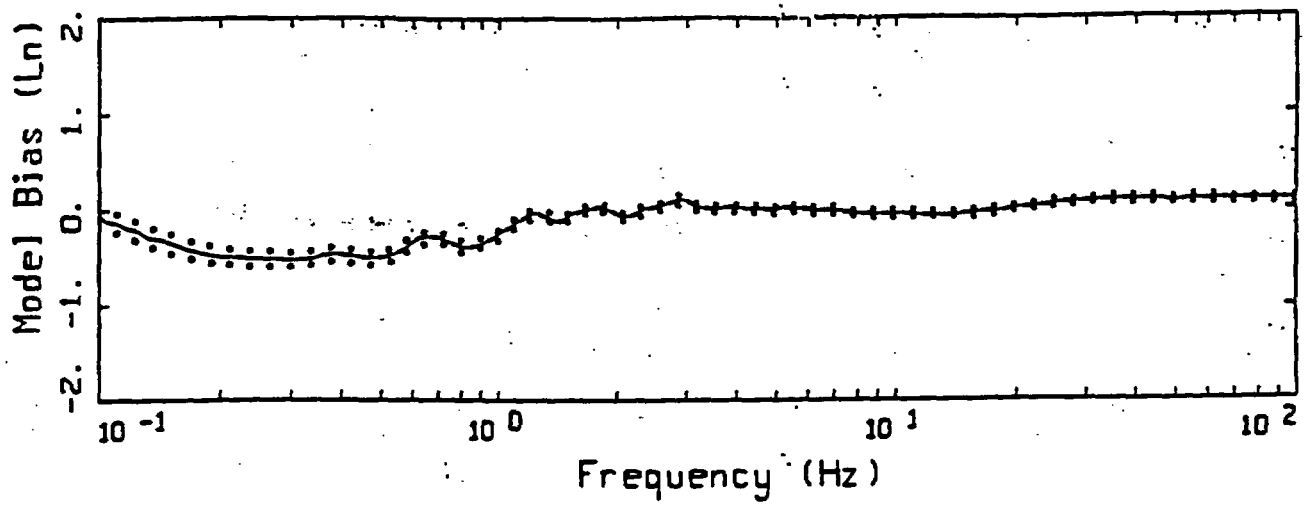

LEGEND
MODELING BIAS
90% CONFIDENCE INTERVAL OF MODELING BIAS
90% CONFIDENCE INTERVAL OF MODELING BIAS

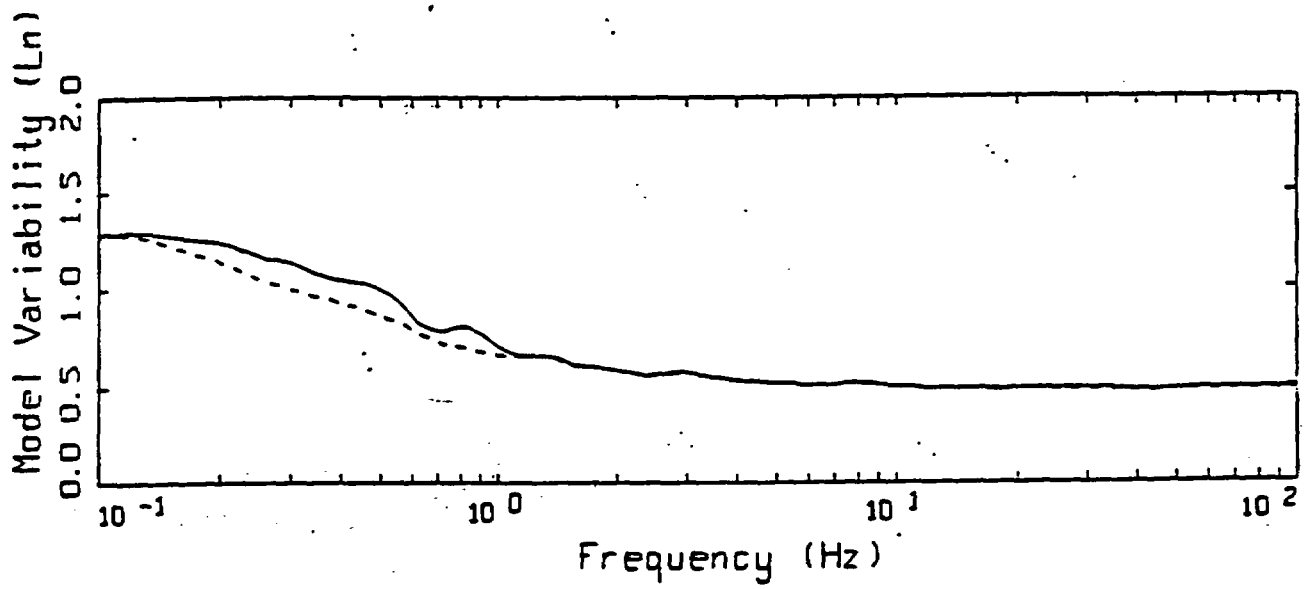

LEGEND
MEAN=0.0
BIAS CORRECTED

16 EARTHQUAKES POINT-SOURCE
NONLINEAR, ALL 503 SITES

Figure 5.152

Calculated Scale Factors
From Silva Point Source
For Yucca Mountain Stress Drop as a Percentage of California
= 60%, 70%, 80%, 90%, 100%

PGA is Freq=0.0
PGV is Freq=-1.0

Mag= 5.00

	Yucca Mtn Stress Drop/ Calif Stress Drop				
Freq	1.0	0.9	0.8	0.7	0.6
0.5	1.0	0.97	0.94	0.91	0.87
1.0	1.0	0.95	0.90	0.85	0.79
2.0	1.0	0.94	0.87	0.81	0.74
5.0	1.0	0.92	0.85	0.77	0.69
10.0	1.0	0.92	0.85	0.77	0.68
20.0	1.0	0.92	0.85	0.77	0.69
0.0	1.0	0.92	0.85	0.77	0.69
-1.0	1.0	0.95	0.90	0.84	0.78

Mag= 5.80

	Yucca Mtn Stress Drop/ Calif Stress Drop				
Freq	1.0	0.9	0.8	0.7	0.6
0.5	1.0	0.96	0.91	0.86	0.81
1.0	1.0	0.94	0.88	0.82	0.75
2.0	1.0	0.93	0.86	0.79	0.72
5.0	1.0	0.92	0.85	0.77	0.69
10.0	1.0	0.92	0.85	0.77	0.68
20.0	1.0	0.92	0.85	0.77	0.69
0.0	1.0	0.92	0.85	0.77	0.69
-1.0	1.0	0.94	0.88	0.82	0.75

Mag= 6.00

	Yucca Mtn Stress Drop/ Calif Stress Drop				
Freq	1.0	0.9	0.8	0.7	0.6
0.5	1.0	0.95	0.90	0.85	0.79
1.0	1.0	0.94	0.88	0.81	0.74
2.0	1.0	0.93	0.86	0.79	0.71
5.0	1.0	0.92	0.85	0.77	0.69
10.0	1.0	0.92	0.85	0.77	0.68
20.0	1.0	0.92	0.85	0.77	0.69
0.0	1.0	0.92	0.85	0.77	0.69
-1.0	1.0	0.94	0.88	0.81	0.74

Calculated Scale Factors
From Silva Point Source
For Yucca Mountain Stress Drop as a Percentage of California
= 60%, 70%, 80%, 90%, 100%

PGA is Freq=0.0
PGV is Freq=-1.0

Mag= 6.50

	Yucca Mtn Stress Drop/ Calif Stress Drop				
Freq	1.0	0.9	0.8	0.7	0.6
0.5	1.0	0.94	0.88	0.82	0.75
1.0	1.0	0.93	0.87	0.79	0.72
2.0	1.0	0.93	0.85	0.78	0.70
5.0	1.0	0.92	0.85	0.77	0.69
10.0	1.0	0.92	0.85	0.77	0.68
20.0	1.0	0.92	0.85	0.77	0.69
0.0	1.0	0.92	0.85	0.77	0.69
-1.0	1.0	0.94	0.87	0.80	0.72

Mag= 7.00

	Yucca Mtn Stress Drop/ Calif Stress Drop				
Freq	1.0	0.9	0.8	0.7	0.6
0.5	1.0	0.93	0.86	0.79	0.72
1.0	1.0	0.93	0.85	0.78	0.70
2.0	1.0	0.92	0.85	0.77	0.69
5.0	1.0	0.92	0.85	0.77	0.69
10.0	1.0	0.92	0.85	0.77	0.68
20.0	1.0	0.92	0.85	0.77	0.69
0.0	1.0	0.92	0.85	0.77	0.69
-1.0	1.0	0.93	0.86	0.78	0.71

Mag= 7.50

	Yucca Mtn Stress Drop/ Calif Stress Drop				
Freq	1.0	0.9	0.8	0.7	0.6
0.5	1.0	0.92	0.85	0.77	0.68
1.0	1.0	0.92	0.84	0.76	0.67
2.0	1.0	0.92	0.84	0.76	0.67
5.0	1.0	0.92	0.85	0.77	0.69
10.0	1.0	0.92	0.85	0.77	0.68
20.0	1.0	0.92	0.85	0.77	0.69
0.0	1.0	0.92	0.85	0.77	0.69
-1.0	1.0	0.93	0.85	0.77	0.69

Section 8:

Proponent Conversions

Section 8.1: YM_{300} / $YM_{surface}$

Section 8.1.1: Silva

Tabulated Values of $YM_{300}/YM_{surface}$
(Silva 1D Vertical Wave Propagation)

$YM_{300}/YM_{surface}$ (1D Simulation- Silva)	
Frequency (hz)	Spectral Ratio
.5	.92
1	.75
2	.54
5	.49
10	.47
20	.46

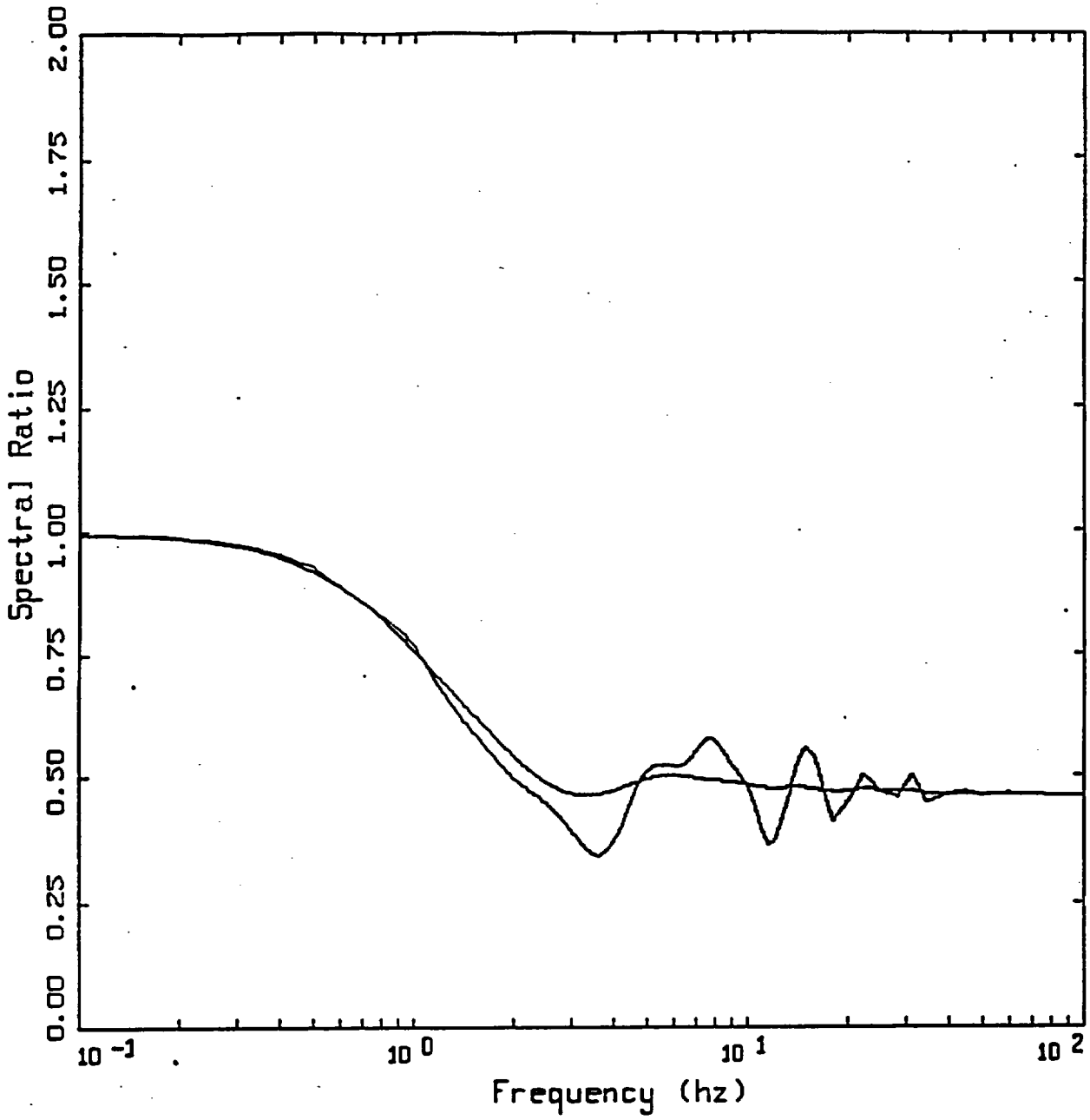

YUCCA 300M OUTCROP TO SURFACE TRANSFER FUNCTION

LEGEND

5 %, TRANSFER FUNCTION

5 %, TRANSFER FUNCTION; 20 Hz smoothing

Section 8.2: $YM_{surface}$ / $CA_{surface}$ (w/o stress drop)

Section 8.2.1: Silva point source stochastic model

Tabulation of $YM_{surface}/CA$ (without source)
(crustal velocity, kappa, Q)
(Silva point source stochastic model)

$YM_{surface}/CA$ (without source)	
Frequency (hz)	Spectral Ratio
.5	1.15
1	1.10
2	.97
5	.83
10	.95
20	1.17

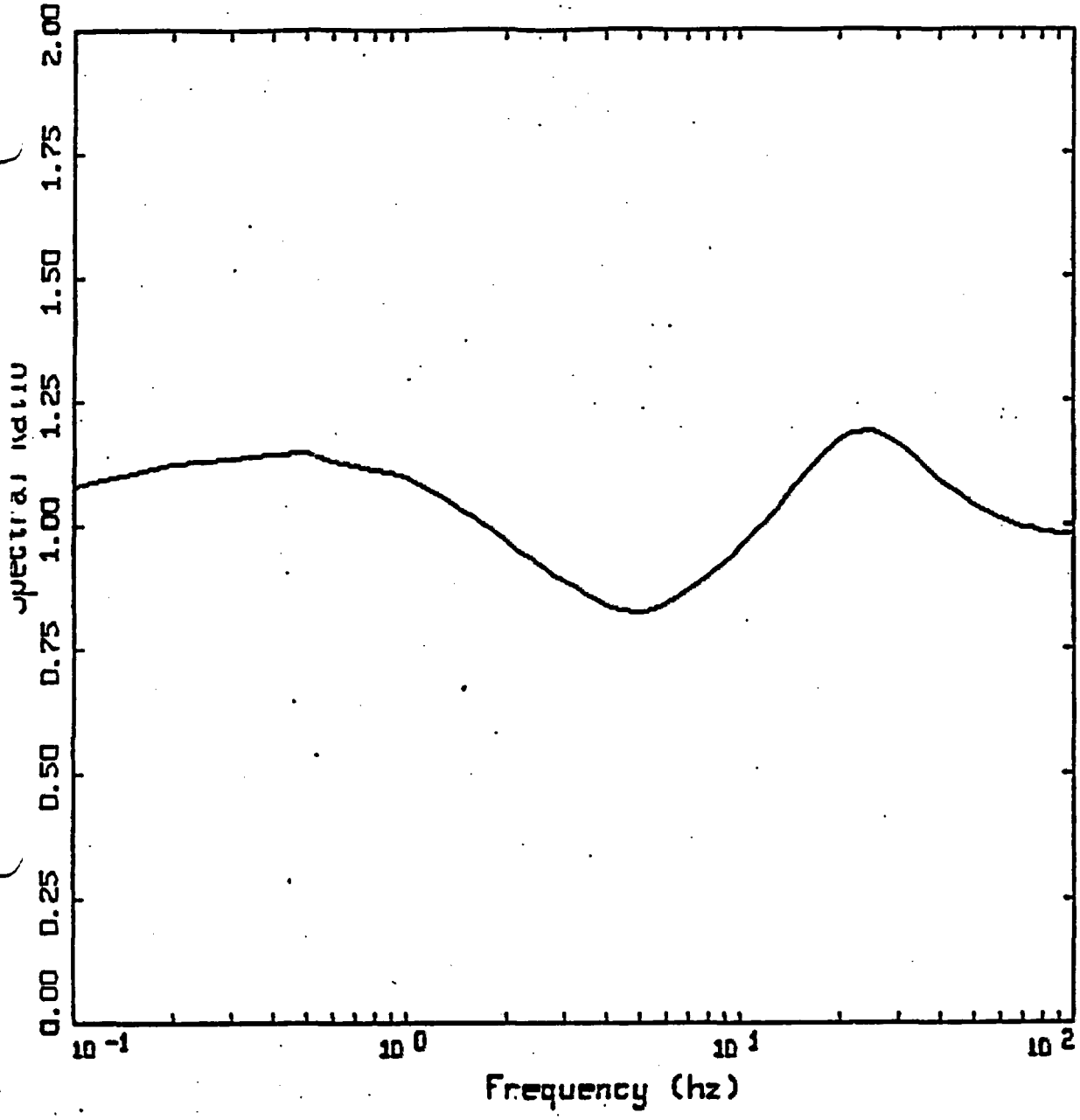

YUCCA TO WNA RESPONSE SPECTRA
TRANSFER FUNCTION

LEGEND

5 %, TRANSFER FUNCTION

Section 8.3:

YM_{300} / $CA_{surface}$

Section 8.3.1: Silva

Tabulation of $YM_{300}/CA_{surface}$ (without source)
(crustal velocity, kappa, Q)
(Silva point source stochastic model)

$YM_{surface}/CA$ (without source)	
Frequency (hz)	Spectral Ratio
.5	1.058
1	0.825
2	0.524
5	0.407
10	0.446
20	0.538

Product of $\frac{YM_{300}}{YM_{surface}} \times \frac{YM_{surface}}{CA_{surface}}$

Section 8.3.2: Campbell

$$\text{Ln(Scale Factor)} = A + B*\text{Ln}(\Delta\sigma)$$

These are the Campbell adjustment factors for Yucca Mountain using the Western U. S. stress drop of 59 bars. Does not include effects of differences in stress drops between California and Yucca Mountain. The first three magnitude distance pairs listed in the table below are for the deep sources and the latter six pairs are for the shallow sources.

Tabulation of Campbell scale factors.

Freq (Hz)	Magnitude	Distance (km)	Campbell (WUS=59 bars)	Sigma	
0.33	5.00	5.00	0.8393	0.0142	
0.50	5.00	5.00	0.8126	0.0064	
1.00	5.00	5.00	0.7118	0.0067	
2.00	5.00	5.00	0.5823	0.0215	
5.00	5.00	5.00	0.4782	0.0103	
10.00	5.00	5.00	0.5787	0.0057	deep
20.00	5.00	5.00	0.7823	0.0038	
PGA	5.00	5.00	0.6157	0.0040	
PGV	5.00	5.00	0.6181	0.0048	
0.33	5.80	10.00	0.8717	0.0093	
0.50	5.80	10.00	0.8039	0.0160	
1.00	5.80	10.00	0.7076	0.0187	
2.00	5.80	10.00	0.5935	0.0102	
5.00	5.80	10.00	0.4814	0.0047	deep
10.00	5.80	10.00	0.5768	0.0029	
20.00	5.80	10.00	0.7674	0.0021	
PGA	5.80	10.00	0.6144	0.0023	
PGV	5.80	10.00	0.6960	0.0038	
0.33	5.80	20.00	0.8719	0.0092	
0.50	5.80	20.00	0.8032	0.0161	
1.00	5.80	20.00	0.7052	0.0187	
2.00	5.80	20.00	0.5890	0.0102	deep
5.00	5.80	20.00	0.4725	0.0046	
10.00	5.80	20.00	0.5585	0.0029	
20.00	5.80	20.00	0.7307	0.0021	
PGA	5.80	20.00	0.5962	0.0025	
PGV	5.80	20.00	0.6913	0.0040	
0.33	5.00	1.00	0.8397	0.0140	
0.50	5.00	1.00	0.8145	0.0063	shallow
1.00	5.00	1.00	0.7168	0.0066	
2.00	5.00	1.00	0.5916	0.0214	

5.00	5.00	1.00	0.4966	0.0103
10.00	5.00	1.00	0.6189	0.0057
20.00	5.00	1.00	0.8729	0.0037
PGA	5.00	1.00	0.6624	0.0037
PGV	5.00	1.00	0.6330	0.0044
0.33	6.50	1.00	0.8454	0.0215
0.50	6.50	1.00	0.8143	0.0170
1.00	6.50	1.00	0.7235	0.0092
2.00	6.50	1.00	0.6087	0.0050
5.00	6.50	1.00	0.5020	0.0025
10.00	6.50	1.00	0.6172	0.0015
20.00	6.50	1.00	0.8506	0.0011
PGA	6.50	1.00	0.6560	0.0014
PGV	6.50	1.00	0.7661	0.0023
0.33	6.50	5.00	0.8451	0.0215
0.50	6.50	5.00	0.8140	0.0171
1.00	6.50	5.00	0.7230	0.0091
2.00	6.50	5.00	0.6075	0.0050
5.00	6.50	5.00	0.4997	0.0025
10.00	6.50	5.00	0.6121	0.0015
20.00	6.50	5.00	0.8394	0.0011
PGA	6.50	5.00	0.6510	0.0014
PGV	6.50	5.00	0.7664	0.0023
0.33	6.50	50.00	0.8450	0.0217
0.50	6.50	50.00	0.8063	0.0171
1.00	6.50	50.00	0.6987	0.0092
2.00	6.50	50.00	0.5616	0.0050
5.00	6.50	50.00	0.4150	0.0025
10.00	6.50	50.00	0.4474	0.0018
20.00	6.50	50.00	0.5454	0.0017
PGA	6.50	50.00	0.5129	0.0019
PGV	6.50	50.00	0.7414	0.0031
0.33	7.00	10.00	0.8544	0.0147
0.50	7.00	10.00	0.8215	0.0101
1.00	7.00	10.00	0.7242	0.0055
2.00	7.00	10.00	0.6040	0.0031
5.00	7.00	10.00	0.4893	0.0016
10.00	7.00	10.00	0.5888	0.0010
20.00	7.00	10.00	0.7867	0.0008
PGA	7.00	10.00	0.6266	0.0009
PGV	7.00	10.00	0.8015	0.0011
0.33	7.50	50.00	0.8617	0.0086
0.50	7.50	50.00	0.8201	0.0061
1.00	7.50	50.00	0.7058	0.0035

Shallow

2.00	7.50	50.00	0.5657	0.0020
5.00	7.50	50.00	0.4174	0.0011
10.00	7.50	50.00	0.4508	0.0008
20.00	7.50	50.00	0.5516	0.0008
PGA	7.50	50.00	0.5238	0.0010
PGV	7.50	50.00	0.8305	0.0004

8.3.3 Comparison of Silva and Campbell Models

The Silva and Campbell models for the differences between CA and YM (without stress drop differences) are compared in the following figure. The Silva model is for a magnitude 6.5 event at a distance of 30 km. The Campbell model has estimates for each of the 7 magnitude- distance pairs in the 16 cases for the preliminary set.

Yucca Mountain LN Scale Factors (w/o source, stress drop scaling)

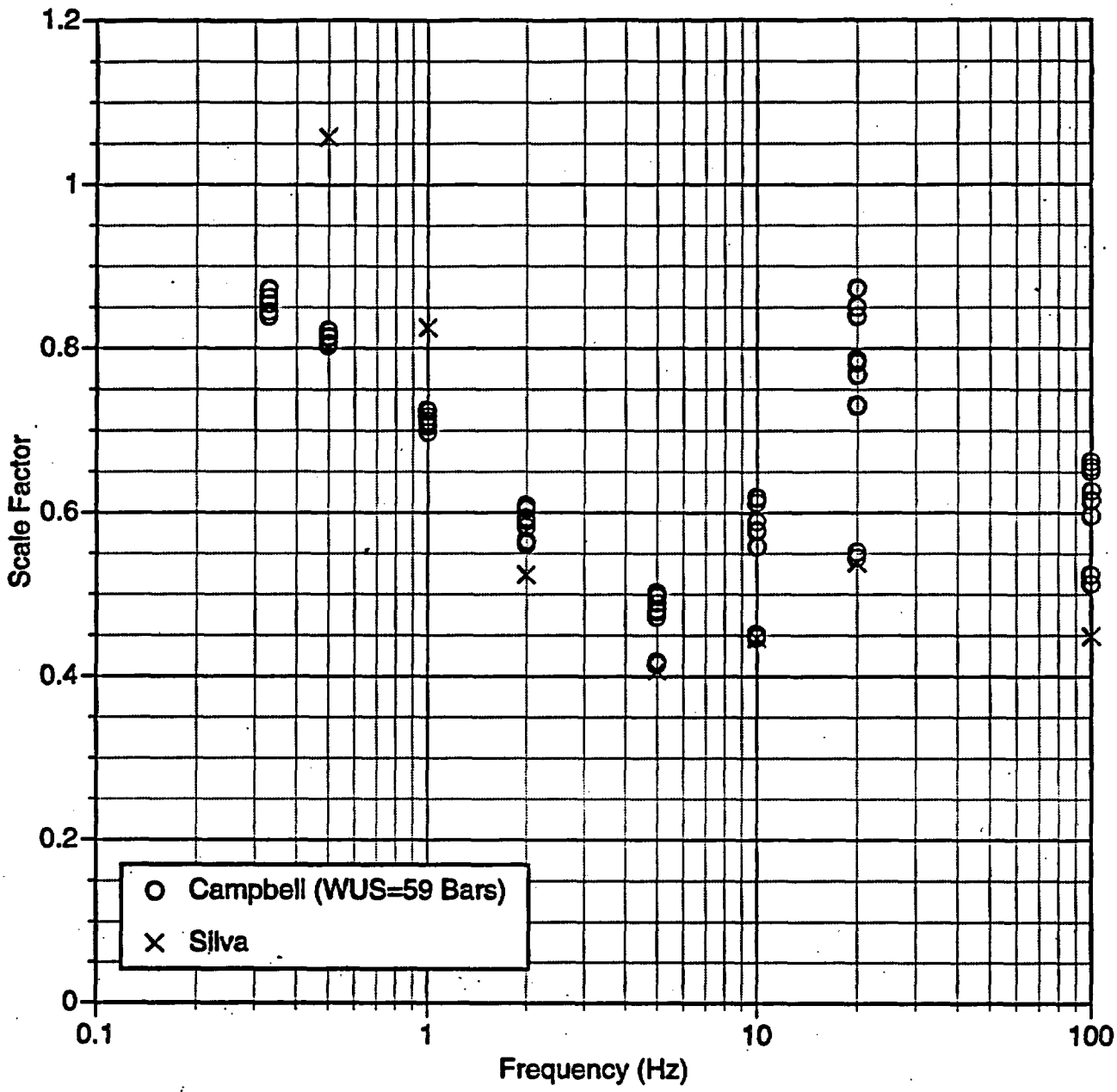

Section 8.4:

$YM_{surface}$ / $CA_{surface}$ (stress drop only)

Section 8.4.2: Silva point source

Equation for $YM_{surface}$ / $CA_{surface}$ (source)
(Silva point source stochastic model)

$$\frac{YM_{surface}}{CA_{surface}}(source) = [C_8 + C_9(M-6)] \times \ln\left(\frac{\Delta\sigma_{YM}}{\Delta\sigma_{CA}}\right)$$

Tabulation of stress drop scaling for Silva.

Freq. (Hz)	Magnitude	Silva (C_8+C_9(M-6))
0.50	5.00	0.2738
1.00	5.00	0.4523
2.00	5.00	0.6010
5.00	5.00	0.7396
10.00	5.00	0.7466
20.00	5.00	0.7437
PGA	5.00	0.7358
PGV	5.00	0.4779
0.50	5.80	0.4243
1.00	5.80	0.5550
2.00	5.80	0.6557
5.00	5.80	0.7396
10.00	5.80	0.7466
20.00	5.80	0.7437
PGA	5.80	0.7358
PGV	5.80	0.5557
0.50	6.50	0.5560
1.00	6.50	0.6449
2.00	6.50	0.7036
5.00	6.50	0.7396
10.00	6.50	0.7466
20.00	6.50	0.7437
PGA	6.50	0.7358
PGV	6.50	0.6237
0.50	7.00	0.6500
1.00	7.00	0.7090
2.00	7.00	0.7378
5.00	7.00	0.7396
10.00	7.00	0.7466
20.00	7.00	0.7437
PGA	7.00	0.7358

PGV	7.00	0.6723
0.50	7.50	0.7440
1.00	7.50	0.7732
2.00	7.50	0.7719
5.00	7.50	0.7396
10.00	7.50	0.7466
20.00	7.50	0.7437
PGA	7.50	0.7358
PGV	7.50	0.7209

Section 8.4.2: Campbell

$$\text{Ln(Scale Factor)} = A + B^{*}\text{Ln}(\Delta\sigma)$$

Tabulation of Campbell scale factors.

Freq. (Hz)	Magnitude	Distance (km)	A	B	Sigma
0.33	5.00	5.00	-1.8182	0.4029	0.0142
0.50	5.00	5.00	-2.0143	0.4431	0.0064
1.00	5.00	5.00	-2.0962	0.4307	0.0067
2.00	5.00	5.00	-2.7287	0.5366	0.0215
5.00	5.00	5.00	-3.5215	0.6827	0.0103
10.00	5.00	5.00	-3.5434	0.7348	0.0057
20.00	5.00	5.00	-3.3357	0.7578	0.0038
PGA	5.00	5.00	-3.5424	0.7498	0.0040
PGV	5.00	5.00	-2.8498	0.5809	0.0048
0.33	5.80	10.00	-1.9172	0.4365	0.0093
0.50	5.80	10.00	-2.0347	0.4455	0.0160
1.00	5.80	10.00	-2.7308	0.5849	0.0187
2.00	5.80	10.00	-3.3151	0.6851	0.0102
5.00	5.80	10.00	-3.7880	0.7497	0.0047
10.00	5.80	10.00	-3.7045	0.7736	0.0029
20.00	5.80	10.00	-3.4625	0.7842	0.0021
PGA	5.80	10.00	-3.6620	0.7787	0.0023
PGV	5.80	10.00	-2.8929	0.6206	0.0038
0.33	5.80	20.00	-1.9166	0.4364	0.0092
0.50	5.80	20.00	-2.0340	0.4451	0.0161
1.00	5.80	20.00	-2.7342	0.5849	0.0187
2.00	5.80	20.00	-3.3226	0.6850	0.0102
5.00	5.80	20.00	-3.8068	0.7498	0.0046
10.00	5.80	20.00	-3.7352	0.7732	0.0029
20.00	5.80	20.00	-3.5079	0.7833	0.0021
PGA	5.80	20.00	-3.6869	0.7774	0.0025
PGV	5.80	20.00	-2.8888	0.6179	0.0040
0.33	5.00	1.00	-1.8212	0.4038	0.0140
0.50	5.00	1.00	-2.0137	0.4435	0.0063
1.00	5.00	1.00	-2.0894	0.4308	0.0066
2.00	5.00	1.00	-2.7145	0.5370	0.0214
5.00	5.00	1.00	-3.4856	0.6832	0.0103
10.00	5.00	1.00	-3.4800	0.7358	0.0057

20.00	5.00	1.00	-3.2367	0.7605	0.0037
PGA	5.00	1.00	-3.4906	0.7550	0.0037
PGV	5.00	1.00	-2.8561	0.5883	0.0044
0.33	6.50	1.00	-2.3178	0.5272	0.0215
0.50	6.50	1.00	-2.6812	0.6072	0.0170
1.00	6.50	1.00	-3.1678	0.6975	0.0092
2.00	6.50	1.00	-3.5374	0.7458	0.0050
5.00	6.50	1.00	-3.8644	0.7787	0.0025
10.00	6.50	1.00	-3.7109	0.7917	0.0015
20.00	6.50	1.00	-3.4162	0.7981	0.0011
PGA	6.50	1.00	-3.6660	0.7957	0.0014
PGV	6.50	1.00	-2.9205	0.6509	0.0023
0.33	6.50	5.00	-2.3170	0.5270	0.0215
0.50	6.50	5.00	-2.6812	0.6071	0.0171
1.00	6.50	5.00	-3.1689	0.6976	0.0091
2.00	6.50	5.00	-3.5393	0.7457	0.0050
5.00	6.50	5.00	-3.8689	0.7787	0.0025
10.00	6.50	5.00	-3.7183	0.7915	0.0015
20.00	6.50	5.00	-3.4293	0.7981	0.0011
PGA	6.50	5.00	-3.6724	0.7954	0.0014
PGV	6.50	5.00	-2.9184	0.6505	0.0023
0.33	6.50	50.00	-2.3133	0.5260	0.0217
0.50	6.50	50.00	-2.6880	0.6064	0.0171
1.00	6.50	50.00	-3.1996	0.6968	0.0092
2.00	6.50	50.00	-3.6146	0.7450	0.0050
5.00	6.50	50.00	-4.0490	0.7773	0.0025
10.00	6.50	50.00	-4.0197	0.7886	0.0018
20.00	6.50	50.00	-3.8311	0.7909	0.0017
PGA	6.50	50.00	-3.8715	0.7857	0.0019
PGV	6.50	50.00	-2.8810	0.6332	0.0031
0.33	7.00	10.00	-2.7489	0.6356	0.0147
0.50	7.00	10.00	-2.9956	0.6865	0.0101
1.00	7.00	10.00	-3.3395	0.7399	0.0055
2.00	7.00	10.00	-3.6419	0.7695	0.0031
5.00	7.00	10.00	-3.9385	0.7906	0.0016
10.00	7.00	10.00	-3.7877	0.7990	0.0010
20.00	7.00	10.00	-3.5155	0.8033	0.0008
PGA	7.00	10.00	-3.7331	0.8009	0.0009
PGV	7.00	10.00	-2.9106	0.6596	0.0011

0.33	7.50	50.00	-3.0150	0.7029	0.0086
0.50	7.50	50.00	-3.1877	0.7331	0.0061
1.00	7.50	50.00	-3.4702	0.7656	0.0035
2.00	7.50	50.00	-3.7680	0.7844	0.0020
5.00	7.50	50.00	-4.1266	0.7978	0.0011
10.00	7.50	50.00	-4.0704	0.8029	0.0008
20.00	7.50	50.00	-3.8746	0.8044	0.0008
PGA	7.50	50.00	-3.9156	0.8017	0.0010
PGV	7.50	50.00	-2.8484	0.6530	0.0004

Availability of Spudich Adjustment Factors
All Distances and d<20 km, N> 3

Empirical Model	Spudich Adjustment			
	Name	G	hor	ver
Campbell 1993-94, hard rock [only for all distances]	C93/94	1	X	
Campbell 1990-94, soft rock	C90/94	0,2	X	
BJF 1994, Site A	BJF94	0,1,2	X	
BJF 1994, Site B	BJF94	0,1,2	X	
Idriss 1991	I93	0,1,2	X	
Sadigh 1993	S93	0,1,2	X	X
Sabetta & Pugliese 1997	SP96	0,1,2	X	
Spudich 1996	SEA96	0,1,2	X	

Spudich Adjustment Factors All Distances - horizontal N>3							
Period	C93/94 hard rock	C90/94 soft rock	BJF94 Site A and SiteB	I93	S93	SP96	SEA96
0.0	.087	-.121	-.180	-.142	-.104	-0.06	-.071
.05	.157	.094	-	-.097	.016	.023	-
.10	.086	.033	-.128	-.145	-.070	-.037	-.022
.15	.102	-.044	-.204	-.168	-.117	-.098	-.059
.20	.122	-.058	-.213	-.172	-.108	-.110	-.043
.30	.233	-.149	-.211	-.158	-.093	-.105	-.020
.40	.304	-.177	-.190	-.143	-.073	-.077	-.001
.50	.309	-.161	-.157	-.098	-.031	-.071	.022
.75	.274	-.238	-.160	-.084	-.071	-.109	-.019
1.00	.274	-	-.164	-.055	-.106	-.100	-.046
1.50	.172	-	-.116	.042	-.058	-.049	-.003
2.00	.126	-	-.219	.042	-.087	-.011	-.074

Spudich Adjustment Factors All Distances - vertical N>3	
Period	S93
0.0	-.065
.05	.096
.10	.019
.15	.046
.20	.065
.30	.105
.40	.092
.50	.051
.75	.025
1.00	.061
1.50	.101
2.00	.158

Spudich Adjustment Factors All Distances - horizontal - Sigma N>3							
Period	C93/94 hard rock	C90/94 soft rock	BJF94 Site A and SiteB	I93	S93	SP96	SEA96
0.0	.770	.966	.973	.801	.828	1.064	.870
.05	1.391	.901	-	.954	1.081	1.486	-
.10	.772	1.067	1.210	.914	.946	1.426	.840
.15	.662	1.110	1.215	.933	.949	1.255	.803
.20	.594	1.081	1.301	.872	.908	1.250	.834
.30	.662	1.398	1.275	.991	.991	1.059	.812
.40	.774	1.077	1.139	.903	.876	.800	.727
.50	.944	1.011	1.031	.795	.780	.731	.660
.75	.696	.865	1.117	.872	.823	.804	.710
1.00	.590	-	1.150	.858	.789	.757	.719
1.50	.709	-	1.201	.871	.799	.775	.738
2.00	.916	-	1.363	.928	.928	.873	.809

Spudich Adjustment Factors All Distances - vertical Sigma N>3	
Period	S93
0.0	.873
.05	.855
.10	.812
.15	.765
.20	.855
.30	.902
.40	.877
.50	.741
.75	.889
1.00	.930
1.50	.771
2.00	.802

Spudich Adjustment Factors d<20 km - horizontal N>3							
Period	C93/94 hard rock	C90/94 soft rock	BJF94 Site A and SiteB	I93	S93	SP96	SEA96
0.0	-	-.196	-.115	-.204	-.197	-.045	-.051
.05	-	-.009	-	-.188	-.135	.045	-
.10	-	-.024	-.059	-.152	-.134	.066	.012
.15	-	-.160	-.166	-.227	-.217	-.054	-.042
.20	-	-.172	-.171	-.218	-.185	-.063	-.015
.30	-	-.264	-.229	-.252	-.210	-.133	-.045
.40	-	-.245	-.195	-.224	-.174	-.079	-.010
.50	-	-.225	-.168	-.182	-.131	-.105	.007
.75	-	-.231	-.095	-.096	-.087	-.086	.039
1.00	-	-	-.050	-.020	-.064	-.026	.054
1.50	-	-	-.056	.023	-.067	-.019	.035
2.00	-	-	-.175	-.002	-.116	-.012	-.057

Spudich Adjustment Factors d<20km - vertical N>3	
Period	S93
0.0	-.141
.05	.021
.10	-.059
.15	-.084
.20	-.026
.30	.003
.40	-.042
.50	-.048
.75	.022
1.00	.047
1.50	.156
2.00	.150

Spudich Adjustment Factors d<20 km - horizontal - Sigma N>3							
Period	C93/94 hard rock	C90/94 soft rock	BJF94 Site A and SiteB	I93	S93	SP96	SEA96
0.0	-	.865	.793	.720	.698	.876	.792
.05	-	.548	-	.607	.635	1.029	-
.10	-	.808	.984	.757	.748	.988	.726
.15	-	.933	1.200	.885	.902	1.144	.818
.20	-	1.167	1.334	1.053	1.052	1.164	.871
.30	-	1.699	1.519	1.214	1.209	1.179	.971
.40	-	1.487	1.391	1.108	1.039	.952	.890
.50	-	1.161	1.154	.858	.778	.837	.741
.75	-	.945	1.075	.797	.707	.799	.689
1.00	-	-	.959	.795	.698	.603	.615
1.50	-	-	1.159	1.017	.907	.708	.735
2.00	-	-	1.338	1.095	1.064	.863	.821

Spudich Adjustment Factors d<20km - vertical Sigma N>3	
Period	S93
0.0	.788
.05	.724
.10	.831
.15	.627
.20	.915
.30	.799
.40	.701
.50	.471
.75	.570
1.00	.479
1.50	.491
2.00	.770

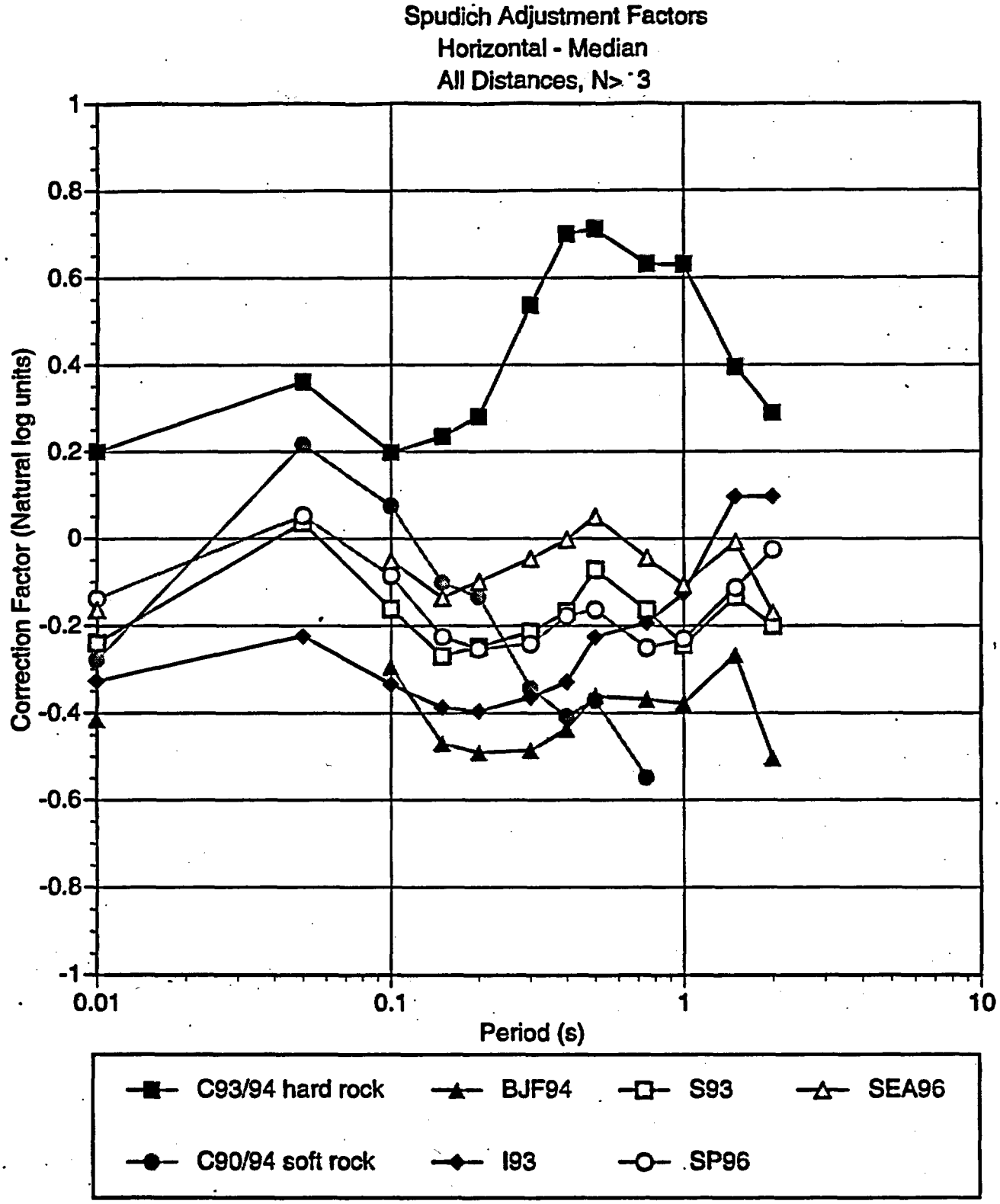
Spudich Adjustment Factors
Horizontal - Median
All Distances, N> 3
Correction Factor (Natural log units)
1
0.8
0.6
0.4
0.2
0
-0.2
-0.4
-0.6
-0.8
-1
0.01
0.1
1
10
Period (s)
C93/94 hard rock
BJF94
S93
SEA96
C90/94 soft rock
I93
SP96

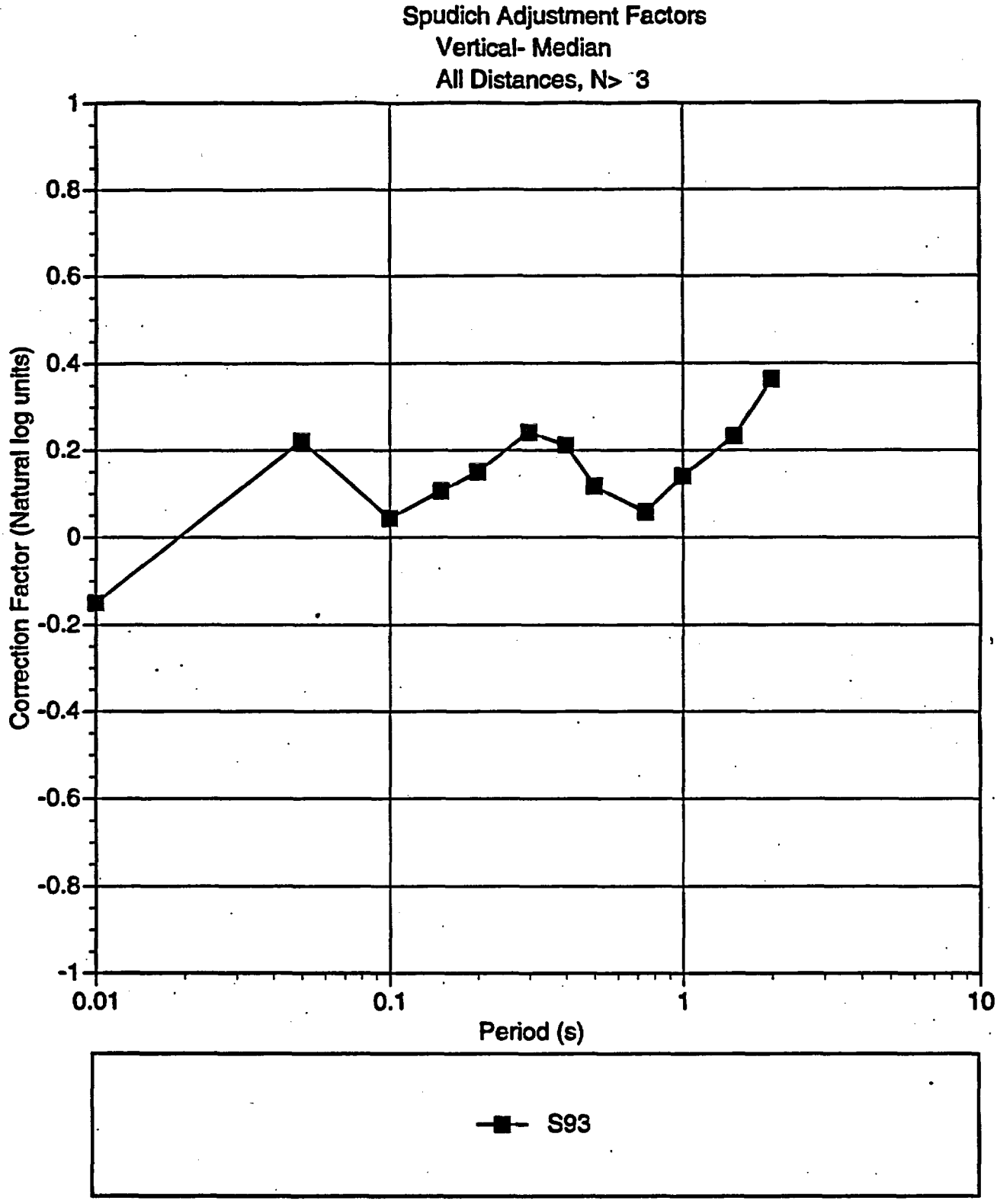
Spudich Adjustment Factors
Vertical- Median
All Distances, N> 3
Correction Factor (Natural log units)
1
0.8
0.6
0.4
0.2
0
-0.2
-0.4
-0.6
-0.8
-1
0.01
0.1
1
10
Period (s)
S93

Spudich Adjustment Factor
Horizontal - Sigma Scale Factor
All Distances, N> 3

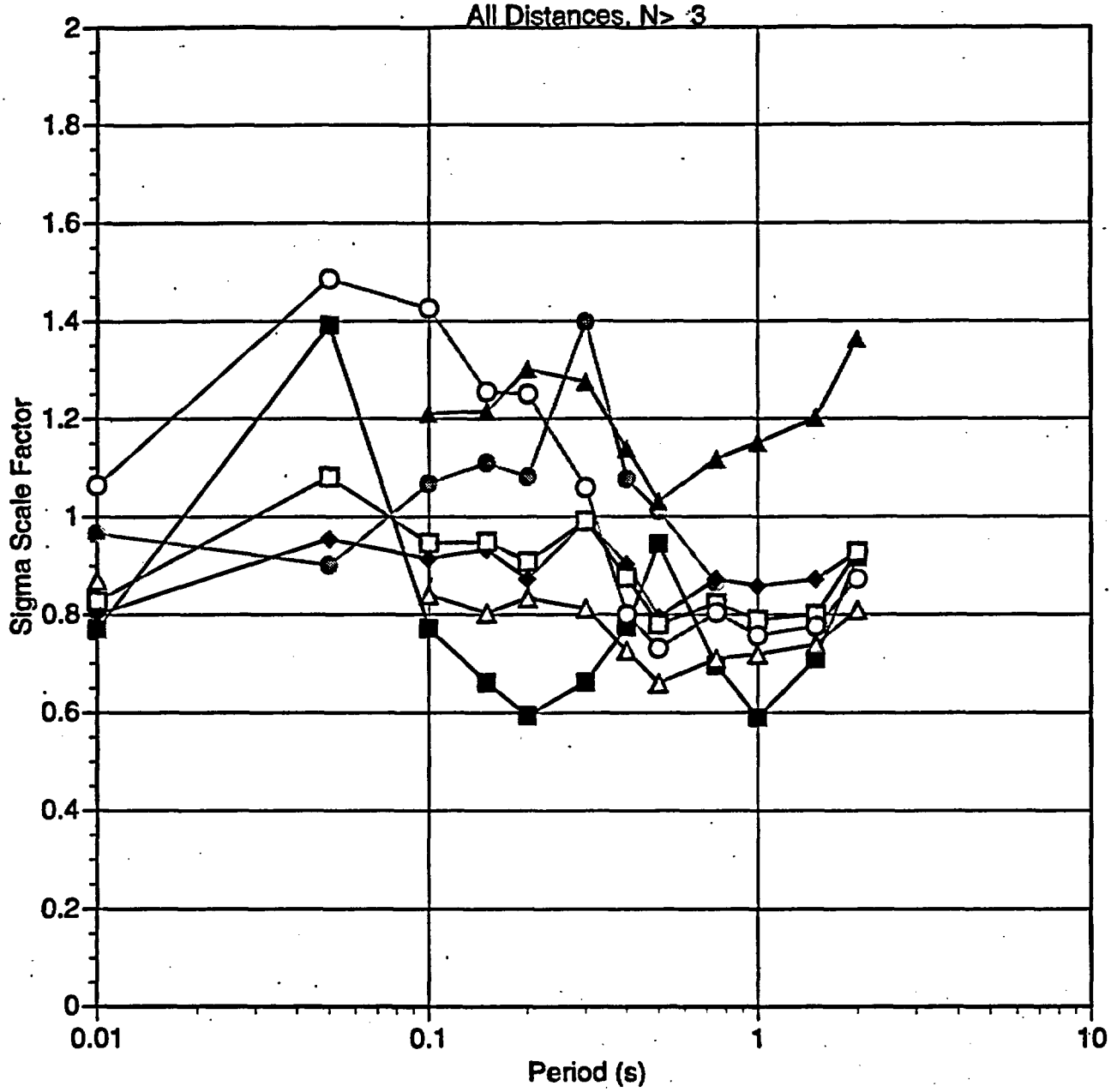

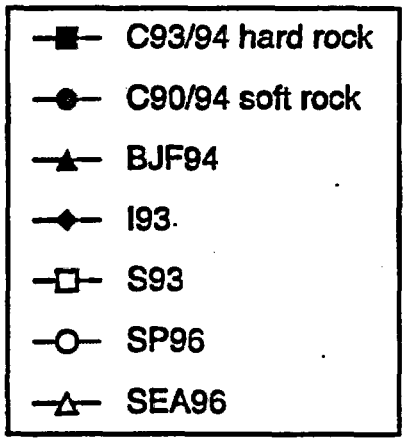

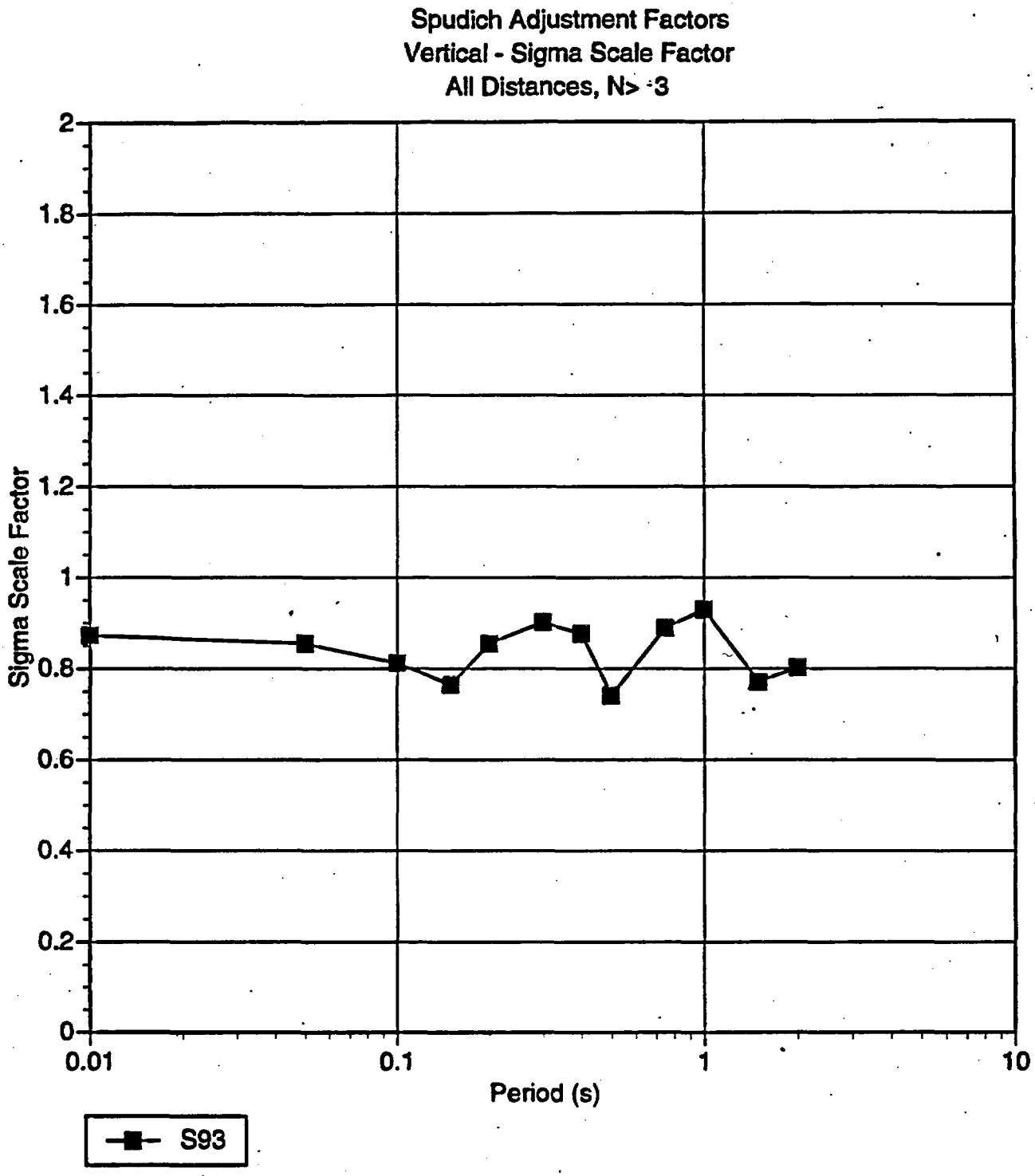
Spudich Adjustment Factors
Vertical - Sigma Scale Factor
All Distances, N> 3
Sigma Scale Factor
2
1.8
1.6
1.4
1.2
1
0.8
0.6
0.4
0.2
0
0.01
0.1
1
10
Period (s)
S93

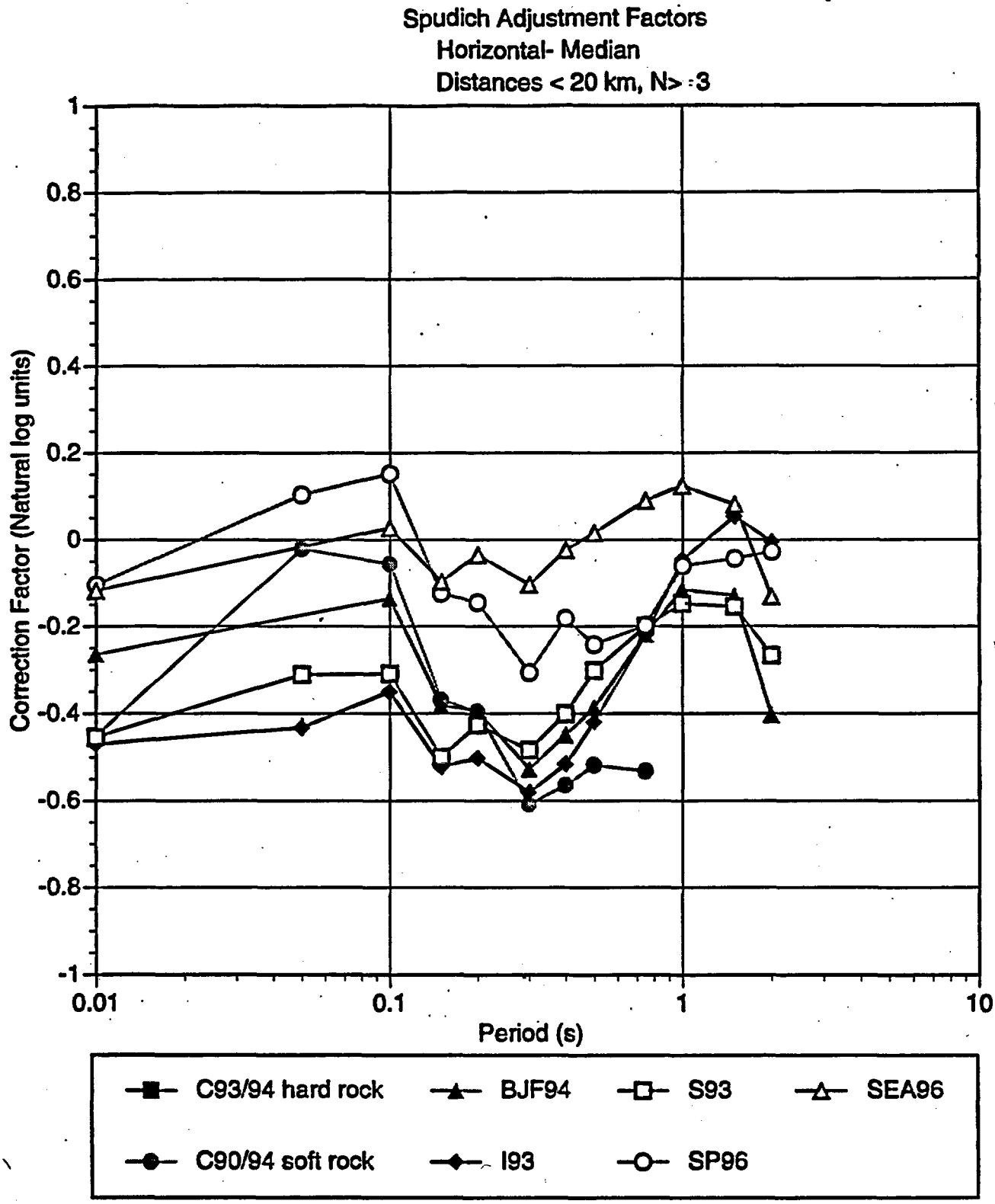
Spudich Adjustment Factors
Horizontal- Median
Distances < 20 km, N> =3
Correction Factor (Natural log units)
1
0.8
0.6
0.4
0.2
0
-0.2
-0.4
-0.6
-0.8
-1
0.01
0.1
1
10
Period (s)
C93/94 hard rock
BJF94
S93
SEA96
C90/94 soft rock
I93
SP96

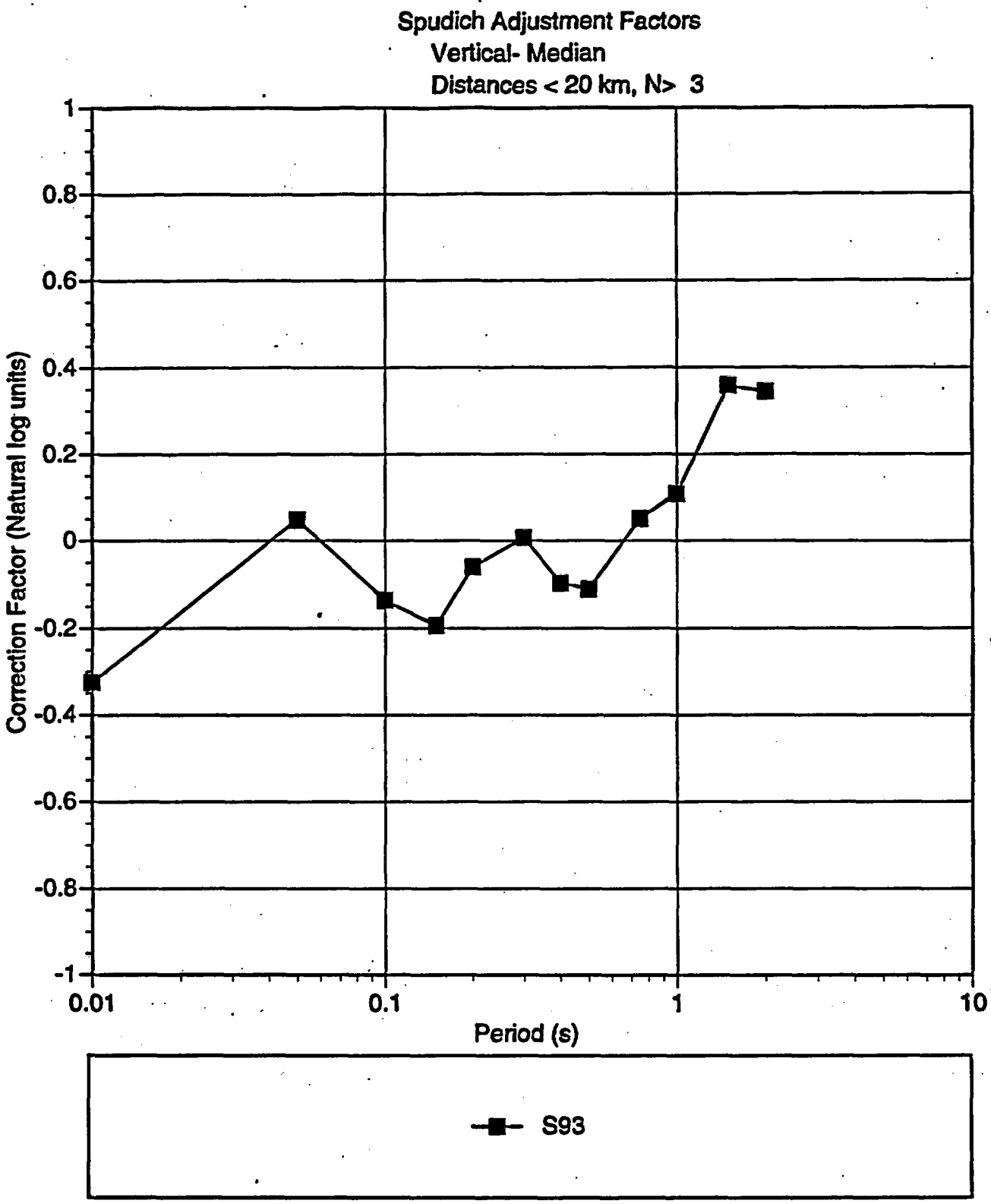
Spudich Adjustment Factors
Vertical- Median
Distances < 20 km, N> 3
Correction Factor (Natural log units)
1
0.8
0.6
0.4
0.2
0
-0.2
-0.4
-0.6
-0.8
-1
0.01
0.1
1
10
Period (s)
S93

Spudich Adjustment Factor
Horizontal - Sigma Scale Factor
d <20km, N> 3

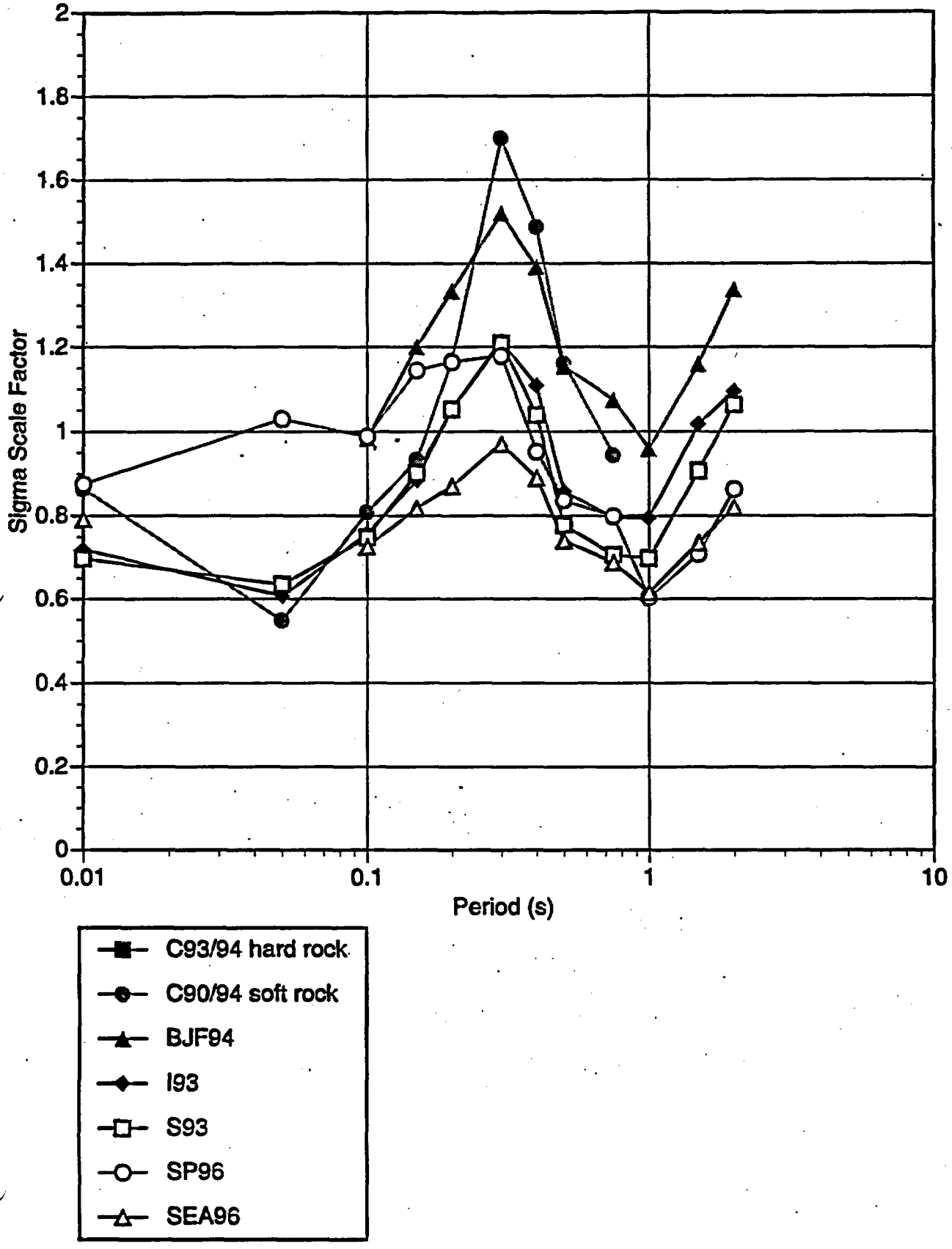

Spudich Adjustment Factors
Vertical - Sigma Scale Factor
d<20 km, N>=3

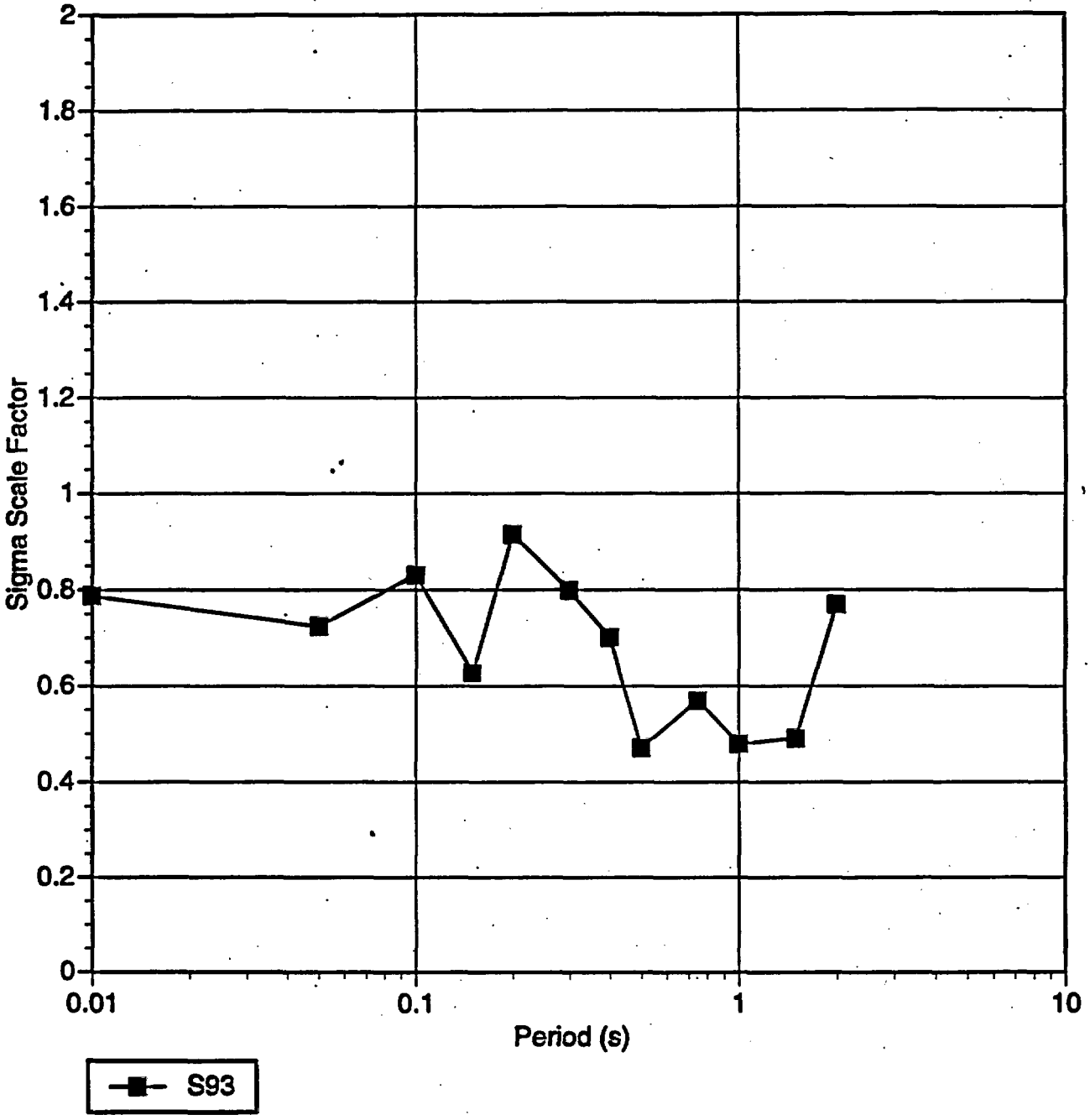

Yucca2Mountain LN Stress Drop Scaling: Magnitude Dependence,
Freq=0.5 Hz

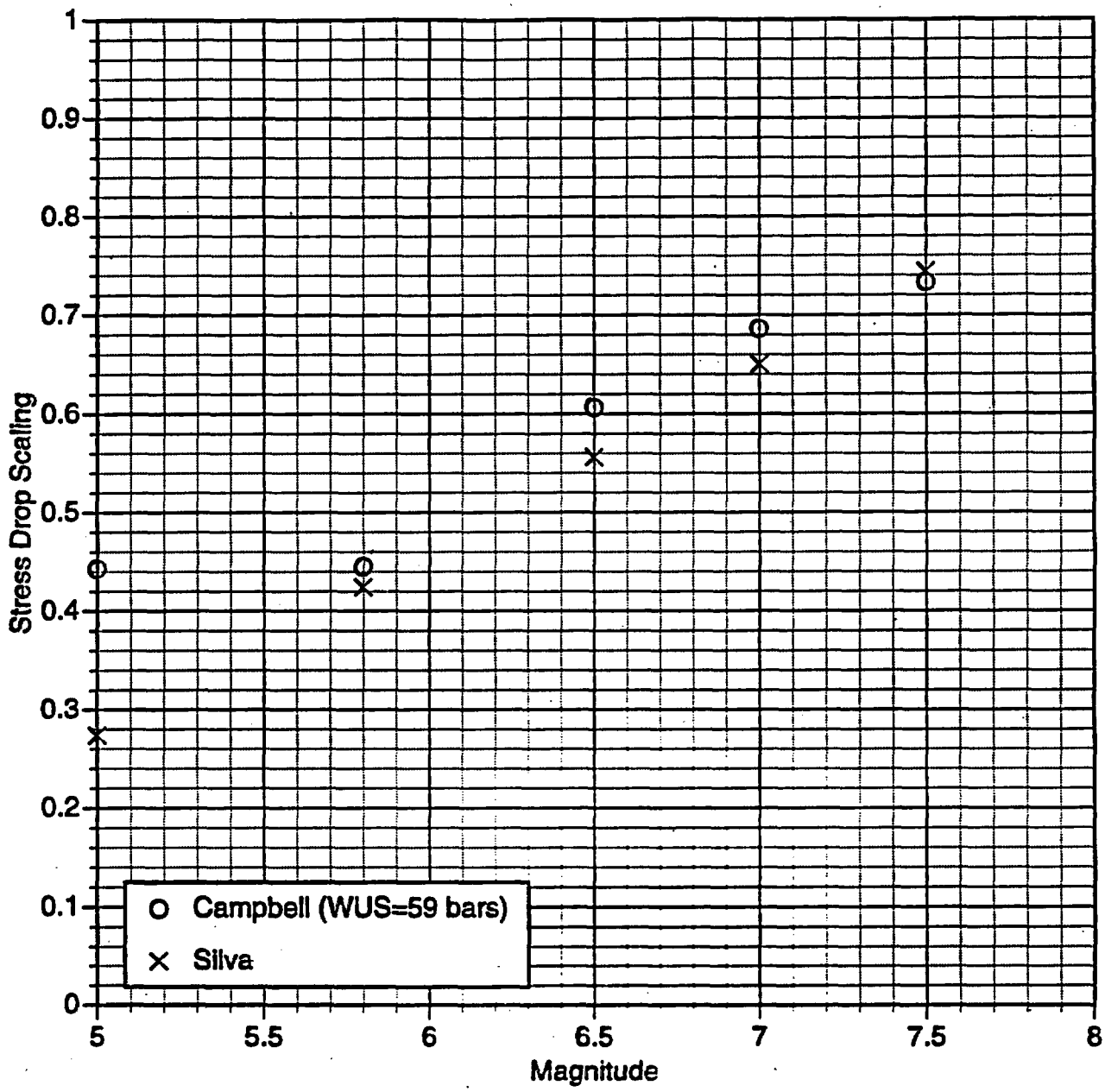

Yucca2Mountain LN Stress Drop Scaling: Magnitude Dependence,
Freq=1.0 Hz

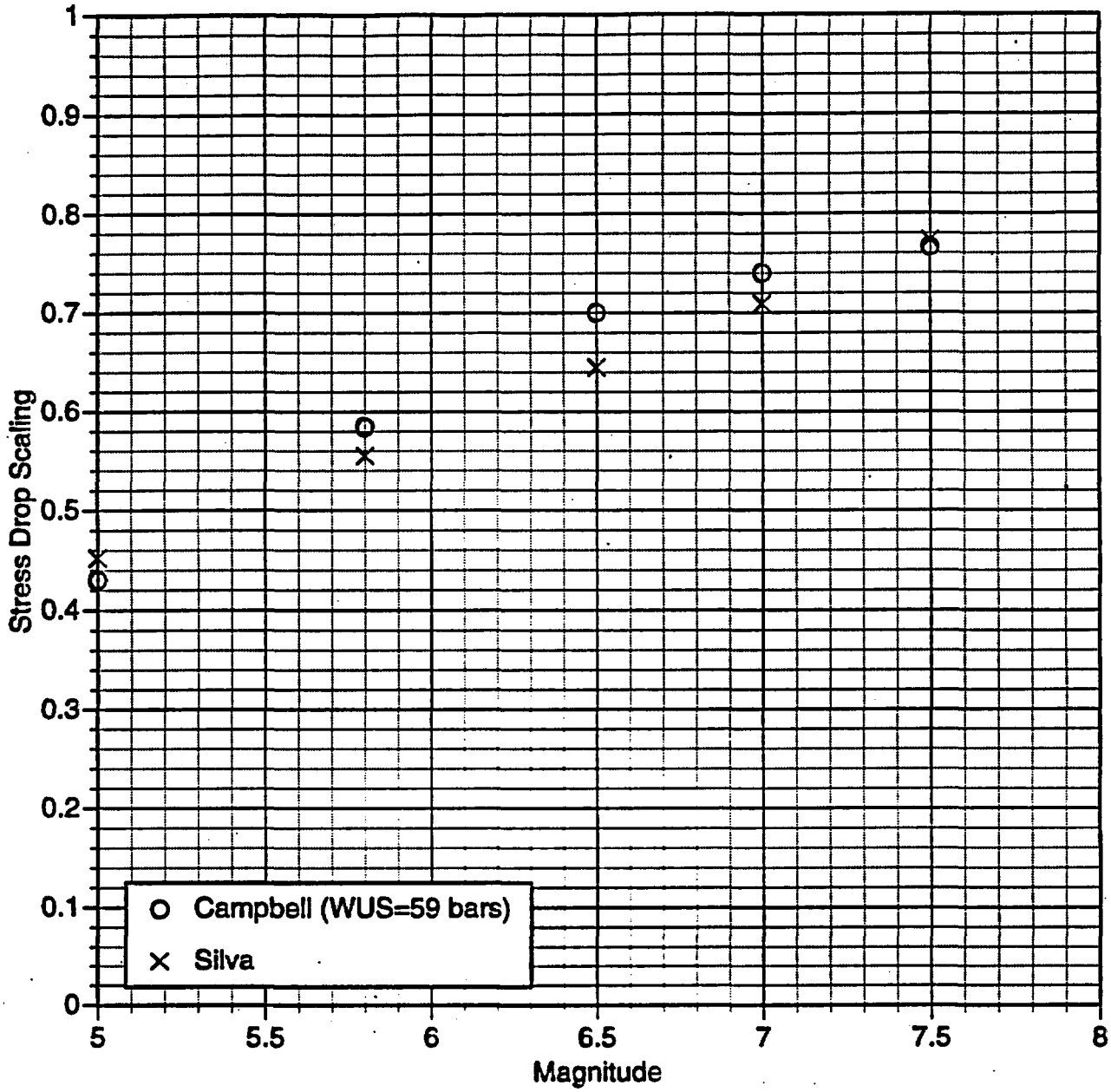

Yucca2Mountain LN Stress Drop Scaling: Magnitude Dependence,
Freq=2 Hz

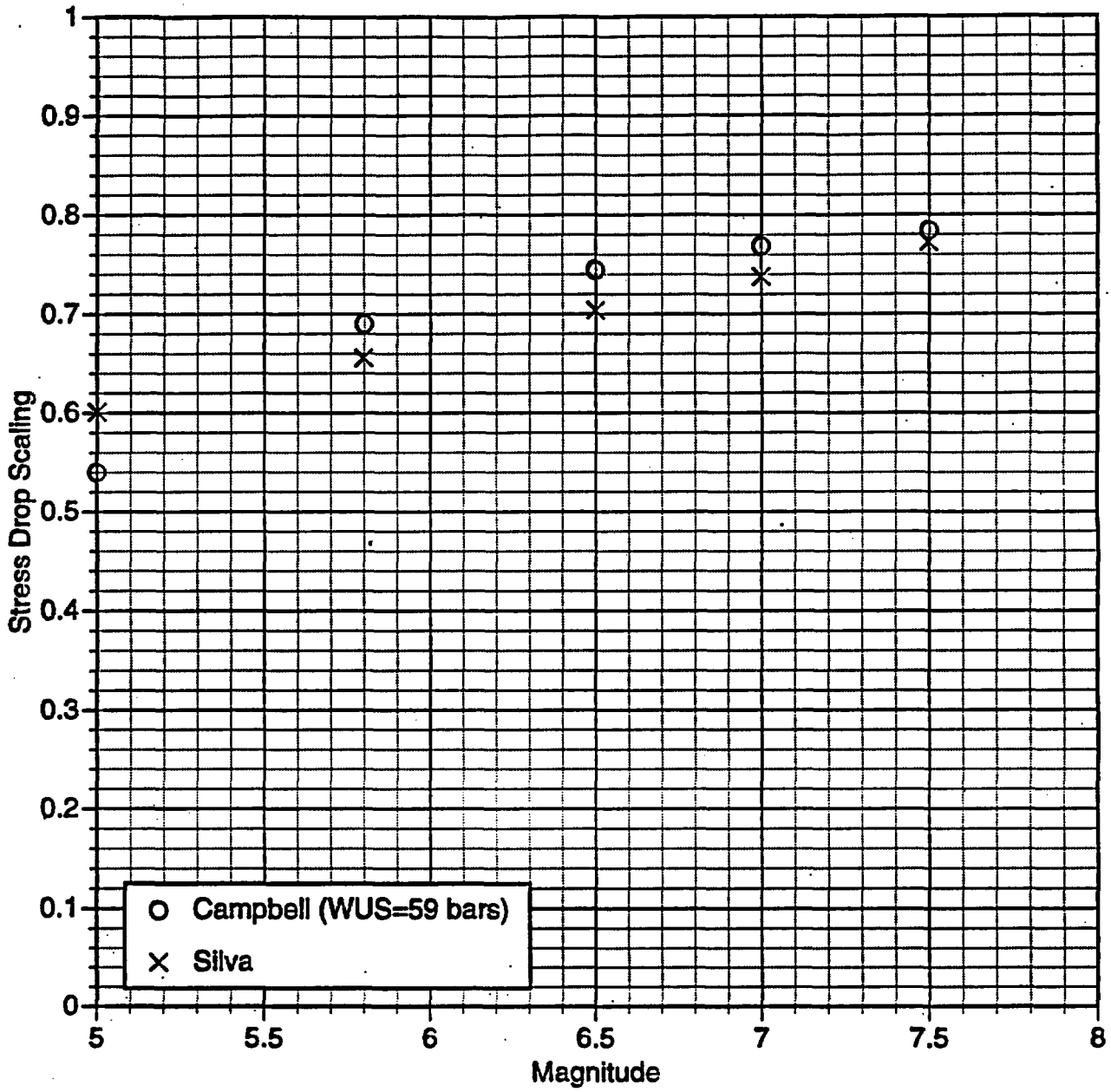

Yucca2Mountain LN Stress Drop Scaling: Magnitude Dependence,
Freq=5 Hz

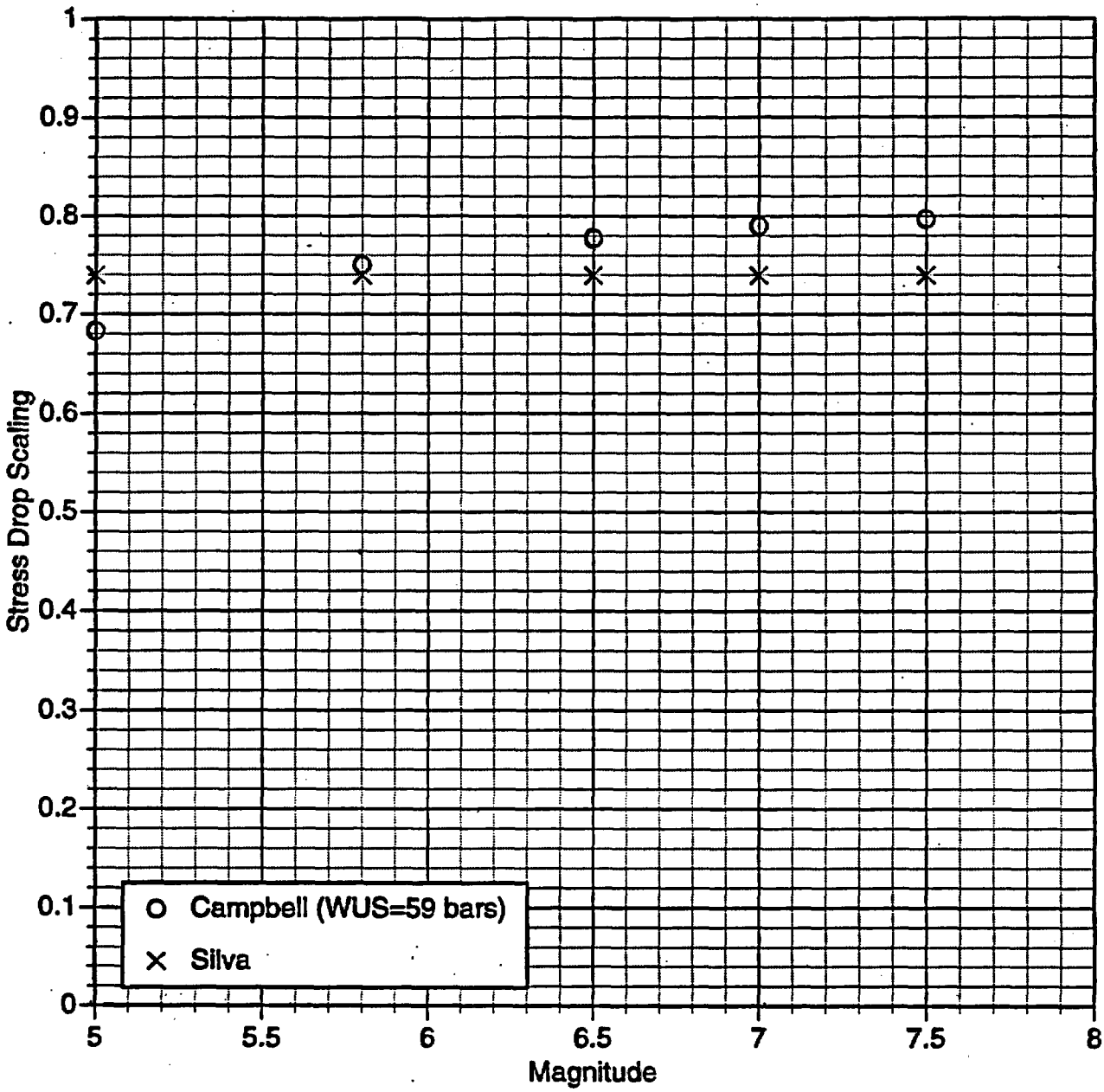

Yucca2Mountain LN Stress Drop Scaling: Magnitude Dependence,
Freq=10 Hz

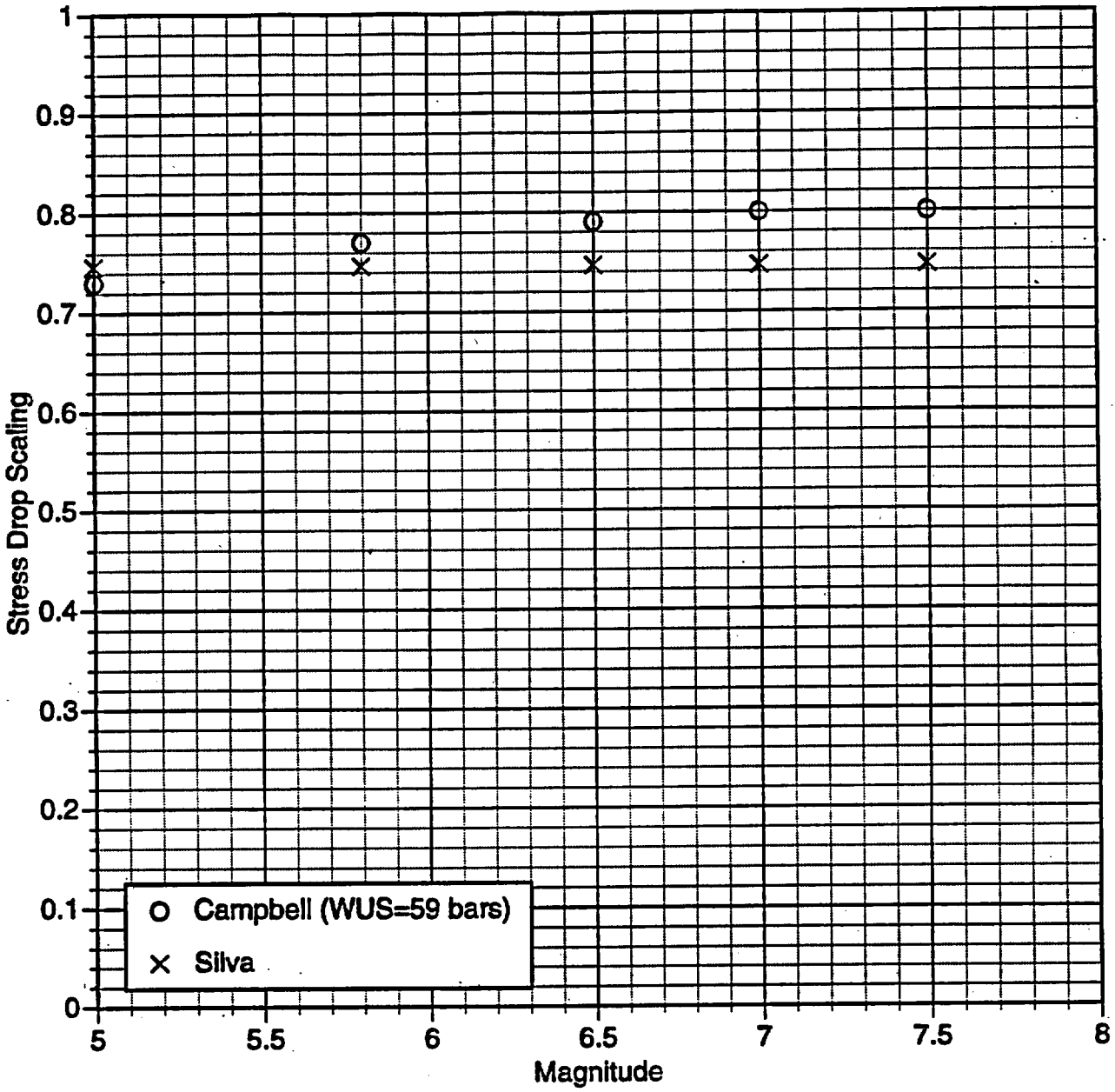

Yucca2Mountain LN Stress Drop Scaling: Magnitude Dependence,
Freq=20 Hz

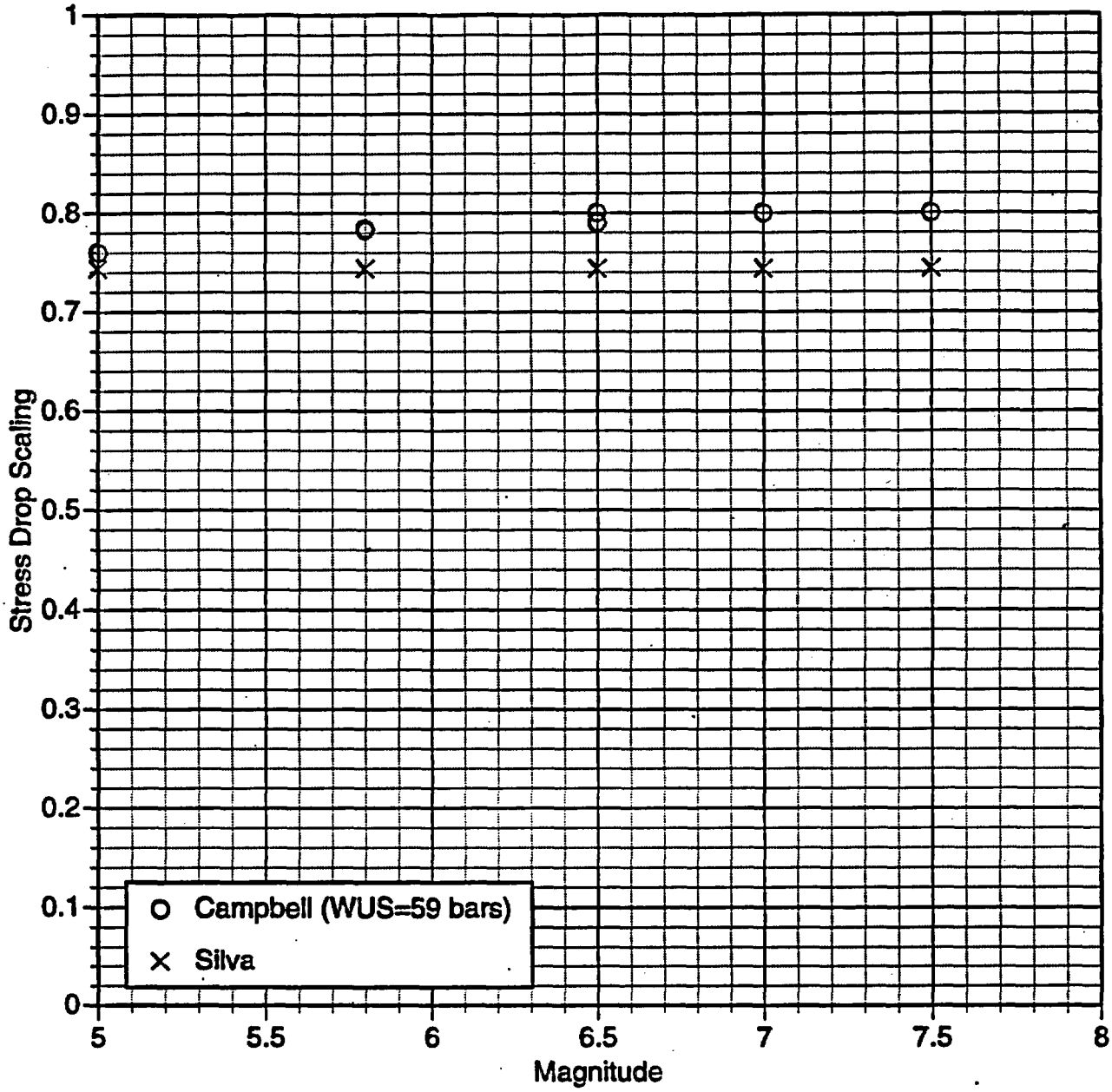

Yucca2Mountain LN Stress Drop Scaling: Magnitude Dependence, PGA

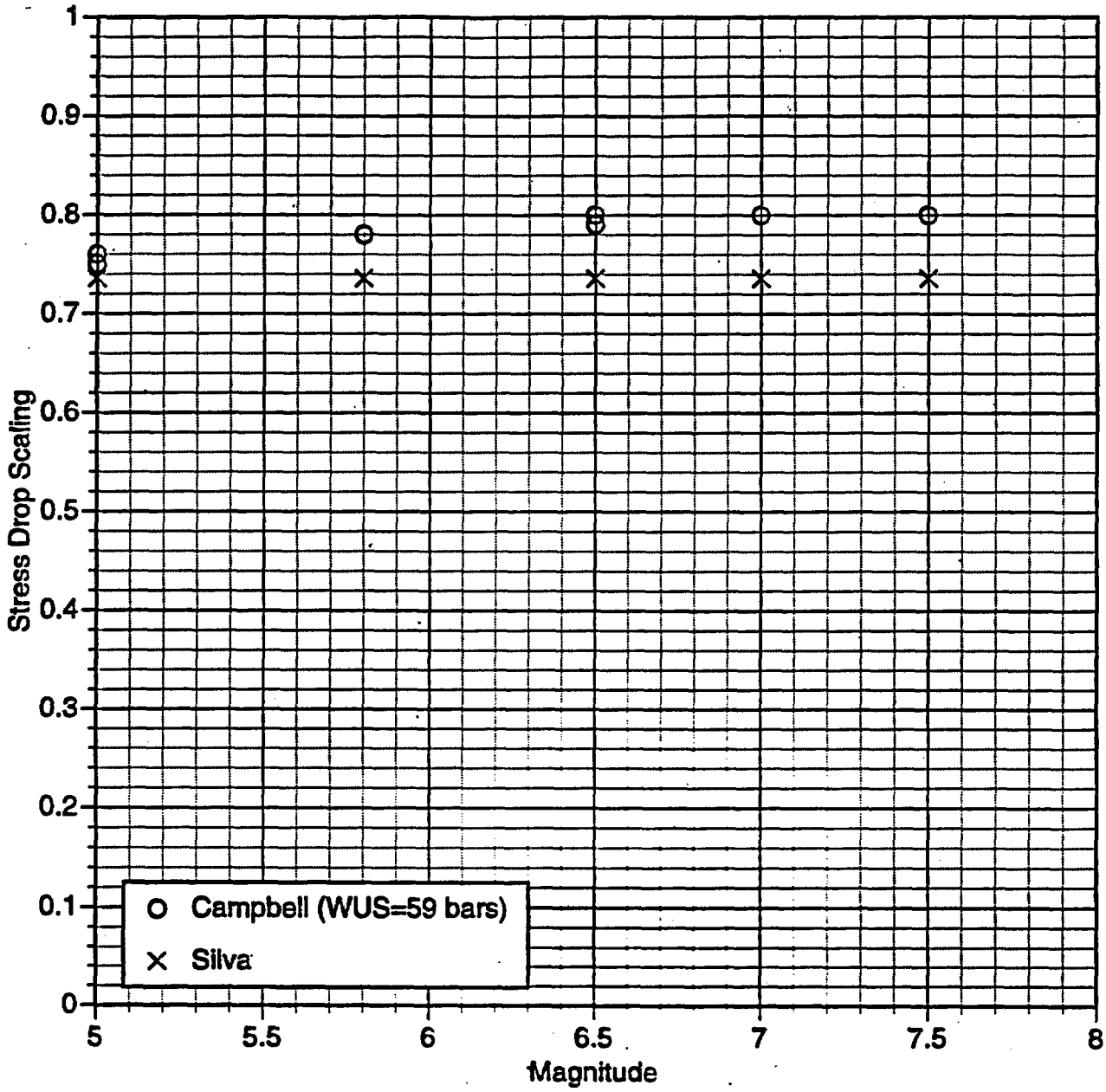

Yucca2Mountain LN Stress Drop Scaling: Magnitude Dependence, PGV

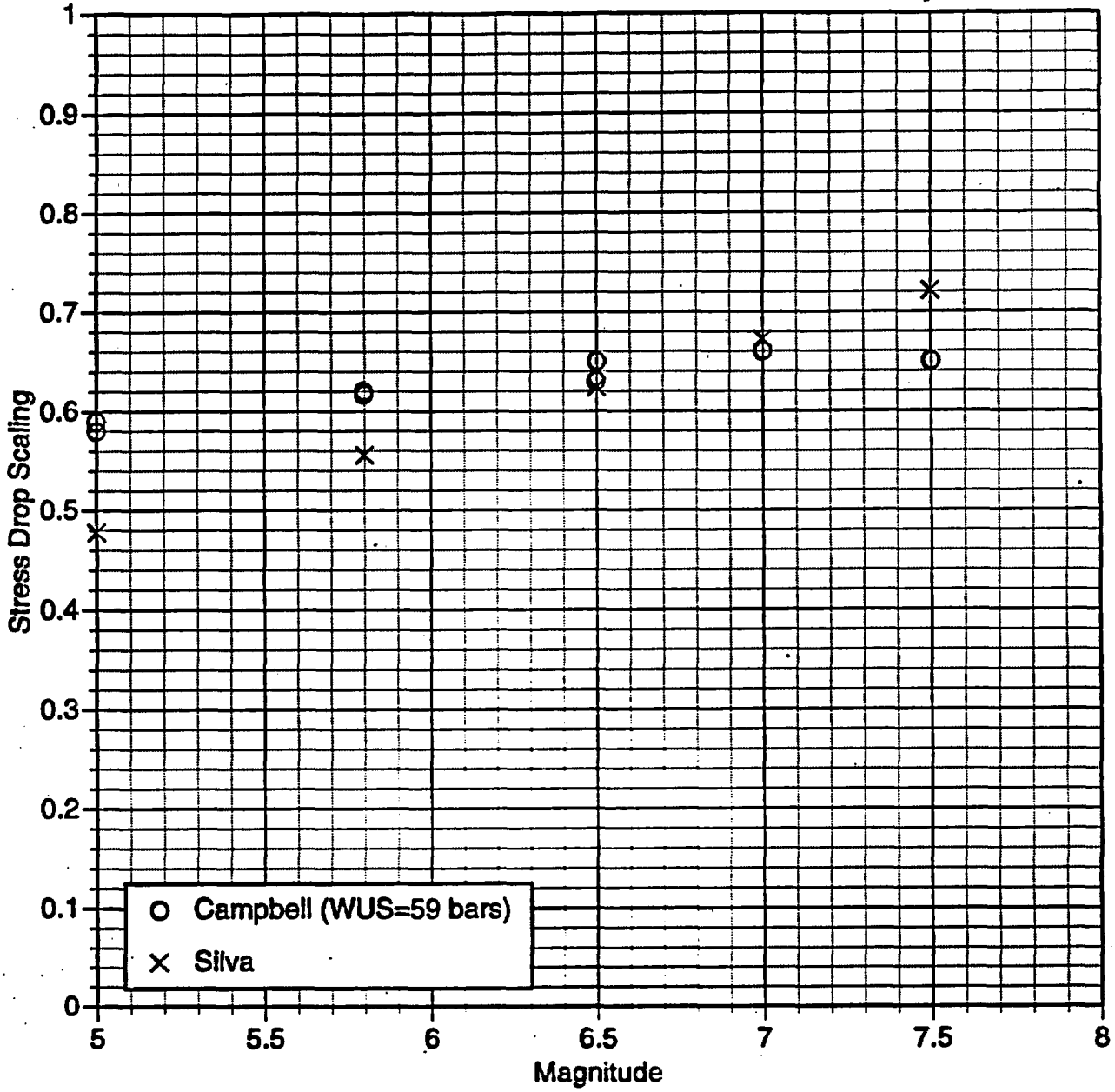

Section 8.5

Vertical to Horizontal Ratios

Regression Results
Vertical-to-Horizontal Ratios for Spectral Points, PGA, and PGV
Silva Point-Source Model, YM_{300} Conditions

Model:

$R \le 64.0$:

$$\ln(\text{Vert/Horiz}) = C_1 + C_2(M-6) + C_3(M-6)^2 + C_4 \ln(\text{Dist}) + C_6[\ln(\text{Dist})](M-6) + C_7\,\text{Dist} + C_8(\text{Kappa} - 0.025)$$

$R > 64.0$:

$$\ln(\text{Vert/Horiz}) = C_1 + C_2(M-6) + C_3(M-6)^2 + C_4 \ln(\text{Dist}) + C_5[\ln(\text{Dist}) - \ln(64.0)] + C_6[\ln(\text{Dist})](M-6) + C_7\,\text{Dist} + C_8(\text{Kappa} - 0.025)$$

1-15-98

Coefficients:

Freq	C_1	C_2	C_3	C_4	C_5	C_6	C_7	C_8	Sigma*
0.20	-0.56431	-0.05686	0.01733	-0.12093	0.74622	0.00281	-0.00505	0.31394	0.18236
0.33**	-0.58057	-0.01874	0.00852	-0.10501	0.73949	-0.00319	-0.00512	0.59524	0.17572
0.40	-0.58681	-0.00409	0.00514	-0.09889	0.73691	-0.00549	-0.00514	0.70330	0.17323
0.50	-0.49973	-0.00204	0.00439	-0.11473	0.61097	-0.00510	-0.00395	0.86771	0.15917
1.0	-0.50075	-0.01074	0.00642	-0.07933	0.60023	-0.00313	-0.00422	1.57476	0.12375
2.0	-0.51179	-0.00462	0.00224	-0.07981	0.51957	-0.00113	-0.00348	3.01062	0.11891
5.0	-0.41454	0.00285	0.00237	-0.07058	0.50832	-0.00337	-0.00362	6.61189	0.10542
10.0	-0.17329	0.02400	0.00509	-0.05598	0.50999	-0.01215	-0.00495	10.05462	0.12195
20.0	0.14158	0.00702	0.00870	-0.12839	0.48953	-0.01152	-0.00504	11.38017	0.14816
100.0	0.05142	-0.03384	0.01011	-0.15336	0.59983	-0.00293	-0.00468	3.48461	0.13003
PGA	-0.00201	-0.02993	0.00925	-0.14378	0.58873	-0.00318	-0.00460	4.04281	0.12994
PGV	-0.41792	-0.08197	0.02438	-0.11403	0.64318	-0.00651	-0.00451	1.39371	0.15329

*** Sigma is computed in the regressions and does not include modeling uncertainty.**

**** Values at 0.33 Hz interpolated from values computed at 0.2 and 0.4 Hz.**

Mar 15, 1997

Data [ln(Vert/Horiz)]used in Vert/Horiz regressions

Freq	Case 1	Case 2	Case 3	Case 4	Case 5	Case 6	Case 7	Case 8
0.20	-0.71949	-0.72526	-0.88236	-0.86779	-0.95237	-0.99036	-0.83488	-0.81925
0.40	-0.76047	-0.76509	-0.89456	-0.88223	-0.92633	-0.96014	-0.80502	-0.79122
0.50	-0.69761	-0.70262	-0.83751	-0.82512	-0.86605	-0.89929	-0.73904	-0.72432
1.00	-0.63934	-0.64311	-0.74896	-0.73888	-0.78008	-0.80754	-0.68486	-0.67380
2.00	-0.67013	-0.67386	-0.77596	-0.76642	-0.79332	-0.81873	-0.69770	-0.68714
5.00	-0.58530	-0.58861	-0.68113	-0.67234	-0.69676	-0.72077	-0.60604	-0.59625
10.0	-0.35320	-0.35588	-0.43745	-0.42913	-0.45721	-0.48213	-0.36525	-0.35575
20.0	-0.14569	-0.15119	-0.30179	-0.28775	-0.34256	-0.38139	-0.19617	-0.17901
100.0	-0.19589	-0.20261	-0.38163	-0.36538	-0.44011	-0.48288	-0.29076	-0.27164
PGA	-0.24124	-0.24756	-0.41674	-0.40132	-0.47102	-0.51173	-0.32860	-0.31053
PGV	-0.51867	-0.52370	-0.66122	-0.64843	-0.77632	-0.81105	-0.69894	-0.68387

Freq	Case 9	Case 10	Case 11	Case 12	Case 13	Case 14	Case 15	Case 16
0.20	-0.84461	-0.81373	-0.90571	-1.31273	-1.29023	-0.96293	-1.32539	-1.29556
0.40	-0.81363	-0.78636	-0.86812	-1.24882	-1.22715	-0.91407	-1.26559	-1.23619
0.50	-0.74819	-0.71910	-0.80513	-1.16339	-1.14433	-0.85087	-1.17791	-1.15201
1.00	-0.69177	-0.66991	-0.73552	-1.04381	-1.02617	-0.77290	-1.05515	-1.03133
2.00	-0.70428	-0.68341	-0.74562	-1.02276	-1.00738	-0.77836	-1.02835	-1.00770
5.00	-0.61215	-0.59280	-0.65079	-0.92006	-0.90476	-0.68078	-0.92670	-0.90598
10.0	-0.37124	-0.35241	-0.40994	-0.71648	-0.69782	-0.43936	-0.73119	-0.70527
20.0	-0.20685	-0.17294	-0.27354	-0.70468	-0.68131	-0.32700	-0.72698	-0.69480
100.0	-0.30263	-0.26486	-0.37618	-0.82728	-0.80372	-0.44266	-0.85394	-0.82221
PGA	-0.33983	-0.30412	-0.40951	-0.84148	-0.81874	-0.47230	-0.86688	-0.83622
PGV	-0.70831	-0.67854	-0.76693	-1.14811	-1.12736	-0.84097	-1.20822	-1.17996

8.5.1-2

Section 8.6

Peak Velocity to Peak Acceleration Ratios

Regression Results
PGV-PGA Ratio
Silva Point Source Model, YM_{300} Conditions

Model:

$R \le 64.0$:

$$\ln(PGV/PGA) = C_1 + C_2(M - 6) + C_3(M - 6)^2 + C_4 \ln(Dist) + C_6[\ln(Dist)](M - 6) + C_7 Dist + C_8(Kappa - 0.025)$$

$R > 64.0$:

$$\ln(PGV/PGA) = C_1 + C_2(M - 6) + C_3(M - 6)^2 + C_4 \ln(Dist) + C_5[\ln(Dist) - \ln(64.0)] + C_6[\ln(Dist)](M - 6) + C_7 Dist + C_8(Kappa - 0.025)$$

Coefficients:

Comp	C_1	C_2	C_3	C_4	C_5	C_6	C_7	C_8	Sigma*
Horiz	4.08192	0.48306	-0.09293	0.08740	-0.04370	0.00262	0.00356	13.68667	0.16943
Vert	3.66602	0.43103	-0.07780	0.11715	0.01075	-0.00071	0.00366	11.03757	0.15323

8.6.1-1

*** Sigma is computed in the regressions and does not include modeling uncertainty.**

Data [ln(PGV/PGA)] used in v/a Regressions:

Comp	Case 1	Case 2	Case 3	Case 4	Case 5	Case 6	Case 7	Case 8
Horiz	3.57462	3.57859	3.68705	3.67697	4.17794	4.20495	4.39293	4.38145
Vert	3.29724	3.30250	3.44271	3.42998	3.87279	3.90582	4.02267	4.00817
	Case 9	Case 10	Case 11	Case 12	Case 13	Case 14	Case 15	Case 16
Horiz	4.40008	4.37739	4.44486	4.73926	4.72312	4.65307	5.04780	5.02602
Vert	4.03167	4.00303	4.08755	4.43315	4.41498	4.28453	4.70699	4.68277

Mar 14, 1997

Woodward-Clyde Memorandum

To: Ground Motion Experts

From: Ann Becker

Office: SLC

Date: February 18, 1997

Subject: Updated Stress Drop Information

Attached is an update to the stress drop computations presented at the second ground motion workshop which reflects 2 changes.

- No modification of the Boore-Joyner amplification function. In the results presented at the workshop, the value of the function above 10 Hz was truncated to the value at 10 Hz. In the attached, no such truncation is incorporated.
- Case 4 rerun with Walt Silva's preferred Q model for California (220 $f^{.6}$) instead of our interpretation of his preferred model (346 $f^{.53}$).

Lastly, in response to a workshop question as to whether the stress drops were 'significantly' different from WNA or California, the 95% confidence limits on the median $\Delta\sigma$ and on the standard deviation of $\ln(\Delta\sigma)$ are included.

Notes on the inversion process are:

- The procedure is a fit of the Fourier amplitude spectra of the data to a Brune-type spectrum with single corner frequency:

$$\text{FAS} \propto \frac{M_o}{R}\frac{f^2}{1+(f/f_c)^\gamma}\exp\left(-\frac{\pi R f}{\beta Q_o f^\eta}\right)A\exp(-\pi\kappa f)$$

  where $\gamma = 2$, Q_o and η are as shown on the results Tables, R is the Joyner-Boore distance tabulated by Spudich et al. (1996), A is the site amplification (transfer function), and M_o is computed for each earthquake. The fit is performed from 0.1 to 20 Hz.

- The inversion is run on f_c which is converted to stress drop using:

$$f_c = \beta\left(\frac{\Delta\sigma}{8.44M_o}\right)$$

Attachments

Table 1: Events Selected For Inversion[1]

	Date	M_W	Number of Rock[2] Sites (Distances)	Number of Soil[3] Sites (Distances)
Abruzzo	5/7/84 17:50	5.8	1 (19.2 km)	4 (30.2, 41.0, 45.6, 49.7)
Borah Peak (Aftershock)	10/29/83 23:29	5.1	2 (22.0, 49.3)	1 (16.9)
Borah Peak (Main Shock)	10/28/83 14:06	6.9	0	2 (83.1, 84.9)
Irpinia A	11/23/80 19:34:54	6.9	6 (10.9, 11.2, 16.2, 24.9, 25.9, 67.7)	2 (36.3, 43.1)
Irpinia B	11/23/80 19:35:04	6.2	6 (8.4, 18.2, 20.3, 22.1, 22.3, 28.9)	4 (41.9, 43.0, 43.9, 64.4)
Little Skull Mtn.	6/29/92 10:14	5.7	2 (23.8, 45.2)	3 (14.1, 58.6, 63.7)
Managua	12/23/72 6:29	6.2	0	1 (3.5)
New Zealand	3/2/87 1:42	6.6	0	2 (18.9, 70.1)
Roermond	4/13/92 1:20	5.3	3 (55.8, 80.7, 102.1)	0

[1] Data are a subset of the extensional data set prepared by Spudich et al. (1996). The selection criterion is a predominantly normal mechanism (rakes between -45° and -135°).

[2] Hard or soft rock (Spudich et al. classes 0, 1, 2)

[3] Deep or shallow soil (Spudich et al classes 5, 6, 7)

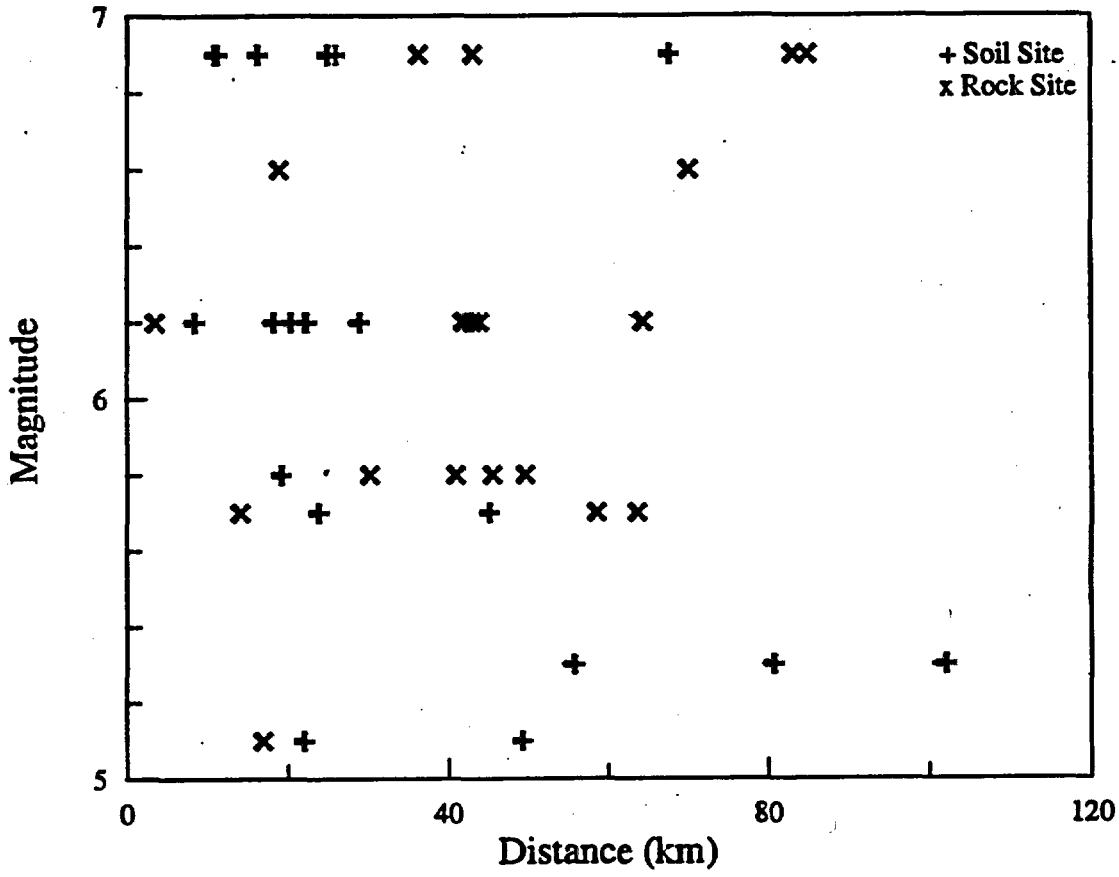

Magnitude and Distance Distribution
Events used in Q/kappa Inversion

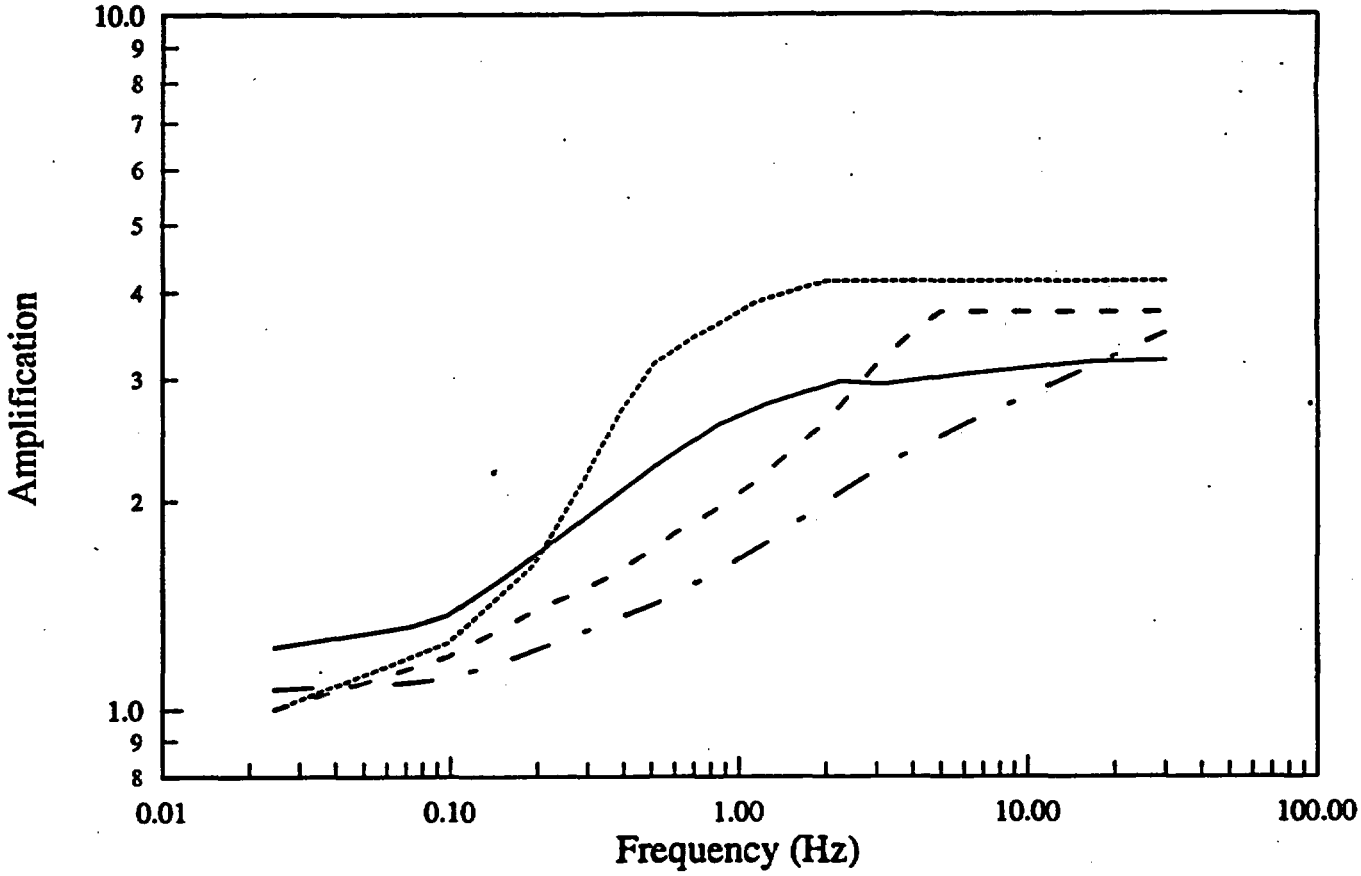

Transfer Functions used in Inversion

— · Boore-Joyner Rock

——— Boore-Joyner Soil

– – – Silva Rock

····· Silva Soil

Table 2: Stress Drops Computed from Inversion of Normal Faulting Data

	32 Independent Sites	12 Independent Sites	32 Independent Sites	32 Independent Sites
Inversion Parameters				
Q Model	$200\ f^{0.4}$	$200\ f^{0.4}$	$200\ f^{0.4}$	$220\ f^{0.6}$ [1]
κ Rock	Float	Float	Float	Float
κ Soil	Float	Float	0.035 Fixed	Float
Spectrum Smoothing	Linear	Linear	Linear	Linear
Transfer Function	Silva	Silva	Boore-Joyner	Silva
Stress Drop (bars)				
Abruzzo	95	95	43	92
Borah Aftershock	18	24	25	18
Borah Main Shock	42	42	189	40
Irpinia A	30	32	25	29
Irpinia B	28	27	23	28
LSM	45	33	68	33
Managua	16	16	6	16
New Zealand	31	31	30	30
Roermond	49	49	98	46
Median $\Delta\sigma$	34	34	37	32
95% Confidence Limits on $\Delta\sigma$ [2]	22 - 53	23 - 52	17 - 84	21 - 49
Standard Deviation of $\ln(\Delta\sigma)$	0.54	0.50	0.99	0.52
95% Confidence Limits on Standard Deviation [3]	0.37-1.04	0.34-0.96	0.67-1.90	0.35-0.99

[1] Silva's preferred values for California events
[2] Computed using t-test
[3] Computed using chi-square test

Table 3: Kappa Computed from Inversion of Normal Faulting Data

	32 Independent Sites	12 Independent Sites	32 Independent Sites	32 Independent Sites
Inversion Parameters				
Q Model	200 $f^{0.4}$	200 $f^{0.4}$	200 $f^{0.4}$	220 $f^{0.6}$
κ Rock	Float	Float	Float	Float
κ Soil	Float	Float	0.035 Fixed	Float
Spectrum Smoothing	Linear	Linear	Linear	Linear
Transfer Function	Silva	Silva	Boore-Joyner	Silva
Kappa (sec)				
Median κ	0.047	0.042	0.047	0.057
κ rock sites	0.057	0.050	0.053	0.065
κ soil sites	0.047	0.045	(0.035 fixed)	0.056
Abruzzo	0.061[1]	0.058[2] 0.062	0.040[3]	0.069[1]
Borah A/S	0.033[1]	0.048[2] 0.043	0.027[3]	0.040[1]
Borah MS	0.013[1]	–[2] 0.013	–	0.031[1]
Irpinia	0.062[1]	0.067[2] 0.055	0.057[3]	0.069[1]
LSM	0.036[1]	0.016[2] 0.031	0.038[3]	0.041[1]
Managua	0.066[1]	–[2] 0.066	–	0.067[1]
New Zealand	0.045[1]	–[2] 0.045	–	0.055[1]
Roermond	0.062[1]	0.062[2] –	0.068[3]	0.079[1]

[1] Kappas shown are the average values for all sites (both rock and soil) for each earthquake.

[2] Kappas shown are the average values for rock sites (upper) and soil sites (lower) for each earthquake.

[3] Kappas shown are the average values for all rock sites for each earthquake; soil kappa values were fixed at 0.035 sec.

MODIFICATION OF THE LUCERNE TIME HISTORY OF THE 1992 LANDERS EARTHQUAKE TO INCLUDE GEODETICALLY DEFINED STATIC DISPLACEMENTS

Robert Graves

Woodward-Clyde Federal Services

Pasadena, CA 91101

May 30, 1996

On the enclosed diskette we have included processed time histories of the Lucerne Valley recording of the 1992 Landers earthquake. The original time histories were obtained from Professor Bill Iwan at Caltech. The horizontal components of these original recordings were oriented along azimuths of 275° and 360°, with respect to north.

Our processing of these records is given by the following steps:

1. Rotate horizontal time histories into a set of orthogonal components oriented along directions parallel and perpendicular to the direction of dynamic fault rupture. Since the Landers earthquake occurred on a segmented fault which bends to the northwest, there is not a unique definition for the strike of the fault. For our purposes, we define the direction of dynamic fault rupture as the average of the strikes of the fault segments which ruptured toward the Lucerne Valley site. This represents all fault segments south of the site to the epicenter. The azimuth of this averaged strike direction is 340° and the component normal to this is 70°. Note that these orientations do not necessarily agree with the local strike of the fault as given by the rupture segment closest to the Lucerne Valley site.

2. These horizontal components were then modified to match the final static displacement at the Lucerne site which was predicted using the geodetic fault model of Ken Hudnut. His model predicts a final displacement of 126 cm to the north and 172 cm to the west. The modification of the records consists of adding an appropriate long-period step function to the original displacement time history such that the resulting time history matches the prescribed static offset. In practice, I calculate the long-period step function in displacement, then differentiate twice to obtain acceleration, and then I add this function to the original acceleration record. The accompanying Figure 1 shows plots of the original (top panel) and modified (bottom panel) time histories. I have also included plots (Figures 2 and 3) which show that the modification has little effect on the response spectra for periods less than 10 sec.

Prof. Jim Anderson
Civil Engineering Department
University of Southern California
Los Angeles, CA 90089-2531

May 30, 1996

Dear Professor Anderson,

On the enclosed diskette we have included processed time histories of the Lucerne Valley recording of the 1992 Landers earthquake. The original time histories were obtained from Professor Bill Iwan at Caltech. The horizontal components of these original recordings were oriented along azimuths of 275° and 360°, with respect to north.

Our processing of these records is given by the following steps:

1. Rotate horizontal time histories into a set of orthogonal components oriented along directions parallel and perpendicular to the direction of dynamic fault rupture. Since the Landers earthquake occurred on a segmented fault which bends to the northwest, there is not a unique definition for the strike of the fault. For our purposes, we define the direction of dynamic fault rupture as the average of the strikes of the fault segments which ruptured toward the Lucerne Valley site. This represents all fault segments south of the site to the epicenter. The azimuth of this averaged strike direction is 340° and the component normal to this is 70°. Note that these orientations do not necessarily agree with the local strike of the fault as given by the rupture segment closest to the Lucerne Valley site.

2. These horizontal components were then modified to match the final static displacement at the Lucerne site which was predicted using the geodetic fault model of Ken Hudnut. His model predicts a final displacement of 126 cm to the north and 172 cm to the west. The modification of the records consists of adding an appropriate long-period step function to the original displacement time history such that the resulting time history matches the prescribed static offset. In practice, I calculate the long-period step function in displacement, then differentiate twice to obtain acceleration, and then I add this function to the original acceleration record. The accompanying Figure 1 shows plots of the original (top panel) and modified (bottom panel) time histories. I have also included plots (Figures 2 and 3) which show that the modification has little effect on the response spectra for periods less than 10 sec.

The records are stored in ASCII with one component to a file. Each file has two header lines followed by the data in (6e13.5) format. The first header line has the form

STAT COMP TITLE

where STAT is the station name, COMP is the component orientation, and TITLE is a character string. The second header line has the form

NT DT XX XX XX XX XX XX XX

where NT is the number of time points, DT is the time step, and the fields XX are not used.

Nine files are included on the diskette, three components each for acceleration, velocity and displacement. The naming convention of these files is illustrated below

filename	component	mode
lcssver.acc	vertical	acceleration
lcss340.acc	340° azimuth	acceleration
lcss070.acc	70° azimuth	acceleration
lcssver.vel	vertical	velocity
lcss340.vel	340° azimuth	velocity
lcss070.vel	70° azimuth	velocity
lcssver.dis	vertical	displacement
lcss340.dis	340° azimuth	displacement
lcss070.dis	70° azimuth	displacement

On the diskette, these files have been compressed using the program PKZIP into a self extracting ZIP file named *lcss.exe*. To extract the individual files from the diskette, simply type the name of the self-extracting ZIP file, *lcss.exe*. Each of the individual files is about 160 kbytes, so a total of about 1.5 Mbytes of space is need for all nine files.

If you have any difficulties retrieving the data from the diskette, or if you have any questions or comments regarding the records themselves, please feel free to call me anytime.

Sincerely,

Robert W. Graves
email: rwgrave0@wcc.com

cc ...

Lucerne Valley, Iwan corrected

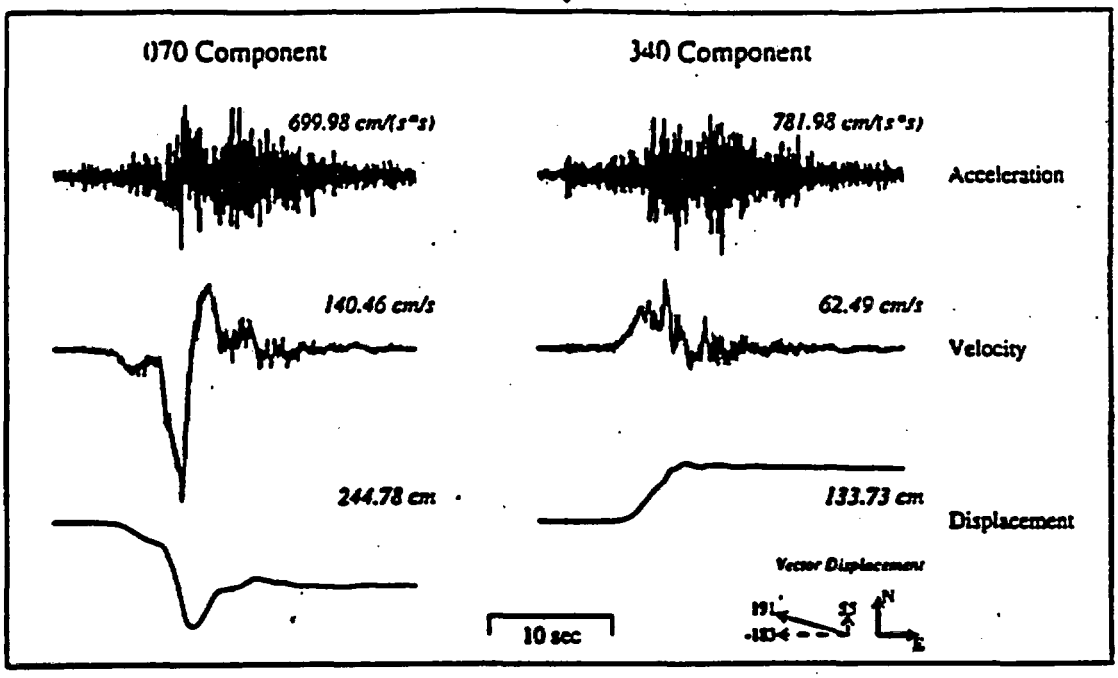

Lucerne Valley, Geodetic statics

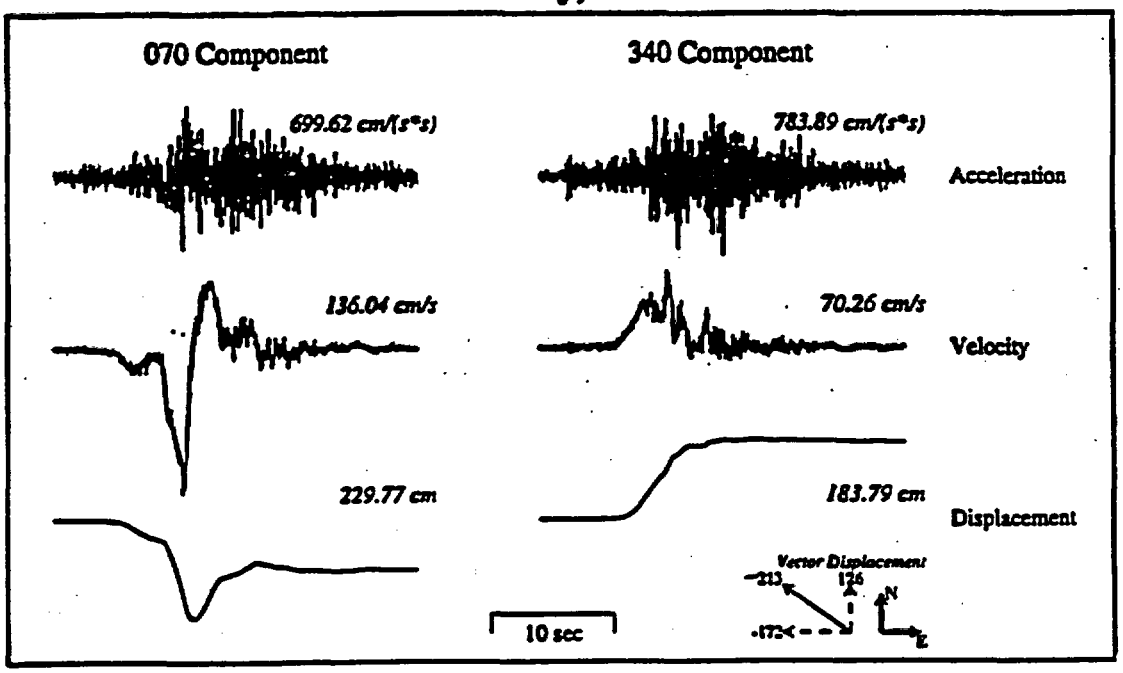

Figure 1

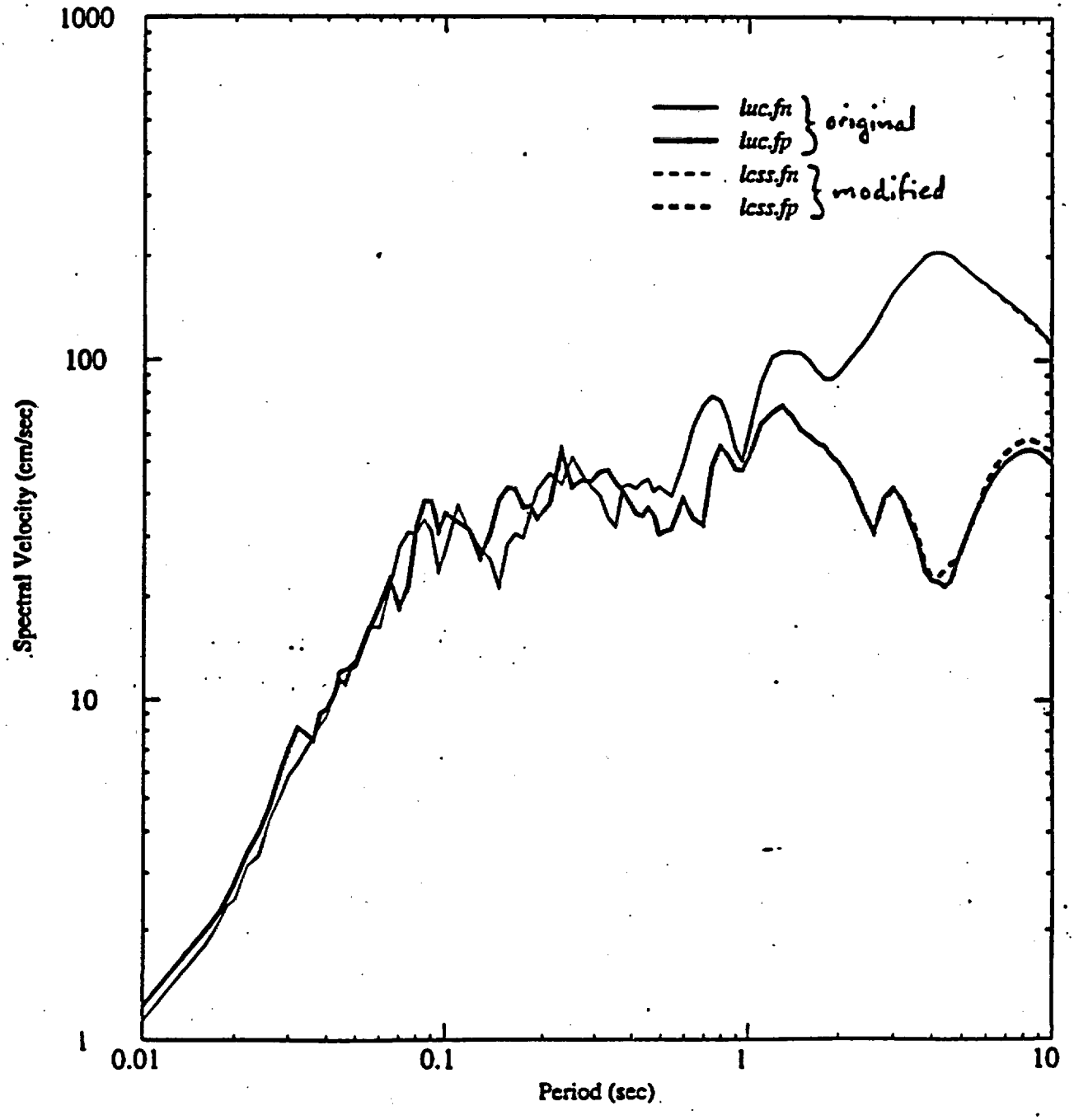
1000
100
10
1
0.01
0.1
1
10
Spectral Velocity (cm/sec)
Period (sec)
luc.fn
luc.fp
original
lcss.fn
lcss.fp
modified

figure 2

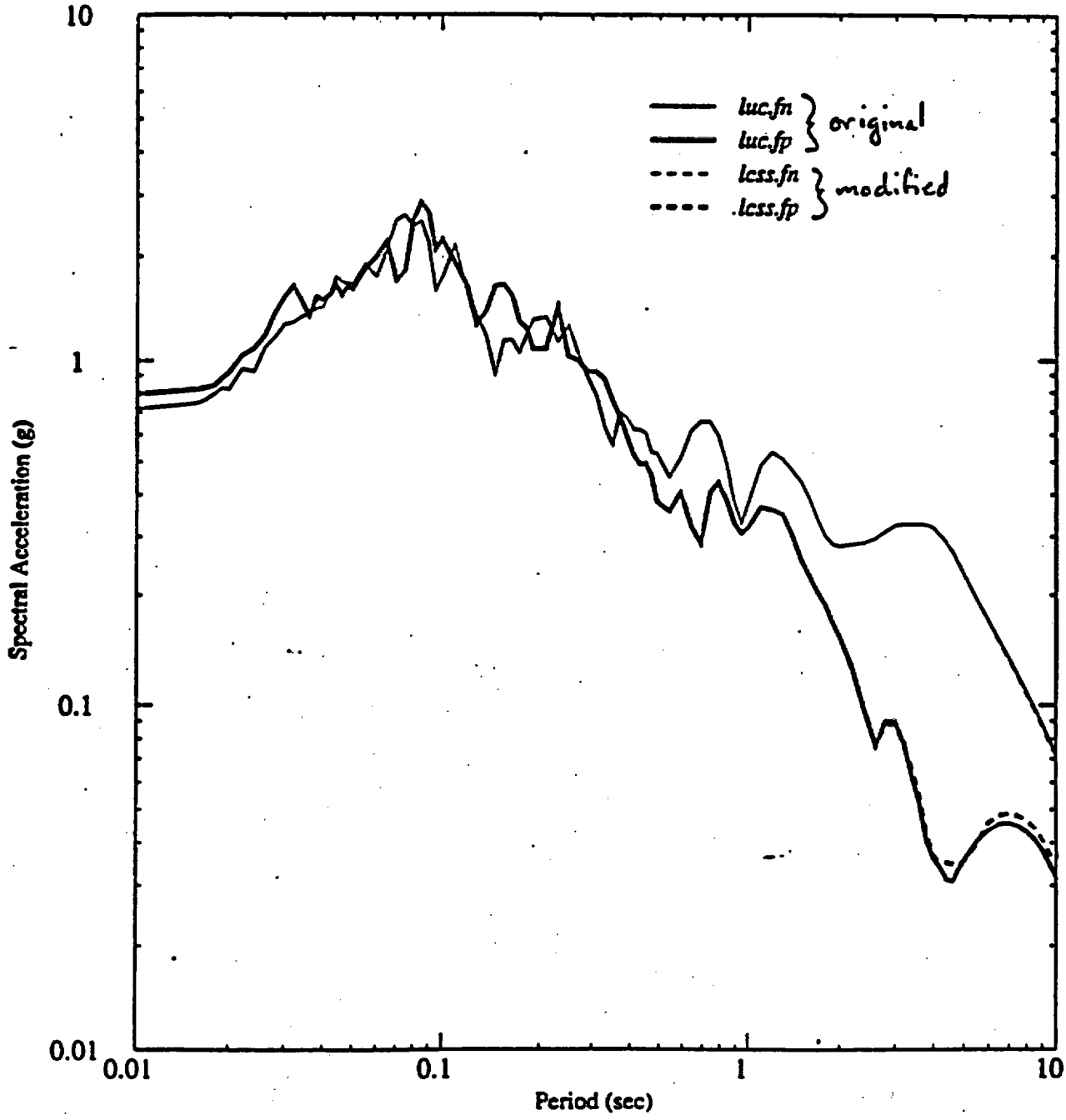
10
1
0.1
0.01
0.01
0.1
1
10
Spectral Acceleration (g)
Period (sec)
luc.fn
luc.fp
original
lcss.fn
lcss.fp
modified

figure 3

Toppling Accelerations of Precarious Rocks in Northern Nevada

Field measurements of the quasi-static toppling accelerations, A_q, for several precariously balanced rocks in northern Nevada are listed in the table below. Accelerations are determined either by the ratio of the toppling force and the estimated mass of the rock ($A_q = f/m$), or by measuring α, the angle between the vertical and the line connecting the center of mass to the rocking point ($A_q = \alpha g$). Approximate dynamic accelerations, A_d, for a time history with the same shape as the El Centro seismogram are obtained by increasing the quasi-static value by 20%. This is based on a series of numerical tests (Shi *et al.*, 1996).

We tested four rocks located at Pearce Ranch, near the fault scarp of the 1915, Pleasant Valley earthquake, and one rock near the Genoa fault.

Rock I.D.	Location	M	d (m)	δ	D (m)	$\bar{F}$	A_q (g)	A_d (g)	Δ	$L.C.$
Pearce Ranch		7.75	3.8	60°W						
PRQ-1	40.3426° N 117.6056° W				10	N75°W	0.20	0.24	±10 %	A
PRQ-1						W20°S	0.22	0.26	±10 %	B
PRQ-1						W35°S	0.22	0.27	±10 %	B
PRQ-3					100	W48°S	0.11	0.13		C
PRQ-4					100	E10°S	0.16	0.20	±10 %	B
Genoa,		7.25	4.5	60°E						
GNO-1	38.9792° N 119.8386° W				200	E20°S	0.21	0.26	±30 %	B

M magnitude of the most recent earthquake
d fault offset at nearest point on fault trace during the most recent earthquake
δ fault dip
D approximate distance of the precarious rock from the fault
$\bar{F}$ direction of the quasi-static toppling force (estimated to be the minimum direction)
A_q quasi-static toppling acceleration
A_d approximate dynamic toppling acceleration ($\sim A_q \times 1.2$)
Δ possible range due to error in estimating the mass, or α
$L.C.$ level of confidence

References

Shi, B., A. Anooshehpoor, Y. Zeug, and J.N. Brune, 1996, Rocking and overturning of precariously balanced rocks by earthquakes, *Bull. Seism. Soc. Am.*, vol. 86, no. 5, pp. 1364-1371.

11.1-2

APPENDIX 1.
BROADBAND GROUND MOTION SIMULATION METHOD

Introduction

The broadband strong motion simulation method is a hybrid method that computes the ground motions separately in the short period and long period ranges and then combines them. We used a transition period of 1 seconds between the short period and long period ranges in the simulations described in this report; Figure A1-1 schematically shows the matched filters for a period of 3 seconds. The method used for short periods is based on the summation of strong motion recordings from smaller earthquakes. The method used for long periods is a standard method for calculating synthetic seismograms based on theoretical Green's functions. This standard method has been used extensively to successfully model the waveforms of long period strong ground motions recorded from many recent earthquakes, and is the basis for the rupture models of earthquakes that are inverted from strong motion recordings.

The fault model is specified as a finite rectangular fault surface that is divided into discrete sub-fault elements, and the motions from these elements are summed and lagged to simulate the propagation of rupture over the fault surface. The parameters required for specifying the source are seismic moment, fault length, fault width, strike, dip, rake, depth of top of fault, hypocenter, rupture velocity, and slip distribution (which may include spatially variable rake and time function of slip). Radiation pattern and fault subevents are treated differently in two different period ranges. For the long period simulation, the fault is discretized finely enough to produce a continuous slip function for periods longer than the transition period, and the theoretical radiation pattern is used.

For the short period simulation, the fault is discretized into sub-fault elements whose dimensions are chosen so as to maintain self-similarity in the spectral shape between the subevent on the fault element and the large event based on an omega-squared scaling relation (Joyner and Boore, 1986), as described by Somerville et al. (1991). The radiation of seismic waves from these sub-fault elements is represented by empirical source functions, which are recorded accelerograms of events having the dimensions of the fault elements and that have been corrected back to the source.

The modeling of wave propagation effects requires the specification of seismic velocities, density, and Q of a flat layered crustal model. Path effects are treated differently in these two different period ranges. At long periods, path effects are represented by Green's functions calculated using an efficient frequency-wavenumber integration scheme (Saikia, 1994). These Green's functions contain the complete response of the anelastic layered medium (all body wave and surface wave phases) for frequencies below a given value (typically chosen to be 5 Hz). They also contain the near-field term in addition to the far-field term, and include the static displacement field of the earthquake. At short periods, path effects are represented by simplified Green's functions calculated using generalized ray theory (Helmberger, 1983). These Green's functions are accurate up to indefinitely high frequencies (typically 50 Hz), and contain all of the significant rays. They are simplified in the sense that they do not include the radiation pattern

and the receiver function. The simplified Green's functions are used to transfer the empirical source functions from the depth, horizontal range and velocity structure in which they were recorded to the depth, horizontal range and velocity structure in which they are to be used for ground motion simulation. Scattering effects in the path are represented empirically by wave propagation effects contained in the recorded source functions.

At long periods, site effects are incorporated by calculating Green's functions using surface velocity, density and Q appropriate for the site. For the short period part of the simulation, the receiver function is included empirically in the recorded source functions; the partitioning of energy among components is treated in a site-specific manner by applying a receiver function correction to the empirical source functions which rotates the recorded wave field into the appropriate partitioning for the velocity structure at the site. Scattering effects near the site are represented by wave propagation effects contained in the empirical source functions that are not modeled by the simplified Green's functions. The site attenuation contained in the empirical source functions is adjusted to provide the value that is appropriate at the site.

In the following sections, we provide more detail about specific aspects of the broadband strong motion simulation procedure. This description addresses the earthquake source, the propagation path, and the site, and summarizes the parameters requiring specification. It also describes important features of the procedure and the validation of the procedure against recorded strong ground motions.

Source

A finite source is used. For the simulation of ground motions from an earthquake for which a rupture model has been inverted, the parameters derived from the inversion provide all of the information needed to characterize the source. For the simulation of ground motion for a future earthquake, the slip distribution is generated from a frequency-wavenumber model of slip distribution whose parameters are constrained by the slip models of past earthquakes (Somerville and Abrahamson, 1991). The slip direction on the fault (rake angle) can vary spatially over the fault, and can also vary in time at a given point on the fault. The rise time (slip velocity) is based on an empirical relation derived from the same ten events. The rupture velocity is assumed to be 0.85 times the shear wave velocity. Radiation pattern and fault subevents are treated differently in two different period ranges.

Long Period: The fault is discretized finely enough to produce a continuous plane for frequencies below one second. The theoretical radiation pattern is used.

Short Period: The fault is discretized into fault elements. The size of the fault elements is chosen so as to maintain self-similarity in the spectral shape between the subevent on the fault element and the large event based on an omega-squared scaling relation (Joyner and Boore, 1986), as described by Somerville et al. (1991). The condition is that the total number of subevents added be the four-thirds power of the moment ratio of the large event to the subevent. The radiation of seismic waves from these fault elements is represented by empirical source functions, which are accelerograms of events having the dimensions of the fault elements that were recorded near the source and have been corrected back to the source. Where multiple empirical source functions are available, the radiation pattern is represented empirically using

these source functions, by selecting recordings having the required theoretical radiation pattern value for each fault element.

Path

For 1D models of crustal structure, path effects are treated differently in two different period ranges.

Long Period: Path effects are represented by Green's functions calculated using an efficient frequency-wavenumber integration scheme (Saikia, 1994). In the frequency-wavenumber integration method, the solutions due to a point source are expressed in terms of a double integral transformation over horizontal wavenumber and frequency by taking temporal and spatial Fourier transforms. For a stack of homogeneous plane layers, the kernel of the integrand is expressed by the propagator matrix. The integral of the kernel over the horizontal wavenumber is carried out numerically at a sequence of different frequencies. Time domain solutions are obtained by an inverse Fourier transform. These Green's functions contain the complete response of the layered medium (all body wave and surface wave phases) for frequencies below a given value (typically chosen to be 5 Hz). They also contain the near-field term in addition to the far-field term, and include the static displacement field of the earthquake. The Green's functions include the effects of a layered Q model.

Short Period: Path effects are represented by simplified Green's functions calculated using generalized ray theory (Helmberger, 1983). These Green's functions are accurate up to indefinitely high frequencies (typically 50 Hz), and contain all of the significant rays. They are simplified in the sense that they do not include the radiation pattern and the receiver function; these are excluded because they are represented empirically in the empirical source functions. The simplified Green's functions are used to transfer the empirical source functions from the depth, horizontal range and velocity structure in which they were recorded to the depth, horizontal range and velocity structure in which they are to be used for ground motion simulation. Scattering effects in the path are represented empirically by wave propagation effects contained in the source functions that are not modeled by the simplified Green's functions used in their correction.

Geometrical ray theory breaks down when there are strong velocity gradients. For calculating the propagation of seismic waves in a layered crust, we need to use generalized ray theory which includes refracted arrivals (head waves) as well as reflected arrivals. In the generalized ray method, the kernel of a double integral transformation is obtained by taking a Laplace transform over time and a spatial Fourier transform over horizontal coordinate. Then, by introducing ray parameter and a relationship between the ray parameter and travel time (Cagniard path), the integral of the kernel which corresponds to an inverse Laplace transform is analytically carried out in order to obtain a time domain solution. The method of generalized rays allows separation of the wavefield into energy that radiates downward and energy that travels upward. To illustrate generalized rays, we describe the decomposition of the wavefield into the following three travel paths:

(1) direct arrival plus surface layer multiples (shallow Love waves);
(2) downgoing (diving) energy paths (lower crustal triplications); and
(3) surface reflected paths which are reflected again below the source (*sS*).

A smooth velocity model composed of approximately 50 layers is shown in Figure A1-2. This figure also displays two generalized ray sets used in constructing the wavefield: the downgoing ray set and the upgoing ray set (excluding the direct arrival). The upper portion of Figure A1-3 displays the various contributions of these three ray sets to the total potential field. These three contributions are the direct ray, a large set of downgoing rays that are reflected back to the surface, and a large set of upgoing rays that are reflected at the surface and are reflected or refracted back to the surface. These responses were produced by applying the Cagniard-de Hoop technique to the generalized rays (Helmberger, Engen & Grand 1985). These three contributions dominate the wavefield, as can be demonstrated by generating complete synthetic seismorgams by the reflectivity method (Saikia, 1994). The upper row shows the decrease in short-period energy with increasing distance as the waves becomes diffracted. The downgoing rays (or diving rays) contribute significantly to the short period content. The Moho reflection SmS and the Moho refracted wave Sn (head wave) produce further complexity, especially due to contributions from *sS*.

Path effects are treated in one of two different methods in 2D crustal models. One method uses generalized rays (Helmberger et al., 1995), and is accurate up to indefinitely high frequencies (typically to 50 Hz). The other method uses finite difference (Helmberger and Vidale, 1988), and contains all body wave and surface wave arrivals for periods longer than a specified cutoff period. This method can also be used for 3-D crustal models.

Site

Site effects are incorporated by calculating Green's functions using the velocity model appropriate for the site. For the short period part of the simulation, the receiver function is included empirically in the empirical source functions; the partitioning of energy among components is treated in a site-specific manner by applying a receiver function correction to the empirical source functions which rotates the recorded partition into that appropriate to the velocity structure at the site. Scattering effects near the site are represented empirically by wave propagation effects contained in the empirical source functions that are not modeled by the simplified Green's functions used in their correction. The site attenuation (kappa) contained in the empirical source functions is adjusted to provide the value that is appropriate at the site. Non-linear effects can be included in an approximate way by using a 1-D equivalent linear approach.

Parameters Requiring Specification

Source: Seismic moment, fault length, fault width, strike, dip, rake, depth of top of fault, hypocenter, rupture velocity, the time function of slip at each point on the fault, and the direction of slip on the fault.

Path: Seismic velocities, density, and Q (material damping factor) of a crustal model that may be plane layered (1D), 2D or 3D. The most sensitive parameters are velocity gradients in the shallow and deep parts of the crust.

Site: Surface seismic velocities, density, and Q (material damping factor). If nonlinear soil response is to be included, we need shear modulus and damping as a function of strain level.

Important Features of the Broadband Ground Motion Simulation Method

As determined from validation against recorded data documented below, the ground motion method is broadband (zero frequency to 50 Hz); is applicable for magnitudes in the range of 5 to 8; and is applicable to distances from 0km to 200km or more. It has no free parameters when used to model the recorded ground motions of an earthquake, and hence no calibration of the model is required. The model has been extensively validated against the recorded strong ground motions of crustal earthquakes using flat layered (1-D) crustal models and more complex (2-D and 3-D) models. At long periods, it contains a theoretically rigorous representation of radiation pattern, rupture directivity and wave propagation effects, and reproduces the recorded ground motion waveforms. At short periods, it uses a theoretically rigorous representation of wave propagation effects which is combined with theoretically-based semi-empirical representations of stochastic processes including source radiation pattern and scattering in the path and site.

The broadband simulation method is based on standard time-domain methods for estimating earthquake source parameters and analyzing seismic wave propagation, and can therefore be readily applied using standard parameterizations of the earthquake source and crustal structure. It has been extensively validated against recorded strong ground motions from both tectonically active regions and tectonically stable regions. It has no free parameters when used to model the recorded ground motions of an earthquake, and hence no calibration of the model is required. The ground motion attenuation function is determined by the crustal structure and the source depth, and thus has predictive power in locations where crustal structure and source depth are available but few strong motion recordings exist. The method can include Green's functions calculated using 2-D or 3-D models of crust structure.

Validation of the Broadband Strong Motion Simulation Method Against Recorded Data

The ground motion model has no free parameters when used to model the recorded ground motions of an earthquake, and hence no calibration of the model is required. The 1-D ground motion model has been validated against the recorded strong ground motions of the following earthquakes: 1978 Tabas (Saikia, 1994); 1979 Imperial Valley (Wald et al., 1988a); 1985 Michoacan, Mexico and Valparaiso, Chile (Somerville et al., 1991); 1987 Whittier Narrows (Wald et al., 1998b; Saikia, 1992); 1988 Saguenay (Somerville et al., 1990; Atkinson and Somerville, 1994); 1988 Nahanni (PG&E, 1988); 1989 Loma Prieta (Somerville et al., 1994a,b); 1994 Northridge (Somerville et al., 1995). The 2-D and 3-D modeling approach, which to date has been applied at periods of 1 sec and longer, has been applied to the ground motions of a Loma Prieta aftershock recorded in the Marina District basin in San Francisco (Graves, 1993); to the ground motions of the 1992 Cape Mendocino earthquake recorded in the Eel River Valley (Graves, 1994a); to the ground motions of the 1994 Northridge earthquake recorded in the northwestern Los Angeles basin (Graves, 1994b); and to the ground motions of the 1995 Kobe earthquake recorded in the Kinki district (Somerville and Graves, 1996).

Uncertainty in Ground Motions Generated using the Broadband Procedure

The uncertainty in ground motions predicted by the model is characterized by the procedure described by Abrahamson et al. (1990). There are two kinds of uncertainty in modeling ground motion, and each contributes about equally to the overall uncertainty. One is variability due to modeling uncertainty associated with the modeling procedure. The other source of uncertainty is that associated with uncertainty in the parameters of future earthquakes. These parameters include the slip distribution, the location of the hypocenter, the slip velocity and the rupture velocity.

The modeling uncertainty is estimated from comparison between recorded and simulated ground motions of earthquakes for which estimates of all of the parameters required by the model are available. The goodness of fit measurement is described by two parameters: the bias and the standard error. In this formulation, the bias measures the difference between recorded and simulated motions averaged over all stations, and provides an indication of whether, on average, the simulation procedure is overpredicting, underpredicting, or evenpredicting the recorded motions. The standard error measures the average difference between the simulated and recorded motions for a single observation, and provides an indication of the uncertainty involved in predicting a single value. The average of all these errors, which include both overprediction and underprediction, is the bias. The standard error in the prediction of a single observation (response spectral velocity at 5% damping) is about a factor of 1.4 (natural logarithm of standard error = 0.35) in the period range of 0.05 to 10 seconds.

References

Abrahamson, N.A., P.G. Somerville, and C.A. Cornell (1990). Uncertainty in numerical strong motion predictions. Proc. *Fourth U.S. Nat. Conf. Earthq. Eng., Palm Springs, CA,* 1, 407-416.

Atkinson, G.M. and P.G. Somerville (1994). Calibration of time history simulation methods, *Bull. Seism. Soc. Am.* 84, 400-414.

Graves, R.W. and P.G. Somerville (1995). Characterization of long period (1-10 sec) ground motions for base isolated structures located in sedimentary basins. Seismic, Shock and Vibration Isolation, PVP-Vol. 319, Proceedings of the 1995 Joint ASME/JSME Pressure Vessels and Piping Conference, Honolulu, Hawaii, July 23-27, 1995.

Graves, R.W. (1993). Modeling three-dimensional site response effects in the Marina District basin, San Francisco, California.

Graves, R.W. (1994a). Simulating the 3D basin response in the Portland and Puget Sound regions from large subduction zone earthquakes, Annual Technical Report to USGS, Award 1434-93-G-2327.

Graves, R.W. (1994b). Preliminary analysis of long-period basin response in the Los Angeles region from the 1994 Northridge earthquake, *Geophys. Res. Lett.*, 22, 101-104.

Helmberger, D.V., G. Engen and S. Grand (1985). Notes on wave propagation in laterally varying structure, J. Geophys. Res. 58, 82-91.

Helmberger, D.V. (1983). Theory and application of synthetic seismograms. in Earthquakes: Observation, Theory and Interpretation, Proc. Int. Sch. Phys. "Enrico Fermi" Course LXXXV, pp. 174-221, eds. Kanamori, H. and E. Boschi, North- Holland, Amsterdam.

Helmberger, D.V., R. Stead, P. Ho-Liu, and D. Dreger (1992). Broadband modeling of regional seismograms: Imperial Valley to Pasadena, Geophys. J. Int. 110, 42-54.

Helmberger, D.V. and J.E. Vidale (1988). Modeling strong motions with two-dimensional numerical codes, *Bull. Seism. Soc. Am.* 78, 109-121.

Helmberger, D.V., L.-S. Zhao, and E. Garnero (1995). Construction of synthetic seismograms for 2D structures: core phases, in *Earthquakes,: Observation, Theory and Interpretation*, n. LXXV, Corso, Italiana di Fisica - Bologna, Italy, in press.

Joyner, W.B. and D.M. Boore (1986). On simulating large earthquakes by Green's function addition of smaller earthquakes, in *Earthquake Source Mechanics*, D. Das, J. Boatwright, and C.H. Scholz (Editors), Maurice Ewing Series 6, American Geophysical Union Monograph 37, 269-274.

Pacific Gas & Electric Company (1988). Final Report of the Diablo Canyon Long Term Seismic Program for the Diablo Canyon Power Plant, Report to the U.S.N.R.C.

Saikia, C.K. (1993). Estimated ground motions in Los Angeles due to a M=7 earthquake on the Elysian thrust fault, *Bull. Seism. Soc. Am.* 83, 780-810.

Saikia, C.K. (1994). Modeling of strong ground motions from the 16 September 1978 Tabas, Iran, Earthquake, *Bull. Seism. Soc. Am.* 84, 31-46.

Saikia, C.K. (1994). Modified frequency-wavenumber algorithm for regional seismograms using Filon's quadrature: modeling of Lg waves in eastern North America. *Geophys. J. Int.* 118, 142-158.

Somerville, P.G. (1992). Engineering applications of strong motion simulation,*Tectonophysics*, 218, 195-219.

Somerville, P.G., J.P. McLaren, L.V. LeFevre, R.W. Burger, and D.V. Helmberger (1987). Comparison of source scaling relations of eastern and western North American earthquakes, *Bull. Seism. Soc. Am.* 77, 322-346.

Somerville, P.G., J.P. McLaren, C.K. Saikia, and D.V. Helmberger (1990). The 25 November, 1988 Saguenay, Quebec earthquake: source parameters and the attenuation of strong ground motion, *Bull. Seism. Soc. Am.* 80, 1118-1143.

Somerville, P.G., M.K. Sen and B.P. Cohee (1991). Simulation of strong ground motions

recorded during the 1985 Michoacan, Mexico and Valaparaiso, Chile earthquakes, *Bull. Seism. Soc. Am.* 81, 1-27.

Somerville, P.G. and N.A. Abrahamson (1991). Characterizing earthquake slip models for the prediction of strong ground motions, EOS 72, 341. (abstract).

Somerville, P.G., K. Irikura, S. Sawada, Y. Iwasaki, M. Tai and M. Fushimi (1993). Characterizing earthquake slip models for the prediction of strong ground motion. Proceedings of the 22nd JSCE Earthquake Engineering Symposium - 1993, Japan Society of Civil Engineers, p. 291-294.

Somerville, P.G., D.J. Wald, and N.F. Smith (1994a). Prediction of near fault ground motions of the 1989 Loma Prieta earthquake using a heterogeneous slip model, unpublished manuscript.

Somerville, P.G., N.F. Smith and R.W. Graves (1994b). The effect of critical Moho reflections on the attenuation of strong motion from the 1989 Loma Prieta, in *"The Loma Prieta, California, Earthquake of October 17, 1989 - Strong Ground Motion,"* U.S.G.S. Professional Paper 1551-A, A67-A75.

Somerville, P.G., R.W. Graves, and C.K. Saikia (1995). Characterization of Ground Motions during the Northridge Earthquake of January 17, 1994. Program to Reduce the Earthquake Hazards of Steel Moment Frame Buildings, SAC Report 95-03.

Somerville, P., C. Saikia, D. Wald, and R. Graves (1996). Implications of the Northridge earthquake for strong ground motions from thrust faults, Bull. Seism. Soc. Am. 86, S115-S125.

Somerville, P.G. and R.W. Graves (1996). Strong ground motions of the Kobe, Japan earthquake of Jan. 17, 1995, and development of a model of forward rupture directivity applicable in California. Proceedings of the Western Regional Technical Seminar on Earthquake Engineering for Dams, Association of State Dam Safety Officials, Sacramento, California, April 11-12, 1996.

Wald, D.J., L.J. Burdick and P.G. Somerville (1988a). Simulation of acceleration time histories close to large earthquakes. *Earthquake Engineering and Soil Dynamics II - Recent Advances in Ground Motion Evaluation*, Geotechnical Special Publication 20, J. Lawrence Von Thun, ed., 430-444.

Wald, D.J., P.G. Somerville and L.J. Burdick (1988b). Simulation of recorded accelerations of the 1987 Whittier Narrows earthquake, *Earthquake Spectra* 4, 139-156.

Wald, D.J. and T.H. Heaton (1994). Spatial and temporal distribution of slip for the 1992 Landers, California earthquake. Bull. Seism. Soc. Am 84, 668-691.

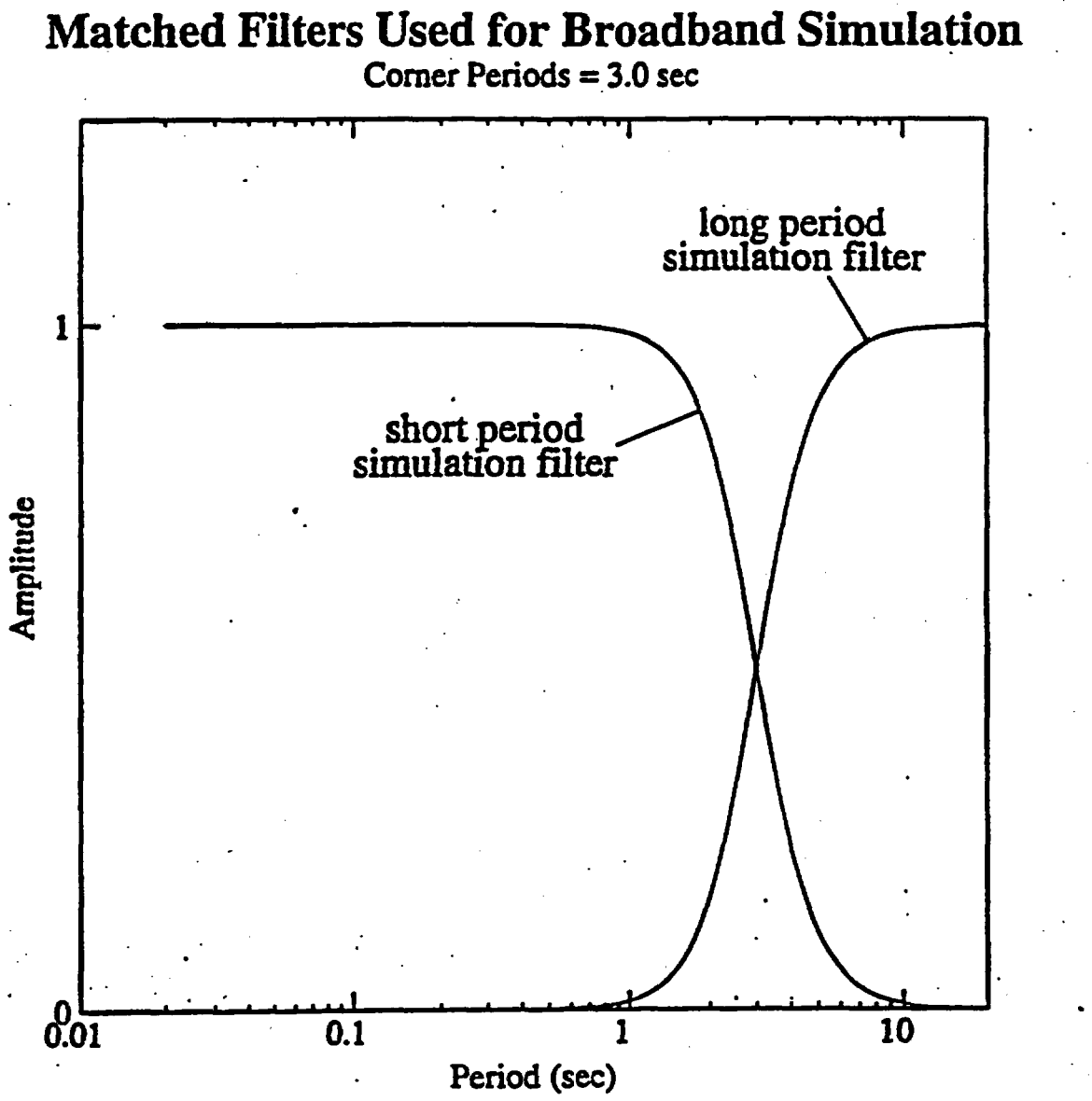

Figure A1-1. Schematic diagram showing the matched filters used to combine the short period and long period simulations. The sum of the matched filters is unity at all periods.

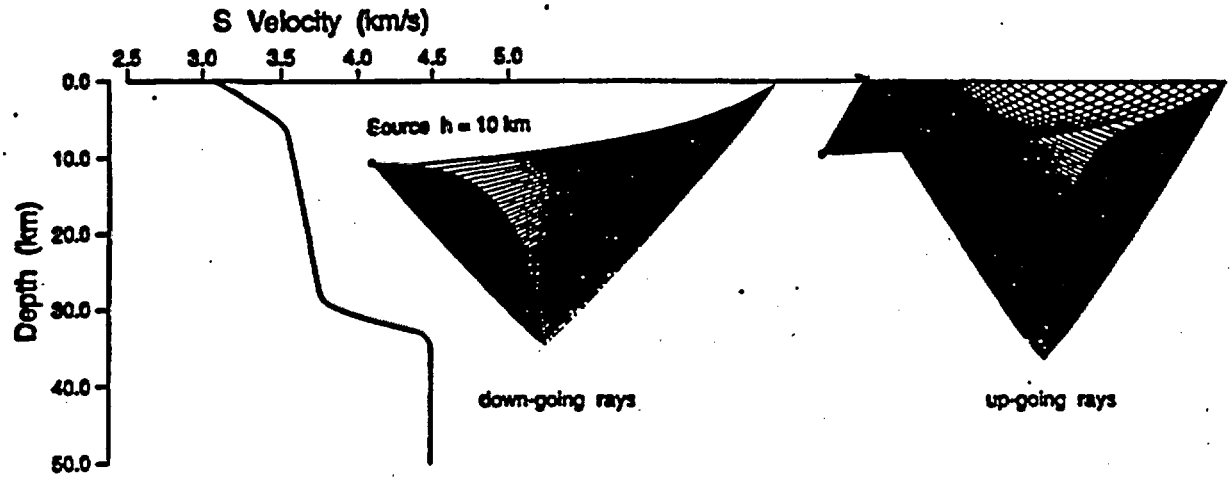

Figure A1-2. A smooth velocity-depth function and generalized ray paths used to construct the synthetic seismograms shown in Figure A1-3. Source: Helmberger et al. (1992).

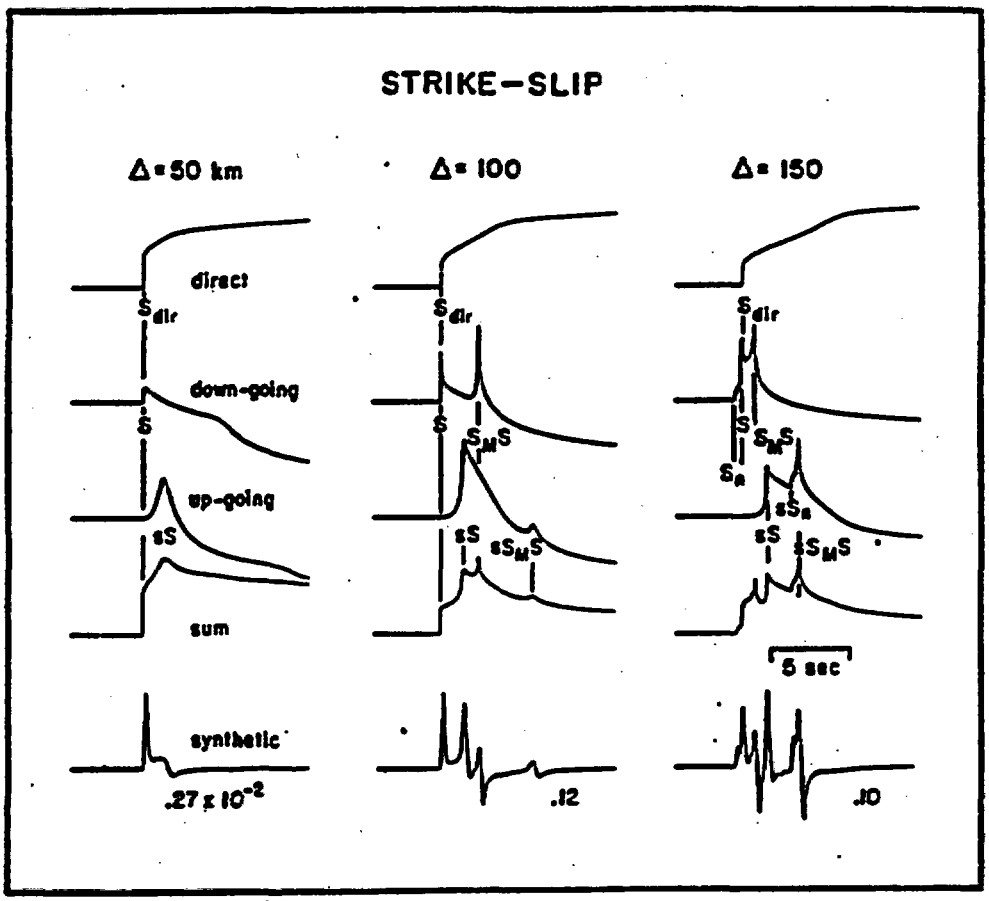

Figure A1-3. Wavefield decomposition showing the response of the direct arrival at the top followed by the contribution from downgoing paths (S) and upgoing paths (sS). The bottom row shows synthetic seismograms computed using a (0.2, 0.2, 0.2) second trapezoidal source. Source: Helmberger et al. (1992).

Woodward-Clyde

Memorandum

To: Ground Motion Experts

From: Norm Abrahamson
Ann Becker

Office: SLC

Date: February 28, 1997

Subject: More Information from Stochastic Model Validation

More specific information regarding Silva's stochastic BLWN/RVT model has been requested. In response, Chapter 2 of the draft version of 'Description and Validation of the Stochastic Ground Motion Model' by Silva et al. is attached. The Chapter provides specific details on the model

As always, if you would like other information from this Report, please let us know.

CHAPTER 2

STOCHASTIC GROUND MOTION MODEL DESCRIPTION

2.1 BACKGROUND

In the context of strong ground motion, the term "stochastic" can be a fearful concept to some and may be interpreted to represent a fundamentally wrong or inappropriate model (abiet the many examples demonstrating that it works well; Boore, 1983, 1986). To allay any initial misgivings which may arise largely through ignorance and bias, a brief discussion of exactly what is stochastic in the stochastic ground motion model seems prudent.

The stochastic point-source model may be termed a spectral model in that it fundamentally describes the Fourier amplitude spectral density at the surface of a half-space (Hanks and McGuire, 1981). The model uses a Brune (1970, 1971) omega-square (Section 2.1) source description of the source Fourier amplitude spectral density which is easily the most widely used and qualitatively validated source description available. Seismic sources ranging from M = -6 (hydrofracture) to M = 8 have been interpreted in terms of the Brune omega-square model over the last 30 years with the general conclusion that it provides a reasonable and consistent representation of crustal sources, particularly for tectonically active regions such as plate margins. A unique phase spectrum can be associated with the Brune source spectrum to produce a complex spectrum and propagated using either exact or approximate (1-2- or 3-D) wave propagation algorithms to produce single or multiple component time histories. In this context the model is not stochastic, it is decidedly deterministic and as exact and rigorous as one chooses. A two-dimensional array of such point-source may be appropriately located on a fault

surface (area) and fired with suitable delays to simulate rupture propagation on an extended rupture plane (Section 2.2). As with the single point-source, any degree of rigor may be used in the wave propagation algorithm to produce multiple component or average horizontal component time histories. The result is a kinematic** finite-source model which has as its basis a source time history defined as a Brune pulse whose Fourier amplitude spectrum follows an omega-square model. This finite-fault model would be very similar to that used in published inversions for slip models (Chapter 4) if the 1-D propagation was treated using a reflectivity algorithm. This algorithm is a complete solution to the wave equation from static offsets to an arbitrarily selected high frequency cutoff (generally 1-2 Hz).

If one were to use recordings of small earthquakes made at a site of interest and whose sources are distributed along the expected rupture surface to model the wave propagation, the result would be an empirical Green function method (Hartzell, 1978). Proceeding further, if one simply had well distributed recordings at close distances to a small earthquake and the recordings are corrected back to the source by removing wave propagation effects using a simple approximation (say 1/R plus a constant for crustal amplification and radiation pattern), an empirical source function is obtained. This can be used to replace the Brune pulse to introduce some natural (although source, path, and site specific) variation into the dislocation time history. If this is coupled to an approximate wave propagation algorithm (asymptotic ray theory) which includes the direct rays and those which have undergone a single reflection, the result is the

**Kinematic source model is one whose slip (displacement) is defined (imposed) while in a dynamic source model forces (stress) is defined (see Aki and Richards 1980 for a complete description).

empirical source function method (EPRI, 1993). Combing the reflectivity propagation (which is generally limited to frequencies $\leq$ 1-2 Hz due to computational demands) with the empirical source function approach (appropriate for frequencies $\geq$ 1 Hz; EPRI, 1993) results in a broad band simulation procedure which is strictly deterministic at low frequencies (where an analytical source function is used) and incorporates some natural variation at high frequencies through the use of an empirical source function (Sommerville, 1995).

All of these techniques are fundamentally similar, well founded in seismic source and wave propagation physics, and importantly, they are all approximate. Simply put, all models are wrong and the single essential element in selecting a model is to incorporate the appropriate degree of rigor through extensive validation exercises. It is generally felt that more complicated models produce more accurate results, however, the implications of more sophisticated models with the increased number of parameters is often overlooked. This is not too serious a consequence in modeling past earthquakes since a reasonable range in parameter space can be explored to give the "best" results. However for future predictions, this increased rigor may carry undesirable baggage in parametric variability (Roblee et al., 1996). The effects of lack of knowledge (epistemic uncertainty; EPRI, 1993) regarding parameter values for future occurrences results in uncertainty or variability in ground motion predictions. It may easily be the case that a very simple model, such as a point-source, can have comparable, or even smaller, total variability (modeling plus parametric) to a much more rigorous model (EPRI, 1993). What is desired in a model is sufficient sophistication such that it captures the dominant and stable features of source, distance, and site dependencies observed in strong ground motions. It is these considerations which led to the development of the stochastic point- and finite-source

models and, in part, leads to the stochastic element of the models.

The stochastic nature or component of the point- and finite-source models is simply an assumption made about the character of ground motion time histories which permits stable estimates of peak parameters (e.g. acceleration, velocity, strain, stress, oscillator response) to be made without computing detailed time histories (Hanks and McGuire, 1981; Boore, 1983). This process uses random vibration theory to relate a time domain peak value to the time history root-mean-square (RMS) value (Boore, 1983). The assumption of the character of the time history for this process to strictly apply is that it be normally distributed random noise and stationary (its statistics do not change with time) over its duration. A visual examination of any time history quickly reveals that this is clearly not the case: time histories (acceleration, velocity, stress, strain, oscillator) start, build up, and then diminish in time. However poor the assumption of stationary Gaussian noise may appear, the net result is that the assumption is weak enough to permit the approach to work surprisingly well, as numerous comparisons with recorded motions and both qualitative and quantative validations have shown (Hanks and McGuire, 1981; Boore, 1983, 1986; McGuire et al., 1984; Boore and Atkinson, 1987, Silva and Lee, 1987; Toro and McGuire, 1987; Silva et al., 1990; EPRI, 1993; Schneider et al., 1993; Silva and Darragh, 1995). Corrections to RVT are available to accommodate different distributions as well as non-stationarity and are usually applied in the estimation of peak oscillator response in calculating response spectra (Boore and Joyner, 1984; Toro, 1985).

2.2 POINT-SOURCE MODEL

The conventional stochastic ground motion model uses an ω-square source model (Brune, 1970,

1971) with a single corner frequency and a constant stress drop (Boore, 1983; Atkinson, 1984). Random vibration theory is used to relate RMS (root-mean-square) values to peak values of acceleration (Boore, 1983), and oscillator response (Boore and Joyner, 1984; Toro, 1985; Silva and Lee, 1987) computed from the power spectra to expected peak time domain values (Boore, 1983).

The shape of the acceleration spectral density, a(f), is given by

$$a(f) = C \frac{f^2}{1+(\frac{f}{f_c})^2} \frac{M_0}{R} P(f) A(f) e^{-\frac{\pi f R}{\beta_0 Q(f)}} \qquad (2\text{-}1)$$

where

$C = (\frac{1}{\rho_0 \beta_0^3}) \cdot (2) \cdot (0.55) \cdot (\frac{1}{\sqrt{2}}) \cdot \pi.$

M_0 = seismic moment,

R = hypocentral distance,

β_0 = shear-wave velocity at the source,

ρ_0 = density at the source

Q(f) = frequency dependent quality factor (crustal damping),

A(f) = amplification,

P(f) = high-frequency truncation filter,

f_c = source corner frequency.

C is a constant which contains source region density (ρ_0) and shear-wave velocity terms and accounts for the free-surface effect (factor of 2), the source radiation pattern averaged over a sphere (0.55) (Boore, 1986), and the partition of energy into two horizontal components ($1/\sqrt{2}$).

Source scaling is provided by specifying two independent parameters, the seismic moment (M_0) and the high-frequency stress parameter or stress drop ($\Delta\sigma$). The seismic moment is related to magnitude through the definition of moment magnitude M by the relation

$$\log M_0 = 1.5\ M + 16.05 \qquad \text{(Hanks and Kanamori, 1979)} \qquad (2\text{-}2).$$

The stress drop ($\Delta\sigma$) relates the corner frequency f_c to M_0 through the relation

$$f_c = \beta\ (\Delta\sigma/8.44\ M_0)^{1/3} \qquad \text{(Brune; 1970, 1971)} \qquad (2\text{-}3).$$

The stress drop is sometimes referred to as the stress parameter (Boore, 1983) since it directly scales the Fourier amplitude spectrum for frequencies above the corner frequency (Silva, 1991; Silva and Darragh 1995). High (> 1 Hz) frequency model predictions are then very sensitive to this parameter (Silva, 1991; EPRI, 1993) and the interpretation of it being a stress drop or simply a scaling parameter depends upon how well real earthquake sources (on average) obey the omega-square scaling (Equation 2-3) and how well they are fit by the single-corner-frequency model. The parameter is a physical parameter if the model is considered to generally work well and its values have physical interpretations in source processes. Otherwise, it simply a high frequency scaling factor.

The spectral shape of the single-corner-frequency ω-square source model is then described by the two free parameters M_0 and $\Delta\sigma$. The corner frequency increases with the shear-wave velocity and with increasing stress drop, both of which may be region dependent.

The amplification accounts for the increase in wave amplitude as seismic energy travels through lower- velocity crustal materials from the source to the surface. The amplification depends on average crustal and near surface shear-wave velocity and density.

The P(f) filter is an attempt to model the observation that acceleration spectral density appears to fall off rapidly beyond some region-dependent maximum frequency. This observed phenomenon truncates the high frequency portion of the spectrum and is responsible for the band-limited nature of the stochastic model. The band limits being the source corner frequency at low frequency and the high frequency spectral attenuation. This spectral fall-off has been attributed to near-site attenuation (Hanks, 1982; Anderson and Hough, 1984) or to source processes (Papageorgiou and Aki, 1983) or perhaps to both effects. In the Anderson and Hough (1984) attenuation model, adopted here, the form of the P(f) filter is taken as

$$P(f) = e^{-\pi\kappa(r)f} \qquad (2\text{-}4).$$

Kappa (r) (κ(r) in Equation 2-4) is a site and distance dependent parameter that represents the effect of intrinsic attenuation upon the wavefield as it propagates through the crust from source to receiver. Kappa (r) depends on epicentral distance (r) and on both the shear-wave velocity (β_s) and quality factor (Q_s) averaged over a depth of H beneath the site (Hough et al., 1988;).

At zero epicentral distance kappa (κ) is given by

$$\kappa = \frac{H}{\overline{\beta_R}\,\overline{Q_S}} \qquad (2\text{-}5).$$

The bar in Equation 2-5 represents an average of these quantities over a depth H. The value of kappa at zero epicentral distance is attributed to attenuation in the very shallow crust directly below the site (Hough and Anderson. 1988; Silva and Darragh, 1995). The intrinsic attenuation along this part of the path is not thought to be frequency dependent and is modeled as a frequency independent, but site dependent, constant value of kappa (Hough et al., 1988; Rovelli et al., 1988). This zero epicentral distance kappa is the model implemented in this study.

The crustal path attenuation from the source to just below the site is modeled with the frequency-dependent quality factors Q(f).

The Fourier amplitude spectrum, a(f), given by Equation 2-1 represents the stochastic ground motion model employing a Brune source spectrum that is characterized by a single corner frequency. It is appropriate for a point-source and models direct shear-waves in a homogeneous half-space (with effects of a velocity gradient through the A(f) filter, Equation 2-1). For horizontal motions, vertically propagating shear-waves are assumed. Validations using incident inclined SH-waves with raytracing to find appropriate incidence angles leaving the source showed little reduction in uncertainty. For vertical motions P/SV propagators are used coupled with raytracting to model incident inclined plane waves (EPRI, 1993).

Equation 2-1 represents an elegant ground motion model that accommodates source and wave propagation physics as well as propagation path and site effects with an attractive simplicity. The model is appropriate to an engineering characterization of ground motion since it captures the general features of strong ground motion in terms of peak acceleration and spectral composition with a minimum of free parameters (Boore, 1983; McGuire et al., 1984; Boore, 1986; Silva and Green, 1988; Silva et al., 1988; Schneider et al., 1993). An additional important aspect of the stochastic model employing a simple source description is that the region dependent parameters can be evaluated by observations of small local or regional earthquakes. Region specific seismic hazard evaluations can then be made for areas with sparse strong motion data with relatively simple spectral analyses of weak motion (Silva, 1992).

In order to compute peak time-domain values, i.e. peak acceleration and oscillator response, RVT is used to relate RMS computations to peak value estimates. Boore (1983) and Boore and Joyner (1984) contain an excellent development of the RVT methodology as applied to the stochastic ground motion model. The procedure, in general, involves computing the RMS value by integrating the power spectrum from zero frequency to the Nyquist frequency and applying Parsevall's relation. Extreme value theory is then used to estimate the expected ratio of the peak value to the RMS value of a specified duration of the stochastic time history. The duration is generally taken as the inverse of the corner frequency (Boore, 1983).

Factors that effect strong ground motions such as surface topography, finite and propagating seismic sources, laterally varying near-surface velocity and Q gradients, and random inhomogeneities along the propagation path are not included in the model. While some or all

of these factors are generally present in any observation of ground motion and may exert controlling influences in some cases, the simple and elegant stochastic point-source model appears to be robust in predicting median or average properties of ground motion (Boore 1983, 1986; Schneider et al., 1993; Silva, 1993). For this reason it represents a powerful predictive and interpretative tool for engineering characterization of strong ground motion.

2.3 FINITE-SOURCE MODEL GROUND MOTION MODEL

In the near-source region of large earthquakes, aspects of a finite-source including rupture propagation, directivity, and source-receiver geometry can be significant and may be incorporated into strong ground motion predictions. To accommodate these effects, a methodology that combines the aspects of finite-earthquake-source modeling techniques (Hartzell, 1978; Irikura 1983) with the stochastic point-source ground motion model has been developed to produce response spectra as well as time histories appropriate for engineering design (Silva et al., 1990; Silva and Stark, 1992). The approach is very similar to the empirical Green function methodology introduced by Hartzell (1978) and Irikura (1983). In this case however, the stochastic point-source is substituted for the empirical Green function and peak amplitudes; PGA, PGV, and response spectra (when time histories are not produced) are estimated using random process theory.

Use of the stochastic point-source as a Green function is motivated by its demonstrated success in modeling ground motions in general and particularly strong ground motions (Boore, 1983, 1986; Silva and Stark, 1992; Schneider et al., 1993; Silva and Darragh, 1995) and the desire to have a model that is truly site and region specific.. The model can accommodate a region

specific Q(f), Green function sources of arbitrary moment or stress drop, and site specific kappa values. The necessity of regional and site specific recordings or the modification of possibly inappropriate empirical Green functions is eliminated.

For the finite-source characterization, a rectangular fault is discretized to provide the locations of NS subfaults of moment M_0^s. The empirical relationship

$$A = M - 4.0 \qquad (2\text{-}6).$$

is used to assign areas to both the target earthquake (if its rupture surface is not fixed) as well as to the subfaults and implies a constant static stress drop of about 30 bars. This relation results from regressing log area on M using the data of Wells and Coppersmith (1994) with the M coefficient fixed at unity. The subevent magnitude M_s is generally taken in the range of 5.0-6.5 depending upon the size of the target event. M_s 5.0 is used for crustal earthquakes with M in the range of 5.5 to 8.0 and M_s 6.4 is used for large subduction earthquakes with $M > 7.5$. The value of NS is determined as the ratio of the target event area to the subfault area. To constrain the proper moment, the total number of events summed (N) is given by the ratio of the target event moment to the subevent moment. The subevent and target event rise times are determined by the equation

$$\log \tau = 0.33 \log M_0 - 8.54 \qquad (2\text{-}7)$$

which results from a fit to the rise times used in the finite-fault modeling exercises in Chapter 5. Slip on each subfault is assumed to continue for a time τ. The ratio of target-to-subevent rise times is given by

$$\frac{\tau}{\tau'} = 10^{0.5\,(M - M')} \qquad (2\text{-}8)$$

and determines the number of subevents to sum in each subfault. This approach is generally referred to as the constant-rise-time model and results in variable slip velocity for nonuniform slip distributions. Alternatively, one can assume a constant slip velocity resulting in a variable-rise-time model for heterogenous slip distributions.

Recent modeling of the Landers (Wald and Heaton, 1994b), Kobe (Wald, 1996) and Northridge (Hartzell et al. 1996) earthquakes suggests that a mixture of both may be present. Longer rise times seem to be associated with areas of larger slip with the ratio of slip-to-rise time (slip velocity) being depth dependent. Lower slip velocities (longer rise times) are associated with shallow slip resulting in relatively less short period seismic radiation. This result may explain the general observation that shallow slip is largely aseismic. The significant contributions to strong ground motions appear to originate at depths exceeding about 4 km (Campbell, 1993; Boore et al., 1994) as the fictitious depth term in the empirical attenuation relation presented in Appendix A suggests. Finite-fault models generally predict unrealistically large strong ground motions for large shallow (near surface) slip using rise times or slip velocities associated with deeper (> 4 km) zones of slip. This is an important and unresolved issue in finite-fault modeling and initial attempts using depth dependent rise times as well as depth dependent slip

velocities in the validation exercises for the earthquakes with shallow slip (Landers and Imperial Valley) had mixed success. A more thorough analysis is necessary, ideally using several well validated models, before this issue can be satisfactorily resolved. As a result, the simple constant rise time model was retained in the validation exercises since it generally performed better than the constant slip velocity model. Reducing the subevent stress drop to 5 bars in the Brune subevent source spectrum for earthquakes with shallow slip provided good results (Chapter 5) and allowed the validations to include shallow slip earthquakes.

To introduce heterogeneity of the earthquake source process into the stochastic finite-fault model, the location of the sub-events within each subfault (Hartzell, 1978) are randomized as well as the subevent rise time. The stress drop of the stochastic point-source Green function is taken as 30 bars, consistent with the static value based on the M 5.0 subevent area using the equation

$$\Delta\sigma = \frac{7}{16}\left(\frac{M_e}{R_e^3}\right) \qquad \text{(Brune, 1970, 1971)} \qquad (2\text{-}8)$$

where R_e is the equivalent circular radius of the rectangular sub-event.

Different values of slip are assigned to each subfault as relative weights so that asperities or non-uniform slip can be incorporated into the methodology. The rupture velocity is taken as depth independent at a value of 0.8 times the shear-wave velocity generally at the half-depth of the slip surface. A random component (20%) is added to the rupture velocity. The radiation pattern is computed for each subfault, a random component added, and the RMS applied to the motions computed at the site.

The ground-motion time history at the receiver is computed by summing the contributions from each subfault associated with the closest Green function, transforming to the frequency domain, and convolving with the Green function spectrum (Equation 2-1). The locations of the Green functions are generally taken at center of each subfault for small subfaults or at a maximum separation of about 5 to 10 km for large subfaults. As a final step, the individual contributions associated with each Green function are summed in the frequency domain multiplied by the RMS radiation pattern, and the resultant power spectrum at the site is computed. The appropriate duration used in the RVT computations for PGA, PGV, and oscillator response is computed by transforming the summed Fourier spectrum into the time domain and computing the 5 to 75% arias intensity (Ou and Herrmann, 1990).

As with the point-source model, crustal response effects are accommodated through the amplification factor (A(f)) or by using vertically propagating shear waves through a vertically heterogenous crustal structure. Propagation path damping, through the Q(f) model, is incorporated from each fault element to the site. Near-surface crustal damping is incorporated through the kappa operator (Equation 2-1). To model crustal propagation path effects, the method of Ou and Herrmann (1990) can be applied from each subfault to the site.

Time histories may be computed in the process as well by simply adding a phase spectrum appropriate to the subevent earthquake. The phase spectrum can be extracted from a recording made at close distance to an earthquake of a size comparable to that of the subevent (generally M 5.0 to 6.5). Interestingly, the phase spectrum need not be from a recording in the region of interest. A recording in WNA can effectively be used to simulate motions appropriate to ENA

(Silva et al., 1989). Transforming the Fourier spectrum computed at the site into the time domain results in a computed time history which includes all of the aspects of rupture propagation, source finiteness, as well as propagation path and site effects.

For fixed fault size, mechanism, and moment, the specific source parameters for the finite-fault are slip distribution, location of nucleation point, and site azimuth. The propagation path and site parameters remain identical for both the point- and finite-source models.

2.4 SITE EFFECTS MODEL

To model soil and soft rock response, an RVT-based equivalent-linear approach is used by propagating either the point- or finite-source outcrop power spectral density through a one-dimensional column. RVT is used to predict peak time domain values of shear-strain based upon the shear-strain power spectrum. In this sense, the procedure is analogous to the program SHAKE (Schnabel et al., 1972) except that peak shear strains in SHAKE are measured in the time domain. The purely frequency domain approach obviates a time domain control motion and, perhaps just as significantly, eliminates the need for a suite of analyses based on different input motions. This arises because each time domain analysis may be viewed as one realization of a random process. In this case, several realizations of the random process must be sampled to have a statistically stable estimate of site response. The realizations are usually performed by employing different control motions whose response spectrum matches a specified target. In the frequency-domain approach, the estimates of peak shear strains as well as oscillator response are, as a result of the RVT, fundamentally probabilistic in nature. Stable estimates of site response can then be rapidly computed permitting statistically significant estimates of

uncertainties based on parametric variations.

The parameters that influence computed response include the shear-wave velocity profile and the strain dependencies of both the shear modulus and shear-wave damping.

Chapter 2 Figure Captions

Figure 2.1. Stochastic Finite-Fault Ground Motion Model.

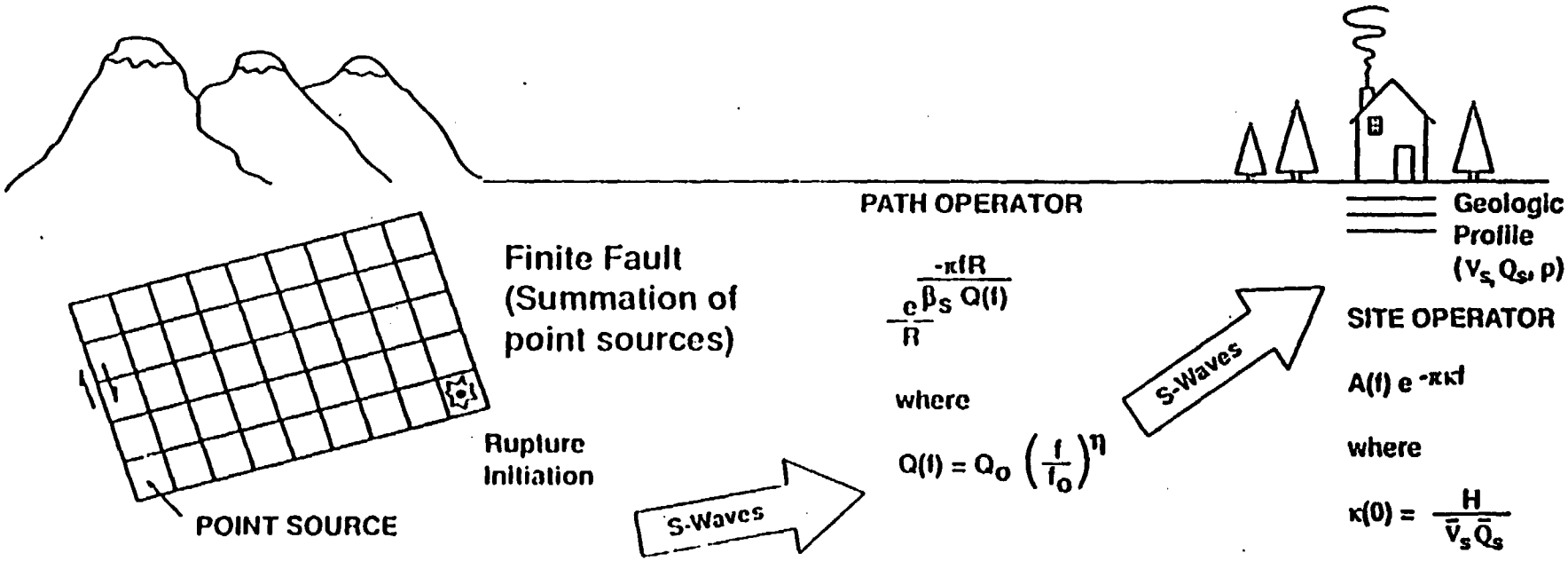
Finite Fault
(Summation of
point sources)
Rupture
Initiation
POINT SOURCE
$\frac{M_o f^2}{1+(f/f_c)^2}$
where
$f_c = \beta_s \left(\frac{\Delta\sigma}{8.44\, M_o}\right)^{\frac{1}{3}}$
S-Waves
PATH OPERATOR
$\frac{e^{\frac{-\pi f R}{\beta_s Q(f)}}}{R}$
where
$Q(f) = Q_o \left(\frac{f}{f_o}\right)^{\eta}$
S-Waves
Geologic
Profile
(V_s, Q_s, ρ)
SITE OPERATOR
$A(f)\, e^{-\pi \kappa f}$
where
$\kappa(0) = \frac{H}{\bar{V}_s \bar{Q}_s}$

Figure 2.1

Woodward-Clyde **Memorandum**

To: Ground Motion Experts

From: Norm Abrahamson
Ann Becker

Office: SLC

Date: February 27, 1997

Subject: BLWN/RVT Validation

Enclosed are portions of a report prepared to validate the stochastic ground motion model. The work was done by Walt Silva et al. for DOE/Brookhaven which recently gave permission for it to be distributed to you. The document is about 3.5" thick, exclusive of appendices. In lieu of providing you with a complete copy, we are sending the Table of Contents; tables summarizing results of inversions for Q, kappa, and stress drop; the complete text of Chapter 5, Model Validation; and selected tables and figures from Chapter 5.

Of course, if you would like any more information from the report, please contact us and we will get you copies as soon as possible.

PE&A 94PJ20
November 15, 1996

DRAFT

DESCRIPTION AND VALIDATION OF THE STOCHASTIC GROUND MOTION MODEL

Principal Investigator
W. Silva

Coordinating Authors
W. Silva, N. Abrahamson, G. Toro, C. Costantino

November 1996

PACIFIC ENGINEERING AND ANALYSIS
311 POMONA AVENUE
EL CERRITO, CALIFORNIA 94530

Prepared for the
ENGINEERING RESEARCH AND APPLICATIONS DIVISION
DEPARTMENT OF NUCLEAR ENERGY
BROOKHAVEN NATIONAL LABORATORY, ASSOCIATED UNIVERSITIES, INC.
UPTON, NEW YORK 11973

CONTRACT NO. 770573

BNL Project Manager
Kamal Bandyopadhyay

CONTENTS

Section		Page
1.0	Introduction	1-1
1.1	Purpose of Study	1-1
1.2	Model Background	1-3
1.3	Applications of the Model	1-6
1.4	Description of Validation Study	1-7
2.0	Stochastic Ground Motion Model Description	2-1
2.1	Background	2-1
2.2	Point-Source Model	2-4
2.3	Finite-Source Model Ground Motion Model	2-10
2.4	Site Effects Model	2-15
3.0	Generic Site Conditions and Crustal Model	3-1
3.1	Site and Crustal Models	3-1
3.2	Generic Site Categories	3-1
3.1.1	Soft Rock	3-2
3.1.2	Deep Soil	3-3
3.3	Profile Randomization	3-4
3.4	Generic Crustal Model	3-8
4.0	Regional Inversions	4-1
4.1	Geographic Provinces	4-1
4.2	Inversion Method	4-1
4.2.1	Point-Source Distance	4-4
4.3	Inversion Results	4-5
4.3.1	Peninsular Range	4-6
4.3.2	North Coast	4-8

CONTENTS (cont.)

Section		Page
4.3.3	Mojave	4-8
5.0	Model Validation	5-1
5.1	Partition and Assessment of Ground Motion Variability	5-1
5.1.1	Assessment of Modeling Variability	5-3
5.1.2	Assessment of Parametric Variability	5-4
5.1.3	Validation Earthquakes	5-6
5.2	Peninsular Range Earthquakes	5-8
5.2.1	1994 Northridge Earthquake	5-8
	5.2.1.1 Point-Source Inversions For Stress Drop and Kappa Values	5-10
	5.2.1.2 Point-Source Modeling Results	5-10
	5.2.1.3 Finite-Source Modeling Results	5-12
	5.2.1.3.1 Assessment of Distance Bias	5-15
	5.2.1.3.2 Assessment of G/G_{max} and Hysteretic Damping Curves	5-17
	5.2.1.3.3 Assessment of Nonlinear Site Response	5-18
5.2.2	1971 San Fernando Earthquake	5-20
	5.2.2.1 Point-Source Inversions For Stress Drop and Kappa Values	5-21
	5.2.2.2 Point-Source Modeling Results	5-21
	5.2.2.3 Finite-Source Modeling Results	5-22
5.2.3	1987 Whittier Narrows Earthquake	5-23
	5.2.3.1 Point-Source Inversions for Stress Drop and Kappa Values	5-24
	5.2.3.2 Point-Source Modeling Results	5-24
	5.2.3.3 Finite-Source Modeling Results	5-25
5.3	North Coast Earthquakes	5-27
5.3.1	Loma Prieta Earthquake	5-27
	5.3.1.1 Point-Source Inversions For Stress Drop and Kappa Values	5-29

CONTENTS (cont.)

Section		Page
	5.3.1.2 Point-Source Modeling Results	5-30
	5.3.1.3 Finite-Source Modeling Results	5-31
	5.3.1.3.1 Assessment of Distance Bias	5-34
	5.3.1.3.2 Assessment of G/G_{max} and Hysteretic Damping Curves	5-35
	5.3.1.3.3 Assessment of Nonlinear Site Response	5-36
5.3.2	1979 Coyote Lake Earthquake	5-38
	5.3.2.1 Point-source Inversions for Stress Drop and Kappa Values	5-39
	5.3.2.2 Point-Source Modeling Results	5-39
	5.3.2.3 Finite-Source Modeling Results	5-40
5.3.3	1984 Morgan Hill Earthquake	5-40
	5.3.3.1 Point-source Inversions for Stress Drop and Kappa Values	5-41
	5.3.3.2 Point-Source Modeling Results	5-42
	5.3.3.3 Finite-Source Modeling Results	5-42
5.4	Mojave Earthquakes	5-44
5.4.1	1992 Landers Earthquake	5-44
	5.4.1.1 Point-Source Inversions For Stress Drop and Kappa Values	5-46
	5.4.1.2 Point-Source Modeling Results	5-46
	5.4.1.3 Finite-Source Modeling Results	5-49
5.4.2	1986 North Palm Springs Earthquake	5-51
	5.4.2.1 Point-Source Inversions For Stress Drop and Kappa Values	5-53
	5.4.2.2 Point-Source Modeling results	5-53
	5.4.2.3 Finite-Fault Modeling Results	5-54
5.5	1978 Tabas Earthquake	5-55
5.5.1	Point-Source Inversions for Stress Drop and Kappa Values	5-56
5.5.2	Point-Source Modeling Results	5-58

CONTENTS (cont.)

Section		Page
5.5.3	Finite-Source Modeling Results	5-58
5.6	Imperial Valley Earthquakes	5-59
5.6.1	Point-Source Inversions for Stress Drop and Kappa Values	5-62
5.6.2	Point-Source Modeling Results	5-64
	5.6.2.1 M 5.3 Aftershock	5-64
	5.6.2.2 M 6.4 Mainshock	5-64
	5.6.2.2.1 Development G/G_{max} and Hysteretic Damping Curves	5-66
5.6.3	Finite-Source Modeling Results	5-68
5.7	1985 Nahanni Earthquake	5-69
5.7.1	Point-Source Inversions for Stress Drop and Kappa Values	5-70
5.7.2	Point-Source Modeling Results	5-71
5.7.3	Finite-Source Modeling Results	5-72
5.8	1987 Superstition Hills(b) Earthquake	5-72
5.8.1	Point-Source Inversions for Stress Drop and Kappa Values	5-73
5.8.2	Point-Source Modeling Results	5-74
5.8.3	Finite-Source Modeling Results	5-75
5.9	1988 Saguenay Earthquake	5-75
5.9.1	Point-Source Inversion for Stress Drop, Kappa and Q(f)	5-77
5.8.2	Point-Source Modeling Results	5-78
5.9.3	Finite-Source Modeling Results	5-79
5.10	1992 Little Skull Mountain Earthquake	5-80
5.10.1	Point-Source Inversions for Stress Drop, Kappa, and Q(f)	5-81
5.10.2	Point-Source Modeling Results	5-82
5.10.3	Finite-Source Modeling Results	5-82
5.11	1992 Cape Mendocino Earthquake	5-84

CONTENTS (cont.)

Section		Page
5.11.1	Point-Source Inversions for Stress Drop and Kappa Values	5-85
5.11.2	Point-Source Modeling Results	5-86
5.11.3	Finite-Source Modeling Results	5-86
6.0	Point-Source Model Validation Comparison to Empirical Attenuation	6-1
6.1	Attenuation with Distance	6-1
6.2	Inversions of Empirical Attenuation	6-5
6.2.1	Transfer Functions	6-6
6.2.2	Inversion Results	6-6
6.2.3	Generic Modulus Reduction and Damping Curves	6-12
	6.2.3.1 G/G_{max} and Hysteretic Curves for Soil	6-12
	6.2.3.2 G/G_{max} and Hysteretic Damping Curves for Rock	6-14
6.3	Comparison Exercises	6-15
6.3.1	Soft Rock Comparisons	6-16
6.3.2	Deep Soil Comparison	6-17
7.0	Point-source Model Validation Comparison to Statistical Spectral Shapes	7-1
7.1	Statistical Shapes	7-1
7.1.1	Soft Rock	7-3
7.1.2	Deep Soil	7-4
7.2	Model Shapes	7-5
7.3	Comparison of Model Spectral Shapes to Statistical and Empirical Shapes	7-6
8.0	Summary and Conclusions	8-1

Table 4.1 Regional Inversions Determination of Crustal Q Models and Average Kappa Values

Region	Number of Stations*	Q_o	η	κ (sec) Rock	κ (sec) Soil
Peninsular Range (Northridge, San Fernando, and Whittier Narrows)	221	174	0.77	0.053	0.058
		264	0.60**	0.051	0.056
		1286	0.00**	0.047	0.052
North Coast (Loma Prieta, Coyote Lake, and Morgan Hill)	92	348	0.32	0.056	0.069
		176	0.60**	0.059	0.072
		814	0.00**	0.053	0.066
Mojave (Landers and North Palm Springs)	86	186	0.64	0.030	0.052
		371	0.60**	0.030	0.056
		1678	0.00**	0.023	0.049
Combined***	399	346	0.53	0.050	0.059
		291	0.60**	0.051	0.060
		1518	0.00**	0.047	0.056

*Note: number of sites for each inversion is 2 (rock and soil)
**Values held fixed
***Shear-wave velocity = 3.50 km/sec, density = 2.7 cgs, crossover distance = 60 km
Starting values $Q_o = 150$, $\eta = 0.60$, $\kappa = 0.040$ sec

Table 4.2 Regional Inversion Determination of Stress Drops and Kappa Values: Peninsular Range

Regional $Q_o^* = 264$, $\eta^* = 0.60$; (Table 4.1)						
Earthquake		M^*		$\Delta\sigma$ (bars)	$ASE_{\Delta\sigma}$ (bars)	
1. Whittier Narrows		6.0		95.7	0.9	
2. Northridge		6.7		62.9	0.6	
3. San Fernando		6.6		36.1	0.6	
Site	Name	Number	Earthquake	κ (sec)	Category	R (km)
1	WHD	USGS 289	1	0.034	D	15.4
2	FAI	USC 90066	1, 2	0.064	D	15.5,46.0
3	ALH	CDMG 24461	1	0.042	D	15.5
4	SMA	CDMG 24401	1	0.052	D	15.6
5	OBR	CDMG 24400	1, 2	0.036	D	15.8,37.2
6	ATH	CDMG 80053	1	0.067	D	16.2
7	CAM	USC 90093	1, 2	0.064	D	16.3,42.7
8	JAB	USC 90094	1	0.042	D	16.6
9	FIG	USC 90032	1	0.058	C	16.6
10	VER	USC 90025	1, 2	0.066	D	17.5,35.2
11	CYP	USC 90033	1, 2	0.063	C	17.6,31.0
12	COM	USC 90073	1	0.054	C	17.7
13	OLD	USC 90095	1	0.051	C	17.7
14	ALT	CDMG 24402	1	0.048	D	18.0
15	BAD	USC 90070	1	0.077	D	18.1
16	NOR	USGS 634	1	0.057	D	18.5
17	RIM	USC 90072	1	0.077	D	18.5
18	DWN	CDMG 14368	1, 2	0.050	D	18.8,45.0
19	BRC	USC 90074	1, 2	0.068	C	18.8,59.3
20	FLT	USC 90034	1, 2	0.058	D	19.0,28.0
21	GR2	USC 90022	1, 2	0.049	D	20.0,31.8

CHAPTER 5

MODEL VALIDATION

5.1 PARTITION AND ASSESSMENT OF GROUND MOTION VARIABILITY

An essential requirement of any numerical modeling approach, particularly one which is implemented in the process of defining design ground motions, is a quantative assessment of prediction accuracy. A desirable approach to achieving this goal is in a manner which lends itself to characterizing the variability associated with model predictions. For a ground motion model, prediction variability is comprised of two components: modeling variability and parametric variability. Modeling variability is a measure of how well the model works (how accurately it predicts ground motions) when specific parameter values are known. Modeling variability is measured by misfits of model predictions to recorded motions through validation exercises and is due to unaccounted for components in the source, path, and site models (i.e. a point-source cannot model the effects of directivity and linear site response cannot accommodate nonlinear effects). Parametric variability results from a viable range of values for model parameters (i.e. slip distribution, soil profile, G/G_{max} and damping curves). It is the sensitivity of a model to a viable range of values for model parameters. The total variability, modeling plus parametric, represents the variance associated with the ground motion prediction and, because it is a necessary component in estimating fractile levels, may be regarded as important as median predictions.

Both the modeling and parametric variabilities may have components of randomness and uncertainty. Table 5.1 summarizes the four components of total variability in the context of

ground motion predictions. Uncertainty is that portion of both modeling and parametric variability which, in principle, can be reduced as additional information becomes available, whereas randomness represents the intrinsic or irreducible component of variability for a given model or parameter. Randomness is that component of variability which is intrinsic or irreducible for a given model. The uncertainty component reflects a lack of knowledge and may be reduced as more data are analyzed. For example, in the point-source model, stress drop is generally taken to be independent of source mechanism as well as tectonic region and is found to have a standard error of about 0.7 (natural log) (EPRI, 1993). This variation or uncertainty plus randomness in $\Delta\sigma$ results in a variability in ground motion predictions for future earthquakes. If, for example, it is found that normal faulting earthquakes have generally lower stress drops than strike-slip which are, in turn, lower than reverse mechanism earthquakes, perhaps much of the variability in $\Delta\sigma$ may be reduced. In extensional regimes, where normal faulting earthquakes are most likely to occur, this new information may provide a reduction in variability (uncertainty component) for stress drop, say to 0.3 or 0.4 resulting in less ground motion variation due to a lack of knowledge of the mean stress drop. There is, however, a component of this stress drop variability which can never be reduced in the context of the Brune model. This is simply due to the heterogeneity of the earthquake dynamics which is not accounted for in the model and results in the randomness component of parametric variability in stress drop. A more sophisticated model may be able to accommodate or model more accurately source dynamics but, perhaps, at the expense of a larger number of parameters and increased parametric uncertainty (i.e. the finite-fault with slip model and nucleation point as unknown parameters for future earthquakes). That is, more complex models typically seek to

reduce modeling randomness by more closely modeling physical phenomena. However, such models often require more comprehensive sets of observed data to constrain additional model parameters, which generally leads to increased parametric variability. If the increased parametric variability is primarily in the form of uncertainty, it is possible to reduce total variability, but only at the additional expense of constraining the additional parameters. Therefore, existing knowledge and/or available resources may limit the ability of more complex models to reduce total variability.

The distinction of randomness and uncertainty is model driven and somewhat arbitrary. The allocation is only important in the context of probabilistic seismic hazard analyses as uncertainty is treated as alternative hypotheses in logic trees while randomness is integrated over in the hazard calculation (Cornell, 1968). For example, the uncertainty component in stress drop may be treated by using an N-point approximation to the stress drop distribution and assigning a branch in a logic tree for each stress drop and associated weight. A reasonable three point approximation to a normal distribution is given by weights of 0.2, 0.6, 0.2 for expected 5%, mean, and 95% values of stress drop respectively. If the distribution of uncertainty in stress drop was such that the 5%, mean, and 95% values were 50, 100, and 200 bars respectively, the stress drop branch on a logic tree would have 50, and 200 bars with weights of 0.2 and 100 bars with a weight of 0.6. The randomness component in stress drop variability would then be formally integrated over in the hazard calculation.

5.1.1 Assessment of Modeling Variability

Modeling variability (uncertainty plus randomness) is usually evaluated by comparing response

spectra computed from recordings to predicted spectra and is a direct assessment of model accuracy. The modeling variability is defined as the standard error of the residuals of the log of the average horizontal component (or vertical component) response spectra. The residual is defined as the difference of the logarithms of the observed average 5% damped acceleration response spectra and the predicted response spectra. At each period, the residuals are squared, and summed over the total number of sites for one or all earthquakes modeled. Dividing the resultant sum by the number of sites results in an estimate of the model variance. Any model bias (average offset) that exists may be estimated in the process (Abrahamson et al., 1990; EPRI 1993) and used to correct (lower) the variance (and to adjust the median as well). In this approach, the modeling variability can be separated into randomness and uncertainty where the bias corrected variability represents randomness and the total variability represents randomness plus uncertainty. The uncertainty is captured in the model bias as this may be reduced in the future by refining the model. The remaining variability (randomness) remains irreducible for this model. In computing the variance and bias estimates only the frequency range between processing filters at each site (minimum of the 2 components) is used. The causal butterworth filter corners are listed for each site (and component) in the Strong Motion Catalogue (Appendix B).

5.1.2 Assessment of Parametric Variability

Parametric variability, or the variation in ground motion predictions due to uncertainty and randomness in model parameters is difficult to assess. Formally, it is straight-forward in that a Monte Carlo approach may be used with each parameter randomly sampled about its mean (median) value either individually for sensitivity analyses (Silva, 1992; Roblee et al., 1996) or

in combination to estimate the total parametric variability (Silva, 1992; EPRI, 1993). In reality, however, there are two complicating factors.

The first factor involves the specific parameters kept fixed with all earthquakes, paths, and sites when computing the modeling variability. These parameters are then implicity included in modeling variability provided the data sample a sufficiently wide range in source, path, and site conditions. The parameters which are varied during the assessment of modeling variation should have a degree of uncertainty and randomness associated with them for the next earthquake. Any ground motion prediction should then have a variation reflecting this lack of knowledge and randomness in the free parameters.

An important adjunct to fixed and free parameters is the issue of parameters which may vary but by fixed rules. For example, source rise time (Chapter 2, Equation 2-7) is magnitude dependent and in the stochastic finite-source model is specified by an empirical relation. In evaluating the modeling variability with different magnitude earthquakes, rise time is varied, but because it follows a strict rule, any variability associated with rise time variation is counted in modeling variability. This is strictly true only if the sample of earthquakes has adequately spanned the space of magnitude, source mechanism, and other factors which may affect rise time. Also, the earthquake to be modeled must be within that validation space. As a result, the validation or assessment of model variation should be done on as large a number of earthquakes of varying sizes and mechanisms as possible.

The second, more obvious factor in assessing parametric variability is a knowledge of the

appropriate distributions for the parameters (assuming correct values for median or mean estimates are known). In general, for the stochastic models, median parameter values and uncertainties are based, to the extent possible, on evaluating the parameters derived from previous earthquakes (Silva, 1992; EPRI, 1993).

The parametric variability is site, path, and source dependent and must be evaluated for each application (Roblee et al., 1996). For example, at large source-to-site distances, crustal path damping may control short-period motions. At close distances to a large fault, both the site and finite-source (asperity location and nucleation point) may dominate, and depending upon site characteristics, the source or site may control different frequency ranges (Silva, 1992; Roblee et al., 1996).

In combining modeling and parametric variations, independence is assumed (covariance is zero) and the variances are simply added to give the total variability.

$$_{ln}\sigma^2_T = {}_{ln}\sigma^2_M + {}_{ln}\sigma^2_P \text{*****} \qquad (5\text{-}1),$$

where

$_{ln}\sigma^2_M$ = modeling variation,

$_{ln}\sigma^2_P$ = parametric variation.

5.1.3 Validation Earthquakes

*****Strong ground motions are generally considered to be log normally distributed.

The validation exercises include all earthquakes with derived slip models (with the exception of the Kobe earthquake), a total of 14. The Little Skull Mountain earthquake, which occurred on the Nevada Test Site, and which does not have a slip model was added because of interest to DOE. A general slip model is derived for this earthquake as the best fitting of a suite of randomly generated models (Chapter 5). Also the largest aftershock (M 5.2) of the 1979 M 6.5 Imperial Valley earthquake was added to provide a linear response constraint to the development of modulus reduction and hysteretic damping curves for Imperial Valley soils (Chapter 5). The total number of earthquakes modeled then is 16 at 502 sites covering the fault distance range of about 1 km to nearly 200 km for WNA data and from about 5 km out to about 450 km for ENA data (Nahanni and Saguenay earthquakes). Table 5.2 lists the earthquakes modeled, magnitudes, fault distance ranges, and number of sites. In the following sections, the earthquakes are treated in Geologic Province groups and then in chronological order for those events which occurred outside the three provinces.

To refine the M_0 verses rise time relation based on the modeling results, rise times are varied about the original empirical relation

$$\log \tau = 0.33 \log M_0 - 8.62 \qquad (5\text{-}2)$$

and the best fitting rise times selected based on a visual examination of the bias estimates. The empirical rise time relation was based on a fit to the rise time data of Heaton (1990) with the slope constrained to 0.33 (similarity constraint; Hartzell, 1978). The selection of best fitting rise

times permits a reassessment of the empirical relation in the context of the stochastic finite-fault model. This approach is not intended to be exhaustive but to determine whether or not any bias exists in the empirical relation and to provide a reasonable basis for incorporating any adjustments. Naturally, if a significant difference is encountered then either rise time must be treated parametrically and randomly varied in prediction exercises or the validations redone with the revised rise time scaling relation.

5.2 PENINSULAR RANGE EARTHQUAKES

The Peninsular Range earthquakes include the M 6.7 Northridge, M 6.6 San Fernando, and M 6.0 Whittier Narrows. The Northridge earthquake is treated first as it has the largest number of sites (Table 5.2) and widest range in levels of motion. The point-source stress drop and kappa values determined from the regional inversion are listed in Table 4.2. The regional Q(f) model determined in the regional 2-site (rock and soil) inversion is 264 $f^{0.6}$ (Chapter 4, Table 4.1).

5.2.1 1994 Northridge Earthquake

For the 1994 M 6.7 Northridge earthquake, a total of 94 sites are modeled: 71 soil and 23 rock. The fault distance range is about 7 km (sites over the rupture surface) to nearly 150 km (Table 5.2). The sites extend from the San Fernando Valley into the Los Angeles Basin to the south and to the San Andreas fault to the north and east (Figure 5.1). The crustal model is from Wald and Heaton (1994) and is listed in Table 5.3. To model rock and soil sites, the generic rock or soil profile (Chapter 3) is simply placed on top of the regional crustal model. The shallow

generic rock profile is truncated at velocities exceeding 1.0 km/sec, the velocity of the top layer of the Wald and Heaton (1994) Northridge crust (Table 5.3).

Both the rock and soil sites are allowed to exhibit material nonlinearity to depths of 500 ft (Table 5.4). For the rock sites, the generic soft rock G/G_{max} and hysteretic material damping curves (Chapter 6) are used. These curves were based on modifications to laboratory test results (Appendix D) required to model the rock site empirical attenuation (Appendix A and Chapter 6). For the soil sites, finite-source modeling (section following point-source results) using both the EPRI cohesionless soil curves (Chapter 6) and the generic deep soil (Chapter 6) curves showed more satisfactory results using the generic deep soil curves. As a result, the soft soil curves are adopted as being appropriate for Peninsular Range or Los Angeles area cohesionless soils.

The kappa values for the rock beneath the nonlinear zones at both rock and soil sites is taken as 0.03 sec (Table 5.3). This value was selected to give a total kappa (including nonlinear zone small strain damping) of about 0.04 sec, a value consistent with the empirical inversions (Table 6.1).

The finite-source model parameters are listed in Table 5.4. The rise time of 1.30 sec represents a best fit over a limited set of trial values and was selected based on a visual examination of the model bias, model variability, and response spectral fits. The static stress drop, based on the area, is about 39 bars and the point-source stress drop resulting from the inversions (Table 4.4) is 62.9 bars. The point-source depth is taken as 11 km, the depth of the largest asperity in the

Wald and Heaton (1994) slip model (Figure 5.2).

5.2.1.1 Point-Source Inversions For Stress Drop and Kappa Values

The Northridge earthquake is included in the Peninsular Range Province set along with the Whittier Narrows and San Fernando earthquakes. The Fourier amplitude spectra for both the recordings and the model predictions, are shown in Figure Set 4.2 and the site specific kappa values are listed in Table 4.2. For the Peninsular Range sites, the average rock kappa value is 0.048 sec and the corresponding soil kappa value is 0.056 sec.

5.2.1.2 Point-Source Modeling Results

The point-source model bias and variability estimates computed over all the 94 sites are shown in Figure 5.3. The bias is generally near zero between about 1 to 20 Hz and shows a slight underprediction at higher frequencies (equivalent to peak acceleration). The strong negative bias at low frequencies (< 1 Hz) is a manifestation of the general tendency for the point-source to overpredict over the low frequency range at large magnitudes (Chapter 6). The dip in the bias estimates near 10 Hz is where the 5% damped pseudo absolute response spectral acceleration is beginning to saturate to peak ground acceleration. The response spectra are generally decreasing with increasing frequency (Figure 5.6) and reach full saturation around 30 Hz where the bias estimates become constant with increasing frequency. Over this relatively constant portion, the bias plots reflect the behavior of peak ground acceleration which is actually controlled by lower frequencies, in the 2 to 6 Hz range, where the spectral acceleration peaks.

The model variability (uncertainty plus randomness) is about 0.5 about 1 Hz and rises

significantly below 1 Hz reflecting the stable point-source low frequency overprediction. The bias corrected variability (randomness) is significantly lower over this frequency range due to the large statistically significant negative bias estimates. The randomness estimates provide a minimum estimate of model variability and represent the reduction in variability (total-randomness) achievable with the model provided the ground motion estimates are corrected for the low frequency overprediction.

To separate site effects, Figures 5.4 and 5.5 show analogous plots for soil and rock sites respectively. For the 71 soil sites, Figure 5.4 shows similar results to the combined estimates due to the greater number of soil sites (71 soil verses 23 rock sites). For the rock sites, Figure 5.5 shows a broad peak of about 0.4 (factor of about 1.5) at intermediate frequencies (about 2-3 Hz) and a general underprediction of about 0.25 (natural log) at high frequencies. Approximately 25% of this positive bias is due to just two sites with very high motions: PUL (Pacoima Upper Left) and ORR (Castaic Old Ridge Route). Figure set 5.6 shows the 5% damped pseudo absolute response spectra, data (log average of 2 horizontal components) and model predictions, with PUL on the bottom of the first page and ORR on the third page. The recorded motions exceed the model predictions by a factor of over 3 at some periods (less than about 2 sec). The recorded motions are very high at these sites for the San Fernando earthquake as well suggesting strong site effects.

Further examination of Figure set 5.6 shows the fundamental cause of the broad peak near 3 Hz and trough at 10 Hz in the rock site bias plot (Figure 5.5). A typical example is site KAG (page 2, Figure set 5.6) which shows the model spectra with a peak near 0.1 sec while the recorded

motions have a spectral peak near 0.3 to 0.4 sec. Much of the difference is due to the previously discussed issue between the median spectrum computed over a range in random profiles and the spectrum computed from a smooth median profile (Chapter 3). The effects of randomizing a profile to produce realistic profile samples with accompanying low and high velocity layers is to reduce the average short period motions and increase intermediate period motions (with respect to the period range of profile influence). This observation was demonstrated in Figure 3.7 which is reproduced here as Figure 5.7. The figure shows the shift in spectral peak to longer periods (from near 0.12 Hz to 0.2 Hz) between the spectrum computed from the smooth base case profile and the median spectrum computed over 30 spectra from randomized profiles. Figure 5.8 (same as Figure 3.5) shows an analogous plot for deep soil illustrating a similar although much less pronounced behavior. The difference is significant; particularly for rock sites, and suggests that an appropriate approach to estimating model bias and variability for use in future predictions is to either use a median prediction at each site or select the best fitting spectrum out of the random selection of site profiles. This would be of interest to try but time has precluded the attempt for this report. As a result, the bias and randomness estimates, particularly for rock sites, must be viewed in the context that they likely represent upper bounds and use of median predictions would generally both smooth and improve the bias estimates.

5.2.1.3 Finite-Source Modeling Results

Figure 5.9 shows the model bias and variability estimates over the total 94 sites for the stochastic finite-source model. The bias is generally small over the effective structural frequency range of about 0.2 to 100 Hz (peak acceleration is at about 30 Hz). At low frequency ($\leq$ 1 Hz)

there is a significant departure from the point-source large negative bias (Figure 5.3) suggesting the appropriateness of the finite-source model as a broad-band methodology.

Not surprisingly (Silva, 1992), for frequencies above 1 Hz, there is little difference in the bias estimates for the point- and finite-source models: both are considered good. Comparing the variability estimates, Figure 5.9 for the finite-source and Figure 5.3 for the point-source, very similar results are obtained, again for frequencies of 1 Hz and above. The bias corrected estimates are nearly identical for the two models ranging from about 0.5 at 100 Hz to about 0.75 at 0.2 Hz (lowest reliable frequency).

Although the present analysis considers many more sites and over a much larger distance range the bias and variability estimates are comparable to those using the much more computationally demanding broad-band simulation procedure which includes near-field terms and a much more rigorous were propagation model (Sommerville et al., 1995). These results are interesting in that the point- and finite-source modeling includes rock, basin edge, and deep basin sites ranging in distance from over the source rupture out to nearly 150 km. This suggests that the simple point-source model (if corrected for low frequency bias), with a very simple 1/R ($1/\sqrt{R}$ for R > twice crustal thickness), predicts broad-band strong ground motions at an average site with an accuracy comparable to much more sophisticated approaches such as the stochastic finite-source and the broad-band simulation procedure. The stochastic finite-source model bias and variability (Figure 5.9) indicates that simple assumptions in the context of source finiteness (Chapter 2) results in a surprisingly accurate and broad-band simulation methodology (Silva, 1992). Additionally, for both the point- and finite-source models, the simple assumption of

vertically propagating shear-waves appears to capture reasonably well strong motion site effects for sites located above the source out to distances of over 100 km.

To separate out soil and rock sites, Figures 5.10 and 5.11 show model bias and variability plots for the two recording site conditions. As with the point-source, due to the large number of soil sites (71 soil, 23 rock), the soil only and combined results are very similar. The soil sites (Figure 5.10) show slightly more negative bias and lower variability indicating the opposite condition must apply to the rock sites (Figure 5.11). This is definitely the case as Figure 5.11 shows, displaying a similar trend in the high frequencies (> 1 Hz) as the point-source rock results (Figure 5.5). As with the point-source, the broad peak near 2 to 3 Hz and trough at 10 Hz is largely attributable to the amplification of the smooth base-case rock profile.

For a qualitative appraisal of the response spectral predictions, Figure 5.12 shows the individual site spectra. Consistent with the bias estimates, the overall fit is generally good over the rather wide distance range. Site CDF, at 147 km is in the Mojave Province and is quite high for the Imperial Valley earthquake as well, perhaps suggesting strong localized effects. For the rock sites, Figure 5.12 shows features similar to the point-source, overprediction around 0.1 sec and underprediction near 0.5 sec, reflecting the rock site bias estimates.

To examine any systematic distance bias and to determine appropriate G/G_{max} and hysteretic damping curves, separate variability and bias estimates were computed for "near source" sites located within about 30 km fault distance. The "near source" criterion of 30 km was selected such that a minimum of 10 rock and 10 soil sites would be included (enough for meaningful

comparative statistics) and that rock outcrop peak accelerations would generally be above 15 to 20%g. The last criterion was to ensure an expectation of discernable nonlinear soil site response with the EPRI (1993) (Chapter 6) modulus reduction and damping curves in the context of the generic deep soil shear-wave velocity profile.

Naturally these sites do not cover the entire province and soil conditions can vary dramatically within any province but this restricted set of stations represent those with high enough loading conditions to permit a possibility of discriminating between the two sets of curves.

Since the empirical attenuation relations for soil, which are dominated by Peninsular Range soils (Appendix A), show significantly less nonlinearity than the EPRI curves suggest (Chapter 6) and the deep soil generic curves (Chapter 6) were derived based on the empirical soil attenuation, it is desirable to see if the modeling can resolve the degree of nonlinearity that is consistent with the empirical attenuation. It was hoped that these "near source" criteria would enable selecting between either the EPRI (1993) curves or the generic deep soil curves (Chapter 6) as being more appropriate for Peninsular Range soils.

It should be emphasized that we are treating generic conditions with the assumption that the soil sites are, on average, similar to the generic deep soil profile and that a shear-wave velocity of about 3,000 ft/sec (bedrock) is reached, on average, at a depth of about 500 ft.

5.2.1.3.1 Assessment of Distance Bias. To consider first any significant distance bias, Figure

5.13 shows the combined sites variability and bias plots for sites within about 30 km (48 sites). The figure shows a more negative high frequency bias and lower variability, particularly for frequencies below about 2 Hz, than is shown for all the sites in Figure 5.9. The more distant sites are modeled less accurately than the close-in sites. To see if this is restricted to rock or soil site conditions, Figures 5.14 and 5.15 show the estimates for soil and rock respectively. Comparing Figures 5.14 for the close-in soil sites and Figure 5.10 for all soil sites, the bias estimates below 1 to 2 Hz are similar while the low frequency variability of the close-in soil sites is lower. Comparing the corresponding figures for the rock sites, Figure 5.11 for all rock sites and Figure 5.15 for the close-in rock sites reveals the same general trend: the low frequency bias is about the same while the variability is reduced for the close-in sites.

In general, the low frequency bias is similar between close-in and all the sites for both rock and soil sites. However, the low frequency variability decreases for the close-in sites suggesting the model is not capturing the greater variability in the more distant sites. This may be a wave propagation effect as the sites move out of the San Fernando basin across changes in crustal structure (Magistrale et al., 1992). It would be of interest to see if empirical Green functions could reduce this "distant site" model variability as these are the conditions under which this approach appears most appealing.

At high frequencies, above about 3 Hz, the "close-in" sites show more negative bias and lower variability (Figures 5.9 and 5.13). This is largely dominated by the soil sites since neither the bias nor the variability estimates change significantly between all the "close-in" sites and the soil "close-in" sites (Figures 5.13 and 5.14).

5.2.1.3.2 Assessment of G/G_{max} and Hysteretic Damping Curves. To assess the appropriate degree of soil nonlinearity in terms of implementing either the EPRI (1993) or the generic deep soil G/G_{max} and hysteretic damping curves for the Peninsular Range soil sites, the finite-fault modeling was repeated using the EPRI (Chapter 6) curves. Figure 5.16a shows the bias and randomness estimates for all 71 soil sites computed using the EPRI curves. Comparing this figure with Figure 5.10 (Figure 5.16b) for the deep soil curves it is apparent that the degree of nonlinearity is discernable for frequencies exceeding about 8 Hz where the bias and randomness estimates differ significantly. The more positive bias estimates resulting from the more nonlinear EPRI curves reflect lower high frequency motions. To concentrate on the higher levels of loading at the "close-in" sites, Figure 5.17a shows the estimates for the soil sites within about 30 km of the rupture. The bias is near zero from 0.2 to 100 Hz. Comparing that figure to Figure 5.14 (Figure 5.17b) illustrating the results using the generic deep soil curves, which shows a negative high frequency (> 1 Hz) bias or overprediction, the conclusion might be reached that the EPRI curves are the more appropriate set. However, these equivalent-linear site response analyses were done with a simple smooth generic profile which results in greater high frequency motions than a median spectrum computed over a suite of random profiles (Chapter 3).

Referring back to Figure 5.8, where this issue is illustrated, the spectrum computed for the generic smooth profile exceeds the median spectrum by about 10% on average for periods shorter than about 1 sec and about 20% for periods shorter than about 0.3 sec. The implication is straightforward in that if at each site, a median spectrum based on equivalent-linear analyses

of a suite of random profiles were used as the site spectral estimate, the high frequency motions would be lower. Unfortunately, the difference in spectral level between the spectrum computed for a smooth base-case profile and a median (or mean) spectrum depends on the level of control motion. The difference increases with loading level due to the nonlinearity of the soil (Chapter 3 and Roblee et al., 1996). As a result, it is not possible to quantify or refine the G/G_{max} and hysteretic damping curves unless the profiles are randomized at each site and the median spectrum is used in the bias estimates. Qualitatively it may be concluded that the high frequency negative bias obtained using the more linear generic soil curves, reflecting about a 20% overprediction, suggests that the generic deep soil curves are the more appropriate of the two sets. Figure 5.8 indicates that if median spectra had been computed at each site using the generic deep soil curves the negative high frequency bias estimates shown in Figure 5.14 would be reduced to near zero, like those in Figure 5.17.

5.2.1.3.3 Assessment of Nonlinear Site Response. Because the bias analyses provided sufficient resolution to discriminate between the EPRI and generic deep soil G/G_{max} and hysteretic damping curves, it is of interest to determine if a similar analysis could reject the hypothesis of linear soil site response. To provide linear site response bias estimates, the finite-source simulation was repeated constraining the number of equivalent-linear iterations to 1. This effectively sets G/G_{max} to 1 and the damping to that at a cyclic shear strain of 10^{-4}%. The resulting kappa value is 0.04 sec (Table 5.4) which is the value determined in the inversions of the empirical attenuation relations for soil sites at small strains (Table 6.1).

The results of the linear site response analyses are compared to the equivalent-linear analyses using the best fitting generic soil curves in Figure 5.18. The bias estimates are for the "close-in" sites and the large significant high frequency negative bias for the linear analyses is quite apparent. The abrupt departure between the linear and nonlinear bias estimates at 3 Hz suggests that for this suite of sites considered and under these loading conditions, nonlinear site response is an important consideration for frequencies exceeding about 3 Hz. Alternatively, the assumed linear kappa value of 0.04 sec may be in considerable error, by at least 100%. This does seen unlikely but remains an unresolved issue until enough small earthquakes (aftershocks) are recorded at these sites to provide estimates of small strain kappa values.

In support of the rejection of the linearity hypothesis, Figure 5.19 shows a corresponding plot for soil sites beyond about 30 km fault distance. Interestingly the bias estimates are nearly identical up to about 3 to 4 Hz where the linear response estimates begin to fall below those of the nonlinear response. The maximum difference is about 0.1 at 10 Hz reflecting about 10% larger motions for the linear analyses. The difference is likely not statistically significant and neither model can be rejected based on these results. However, if the kappa values were increased by a significant amount, even by only 50%, the high frequency linear bias estimates would decrease significantly (nearly the same percentage as the kappa increase; Silva, 1992) resulting in strongly positive bias estimates. We are left then with explaining the high kappa values close to the source yet average soil kappa values at similarly classified sites beyond 30 km. It does appear that the rejection of linearity for the "close-in" sites is the most physically consistent hypothesis.

Parenthetically, these results suggest an envelope of clear detectibility of soil nonlinearity for generic Peninsular Range soils. Magnitudes significantly above about 6.5, distances within about 30 km (expected rock outcrop peak acceleration above about 20%g), frequencies above about 3 Hz, and, for statistical stability, at least 20 stations.

This represents a set of rather stringent conditions and it is not surprising why the debate between engineers and seismologists over nonlinear soil response raged for so long.

5.2.2 1971 San Fernando Earthquake

A total of 39 sites, 21 rock and 18 soil, are modeled for the M 6.6, 1971 San Fernando earthquake over the fault distance range of about 3 to 218 km (Table 5.2). The site distribution is shown in Figure 5.20. Because only a homogeneous half-space crustal model was used in determining the source model (Heaton, 1982), the Northridge crustal model of Wald and Heaton (1994) was adopted (Table 5.3). The simple half-space model used by Heaton (1982) was justified in that only close-in sites were used which are dominated by energy propagating upward from the source. The main issue is the lack of amplification in the half-space model which may have been mapped into the source (slip) model. This is likely the case as the finite-source model shows a significant broad-band negative bias. The use of an appropriate crustal shear-wave velocity gradient in the source inversion would likely result in a broader and perhaps deeper shallow asperity.

As with the Northridge earthquake, rock and soil sites have potential nonlinear zones to 500 ft and use the same kappa values and G/G_{max} and hysteretic damping curves (Table 5.5).

The finite-source parameters are listed in Table 5.5. The best fitting rise time is 1.25 sec and the static stress drop 34.3 bars. The point-source stress drop is 36.1 bars (Table 4.4), about the same as that of the static value. The point-source depth is taken as 8 km, midpoint between the shallow and deep asperities of the Heaton (1982) slip model.

The slip model used (Figure 5.21) was generated as the combination of the two Heaton (1982) rupture models on subparallel faults San Fernando and Sierra Madre, onto the larger and deeper Sierra Madre Fault. This was necessary since the current stochastic finite-fault model cannot accommodate articulated rupture planes. As a result, some of the fault distances for the closest sites may be inappropriate. However, judging from the fit of response spectra, the effect does not appear to be a controlling factor. It may have a much greater influence in a time domain comparison of the arrival times of significant phases which likely led to the two rupture surfaces.

5.2.2.1 Point-Source Inversions For Stress Drop and Kappa Values

The San Fernando earthquake is included in the Peninsular Range Province set along with the Northridge and Whittier Narrows earthquakes. The Fourier amplitude spectra for both the recordings and the model predictions, are shown in Figure Set 4.2 and the site specific kappa values are listed in Table 4.2. For the Peninsular Range sites, the average rock kappa value is 0.048 sec and the corresponding soil kappa value is 0.056 sec.

5.2.2.2 Point-Source Modeling Results

Bias and variability estimates are shown in Figure 5.22 computed over all 39 sites for the point-source using a stress drop of 36.1 bars. The bias shows the typical negative low frequency

point-source overprediction. Reprocessing by PE&A has extended the useable bandwidth from about 0.3 to 30 Hz (plots are on structural frequency for response spectra) over this distance range so the reliability of the estimates decreases significantly below about 0.3 Hz. At higher frequency the bias is positive indicating a slight underprediction. The variability plot shows values larger than for the Northridge earthquake, about 0.6 from about 0.4 to 100 Hz.

Bias and variability plots for the 18 soil and 21 rock sites separately are shown in Figures 23 and 24 respectively. For the soil sites, the high frequency (> 1 Hz) bias is about zero and increases to about 0.25 for rock sites (Figure 5.24). Apparently the slight underprediction over all sites (Figure 5.22) is being driven by the rock sites. Interestingly the randomness plots are similar, around 0.6. Considering the distance range, about 3 to 200 km, the level of randomness and generally small bias values is very encouraging for this complicated source.

Examining the spectral plots in Figure set 5.25, it appears that a significant contribution to the rock site underprediction may be due to sites PCD (Pacoima) and ORR (Castaic). This was the case with the Northridge earthquake as well and indicates the possibility of strong local effects at these sites.

5.2.2.3 Finite-Source Modeling Results

The bias and randomness plots for the finite-source are shown in Figure 5.26 for all the sites. The bias is nearly constant at about -0.25 and decreases to nearly -0.4 around 0.5 Hz. The low frequency overprediction of about 1.4 is similar for the soil and rock sites (Figures 5.27 and 5.28) and is probably related to the use of a homogenous half-space in deriving the slip model(s)

(Heaton, 1982). Since a combination of integrated velocity and displacement strong motion records were used as the near-source constraints on the slip model(s), the dominant periods are long and generally greater than about 1 to 2 sec and probably do not exceed 10 sec (Appendix B). The crustal amplification for the generic rock and soil models at a period of 5 sec is about 1.3 and 1.4 respectively (Figures 6.4 and 6.5), in general agreement with the finite-source low frequency negative bias. Use of a crustal model in deriving the San Fernando earthquake slip model(s) should result in a smaller (near zero) bias perhaps by adjusting parameters such as rise time, asperity sharpness (stress drop), and asperity depth. The finite-fault variability estimates are larger than those of the point-source possibly reflecting the issue of the crustal gradient. Not unrelated, this larger finite-fault variability may be an indication that subparallel rupture surfaces or a fault plane articulated with depth (Heaton and Helmberger, 1979) are required to better fit the strong motion data.

The response spectra, data and model predictions for the finite-fault are shown in Figure Set 5.29. In general the model captures the overall spectra reasonably well.

5.2.3 1987 Whittier Narrows Earthquake

The M 6.0 Whittier Narrows earthquake modeling and inversions has the 2nd largest number of sites of all the earthquakes considered, at total of 88. Of the 88 sites modeled, only 18 are rock leaving 70 soil sites. Unfortunately, there are simply not very many rock sites available for this earthquake. The fault distance range is about 10 to 80 km due to deep source (Hartzell and Iida, 1990) and Figure 5.30 shows the site distribution. The Wald and Heaton (1994) crustal model is used (Table 5.3) since it is very similar to the model used in the inversions for slip

distribution (Hartzell and Iida, 1990). Rock and soil sites are produced by placing the generic profiles on top of the crustal model and are potentially nonlinear to a depth of 500 ft (Table 5.6), exactly the same as for the Northridge and San Fernando earthquakes. Generic rock and generic deep soil G/G_{max}, and hysteretic damping curves (Table 5.6) are used consistent with the results of the Northridge earthquake for the Peninsular Range soils.

The source parameters are listed in Table 5.6. The point-source and finite-source stress drops are 95.7 and 27.3 bars respectively and the point-source depth is 15 km, the depth to the largest asperity. The best fitting rise time is 0.25 sec and the slip model (Figure 5.31) is from Hartzell and Iida (1990). It should be noted that Hartzell and Iida did not use any data in their slip model inversions at epicentral distances exceeding about 15 km as they wished to minimize wave propagation effects. This appears to have an impact on the current finite-fault modeling as the distant sites (beyond about 30 km fault distance) are not fit as nearly well as the closer sites.

5.2.3.1 Point-Source Inversions for Stress Drop and Kappa Values

The Whittier Narrows earthquake is included in the Peninsular Range inversions (Chapter 4). The Fourier amplitude spectra are shown in Figure Set 4.2 and the site specific kappa values are listed in Table 4.2.

5.2.3.2 Point-Source Modeling Results

For all 88 sites, the model bias and variability plots are shown in Figure 5.32. The bias is essentially zero for frequencies above 1 Hz. The point-source low frequency overprediction is quite strong for this earthquake, about 0.6 from near 1 Hz to about 0.3 Hz, the approximate low

frequency range of the data. The bias corrected variability (randomness) averages about 0.6 while the uncorrected values rise sharply below 1 Hz. Overall the simple point-source appears to capture ground motions quite well for frequencies above 1 Hz.

For the soil and rock sites, Figures 5.33 and 5.34 show the corresponding analyses. Figure 5.33, for soil sites, shows a slight high frequency overprediction while Figure 5.34 shows the opposite for the rock sites. As with the San Fernando earthquake (unlike the Northridge), the variability for the soil sites is lower than for the rock sites.

To examine directly the fits to the response spectra, Figure Set 5.35 shows the model and data 5% damped response spectra. As with the other earthquakes, the simple point-source model generally performs well in matching the overall level of the recorded motions. Notable exceptions are the 4 most distant sites, all rock, which show large short period underpredictions. Site CSR is Castaic Old Ridge Route which showed a substantial underprediction for the Northridge and San Fernando earthquakes as well.

5.2.3.3 Finite-Source Modeling Results

For the finite-source model, the bias and randomness plots are shown in Figures 5.36, 5.37 and 5.38 for all 88 sites, 71 soil, and 17 rock sites respectively. Over all the sites the bias is small and shows a distinct overprediction, or valley, near 0.8 Hz. From Figure 5.32, for the point-source, it appears this is present there as well and may be associated with resonances in the shear-wave velocity profiles. Using the median (or mean) spectrum from randomized profiles (Appendix C) would eliminate any profile resonances and result in much smoother bias and

variability estimates.

The bias plot for the soil sites (Figure 5.37) is similar to all the sites (Figure 5.36) due to the larger number of soil sites (71 soil verses 17 rock). The slightly more negative high frequency bias for soil sites suggests that the rock sites are substantially underpredicted. For the soil sites, the variability is about 0.5 at high frequencies and shows the usual low frequency increase at low frequency. The effects of the profile resonances are clearly seen in the randomness plots as low frequency peaks.

For the 17 rock sites, Figure 5.38 shows the bias and variability plots illustrating a significant broad-band underprediction and much larger variability. To examine whether this underprediction is distant dependent, Figure 5.39 and 5.40 show the bias and randomness plots for soil and rock sites respectively at fault distances less than about 30 hrs. For the soil sites, the close-in results (Figure 5.39) suggest a slightly larger overprediction and about the same level of variability as all soil sites (Figure 5.37). However for rock sites, Figure 5.40 shows a near zero bias and significantly lower variability than for all the rock sites (Figure 5.38). Apparently the more distant ($\geq$ 30 km) rock sites are significantly underpredicted and show considerable unmodeled variation. This result is similar to the Northridge earthquake but in that case the distant ($\geq$ 30 km) soil and rock sites showed higher variability.

To examine this rock site underprediction ($\geq$ 30 km) more closely, Figure Set 5.41 shows the response spectra for each site. In general the predictions are in agreement with the recorded motions with some very good matches and with several sites showing significant departures.

The most distant rock sites, VAS, VIR, RIV, MAL, CSH, and CSR illustrate the higher frequency underprediction with CSR (Castaic Old Ridge Route) the major contributor. The less severe tendency for the distant soil sites to be underpredicted is illustrated in the spectra plots as well. The point-source (Figure Set 5.35) does a much better job (except for CSR) using simple $1/\sqrt{R}$ geometric attenuation. It would be of interest to see if Hartzell and Iida would have similar results or if the inclusion of sites beyond 15 km epicentral distance would have resulted in changes to their slip model.

For 88 sites ranging in fault distance from about 10 to 80 km, both the point- and finite-source models predict the motions very well as the all-site bias and variability plots suggest. This is encouraging since the slip model was determined from data recorded at sites within 15 km epicentral distance.

5.3 NORTH COAST EARTHQUAKES

In this North Coast Province group, the Loma Prieta earthquake is treated first as it has by far the largest number of sites spanning the greatest distance range. The Loma Prieta presentation is followed chronologically by the 1979 M 5.7 Coyote Lake and 1984 M 6.2 Morgan Hill earthquakes. The site kappa values and stress drops determined in the point-source inversion (Chapter 4) are listed in Table 4.3. The regional Q(f) models and average kappa values from the regional inversions are 176 $f^{0.6}$ and 0.053 sec and 0.083 sec for rock and soil sites respectively and are listed in Table 4.1

5.3.1 Loma Prieta Earthquake

For the 1984 M 6.9 earthquake, a total of 53 sites covering the fault distance range of about 5 to 90 km (Table 5.2) are modeled. The sites are comprised of 33 rock and 20 soil. Most of the rock sites are located beyond about 30 km (20) while most of the soil sites (17) are "close-in" or within about 30 km of the source.

The site distribution is shown in Figure 5.42. The soft Geomatrix side E (Bay mud) sites are not modeled at this time as there are too few recordings to constrain an attenuation relation for the comparison exercises. Also the additional effort in developing a generic profile, producing amplification factors, and assessing appropriate G/G_{max} and hysteretic damping curves is not warranted in validating the model. The presumption being that there is nothing unusual about the response of soft sites that would violate the appropriateness of the site response model, particularly under the moderate levels of loading during the Loma Prieta earthquake. Additionally, the soft sites Treasure Island and Lotung (Taiwan) were successfully modeled in the EPRI (1993) assessment of equivalent-linear verses nonlinear site response analyses.

The crustal model is from Wald et al. (1991) and is listed in Table 5.7 and is the same crustal model used in determining the slip distribution. To model rock and soil sites, the generic rock or soil profile (Chapter 3) is simply placed on top of the regional crustal model. The shallow generic rock profile is truncated at velocities exceeding 1.0 km/sec, the velocity of the top layer of the crustal model (Table 5.7).

Both the rock and soil sites are allowed to exhibit material nonlinearity to depths of 500 ft (Table 5.8). For the rock sites, the generic soft rock G/G_{max} and hysteretic material damping curves

(Chapter 6) are used. These curves were based on modifications to laboratory test results (Appendix D) required to model the rock site empirical attenuation (Appendix A and Chapter 6). For the soil sites, both the EPRI cohesionless soil and deep generic soil curves (Chapter 6) and used to provide an assessment of which set is more appropriate for North Coast soils. In the initial analyses the EPRI curves are used.

The kappa values for the rock beneath the nonlinear zones at both rock and soil sites is taken as 0.03 sec (Table 5.8). This value was selected to give a total kappa (including nonlinear zone small strain damping) of about 0.04 sec, a value consistent with the empirical inversions at low levels of loading (Table 6.1).

The finite-source model parameters are shown in Table 5.8. The rise time of 1.60 sec represents a best fit over a limited set of trial values and was selected based on a visual examination of the model bias, model variability, and response spectral fits. The static stress drop, based on the area, is about 33 bars and the point-source stress drop resulting from the inversions (Table 4.3) is 73.7 bars. The point-source depth is taken as 12 km, the depth of the largest asperity in the Wald et al. (1991) slip model (Figure 5.43).

5.3.1.1 Point-Source Inversions For Stress Drop and Kappa Values

The Loma Prieta earthquake is included in the North Coast Province set along with the Coyote Lake and Morgan Hill earthquakes. The Fourier amplitude spectra for both the recordings and the model predictions, are shown in Figure Set 4.3 and the site specific kappa values are listed in Table 4.4. For the North Coast sites, the average rock kappa value is 0.053 sec and the

corresponding soil kappa value is 0.083 sec. The average North Coast soil kappa value is significantly higher than the corresponding Peninsular Range value of 0.058 sec. Since the average rock site kappa values are nearly the same for both provinces (0.056 sec for the Peninsular Range), this suggests that the North Coast soil sites have either intrinsically higher material damping or are exhibiting a higher degree of material nonlinearity.

5.3.1.2 Point-Source Modeling Results

The point-source model bias and variability estimates computed over all the 53 sites are shown in Figure 5.44. The bias is generally near zero (within the ± 90% confidence limits) between about 1 to 20 Hz and shows a slight underprediction at higher frequencies (equivalent to peak acceleration). The trend in the negative bias at low frequencies (< 1 Hz) is a manifestation of the general tendency for the point-source to overpredict over the low frequency range at large magnitudes (Chapter 6).

The model variability (uncertainty plus randomness) is about 0.6 above 2 Hz and rises significantly below 2 Hz, reflecting unmodeled low frequency site variations as the bias is near zero.

To separate site effects, Figures 5.45 and 5.46 show analogous plots for soil and rock sites respectively. For the 20 soil sites, Figure 5.45 shows a lower, near constant bias for frequencies above about 1 Hz. For the rock sites, Figure 5.46 shows a broad peak of about 0.3 (factor of about 1.4) at intermediate frequencies (about 1 to 5 Hz) and a general underprediction of about 0.2 (natural log) at very high frequencies. It appears that much of this positive bias may be due

to just 5 sites with very high motions: PRS, CFH, BRK, CGB, and PTB, all rock sites and at distances beyond about 70 km. Figure set 5.47 shows the 5% damped pseudo absolute response spectra, data (log average of 2 horizontal components) and model predictions, with the most distant sites on the last page. The recorded motions exceed the model predictions by a factor of over 3 at some periods. These recorded motions are very high at these sites but other nearby rock sites, such as YBI, PHT, and TLH, reflect closer to expected levels (about 0.05g) suggesting strong site effects. Similar results are also observed in the finite-source analyses which incorporates crustal propagation effects (Chapter 2). This suggests that the underprediction at the distant rock sites is not a result of the simple point-source $1/\sqrt{R}$ geometrical attenuation at these distances.

In general however, the point-source performs well with a low bias and small randomness (Figure 5.44) over this wide distance range.

5.3.1.3 Finite-Source Modeling Results

Figure 5.48 shows the model bias and variability estimates over the total 53 sites for the stochastic finite-source model. The bias is generally small over the frequency range of about 0.3 to 100 Hz (peak acceleration is at about 30 Hz). Near 1 Hz there is a small underprediction and an overprediction near 10 Hz. At higher frequency the bias is near zero.

Not surprisingly (Silva, 1992; Schneider et al., 1993), for frequencies above about 0.5 Hz, the difference in the bias estimates for the point- and finite-source models is small: both are considered good. Comparing the variability estimates, Figure 5.48 for the finite-source and

Figure 5.44 for the point-source, very similar results are obtained, again for frequencies of about 0.5 Hz and above. The bias corrected estimates are nearly identical for the two models ranging from about 0.5 at 100 Hz to about 0.75 at 0.2 Hz (lowest reliable frequency), very similar to the results obtained for the Northridge earthquake analyses.

To separate out soil and rock sites, Figures 5.49 and 5.50 show model bias and variability plots for the two recording site conditions: soil and rock. As with the point-source, due to the larger number of rock sites (33 rock verses 20 soil), the rock only and combined results are very similar. The soil sites show a near zero bias from about 0.3 Hz to 100 Hz while the rock sites show the low frequency underprediction and high frequency (10 Hz) overprediction seen in the results for all the sites (Figure 5.48). The variability for soil is low, about 0.4 from high frequency to near 2 Hz where it increases to about 0.75 with decreasing frequency. For rock sites, Figure 5.50 shows higher levels above 2 Hz and similar values as soil for frequencies below 2 Hz, not unlike the point-source results. In general however, the finite-source rock motions are larger than those of the point-source for frequencies above about 5 Hz.

For a qualitative appraisal of the response spectral predictions, Figure Set 5.51 shows the individual site spectra. Consistent with the bias estimates, the overall fit is generally good over the rather wide distance range. As with the point-source spectra, the most distant 5 rock sites (last page) show large underpredictions. Since the finite-source model incorporates crustal wave propagation effects (Ou and Herrmann, 1990), these large motions may be due to some localized effects.

To examine any systematic distance bias and to determine appropriate G/G_{max} and hysteretic damping curves, separate variability and bias estimates were computed for "near source" sites located within about 30 km fault distance. As with the Northridge earthquake, the "near source" criterion of 30 km was selected such that a minimum of 10 rock and 10 soil sites would be included (enough for meaningful comparative statistics) and that rock outcrop peak accelerations would generally be above 15 to 20%g. The last criterion was to ensure an expectation of discernable nonlinear soil site response with the EPRI (1993) (Chapter 6) modulus reduction and damping curves in the context of the generic deep soil shear-wave velocity profile.

Naturally these sites do not cover the entire province and soil conditions can vary dramatically within any province but this restricted set of stations represent those with high enough loading conditions to permit a possibility of discriminating between the EPRI and generic deep soil sets of curves (Chapter 2).

Since the empirical attenuation relations for soil, which are dominated by Peninsular Range soils (Appendix A), show significantly less nonlinearity than the EPRI curves suggest (Chapter 6) and the deep soil generic curves (Chapter 6) were derived based on the empirical soil attenuation, it is desirable to see if the modeling can resolve the appropriate degree of model nonlinearity. It was hoped that these "near source" criteria would enable selecting between either the EPRI (1993) curves or the generic deep soil curves (Chapter 6) as being more appropriate for North Coast soils.

It should be emphasized that we are treating generic conditions with the assumption that the soil

sites are, on average, similar to the generic deep soil profile and that a shear-wave velocity of about 3,000 ft/sec (bedrock) is reached, on average, at a depth of about 500 ft.

5.3.1.3.1 Assessment of Distance Bias. To consider first any significant distance bias, Figure 5.52 shows the combined sites variability and bias plots for sites within about 30 km (30 sites). The figure shows a more negative high frequency bias and lower variability than is shown for all the sites in Figure 5.48. The more distant sites are modeled less accurately than the close-in sites. To see if this is restricted to rock or soil site conditions, Figures 5.53 and 5.54 show the close-in estimates for soil and rock respectively. Comparing Figures 5.53 for the close-in soil sites and Figure 5.49 for all soil sites, the bias estimates below are similar while the variability of the close-in soil sites is generally lower. Comparing the corresponding figures for the rock sites, Figure 5.50 for all-rock sites and Figure 5.54 for the close-in rock sites show a more negative bias for the close-in rock sites (as expected) while the variability is about the same.

In general, the bias and variability estimates for the "close-in" sites is similar to all the sites. For the soil sites, the close-in sites reflect a lower variability than all the soil sites while the converse is true for the rock sites. For rock sites, the "close-in" bias shows a high-frequency overprediction for frequencies above about 4 Hz that is stronger than all rock sites due to the large underprediction at the most distant rock sites.

The "close-in" soil sites (Figure 5.53) show a slightly negative bias and low high-frequency variability indicating they are modeled reasonably well and may provide sufficient resolution to

distinguish G/G_{max} and hysteretic curves as well as to test the hypothesis of soil site linearity. The slight high frequency negative bias would be reduced through the use of a median model spectrum.

5.3.1.3.2 Assessment of G/G_{max} and Hysteretic Damping Curves. To assess the appropriate degree of soil nonlinearity in terms of implementing either the EPRI (1993) or the generic deep soil G/G_{max} and hysteretic damping curves for the North Coast soil sites, the finite-fault modeling was repeated using the deep soil (Chapter 6) curves. Figure 5.55a shows the bias and randomness estimates for all 30 soil sites computed using the generic deep soil curves. Comparing this figure with Figure 5.49 (Figure 5.55b) for the deep soil curves it is apparent that the degree of nonlinearity is discernable for frequencies exceeding about 8 Hz where the bias and randomness estimates show a significant difference. The more negative bias estimates resulting from the more linear deep soil curves reflect larger high frequency motions. To concentrate on the higher levels of loading at the "close-in" sites, Figures 5.56a and b show the estimates for the soil sites within about 30 km of the rupture. The bias is strongly negative for frequencies above about 6 Hz. The results using the EPRI curves (Figure 5.53), which show a slightly negative high frequency (> 1 Hz) bias or overprediction, appear to be more consistent with observed motions. Using a median spectrum computed over a suite of random profiles (Chapter 3) would result in somewhat lower high frequency motions reducing the negative bias by about 0.1 to 0.2 log (natural) units.

Referring back to Figure 5.8, where this issue is illustrated, the spectrum computed for the

generic smooth profile exceeds the median spectrum by about 10% on average for periods shorter than about 1 sec and about 20% for periods shorter than about 0.3 sec. The implication is straightforward in that if at each site, a median spectrum based on equivalent-linear analyses of a suite of random profiles were used as the site spectral estimate, the high frequency motions would be lower. Unfortunately, the difference in spectral level between the spectrum computed for a smooth base-case profile and a median (or mean) spectrum depends on the level of control motion. The difference increases with loading level due to the nonlinearity of the soil (Chapter 3 and Roblee et al., 1996). As a result, it is not possible to quantify or refine the G/G_{max} and hysteretic damping curves unless the profiles are randomized at each site and the median spectrum is used in the bias estimates. Qualitatively it may be concluded that the high frequency negative bias obtained using the more linear generic soil curves, reflecting about a 50% overprediction at 10 Hz, suggests that the EPRI curves are the more appropriate of the two sets. Figure 5.8 indicates that if median spectra had been computed at each site using the generic deep soil curves the negative high frequency bias estimates shown in Figure 5.53 would be reduced to near zero, or slightly positive.

5.3.1.3.3 Assessment of Nonlinear Site Response. Because the bias analyses provided sufficient resolution to discriminate between the EPRI and generic deep soil G/G_{max} and hysteretic damping curves, it is of interest to determine if a similar analysis could reject the hypothesis of linear soil site response. To provide linear site response bias estimates, the finite-source simulation was repeated constraining the number of equivalent-linear iterations to 1 as in the similar Northridge linear analyses. The resulting kappa value is 0.04 sec (Table 5.8)

which is the value determined in the inversions of the empirical attenuation relations for soil sites at small strains (Table 6.1).

The results of the linear site response analyses are compared to the equivalent-linear analyses using the best fitting EPRI curves in Figure 5.57. The bias estimates are for the "close-in" sites and the large high frequency negative bias resulting from the linear analyses is quite apparent. The abrupt departure between the linear and nonlinear bias estimates at about 3 Hz, the same frequency as in the Northridge analyses, suggests that for this suite of sites and under these loading conditions, nonlinear site response is an important consideration for frequencies exceeding about 3 Hz. Alternatively, the assumed linear kappa value of 0.04 sec may be in considerable error, by at least 100%. This seems unlikely but remains an unresolved issue until enough small earthquakes (aftershocks) are recorded at these sites to provide estimates of small strain kappa values.

Unfortunately, beyond 30 km, only 3 soil sites are available and the resulting bias estimates are too poorly constrained (90% confidence level is a factor of 2) to draw any substantial inferences about the appropriateness of the small strain kappa value of 0.04 sec. The bias estimates are high but they reflect a broad band underprediction of about 0.4 ($\pm$ 1) for frequencies above about 0.7 Hz. This is apparent in the response spectra plots for soil sites A2E, HWB, and TIB with TIB dominating the broad band underprediction. Since kappa would affect frequencies exceeding about 3 Hz (for kappa values around 0.04 sec), it is not likely that the small strain soil kappa value of 0.04 sec is seriously in error and the hypothesis of linear soil response may be rejected, although somewhat less convincingly than for the Northridge analysis.

As for the Northridge analyses, these results suggest an envelope of clear detectibility of soil nonlinearity for generic Peninsular Range and North Coast soils. Magnitudes significantly above about 6.5, distances within about 30 km (expected rock outcrop peak acceleration above about 20%g), frequencies above about 3 Hz, and, for statistical stability, at least 20 stations.

5.3.2 1979 Coyote Lake Earthquake

A total of 7 soil and 3 rock sites are modeled for the M 5.7 Coyote Lake earthquake. The sites range in distance from about 3 to 30 km (Table 5.2) and are on the westerly site of the rupture. Figure 5.58 shows the site locations with the linear string of sites comprising the Gilroy array. The low number of sites is a consequence of the small magnitude. All 10 sites in the strong motion database (Appendix B) were included in the inversions and forward modeling as they represent the "free field" sites which recorded useable data over a reasonable bandwidth.

The crustal model is from Liu and Helmberger (1983) and is listed in Table 5.9. It is the same model as used in the inversions for the slip model (Liu and Helmberger, 1983). As in the previous cases, the generic rock and soil shear-wave velocity profiles are placed on top of the regional crustal model. The kappa values beneath the shallow rock and deep soil profiles are 0.03 sec resulting in a total kappa value of 0.04 sec for both rock and soil sites (Table 5.10).

For both rock and soil sites, nonlinear zones extend to 500 ft and the soft rock and EPRI G/G_{max} and hysteretic damping curves are used for rock and soil sites respectively (Table 5.10).

The point- and finite-source model parameters are listed in Table 5.10. The best fitting rise time

is 0.36 sec and the static stress drop is 14.6 bars. The rupture surface is 10.0 x 7.6 km, 76 km^2 and is on the borderline for finite-fault modeling with M 5.0 subevents: only 9 subfaults are required. The slip model is shown in Figure 5.59.

The point-source depth is taken as 8 km and the stress drop resulting from the inversions is 70.1 bars (Table 4.3).

5.3.2.1 Point-source Inversions for Stress Drop and Kappa Values.

The Coyote Lake earthquake is included in the North Coast Province inversions (Chapter 4) along with the Loma Prieta and Morgan Hill earthquakes. The Fourier amplitude spectra are shown in Figure Set 4.3 and the site specific kappa values are listed in Table 4.3.

5.3.2.2 Point-Source Modeling Results

For all 10 sites (7 soil and 3 rock) the model bias and variability plots are shown in Figure 5.60. The bias is low, near zero, for frequencies above about 0.4 Hz, the approximate lowest frequency for which the analyses are reliable. The variability is also very low above 20 Hz (about 0.25) and rises to about 0.4 below 20 Hz. With only 7 soil and 3 rock sites, separate bias and randomness estimates are too poorly constrained to be reliable and are not shown. In general the soil sites follow closely the all sites, while the rock sites show the typical high frequency negative bias and generally higher randomness.

The response spectra plots are shown in Figure 5.61 and reflect a generally good match. Clearly

the soil sites are modeled more closely than the rock sites which show the short period overprediction. However, the effects of using the median spectrum in lieu of a single run with the base case profile is much more severe than for soil sites (Chapter 3) and would substantially reduce the rock site overprediction.

5.3.2.3 Finite-Source Modeling Results

Figure 5.62 shows the model bias and variability estimates for the finite-source model. The model bias is slightly more negative than for the point-source at high frequency (above about 4 Hz) and the ± 90% confidence limits are wider suggesting higher variability. This is shown in the variability plot which suggests that the point-source captures the site-to-site variations more accurately than does the finite-source, particularly for frequencies above about 1 Hz. These results are also clearly seen in the spectra plots (Figure 5.63) which indicates that the point-source model provides more accurate ground motion estimates for this earthquake than does the finite-source model. Too few subevents are being summed using an M 5.0 subevent to smooth out summation periodicities. Either using a smaller subevent or modifying the subevent rise time distribution would be necessary to improve the finite-source model's predictions. Neither approach is warranted as the results are considered acceptable.

5.3.3 1984 Morgan Hill Earthquake

A total of 21 soil and 8 rock sites are modeled for the M 6.2 Morgan Hill earthquake. The sites range in fault distance from about 1 to 70 km (Table 5.2). Figure 5.64 shows the site locations with the linear string of sites comprising the Gilroy array. The sites extend from San Jose (SJR)

up to the San Francisco International Airport (SFO).

The crustal model is from (Hartzell and Heaton, 1986) and is listed in Table 5.11. It is the same model as used in the inversions for the slip model (Hartzell and Heaton, 1986). As in the previous cases, the generic rock and soil shear-wave velocity profiles are placed on top of the regional crustal model. The kappa values beneath the shallow rock and deep soil profiles are 0.03 sec resulting in a total kappa value of 0.04 sec for both rock and soil sites (Table 5.12).

For both rock and soil sites, nonlinear zones extend to 500 ft and the soft rock and EPRI G/G_{max} and hysteretic damping curves are used for rock and soil sites respectively (Table 5.12).

The point- and finite-source model parameters are listed in Table 5.12. The best fitting rise time is 0.70 sec and the static stress drop is 10 bars. The rupture surface is 27.0 km long and 11.5 km wide and the slip model is shown in Figure 5.65.

The point-source depth is taken as 8 km and the stress drop resulting from the inversions is 49 bars (Table 4.3).

5.3.3.1 Point-source Inversions for Stress Drop and Kappa Values.

The Morgan Hill earthquake is included in the North Coast Province inversions along with the Loma Prieta and Coyote Lake earthquakes (Chapter 4). The Fourier amplitude spectra are shown in Figure Set 4.3 and the site specific kappa values are listed in Table 4.3.

5.3.3.2 Point-Source Modeling Results

For all 29 sites (21 soil and 8 rock) the model bias and variability estimates are shown in Figure 5.66. The bias is low and slightly negative for frequencies near 1 Hz and above and shows the typical point-source low frequency overprediction down to about 0.5 Hz, the lowest frequency of reliable analyses. The variability is higher at high frequency (near 0.5) than for the Coyote Lake earthquake and about the same for frequencies below 10 Hz.

The soil and rock site results are shown in Figures 5.67 and 5.68 respectively with the soil (21 sites) generally reflecting the all-sites results. As is usually the case, the rock (8 sites) bias estimates are more negative at high frequency (around 10 Hz) and the variability is higher than the soil.

The response spectra plots are shown in Figure Set 5.69 and reflect a reasonably good match. The soil sites are generally modeled more closely than the rock sites which show a more broad band overprediction. However, the effects of using the median spectrum in lieu of a single run with the base case profile is much more severe than for soil sites (Chapter 3) and would substantially reduce the rock site overprediction.

5.3.3.3 Finite-Source Modeling Results

Figure 5.70 shows the bias and variability estimates for the finite-source model computed over all the sites. In general, it is similar to the point-source results (Figure 5.66) but with slightly larger high frequency ($\geq$ 10 Hz) motions. The high frequency variability is lower than the point-source results but rises steeply at low frequency where peaks appear at 0.5 and at 0.9 Hz.

The peaks also occur in the point-source variability estimates (Figure 5.66) but are much less pronounced.

The soil site results are plotted in Figure 5.71 and are very similar to the all-site results due to the larger number of soil sites (21 soil verses 8 rock). The rock site bias and variability estimates, Figure 5.72, are very similar to the point-source bias results (Figure 5.68) but show a lower high frequency variability, similar to the soil site results. For this earthquake, the finite-source model is capturing additional high frequency site-to-site variability which the point-source model is neglecting.

Interestingly, the 0.5 and 0.8 Hz peak are strong in both the rock site and soil site variability estimates for the finite-source as well as in the point-source rock site results but are subdued in the point-source soil site variability estimates. The cause of these peaks is likely related to profile resonances that may be enhanced by peaks in the finite-source spectrum. If they are related to the finite-fault, site azimuth could play a role enhancing differing spectral components due to rupture propagation effects or directivity.

The effects of the profiles can be seen in the point-source spectra plots (Figure Set 5.69) for rock and soil sites. Soil site G02 (Gilroy Array N0. 2) and adjacent rock site G01 (Gilroy Array No. 1) show clear 1 sec and 2 sec profile resonances. The corresponding plot for the finite-source (Figure Set 5.73) shows an enhanced 1 sec resonance at site G02 as well as an enhanced 2 sec resonance at site G01. Both of the sites are at essentially the same azimuth, south of the rupture surface (Figure 5.64) with the rupture propagating toward them (Hartzell and Heaton,

1986). This may be a case where rupture directivity has enhanced profile resonances and clearly illustrates the need to randomize the profiles and use median spectral estimates. This would smooth out the profile resonances and provide for more robust bias and variability estimates.

5.4 MOJAVE EARTHQUAKES

The Mojave Province includes the M 7.2 Landers, and the M 6.0 North Palm Springs earthquakes. The Landers earthquake is treated first as it has the largest number of sites (Table 5.2) and widest range in levels of motion. The point-source stress drop and kappa values determined from the regional inversion are listed in Table 4.4. The regional Q(f) model determined in the regional 2-site (rock and soil) inversion is 371 $f^{0.6}$ (Chapter 4, Table 4.1).

5.4.1 1992 Landers Earthquake

For the 1992 M 7.2 Landers earthquake, a total of 57 sites are modeled: 52 soil and 5 rock. The fault distance range is about 1 km to nearly 180 km (Table 5.2). The sites extend from the Mojave desert into the Los Angeles Basin to the west (Figure 5.74). The crustal model is from Wald and Heaton (1994b) and is listed in Table 5.13. To model rock and soil sites, the generic rock or soil profile (Chapter 3) is simply placed on top of the regional crustal model. The shallow generic rock profile is truncated at velocities exceeding 1.98 km/sec, the velocity of the top layer of the Wald and Heaton (1994b) Northridge crust (Table 5.13).

Both the rock and soil sites are allowed to exhibit material nonlinearity to depths of 500 ft (Table 5.14). For the rock sites, the generic soft rock G/G_{max} and hysteretic material damping curves

(Chapter 6) are used. These curves were based on modifications to laboratory test results (Appendix D) required to model the rock site empirical attenuation (Appendix A and Chapter 6). For the soil sites, the EPRI cohesionless soil curves (Chapter 6) are used as not enough soil sites are available with sufficiently high motions to discriminate between EPRI and the generic deep soil curves. For the Peninsular range soil sites, the generic deep soil curves are used along with the Northridge crustal model (Table 5.3).

The high shear-wave velocity of the top layer of the Mojave crustal model, 1.98 km/sec, is significantly higher than either the North Coast or Peninsular Range Provinces (1.0 km/sec) and is more like CEUS conditions than WUS (EPRI, 1993). Silva and Darragh (1995) obtained an average kappa value of 0.03 sec by fitting response spectral shapes for the three Mojave rock sites LUC, 29P, SIL (Table 4.4). This values is in agreement with the 0.03 sec value obtained in the regional inversions (Table 4.1) and reflects the dependence of kappa on shallow (1 to 2 km) crustal rock properties: harder rocks are associated with lower kappa values (lower damping) than soft rock site conditions (Silva and Darragh, 1995). As a result, the kappa values for the rock beneath the nonlinear zones (500 ft, Table 5.14) at both rock and Mojave soil sites is taken as 0.025 sec. This gives a total kappa value of 0.03 sec for Mojave rock and soil sites. For Peninsular Range soil sites the rock kappa value is 0.03 sec for total small strain kappa of 0.04 sec (Table 5.4).

The finite-source model parameters are listed Table 5.14. The rise time of 1.80 sec represents a best fit over a limited set of trial values and was selected based on a visual examination of the model bias, model variability, and response spectral fits. The static stress drop, based on the

area, is about 15 bars and the point-source stress drop resulting from the inversions (Table 4.4) is 40.7 bars. The point-source depth is taken as 8 km, the depth of the largest asperity in the Wald and Heaton (1994b) slip model (Figure 5.75).

5.4.1.1 Point-Source Inversions For Stress Drop and Kappa Values

The Landers earthquake is included in the Mojave Province set along with the North Palm Springs earthquake. The Fourier amplitude spectra for both the recordings and the model predictions are shown in Figure Set 4.4 and the site specific kappa values are listed in Table 4.4. For the Mojave sites, the average rock kappa value is 0.025 sec with the average value for soil of 0.050 sec.

5.4.1.2 Point-Source Modeling Results

For the point-source model, the bias and variability plots are shown in Figure 5.76 for all the sites. Over most of the frequency range, the bias reflects a general underprediction, particularly at low frequency (around 1 Hz). The peaks and troughs are related to the profile resonances with a trough in bias reflecting a profile resonance peak. The variability is generally low, below 0.5, above 1 Hz and shows the typical increase at low frequency due to unmodeled site variations. In general, Figure 5.76 shows that the point-source is capable of surprisingly accurate ground motion predictions for an M 7.2 extended rupture and for distances out to nearly 200 km (Table 5.2).

Because there are only 5 rock sites (3 within about 90 km, Figure 5.79) out of 57 total sites separate plots are not shown for rock site and soil sites analyses. In general, the rock sites show

a broadband negative bias that is controlled by 2 sites 29P and SIL (Figure 5.79).

To examine more closely the positive bias (underprediction) shown over all the sites (Figure 5.76), separate bias and variability estimates are shown computed for the Peninsular Range sites and Mojave sites alone. Figure 5.77 shows the results for the Peninsular Range sites, beginning with site POM at about 120 km (Figure 5.79). The figure shows a much more positive bias, except around 3 to 20 Hz where the bias is considered low. The increase in bias estimates at very high frequency, above 20 Hz actually reflects peak ground acceleration and is controlled by much lower frequencies; in the range where the response spectral accelerations peak over these distances, 100 to 200 km. The model bias then shows a large low frequency ($\leq$ 3 Hz) underprediction averaging about 0.5, a factor of about 1.6. This low frequency underprediction is apparent in the spectral plots, Figure 5.79, especially for the very distant sites beyond about 150 km. This feature is very similar to the intermediate period underprediction seen in the point-source model comparisons to empirical attenuations for M 7.5 at distances 100 and 200 km (Chapter 6, Figure Sets 6.10 and 6.11). Since the Peninsular Range sites are all soil (Figure 5.09), basin effects are suspected but, in the comparison to the empirical attenuation (Chapter 6), the same underprediction was present for both rock and soil sites. It is obviously an aspect of wave propagation not accounted for in the point-source model and may be related to intermediate to short period surface wave development or 2-D effects in crossing province boundaries with very different crustal structures.

To complete the picture, Figure 5.78 shows the analyses for the Mojave Province sites only. The distance range is about 1 to 100 km, site POM (Figure 5.79) is the first soil site in the

Peninsular Range province, and the bias estimates are near zero above 1 Hz and show the typical point-source overprediction below 1 Hz. The variability is low, about 0.5 above 0.5 Hz, suggesting that the model is performing quite well on average out to 100 km. These results are in general agreement with the empirical comparisons which indicate that the distance underprediction is magnitude dependent, increasing with increasing magnitude.

While not many data constrain the empirical attenuation relation for distances beyond 100 km for M larger than 7, the Landers results along with the empirical comparisons (Chapter 6) suggest caution in applying the point-source model for M larger than about 7¼ and for distances greater than 100 km. For these cases there is a reasonably high likelihood that the predictions could be low for frequencies below about 3 Hz, unless a high stress drop was used as compensation. This is of little consequence for WNA where the hazard is dominated by much closer sources but could be an issue in CEUS. If the underprediction is related to wave propagation effects not accommodated in the currently implemented point-source model, the same conditions may or may not apply in typical CEUS crustal structures. This is an important issue to resolve and the next section on the finite-fault model results will produce some useful insights.

Figure Set 5.79 shows the spectra plots and indicates that the point-source simulations do very well within about 100 km and begin to seriously underpredict (at low frequency) beyond. Interestingly, site LUC, at a fault distance of about 1 km from an 80 km long rupture (Table 5.14) is modeled very well by the simple point-source for periods as long as to 10 sec (The

Lucern recordings have been processed to retain appropriate long period energy (Bill Iwan, personal communication).

5.4.1.3 Finite-Source Modeling Results

For all 57 sites, the bias and variability estimates are shown in Figure 5.80. Overall the bias is lower than for the point-source (Figure 5.76) with a broad positive peak in the 1 to 3 Hz range. The bias corrected variability is also lower throughout most of the frequency range suggesting the finite-source is capturing more site-to-site variations in the recorded motions.

To examine the Peninsular Range sites only, Figure 5.81 can be compared to the point-source results shown in Figure 5.77. For the finite-source, the bias is much lower, particularly at low frequency ($\leq$ 1 Hz) where the bias has decreased by 100%, from about 0.6 to around 0.3 (the profile resonances in the bias estimates would be smoothed out using a median response spectrum for each site). The randomness has also decreased substantially however the bias corrected estimates are essentially the same indicating that the source finiteness is not capturing more site-to-site variation but is simply producing larger motions beyond 100 km an average. These results are in agreement with the discussion on Attenuation With Distance in Chapter 6. The effects of source finiteness has a strong impact on the attenuation of motion with distance or far field slope (fall off beyond 1 source depth). Large source areas have a smaller slope simply due to the effects of finiteness. This feature is demonstrated in Chapter 6 and is consistent with the strong motion data. It is quite apparent in the Landers analyses for sites beyond about 100 km.

Returning to the point- and finite-source bias estimates for the Peninsular Range sites (Figures 5.77 and 5.81), although the underprediction has been substantially reduced with the finite-source, a significant positive bias (about 0.3) exists for frequencies below about 3 Hz. To see if this is also the case for the closer sites ($\leq$ 100 km), Figure 5.82 shows the bias and variability estimates computed over the 18 Mojave Province sites. The bias results are very similar to the point-source (Figure 5.78) and show a near zero bias above 1 Hz and a sharp fall off to overprediction below. Above about 5 Hz, the finite-source randomness is much lower than the point-source indicating that within 100 km, the finiteness is capturing aspects of site-to-site variation unmodeled in the point-source simulations.

The low frequency negative bias in both the point- and finite-source simulation results is intriguing. It is expected in the point-source and was present to a much lesser extent in the Northridge earthquake analyses (Figure 5.9). It may simply be related to including low velocity materials above the crustal models. The finite-fault low-frequency decrease in bias begins around 1 Hz, the approximate high frequency limit in the inversions for slip which use the crustal models without surficial materials. Neglect of the soil column amplification (the inversions are generally dominated by soil sites) results in a factor of about 2 over rock at 1 Hz (Figures 6.4 and 6.5). It would be of interest to use the stochastic finite-fault model, which incorporates site effects and material nonlinearity in slip model inversions. The result would likely reduce the low frequency bias by perhaps broadening the asperities.

The finite-source plots are shown in Figure 5.83 and generally reflect a good overall fit to the recorded motions. The distant motions, beyond about 100 km (Peninsular Range soil sites begin

with site POM) show the tendency to underpredict for periods longer than about 0.3 sec, the trend clearly seen in the bias estimates at about 3 Hz and below (Figure 5.81). This tendency is not nearly as severe as in the point-source spectra plots (Figure 5.79) and, with the bias estimates, indicates that source finiteness has not completely resolved the issue of low frequency underprediction beyond 100 km (the Peninsular Range sites). The underprediction may be generic or related to a region specific 2-D crustal path effect in propagating from the Mojave crust to the Northridge crust. The relatively broad band nature of the underprediction, below about 4 Hz and with a broad peak in the 1 to 3 Hz range, does not suggest basin effects. Also the comparisons to the empirical attenuation (Chapter 6) showed the point-source underprediction for M 7.5 at 100 and 200 km occurred for both rock and soil sites.

The underprediction issue for both the point- and finite-source models is potentially important for ground motion predictions for large magnitude earthquakes at distances exceeding about 100 km, and for frequencies below about 3 to 4 Hz.

5.4.2 1986 North Palm Springs Earthquake

The M 6.0 North Palm Springs earthquake modeling includes a total of 29 sites, 20 soil and 9 rock (Table 5.2). The distance range is about 1 to 90 km. Figure 5.84 shows the site map with the majority of stations located to the southwest of the rupture. The crustal model is from Hartzell (1989) and is listed in Table 5.15. As usual, the generic rock and soil profiles are placed on top of the regional crustal model. The shallow generic rock profile is truncated at a velocity of 1.7 km/sec, the velocity of the top layer of the Hartzell (1989) crustal model.

Both rock and soil sites are allowed to have nonlinear response to depths of 500 ft. For rock sites the G/G_{max} and hysteretic damping curves for generic rock (Chapter 6) are used while the EPRI curves are used for the cohesionless soils as with the Landers earthquake, a kappa value of 0.025 sec is used for the rock beneath the profiles to give a total small-strain kappa value of 0.03 sec for both rock and soil sites (Table 5.16).

The finite-source model parameters are listed in Table 5.16. The rise time of 0.45 sec represents a best fit over a suite of several trial values. The rupture area is large, 22 km by 15 km, giving a static stress drop of only 4.5 bars. The point-source stress drop is 62.8 bars (Table 5.16). Because the fault dips 46° to the northeast stations WWT and NPS are located over the rupture surface.

The slip model used is based on the use of aftershocks as Green functions and results basically in a single large asperity at a depth of about 10 km (Hartzell, 1989). The best fitting slip model resulting from the use of synthetic Green function contains a number of distributed asperities, some shallow, and results in a large high frequency ($\geq$ 1 Hz) underprediction by about 80%. Since the slip model inversions are for frequencies less than 1 Hz, this large difference in the high frequency motions between the two slip models was not apparent to Hartzell (1989). Because the slip model resulting from the empirical Green function inversions provided the closer high frequency fit, it was adopted for the analyses. Additionally, the current analyses incorporate shallow rock and soil shear-wave velocities while the synthetic Green functions were computed for the basic crustal model with a surface velocity of 1.7 km/sec. As a result, the use of the slip model based on the empirical Green functions is considered more consistent with the

current analyses. As the Landers earthquake analyses indicated, it would be of considerable interest to determine slip models for these earthquakes using the broadband stochastic finite-fault which accommodates nonlinear site effects in an inversion mode.

5.4.2.1 Point-Source Inversions For Stress Drop and Kappa Values

The North Palm Spring earthquake is included in the Mojave Province set along with the Landers earthquake. The Fourier amplitude spectra for both the recordings and the model predictions, are shown in Figure Set 4.4 and the site specific kappa values are listed in Table 4.4. For the Mojave sites, the average rock kappa value is 0.025 sec and the corresponding soil kappa value is 0.058 sec.

5.4.2.2 Point-Source Modeling results

Bias and variability estimates are shown in Figure 5.86 computed over all 29 sites for the point-source using a stress drop of 62.8 bars. The bias shows the typical negative low frequency point-source overprediction with the low frequency limit for reliable analyses at about 0.5 Hz. At higher frequency, the bias is positive indicating a slight underprediction. The variability plot shows values larger than for the Landers earthquake, about 0.5 from about 2 to 100 Hz.

For the 20 soil and 9 rock sites, Figures 5.87 and 5.88 show the corresponding analyses. As expected, due to the larger number of soil sites, the soil site results are very similar to all the sites. The rock sites however show a high frequency underprediction or negative bias of nearly 0.4 (factor of 1.4) above about 6 Hz. The rock site variability is higher than for the soil, which is not unexpected, and is quite poor below about 4 Hz.

The response spectra plots, Figure 5.89 also show the generally poor results at the rock sites while most of the soil sites are modeled reasonably well. Results of similar quality were obtained by Hartzell (1989) who attributes the difficulty in modeling this earthquake to the "extremely complex and varied geology".

5.4.2.3 Finite-Fault Modeling Results

Figure 5.90 shows the bias and variability estimates for the finite-source model over all the sites. The overall bias is positive above about 0.5 Hz and the point-source low frequency overprediction is not present. The variability is high however, about 0.6 throughout much of the reliable frequency range. The randomness is also high reflecting unmodeled site-to-site variation that is larger than the point-source for frequencies exceeding about 1 Hz (Figure 5.86).

For the soil and rock sites separately, Figures 5.9 and 5.92 show the bias and variability estimates. As with the point-source results, the soil is near zero and the rock shows a strong underprediction at high frequencies.

The spectra plots, Figure Set 5.93, reflect the generally acceptable fit to the soil sites and rather poor results for the rock sites. Even the results for the soil sites are perplexing. For example sites NPS and MVF are both soil, nearly over the rupture surface (Figure 5.84), and at about 10 km fault distance (Appendix B) yet there is a difference of at least 3 in recorded peak accelerations. Site NPS look more like a rock spectrum and MVF has very large 2 sec motions that the finite-fault modeling is not capturing. Based on both the point- and finite-source modeling results, it is comforting that a highly regarded colleague (Hartzell, 1989) experienced

similar difficulties with this earthquake.

5.5 1978 TABAS EARTHQUAKE

Data from only 4 sites are available for the M 7.4 Tabas earthquake: 3 rock and 1 soil. The fault distance range is about 3 to 90 km Table (5.2) and the site distribution is shown in Figure 5.94. The crustal model is listed in Table 5.17. The model is from Hartzell and Mendoza (1991) and is about 45 km thick, much thicker than typical California models (Chapter 3, and Table 5.3). It also has a high velocity surface layer (1.65 km/sec). Both aspects make it more like typical ENA crustal models than WNA (EPRI, 1993) and low kappa values (Silva and Darragh, 1995) might be expected to result from the inversions.

For both the rock and soil models, the generic shallow shear-wave profiles were placed on top of the Hartzell and Mendoza (1991) crust. Because the inversions did not show low ENA type kappa values for the rock sites (Table 5.18), a standard WNA value of 0.03 sec was used for the rock beneath the soil profiles (Table 5.19). Although the shear-wave velocity of the top crustal layer is about 5,400 ft/sec (Table 5.17) and would be expected to reflect a lower kappa value, the results from the inversions and modeling, limited by only 4 sites (3 close-in), suggest nominal WNA conditions. In this context, the Q_0 was fixed at 291, the value resulting from the combined WNA inversions (Table 4.1).

As with the previous earthquakes, nonlinear zones extend to 500 ft for both rock and soil sites (Table 5.19). The G/G_{max} and hysteretic damping curves are the same for the soft rock sites but the EPRI curves are used for the soil site (BOS) as well as all non-Peninsular Range cohesionless

soil sites (the Imperial Valley, Section 5.6, required more linear curves than the generic deep soil). In this case, with only one soil site and with relatively low motions, either set of curves would provide about the same results. Unless the ground motion data clearly demand more linear response such as in the Northridge earthquake, the EPRI curves are preferred, since they are based on laboratory testing (Chapter 6) and provide good results with the North Coast Loma Prieta earthquake (Section 5.3).

The finite-fault parameters are listed in Table 5.19. The slip model is from Hartzell and Mendoza (1991) and is shown in Figure 5.95. The rupture surface strikes 33° and dips 25° to the NE with a rake of 114°. The rise time is 3.53 sec based on several trial values and the subevent stress drop is fixed at 5 bars. The low subevent stress drop (nominally about 30 bars using the rupture area verses magnitude relation in Chapter 2) was found to be necessary for earthquakes with significant amounts of shallow slip (Chapter 2). The nominal 30 bar subevent stress drop results in short period motions a factor of 2 to 3 too large. The 5 bar value is based on an extensive modeling exercise for the Landers earthquake examining the effects of slip and depth dependent rise times as well as slip velocities. The simple, non-physical, lowering of the subevent corner frequency produced the best overall results but leaves the issue of how to model short period motions from shallow slip physically unresolved.

The static stress drop is 12.3 bars and the point-source stress drop is 21.5 bars (Table 5.19).

5.5.1 Point-Source Inversions for Stress Drop and Kappa Values

As with the Province inversions (Chapter 4), smooth transfer functions are incorporated for the

rock and soil sites. The rock sites include the generic shallow soft rock profile and the soil sites the generic deep soil (Chapter 3): both overlie the Hartzell and Mendoza (1991) crust (Table 5.17).

Results of the 4 station inversions are shown in Table 5.18. The average kappa value is 0.046 sec with the average of the 3 rock sites of 0.040 typical WNA values. The kappa values are a bit higher but in general agreement with those of Shoja-Taheri and Anderson (1988). The higher values obtained in this work reflects the inclusion of crustal and site amplification. The stress drop is low, about 22 bars (Table 5.18). If the rock sites are very hard, as the crustal model suggests, not using a transfer function which includes the shallow soft rock profile would result in lower kappa values and a higher stress drop. There are simply too few data (sites) and poorly known site conditions to resolve this issue.

The fits to the Fourier amplitude spectra are shown in Figure 5.96 and are good at high frequency (> 3 Hz) for the 3 close-in sites. The distant site (FER) appears to have a strong amplification from about 1 to 10 Hz. The fits at low frequency are poor and using the log average spectra (equal weighing with frequency, Chapter 4) does not offer any improvement: the stress drop decreases to 14 bars and the average kappa decreases to 0.031 sec.

The slip model is largely driven by teleseismic data as only 3 strong motion sites were used in the slip model inversion (Hartzell and Mendoza, 1991). The large misfit seen in the point-source Fourier amplitude spectrum (Figure 5.96) at site TAB is also poorly fit in the Hartzel and Mendoza inversion and in the modeling of Saikia (1994) as well. Because of the few close-in

data (3 sites) and poorly known site conditions as well as crustal structure, the slip model may simply be poorly known.

5.5.2 Point-Source Modeling Results

Figure 5.97 shows the point-source bias and randomness plots. With only 4 sites, little information is contained in the estimates as the range in the ± 90% confidence limits suggest. The bias is essentially zero but again showing the low frequency (<1 Hz) point-source overprediction. The model variability is high and somewhat uniform at about 0.8.

The response spectra are shown in the next figure (Figure 5.98) and appear to capture the spectral shapes reasonably well. Perhaps a more refined distance measure accommodating the effects of sites located over dipping faults would improve the fit (reduce the variability, Chapter 4).

5.5.3 Finite-Source Modeling Results

The bias and variability estimates for the finite-source are similar to the point-source and are shown in Figure 5.35. The finite-source bias is more positive than the point-source for frequencies above 1 Hz and remains high at low frequencies reflecting a broad-band underprediction. The variability is the same as well, about 0.8, over most of the frequency range.

The response spectra are shown in Figure 5.100 and indicate a generally good fit except at site TAB. Eliminating this site results in a near zero bias from 0.1 to 100 Hz and significantly

reduces the variability. The large underprediction at this site drives the bias and variability estimates and suggest, due to its wideband nature, a generic problem with the slip model, station location, or instrument.

Except for site TAB both the point- and finite-source models perform reasonably well. The point-source overpredicts at the three sites which the finite-source models very well. This is probably due to too high a stress drop resulting from the inversions as the single site, TAB with high recorded motions, would have a large effect representing 25% of the data.

5.6 IMPERIAL VALLEY EARTHQUAKES

The analyses for the 1979 Imperial Valley earthquakes include the M 6.4 mainshock and the M 5.3 (Liu and Helmberger, 1985) aftershock. For the mainshock 33 soil and 2 rock sites are modeled, covering the distance range of about 1 to 50 km (Tables 5.2 and 5.22). The aftershock includes 16 soil sites (no rock site data are available) over the fault (hypocentral) distance range of about 12 to 52 km (Tables 5.2 and 5.23). For the mainshock, the site location map is shown in Figure 5.101.

The crustal model is from Liu and Helmberger (1980) with the top 98m replaced by a smoothed version of the El Centro profile (Bycroft, 1980). The shallow profile is based on downhole borehole measurements taken at the old El Centro strong motion site (new E09) and is listed in Table 5.20. The top 500 ft of the profile is shown in Figure 5.102 and the entire crustal model is shown in Figure 5.103. The crustal model (except for the top 93m) is the same model used

in the Liu and Helmberger (1985) study of the M 5.3 aftershock and is very similar to the crustal model used by Hartzell and Heaton (1983) in their inversions for the M 6.4 mainshock slip model. For rock sites, the shallow generic rock profile replaces the top 2.4 km of the generic Imperial Valley profile where the shear-wave velocity reaches 1.0 km/sec (Figure 5.103). This velocity occurs at a depth of about 100 ft (34m) in the generic rock profile (Figure 3.2)

In a similar manner as the other analyses, nonlinearity is permitted to depths of 500 ft in both the rock and soil profiles (Table 5.21). For the soil site, the shear-wave velocity at 500 ft is only 1,312 ft/sec (Table 5.21, Figure 5.102) and, with this stiffness, considerable nonlinear response would be expected at even greater depths under the 1979 M 6.4 loading conditions (over 50%g at some soil sites). It is assumed that the soils at greater depths are too dense to exhibit significant nonlinearity and are constrained to have linear response.

For the rock sites, the generic soft rock G/G_{max} and hysteretic curves are used. For the soil sites, analyses with the EPRI and generic deep soil curves showed too much nonlinear response and a separate set of curves are developed. Since the Imperial Valley soils generally consist of clays with classifications ranging from CL to CH and silty dense sands to at least 400 ft (NUREG, CR-1643), it is not surprising that the curves for cohesionless soils appear to be inappropriate. What is surprising however, is the small degree of nonlinearity shown in the soils, substantially less than the cohesive soil curves of Vucetic and Dobry (1991) would predict for this PI range, about 10 to 40% (Turner and Stokoe, 1982). Unless some modification of the

Vucetic and Dobry (1991) curves were made for the effects of confining pressure, use of their curves, as well as the EPRI and generic deep soil curves, greatly overdamp the motions.

The kappa values beneath the nonlinear zones is taken as 0.02 sec. This gives a total small strain kappa value of 0.03 sec for both the rock and soil sites. The soil site kappa value of 0.03 sec is based on Durward et al. (1996) who found a kappa value of 0.03 sec at low levels of ground motion by analyzing 24 earthquakes recorded at and near the El Centro array in the Empirical Valley.

For the rock site, the total kappa value is also 0.03 sec using a kappa of 0.02 sec for the materials below about 500 ft where the shear-wave velocity is 3,773 ft/sec in the Liu and Helmberger (1985) crust. The kappa values of 0.02 sec and 0.03 sec are not constrained by any local or regional data and a total kappa value of 0.04 to 0.05 sec would be more consistent with the empirical inversions as well as Peninsular Range rock sites. However, it is a bit difficult to imagine a kappa of 0.03 to 0.04 sec to be associated with rock with shear-wave velocities close to 4,000 ft/sec and higher while 0.02 sec is constrained for soil materials with velocities of 1,300 ft/sec: both at depths of about 500 ft. Since there are only 2 rock sites, the issue is not significant and assuming 0.02 sec results in the same low strain total kappa value of 0.03 sec for both rock and soil sites.

The finite-source model parameters are listed in Table 5.21 and the Hartzell and Heaton (1983) slip model is shown in Figure 5.104. The slip model largely consists of a single dominant asperity at a depth of about 8 km located almost directly beneath site EMO (Meloland Overpass,

Figure 5.101). The slip model has a considerable amount of shallow slip resulting in the use of a subevent stress drop of 5 bars. This is consistent with the Landers and Tabas earthquakes and is necessary to keep from dramatically overpredicting the high frequency ($\geq$ 1 Hz) motions. The rise time of 0.73 sec is a best fit over a limited number of trial values. The static stress drop is 12.6 bars and the point-source value from the inversion is 23.2 bars (Table 5.22). The point-source depth is taken as 8 km for the mainshock and 9.5 km for the aftershock (Liu and Helmberger, 1985).

5.6.1 Point-Source Inversions for Stress Drop and Kappa Values

In the inversions for stress drop and kappa values, smooth mean transfer functions are used to incorporate amplification appropriate for the Imperial Valley soil and rock sites. Magnitudes are held fixed (Chapter 4). The Q(f) model is also fixed at the Peninsular Range value of 264 for an η fixed at 0.6 (Table 4.1), as the distance range is too small to constrain the Q(f) models.

The point-source inversion results, stress drop and kappa values, are listed in Tables 5.22 and 5.23 for the mainshock and aftershock respectively.

Due to nonlinear site effects, the inversions consider the mainshock and aftershock in separate analyses as the same kappa value at a common site may not be appropriate for both earthquakes. This effect can be seen in the kappa values for the 2 common sites which experienced the highest motions during the mainshock: sites E07 and E06. The sites straddle the Imperial fault (Figure 5.101) and have average kappa values of about 0.07 sec for the mainshock (Table 5.22) and

about 0.04 sec for the aftershock (Table 5.23), a significant difference.

The stress drops are low, about 23 and 29 bars with the aftershock value slightly larger than the mainshock stress drop. Interestingly, the shallow slip events which require low subevent stress drops (Landers and Tabas) seem to have low point-source stress drops as well. The average kappa values over all the soil sites are 0.050 sec for the mainshock and a slightly lower value of 0.042 sec for the aftershock.

The fits to the Fourier amplitude spectra for the mainshock and aftershock are shown in Figure Sets 5.105 and 5.106 over the frequency range used in the inversions. For the mainshock, Figure Set 5.105, the overall fits are reasonably good over most of the bandwidths with some features of interest in the close-in sites. The closest sites, EMO, E07, and E06 show a large low frequency (0.3 Hz) peak which is absent in the two following close-in sites AEP and AGD. The close-in sites which do not have the low-frequency peak are to the south of the northward propagating rupture while sites EMO, E07, and E06 are in the direction of rupture propagation. The low frequency peak is the result of rupture directivity and is quite strong for these sites adjacent to the rupture surface. As the El Centro array sites move outward, away from the rupture, the peak diminishes slowly until beyond about 15 km where it diminishes rapidly (sites E02 and E12). A similar trend is not seen in the high frequencies suggesting that directivity is predominately a low frequency phenomenon (Silva, 1992). While nonlinearity would reduce the effects of directivity at high frequencies (Bill Joyner, personal communication), the surprisingly low degree of nonlinear response at these sites (except for sites EMO and E07) indicates that soil nonlinearity may not be reducing high frequency directivity effects to a significant degree.

Similar plots for the aftershock are shown in Figure Set 5.106. As with the mainshock, the fits are generally good with most of the reliable data at frequencies of 1 Hz and above. For both earthquakes, site DTA (DLT in the mainshock) are poorly fit. The model severely underpredicts the motions over a wide bandwidth resulting in anomalously low kappa values. In the forward modeling with both the finite (mainshock only) and point-sources the fit is equally poor. The reason for these underpredictions is not known.

5.6.2 Point-Source Modeling Results

5.6.2.1 M 5.3 Aftershock

Figure 5.107 shows the model bias and variability estimates computed over all 16 sites for the aftershock. The bias is near zero above 1 Hz (the low frequency limit of reliable analyses) to about 10 Hz and positive (about 0.2) above. The variability is nearly constant at about 0.5 from about 1 Hz to 100 Hz. This is not considered high as small magnitude earthquakes show more site-to-site variability than do large ($M \geq 6.5$) earthquakes (Appendix A).

The response spectra plot are shown in Figure Set 5.108 and reflect a generally good fit out to about 1 sec. The high frequency underprediction is largely driven by site DLT, which shows a peak acceleration underprediction of more than a factor of 3.

5.6.2.2 M 6.4 Mainshock

For the mainshock, Figure 5.109 shows the point-source model bias and variability plots computed over all 35 sites. The bias is small from about 0.2 Hz (the lower limit of the data)

to 100 Hz. The variability is also low for a small magnitude and is fairly uniform at about 0.5 over most of the frequency range.

Considering just the 33 soil sites, Figure 5.110 shown the corresponding bias and variability estimates. The bias is less positive and the variability has dropped slightly indicating a general improvement. The 2 rock sites (CPR and SOP) are poorly fit with large underpredictions, which can be seen the response spectra plots in Figure Set 5.111. For the soil sites, the predicted spectra provide a reasonably good match to the recorded motions with the exception of site DTA, which also shows a large and broadband underprediction.

Sites EMO and E07, the first 2 plots in Figure Set 5.111, show a mismatch in the spectral peaks between the simulations and recorded motions indicating too little nonlinear response in the equivalent linear analyses. These 2 sites appear to have undergone the greatest degree of nonlinearity and the derived G/G_{max} and hysteretic damping curves are probably too linear for these sites. However, for the remaining sites, the computed motions appear to capture the shapes and overall levels of the recorded motions reasonably well. The spectral peaks in the other close-in sites (E06, AEP, AGR, and E05) are near 0.2 sec in both the recorded and simulated motions.

A constraint on the possible nonlinearity is also possible by comparing the peak response in the aftershock spectra to those of the mainshock. At sites E06 and E07 for the aftershock (Figure Set 5.111) the peak spectral amplification is in the 0.2 to 0.3 sec range and shifts to about 0.6 to 0.8 sec during the mainshock for the 2 closest sites: EMO and E07 (examining the spectral

peak computed using the mainshock coda should show the peak shift back to shorter periods, Silva et al., 1986). At sites E06, E07, and E08 the peak response shows little or no shift between mainshock and aftershock indicating little increase in nonlinearity between the mainshock and aftershock. Profile randomization and use of the median spectrum will result in a shift of the peak response to longer periods (Figure 3.5) but not to the extent required to match the recorded motions of the mainshock shown in Figure Set 5.111. The result being that sites EMO and E07 appear to require more nonlinear curves than the remaining El Centro sites and there is little to suggest that they were subjected to significantly larger motions than sites E06 or E08, only 1 to 3 km more distant (Figure 5.10).

5.6.2.2.1 Development G/G_{max} and Hysteretic Damping Curves The sites of the El Centro array (including sites EMO and HVP) with peak accelerations ranging from about 12%g to 50%g are used to develop a set of G/G_{max} and hysteretic damping curves that are consistent with the assumed generic Imperial Valley profile and recorded motions.

The Imperial Valley earthquake effective source zone consists of a single large asperity located nearly directly below the El Centro array. Possibly because of this, the point-source model produces more accurate modeling results (lower bias and variability) than the finite-source model, particularly over the El Centro array. As a result, it is used to generate the control motions in the development of the modulus reduction and damping curves.

To assess the degree of nonlinear response across the 15 sites of the study array as well as the

effects of the EPRI and generic deep soil curves on the simulated motions, Figure 5.112 shows bias estimates for the suite of analyses. In the context of the assumptions in the analyses, the EPRI and generic deep soil curves show considerably more nonlinear response than appears appropriate and the linear analysis, with a constant kappa value of 0.03 shows sec a negative bias for frequencies above about 5 Hz. There is a strong contribution to this overprediction by sites EMO and E07 and the bias estimates indicate that most of the sites exhibited small degrees of nonlinear response.

A series of analyses using various suites of curves resulted in a depth dependent set with separate curves for 0 to 300 ft and beyond 300 ft. The curves are shown in Figure 5.113 and are intended to provide the best overall fit to the study site data. They result in a slightly positive bias (Figure 5.112) which would increase only slightly with randomization as the generic profile COV of about 0.4 (Appendix C) would be reduced to about 0.2 reflecting deep sites located in the same depositional environment.

Recent application of the profile correlation model to over 100 measured shear-wave velocity profiles at the Department of Energy Savannah River Site has shown a significant reduction in the profile shear-wave velocity COV over the generic value of about 0.4. This occurs for sites located kilometers apart and appears to be a result of similar depositional environment. There is another reduction in COV in going from the km scale to footprint scale (tens to hundreds of feet) which is much less dramatic. These results are important and show two step reductions in deep soil profile variability: a factor of 100% in going from generic (all North America) to km scale separation within the same depositional environment and another, smaller reduction

over scales of tens to hundreds of feet (Gabe Toro, personal communication).

As a result of the reduced COV expected for the Imperial Valley study sites, the slightly positive bias resulting from the Imperial Valley analyses with the curves is considered acceptable. The curves are likely too linear for sites EMO and E07 but appear to be appropriate for the other 13 sites (Figure 5.111).

The variability estimates over the study sites (Figure 5.112) is low, less than about 0.4 over the frequency range of reliable data (above about 0.2 Hz). In general the point-source model performed quite well for both the mainshock and aftershock at most of the sites.

5.6.3 Finite-Source Modeling Results

Figure 5.114 shows the bias and variability estimates for the finite-source model computed over all 35 sites. The bias is positive (about 0.2) at 2 Hz and above and the variability is uniformly high (0.6 to 0.7) over the entire bandwidth. Both the bias and variability estimates for the finite-source are larger than the point-source (Figure 5.109) indicating it is doing a poorer job of fitting the data.

As with the point-source model results, the rock sites (CPR and SUP) are underpredicted by a considerable degree and the bias and variability estimates improve slightly considering only the soil sites (Figure 5.115). In general, the point-source results are significantly better than the finite-source results and the reason for this difference is apparent in the plot of the response spectra, Figure Set 5.116. For sites in the direction of rupture EMO, E07, E06, E05, E08, etc.

both the point- and finite-source models give comparable results (Figure Sets 5.115 and 5.111). However for the sites which are located in the opposite azimuth, such as AEP, AGR, BCR, SHP, etc., the finite-source model shows consistently lower short period motions than the point-source simulations with a large underprediction of the recorded motions at short periods ($\leq$ 1 sec). Since the slip models are determined at periods exceeding about 1 sec this observation brings up the important issue that the sources of short period ($\leq$ 1 sec) radiation may not, under all circumstances, coincide with the sources of long period ($\geq$ 1 sec) radiation. Inversions for slip models using a broadband finite-fault source model with nonlinear site effects may reveal non-coincident sources of short and long period energy. The Imperial Valley modeling results suggest that the sites located to the southeast of the asperity may require additional source(s) of short period energy located at closer distances.

5.7 1985 NAHANNI EARTHQUAKE

The M 6.8 December 23, 1985 Nahanni earthquake occurred in western Canada but is considered to have important features in common with ENA earthquakes: thrust mechanism with regional compressive stresses, area of low seismicity rates, and a high velocity crust (Hartzell et al., 1994). As a result, the Nahanni earthquakes are generally considered to be ENA analogues and representative of source, path, and site characteristics to be expected in geographical ENA. Because of this, low kappa values are expected (Silva and Darragh, 1995) and the Q(f) model determined in the Saguenay inversion (Section 5.9) is used.

Only 3 sites, all hard rock, recorded this earthquake and all are within about 16 km of the rupture surface (Table 5.2). Figure 5.117 shows the site map with sites S1 and S2 located over

the fault rupture. The rupture surface dips 25° to the southwest and the top edge is at a depth of 4 km (Hartzell et al., 1994). The slip model is shown in Figure 5.118 and consists of 2 large asperities at depths of about 4 and 8 km (the hypocenter). Consistent with the modeling results for other earthquakes with significant shallow slip; Landers, Tabas, and Imperial Valley, the subevent stress drop is taken as 5 bars.

The crustal and source models are from Hartzell et al. (1994). The crustal model is listed in Table 5.24 and the source parameters are listed in Table 5.25. Because the sites are all hard rock and an appropriate shallow rock profile is unavailable, linear site response analyses are done in the modeling using the site specific kappa values resulting from the point-source inversion (Table 5.26).

The source rise time is 1.15 sec and both the static and point-source stress drops are about 13 bars (Table 5.25). The low stress drops are consistent with those of the other earthquakes with significant shallow slip, generally less than about 20 bars. Since 2 of the 3 sites are over the rupture surface, the point-source depth is taken as 4 km, the depth of the shallowest asperity.

5.7.1 Point-Source Inversions for Stress Drop and Kappa Values

As with the previous inversions, a smooth transfer function is used to accommodate the amplification of the Hartzell et al. (1994) crustal model (Table 5.24) from 8 km (depth of largest asperity, Figure 5.119) to the surface. The Q(f) model is fixed at 317 $f^{0.6}$, the best fit values from the Saguenay earthquake inversion (Section 5.9).

The results of the inversion are shown in Table 5.26. The point-source stress drop is low, 13.4 bars, and the kappa values average 0.016 sec, consistent with the average value of 0.012 sec found by Silva and Darragh (1995) for the same sites from eyeball fits using templates of response spectral shapes.

For this earthquake, because of the low kappa values and short distances, the bandwidth is extended to 50 Hz in the inversions. Results using a constant log (df) (frequency spacing) to produce even weighing across the bandwidth (Chapter 4) resulted in a lower stress drop (about a factor of 2), lower kappa values, and a poorer fit. The fits to the Fourier amplitude spectra are shown in Figure 5.119 over the frequency range used in the inversion. As usual, the point-source model is high relative to the recorded motions at low frequency and in general agreement at intermediate to high frequency. The large underprediction at site 1, averaging over a factor of 2 around 3 Hz is due in large part to the inclusion of the "moose kick" which occurred about 9 seconds into the record. This arrival, at just over 1g, is not present at the other 2 sites and is believed to have a very localized source beneath or adjacent to site 1. Similar difficulty was experienced by Hartzell et al. (1994) in modeling the records at this site.

5.7.2 Point-Source Modeling Results

For the point-source model, the spectra plots are shown in Figure 5.120. Sites 2 and 3 show reasonable agreement to the recorded motions but are high at long period and underpredict at short period. Site 1 shows the large underprediction present in the Fourier amplitude spectra.

The bias and variability estimates (Figure 5.121) are unconstrained but reflect the generally fair

fits obtained over all three sites.

5.7.3 Finite-Source Modeling Results

For the finite-source model, spectra and bias and variability plots are shown in Figures 5.122 and 5.123. The results are similar to those of the point-source, with a slight improvement at sites 1 and 3 but a broadband overprediction at site 2. The bias is lower at high frequencies but because neither the bias nor variability estimates are constrained, the difference between the point- and finite-source model is not resolvable.

In general, for both models, the fits may be considered fair, a similar conclusion reached by Hartzell et al. (1994) from their waveform modeling results.

5.8 1987 SUPERSTITION HILLS(B) EARTHQUAKE

The 1987 Superstition Hills earthquake modeled is event (B) which is the larger of the two earthquakes that occurred on November 24, 1987. The magnitude, M 6.7, is based on teleseismic observations and is incompatible with the strong motion data. Both the waveform modeling of Wald et al. (1990) and the current inversions find M 6.4 to be more consistent with the strong motion data.

A total of 12 sites (1 rock), all the available strong motion data (appendix B), are used in the inversion and forward modeling. Figure 5.124 shows the site map with the general area located in the northern Imperial Valley just south of the Salton Sea and north of the El Centro array.

As a result of the close proximity to the site area of the 1979 Imperial Valley earthquake, the same soil and rock profiles are used (Table 5.20). In addition, because the Superstition Hills site area reflects depositional environment similar to the El Centro array area, the Imperial Valley G/G_{max} and hysteretic curves (Figure 5.113) are used.

The slip model is from Wald et al. (1990) and is shown in Figure 5.125. The mechanism is vertical strike-slip and the top edge of the rupture is at a depth of 0.5 km. As with the Imperial Valley slip model (Figure 5.104), there is considerable shallow slip and a subevent stress drop of 5 bars is used. The rise time is 0.74 sec (Table 5.27) and is a best fit over a suite of trial values.

The point- and finite-source stress drops are 43.4 bars and 31.2 bars respectively. The static stress drop of 31.2 bars is the highest of the shallow slip events: Landers, Tabas, Imperial Valley, and Nahanni. The point-source depth is 9.0 km, the depth of the largest asperity in the Wald et al. (1990) slip model (Figure 5.125).

5.8.1 Point-Source Inversions for Stress Drop and Kappa Values

In the Superstition Hills earthquake inversions, the same rock and soil site transfer functions are used as for the Imperial Valley analyses. The inversion results are listed in Table 5.28. The stress drops are shown for M 6.4 and 6.7 with the preferred M 6.4 kappa values. The M 6.4 stress drop is 43.4 bars and the average soil kappa value is 0.051 sec, in agreement with the soil site average of 0.050 sec for the Imperial Valley mainshock (Table 5.22). The single rock site has a kappa value of 0.028 sec, slightly lower than the 0.034 value obtained for the same site

in the Imperial Valley inversion results.

The fits to the Fourier amplitude spectra are shown in Figure Set 5.126. Except for the rock site SSM, the point-source spectra provide a generally good match to the vector sum (divided by $\sqrt{2}$) spectra of the recorded motions.

5.8.2 Point-Source Modeling Results

Figure 5.127 shows the estimates of the model bias and variability for the point-source over all 11 sites. The bias is slightly negative (overprediction) and uniform from about 0.3 Hz (lower limit of reliable analyses) to 100 Hz. The variability is low over the same frequency range averaging about 0.4. In general the model is doing very well with a tendency to overpredict on average. These results are reflected in the response spectra plots shown in Figure 5.128. The overprediction is easily seen and is largest at site BRW. Except for the rock site, SSM, the model is capturing the overall levels and shapes reasonably well. Site PTS, the first plot in Figure 5.128, is almost directly over the fault (Figure 5.124) and shows a small short period overprediction. This is analogous to sites EMO and E07 (Figure Set 5.111) for the Imperial Valley earthquake. All three sites show similar levels of recorded motions and approximately the same degree of overprediction. This supports the conclusion that the Imperial Valley curves (Figure 5.113) are somewhat too linear at the cyclic shear strains generated at these sites but are appropriate for the other sites. A set of curves more appropriate for these three sites may reflect much sharper curvature at effective strains around 0.1%, the average strains generated over the top 50 ft at these sites. More analyses are required to refine the Imperial Valley curves and the current results are considered as acceptable.

5.8.3 Finite-Source Modeling Results

For the finite-source model, the bias and variability estimates are shown in Figure 5.129. For this earthquake, both the bias and variability estimates are quite similar for the point- and finite-source models. The bias is low, slightly negative and the variability is reasonably uniform at about 0.4 over most of the bandwidth. On average there is little statistical difference in the accuracy of the two models for this earthquake.

The corresponding response spectra plots are shown in Figure 5.130 and are similar to the point-source results (Figure 5.128).

In general both the point- and finite-source models provide a good fit to the recorded motions for this earthquake with the exception of the single rock site SSM.

5.9 1988 SAGUENAY EARTHQUAKE

The M 5.8 Saguenay earthquake occurred in the Quebec Province of Canada, well within geographic ENA. The earthquake represents the largest and most widely recorded event to occur in the ENA tectonic environment. Because of its relatively large high frequency motions, this earthquake has generated considerable uncertainty in quantifying strong ground motions in ENA (EPRI, 1993). The source spectrum of this earthquake is incompatible with the simple Brune single corner frequency omega-square source spectrum (Chapter 2), having a larger high frequency (frequencies above the corner frequency) spectral level relative to the low frequency spectra level than the simple Brune model predicts. To match the high frequency spectral level,

a large point-source stress drop is required (Ou and Herrmann, 1990; Somerville et al., 1990; EPRI, 1993). With a simple Brune source this results is large overprediction of the low frequencies and has resulted in the application of the two-corner spectral model to ENA (Atkinson, 1993). However, although the two-corner source spectral model matches the shape of the Saguenay ground motion spectra much better than the single-corner Brune model, it still dramatically underpredicts the absolute levels of the Saguenay data. To match the Saguenay mainshock high frequency spectral levels, the two-corner source model requires much higher frequency levels than the rest of the ENA recorded motions upon which model is based. The case is clear that the recorded high frequency motions from the 1988 Saguenay mainshock require special consideration regardless of how they are modeled. As a result, both the point-source and finite-source models for this earthquake show significant and unique departures from all of the other earthquakes modeled in this study.

For the Saguenay earthquake, 22 sites (all rock) are modeled covering the fault distance range of 47 to 460 km (Table 5.2). The site location map is shown in Figure 5.131 and spans a wide area as the most distant site (WBOZ) is at over 400 km epicentral distance.

The slip model is from Hartzell et al. (1994) and is plotted in Figure 5.132. It consists of a single asperity with a concentrated high slip region at a depth of about 26 km. The top edge of the rupture surface is at a depth of 22 km and dips eastwardly at 65°.

The crustal model is from Hartzell et al. (1994) and is listed in Table 5.29. Because all the sites are hard rock and an appropriate shallow generic profile is unknown, only the basic crustal

model is used along with linear site response analyses fixing the kappa values to those determined from the inversions (Table 5.31).

The source parameters are listed in Table 5.30. The point-source stress drop is very high, 572 bars, and the static stress drop is about 14 bars. The point-source depth is about 26 km, the center of the high slip region the single asperity (Figure 5.132). The subevent stress drop is 200 bars and the rise time is 0.46 sec. Both values represent a best fit over a very limited set of trial values.

5.9.1 Point-Source Inversion for Stress Drop, Kappa and Q(f)

To accommodate crustal amplification from a depth of 25 km to the surface, a smooth crustal transfer function is used in the inversions. The inversion results are listed in Table 5.31 with a stress drop of 572.2 bars and an average kappa value of 0.023 sec, significantly lower than the WNA average of about 0.04 sec (Chapter 6) and in general accord with the value of 0.016 sec from the Nahanni inversion. Interestingly, the kappa values at the GSC sites, which are located within and on the edge of the Grenville Province, are significantly lower than the ECTN values. The ECTN sites listed in Table 5.31 are all located in the Appalachian thrust belt, a region of crustal transition and the kappa values may reflect softer shallow (1 to 2 km) crustal rocks.

To obtain a Q(f) model appropriate for the region, the distant ECTN sites were added. Since these stations have only a vertical component, a constant H/V factor of 1.4 has been used to approximately convert them to an average horizontal component. Use of a more accurate

empirical frequency dependent H/V relation (Atkinson and Boore, 1994) is complicated by the choice of appropriate crustal amplification factors to apply to the corrected horizontal components. As a result, the simple constant factor is used. The resulting Q(f) model is 317 $f^{0.86}$. Interestingly, the Q_o value of 317 is very similar to WNA values for η fixed at 0.6 (Table 4.1). The main difference is in the stronger frequency dependence for the Saguenay data. At 10 Hz the Saguenay Q is approximately double (factor of 1.8) the WNA assuming the same Q_o value. At 1 Hz these results suggest that, apart from crustal propagation effects, WNA and ENA motions should attenuate in about the same manner.

The fits to the Fourier amplitude spectra over the bandwidths used at each site are plotted in Figure Set 5.133. The high frequency spectral levels are fit fairly well with the 572 bar stress drop, except for the most distant site at 460 km. The consequence of boosting the high frequencies with a single corner frequency is shown in the large low frequency overprediction at most of the sites.

5.8.2 Point-Source Modeling Results

The point-source bias and variability plots are shown in Figure 5.134. For frequencies at 1 Hz and above, the range of reliable analyses, the bias increases from a strong overprediction (a factor of about 1.5) to a constant of about 0.2 (a 20% underprediction) at 10 Hz. The variability is high ranging from about 0.5 at high frequency ($\geq$ 10 Hz) and increases to about 0.75 around 1 Hz. These high values are to be expected as the distance ranges out to nearly 500 km and 9 of the 22 sites are vertical components (Table 5.31), corrected to horizontal using a constant

factor. Taking these factors into consideration, the bias and variability plots are considered to reflect generally good results for the point-source model.

The response spectra plots are shown in Figure Set 5.135 and reflect a fair fit at high frequency and the low frequency overprediction, especially for the closer sites.

5.9.3 Finite-Source Modeling Results

For the finite-source model, the bias and variability estimates are shown in Figure 5.136. For both the bias and variability, the results are very similar to the point-source with the finite-source variability slightly larger.

The response spectra are shown in Figure Set 5.137 and are similar to the point-source results as well. At the two closest sites, 516 and 517, the finite-source levels near 1 Hz are too high. Overall, the motions are predicted fairly well, except at site WBO, the most distant site, which shown a very significant broadband underprediction.

The 200 bars subevent stress drop is a necessary ingredient in the finite-fault modeling. This value raises the spectral levels by a factor of about 2 for frequencies higher than the subevent corner, around 1 Hz. Interestingly, the 200 bar subevent stress drop results in a corner frequency of about 2 Hz, similar to that obtained by Somerville et al. (1990) for their empirical source function. They found that enriched high frequency energy was needed to match the strong motion amplitudes and used the closest strong motion recording to obtain a source function with appropriate spectral levels.

These results are all consistent and indicate that the Saguenay mainshock source is significantly different in spectral composition than any of the earthquakes modeled here. Special consideration must be taken with either point- or finite-source models to match both the high and low frequency spectral levels of this earthquake. In general, both the point- and finite-source models are considered to provide a fair fit to the recorded motions with both models showing too high low frequency motions, particularly for the closer stations.

5.10 1992 Little Skull Mountain Earthquake

The M 5.7 Little Skull Mountain earthquake occurred on the nuclear test facility (NTS) near Las Vegas, Nevada within the southern Great Basin tectonic region. In addition to the mainshock, the two largest aftershocks are used in the inversions to help constrain the kappa values at the common sites.

A total of 8 sites (all rock) are used in the inversions and forward modeling exercise. The mainshock was recorded at all 8 sites, spanning the distance range of 15 to 98 km (Table 5.2). The M 4.5 aftershock was recorded at 5 sites and the smaller M 4.2 aftershock at just 3 sites (Table 5.34). Only the mainshock is modeled and the site map is shown in Figure 5.138. The crustal model is based on a regional earthquake location model refined at the near surface by shallow geophysical data. The crustal model is listed in Table 5.32 and consists of a shallow stiff Tuff layer 40m thick overlying much more competent materials. The shallow Tuff, with shear-wave velocities around 2,000 ft/sec, would be expected to exhibit some nonlinear response at high levels of loading ($\geq$ 30%g). For the Little Skull Mountain earthquake, the highest peak

acceleration is about 20%g, as a result linear analyses are used with the inversion kappa values (Table 5.34).

The source parameters are listed in Table 5.33. The point-source and finite-source stress drops are 63.7 bars and 21.9 bars respectively. The point-source depth is taken at the hypocentral depth, 12 km. The rupture surface is about 7 x 7 km^2 and is based on the aftershock zone. The top edge of the rupture surface is at a depth of 5.8 km and dips 70° to the southeast. The slip distribution is shown in Figure 5.139 and was selected as the best fit from a suite of 30 randomly generated slip models (Silva, 1992). The best fit rise time is 0.38 sec and the subevent stress drop is 30 bars.

5.10.1 Point-Source Inversions for Stress Drop, Kappa, and Q(f)

As with the other inversions, a smooth transfer function is used to include the amplification from the source at 12 km to the surface. Results of the inversion are listed in Table 5.34 for the mainshock and two aftershocks. The mainshock stress drop is 63.6 bars with the aftershocks having significantly lower values. The Q(f) model is 256 $f^{0.47}$ which is lower than the WNA model of 291 $f^{0.6}$ resulting from the combined inversion of the Peninsular Range, North Coast, and Mojave earthquakes (Table 4.1). The kappa values average 0.023 sec, a value significantly below the WNA kappa of 0.04 sec resulting from the inversions of the empirical attenuation (Chapter 6). Apparently the shallow crustal rocks of the region are less attenuating those of tectomically more active California.

The Fourier amplitude spectra plots are shown in Figure Set 5.140 for the mainshock and the

two aftershocks. At high frequencies, the fits are good while the model is high at intermediate frequencies. The spectral sag in the mainshock motions is interesting. It may be related to source finiteness (cancellation) as its frequency varies with station azimuth. However, it is quite strong at 100 km, 10 source dimensions away. It is clear that it is not a crustal or site resonance as none of the higher modes appear to be present. It would be interesting to see the results from a formal inversion for a slip model using these data.

5.10.2 Point-Source Modeling Results

Figure 5.141 shows the mainshock bias and variability estimates computed over the 8 sites. The ± 90% confidence limits are wide due to the small number of sites. The bias shows the typical low frequency point-source overprediction ranging from about -1 at 0.5 Hz (the lower limit of reliable analyses is about 0.2 Hz) and increasing to near zero around 5 Hz. The variability is low above 10 Hz and about 0.5 from about 2 to 10 Hz. Below 2 Hz, it is very high but the randomness (bias corrected variability) remains nearly uniform: most of the sites have a large misfit from 0.2 to 2 Hz which is constant in sign. This is easily seen in the response spectra plots shown in Figure Set 5.142. The point-source model is doing generally well at short period ($\leq$ 0.5 sec), overpredicting at longer periods, and converging to the recorded motions at long periods ($>$ 1 sec) as the high-pass filter corners are approached.

5.10.3 Finite-Source Modeling Results

As previously discussed, since a slip model was not available for this earthquake a suite of random models were generated using a method which preserves asperity characteristics such as size, number, and location. To calibrate the method, asperity characteristics were measured for

10 slip models determined by waveform modeling (published slip models) and a statistical model developed which preserves the observed statistical properties. The method was tested by generating suites of random slip models for the Loma Prieta and Whittier Narrows earthquakes and computing bias and variability estimates using the ensemble average spectra at each site. The resulting bias and variability estimates were compared to estimates computed using the published slip models based on waveform modeling. In general the bias and variability estimates computed using the simulated slip models were comparable to or lower than those computed using the "real" slip models. As a result it is believed that the slip model simulation procedure produces reasonable representations of actual slip models derived from inversions of recorded motions.

To select the best random slip model, simulations were performed for each slip model and the one which produced the lowest overall bias and uncertainty estimates was selected. The resulting estimates are shown in Figure 5.143. The bias is near zero at 3 hz above and shows an increasing overprediction to about 1 Hz where it increases with decreasing frequency. The $\pm$ 90% confidence are wide, wider than for the point-source suggesting higher variability. This is indeed the case and the finite-source variability is generally larger than that of the point-source above about 1 Hz.

The response spectra plots for the finite-source simulations are shown in Figure 5.144 and show about the same level of fit at high frequencies but with smaller low frequency motions. These results are surprisingly good considering the slip model was randomly selected. It would be of interest to perform a formal inversion for the best fitting slip distribution using the stochastic

finite-fault model to determine how much the fit is improved and over what frequency range.

5.11 1992 Cape Mendocino Earthquake

The M 6.8 Cape Mendocino earthquake occurred near the town of Petrolia in Northern California and may represent the largest event associated with the Cassadia subduction zone with instrumental recordings. The teleseismic M 7.1, which is based on very long period data (≥ 45 sec) is incompatible with the 20 sec body waves (Hagerty and Schwartz, 1996) as well as the strong motion data. The lower M 6.8 was determined by Hagerty and Schwartz (1996) and is the preferred value in the strong motion inversions as well. To reduce the strong coupling between magnitude and corner frequency in the inversions, magnitude is held fixed at M 6.7 in the inversion for stress drop and kappa values.

A total of 5 sites (1 rock) were used in the inversions and forward modeling (Table 5.37). The fault distance range is 8 to 45 km (Table 5.2) and the site map is shown in Figure 5.145. Sites CMP and PET are located over the rupture surface. The crustal model is from Graves (1994) and the generic shallow rock and soil profiles are placed on top of the regional crustal model. Nonlinear zones for both rock and soil sites extend to 500 ft with a total low strain kappa of 0.04 sec (Table 5.36) for both site conditions. For the rock sites, the generic soft rock G/G_{max} and hysteretic damping curves are used. Since too few soil site recordings are available to reliably discriminate between the EPRI and generic deep soil curves, the EPRI curves assumed to be appropriate for the soil sites. The source parameters are listed in Table 5.36. The slip model is from Graves (1994) and is shown in Figure 5.146. It consists predominately of a

single large asperity at a down dip depth of about 20 km:(9.6 km depth). The rupture surface dips 140 to the northeast with the top edge at a depth of 4.2 km. The rise time is 1.40 sec and the subevent stress drop is 30 bars. The point-source and finite-source stress drops are 27.2 bars and 13.2 bars respectively (Table 5.36).

5.11.1 Point-Source Inversions for Stress Drop and Kappa Values

As in the other inversions, smooth mean transfer functions appropriate for rock and soil sites are used. The Q(f) model is fixed at the North Coast value (176 $f^{0.6}$, Table 4.1) and the inversion results are listed in Table 5.37. The point-source stress drop is 27.2 bars and the average soil kappa value is 0.068 sec. The rock site, CPM, has a low kappa for California rock, 0.026, suggesting reasonably hard rock conditions. This low kappa value may have contributed to the unusually high short period motions which exceeded 1g at this site.

The Fourier amplitude spectra are shown in Figure 5.147 and reflect a generally good fit over most of the frequency ranges. Sites CPM and EUR show an underpredictions below about 3 Hz to about 0.2 Hz. The broad peak at site CPM (Cape Mendocino) from about 3 to 8 Hz is likely driving the high levels of the short period response spectra seen at this site. Taking the peak Fourier amplitude spectra as about 130 cm/sec^2 at the 7 Hz peak, and assuming the bandwidth is 2 Hz around the peak, results in a time domain estimate of 0.93g: close to the average of about 1.2g for the horizontal components. Interestingly, this peak is present to a lesser extent at all the close-in sites, PET, FOR, and RIO and decreases in prominence with distance very rapidly. This observation suggests that it is source related and perhaps enhanced by local site conditions at the Cape Mendocino site. Overall, fits to the Fourier amplitude spectra are

considered good.

5.11.2 Point-Source Modeling Results

With only 5 sites, the bias and variability estimates are poorly constrained. This is reflected in the large range in the ± 90% confidence limits shown in Figure 5.147. The bias estimates indicate a general and large underprediction at high frequencies beginning at about 1 Hz. The variability is high, nearly 0.75, above 1 Hz, indicating a generally poor fit. This is seen in the response spectra plots shown in Figure 5.148. Basically none of the sites are fit very well, possibly due to the point-source distance definition (Chapter 4) being poor in cases where the sites are over or near the edges of shallow dipping rupture surfaces.

5.11.3 Finite-Source Modeling Results

Significantly better results are seen in the finite-source modeling as Figure 5.149 illustrates. The bias is small at 0.5 Hz and above and the variability has decreased to about 0.5 over the same frequency range. The response spectra fits, Figure 5.150, reflect the improvement and show reasonably good fits at sites CPM, EUR, PET, and RIO. A lower kappa value (0.025 sec) at site CPM would increase the spectral levels below 0.1 sec by about 20 to 30%, nearly the level of the recorded motions. Apparently the anomalously large motions at CPM are largely being captured by the source finiteness coupled with hard rock site conditions. A more refined slip model would hopefully improve the fit at site FOR. Overall the fit with the finite-source simulations is clearly superior to that of the point-source and suggests that for sites located over or adjacent to shallow dipping ruptures, the current point-source distance metric warrants improvement.

5.12 Model Bias and Variability Estimates

The bias and variability estimates computed over all the earthquakes (16) and sites (503) reflect the magnitude range M 5.3 (Imperial Valley aftershock) to M 7.4 and a site distance range of 1 to 218 km (460 km for CEUS). This represents a comprehensive data set and is expected to provide a statistically robust assessment of both the point- and finite-source models.

5.12.1 Point-Source Model

Final model bias and variability estimates for the point-source model are shown in Figures 5.152, 5.153, and 5.154 for all, soil, and rock sites respectively. Over all the sites (Figure 5.152) the bias is slightly positive for frequencies greater than about 10 Hz and is near zero from about 10 Hz to 1 Hz. Below 1 Hz, the stable point-source overprediction is reflected in the negative bias. The analyses are considered reliable down to about 0.3 Hz where the point-source shows about a 40% overprediction.

The model variability is low, about 0.5 above about 3 to 4 Hz and increases with decreasing frequency to near 1 at 0.3 Hz. Above 1 Hz, there is little difference between the total variability (uncertainty plus randomness) and randomness (bias corrected variability, Section 5.1.1) reflecting the near zero bias estimates. Below 1 Hz there is considerable uncertainty contributing to the total variability suggesting that the model can be measurably improved as its predictions tend to be consistently high at very low frequencies ($\leq$ 1 Hz). This stable misfit may be interpreted as the presence of a second corner frequency for WNA sources (Atkinson and Silva, 1996).

For the soil sites, Figure 5.153 shows a slight improvement at 1 Hz and above in both the bias and variability estimates. This indicates that the rock sites must reflect the converse and Figure 5.154 does show larger bias and variability estimates than the results for all the sites. Soil sites are modeled more accurately than rock sites. This suggests that strong ground motions at rock sites are more variable than motions at soil sites and the model is not capturing the increased site-to-site variation. The larger rock site bias above 10 Hz suggests a small stable underprediction possibly due to the use of a single smooth rock profile rather than randomizing the profile and using a mean spectrum. This is consistent with the trend seen in the individual earthquake analyses: soil sites are modeled more accurately than rock sites.

For the finite-fault, Figures 5.155, 5.156, and 5.157 show the corresponding bias and variability estimates. For all the sites, the finite-source model provides slightly smaller bias estimates and, surprisingly, slightly higher variability for frequencies exceeding about 5 Hz. The low frequency ($\leq$ 1 Hz) point-source overprediction is not present in the finite-source results, indicating that it is giving accurate predictions over a broad frequency range, from about 0.3 Hz (the lowest frequency of reliable analyses) to the highest frequency of the analyses. For the soil and rock sites, a trend similar to the point-source results is present: the bias is larger and the variability is higher for rock site conditions than for soil site conditions.

In general, for frequencies of about 1 Hz and above the point-source and finite-source give comparable results: the bias estimates are small (near zero) and the variabilities range from about 0.5 to 0.6. These estimates are low considering the analyses are based on a data set comprised of earthquakes with M less than M 6.5 (288 of 513 sites) and high frequency ground motion

variance decreases with increasing magnitude, particularly above M 6.5 (Youngs et al., 1995; Appendix A). Additionally, for the vast majority of sites, generic site conditions were used (inversion kappa values were used for only the Saguenay and Nahanni analyses, 25 rock sites). As a result, the model variability (mean = 0) contains the total uncertainty and randomness contribution for the site. The parametric variability due to uncertainty and randomness in site parameters: shear-wave velocity, profile depth, G/G_{max} and hysteretic damping curves need not be added to the model variability estimates. It is useful to perform parametric variations to assess site parameter sensitivities, but only source and path damping Q(f) parametric variabilities require assessment on a site specific basis and added to the model variability. The source uncertainty and randomness components include point-source stress drop and finite-source slip model and nucleation point variations (Silva, 1992).

As an additional assessment of the stochastic models, bias and variability estimates were made over all earthquakes (except Saguenay since it was not used in the regressions) and sites using the empirical attenuation relation. For all the sites, the estimates are shown in Figure 5.158. Interestingly, the point-source overprediction below about 1 Hz is present in the empirical relation perhaps suggesting the model functional form for spectral shape requires refinement. Comparing these results to the point- and finite-source results (Figures 5.152 and 5.155) shows comparable bias and variability estimates. Over all the sites, the numerical models perform about as well as the well constrained empirical model (removing the Saguenay earthquake slightly improves the model results).

Considering just soil sites, Figure 5.159 shows similar bias estimates as the models (Figures

5.153 and 5.156) but the model variability is slightly lower. The models, point- and finite-source, are slightly more accurate than the empirical relation. For the rock sites, Figure 5.160, model simulations are comparable to the empirical relation, except the point-source and finite-source models (Figures 5.154 and 5.155) show a slight positive bias at 3 Hz and above 20 Hz. In general, both the point- and finite-source models produce ground motion estimates that are as accurate as the empirical model when averaged over all sites. It is likely that there is a distance bias and the models perform better than the empirical at close distances and worse at large distances (particularly the point-source model). These results are very encouraging and provide an addition qualitative validation of the point- and finite-source models. Prarantheticaly this approach provides a rational basis for evaluating empirical attenuation models.

5.13 Revised Rise Time Seismic Moment Relation

To complete the finite-fault analyses, the revised rise time verses seismic moment relation is shown in Figure 5.161. It reflects slightly longer (12%) rise times than the empirical relation

$$\log(\tau) = 0.33 \log(M_o) - 8.62 \qquad (5\text{-}3)$$

which was based on rise times determined by waveform modeling (Heaton, 1990). The revised relation is given by

$$\log(\tau) = 0.33 \log(M_o) - 8.54 \qquad (5\text{-}4)$$

and is an eyeball fit to the best fit rise times resulting from the finite-fault modeling (Figure 5.158, Table 5.38). The 12% increase is not considered to indicate a significant difference from the empirical relation since uncertainty in rise times determined by waveform modeling is generally considered high. The revised relation results in slightly lower motions (about 5 to 10%) and provides slightly better bias estimates. As a result, it is retained as a refinement of the finite-source model.

Because the finite-source bias estimates were based on the best fitting rise times with Equation 5-3 providing starting values, new bias estimates should be computed using the revised rise time/moment scaling relation (Equation 5-4). However, because the best fitting rise times are very close to the revised model (within about ± 10%), the impacts on the bias estimates would be very small.

5.14 Point-Source Stress Drop Summary and Generic WNA Parameters

Table 5.39 lists the point-source stress drops determined for each earthquake. The average (log) for WNA earthquakes (including Tabas) is about 47 bars. This value is consistent with the 59 bar average over mechanism and magnitude (M 5.5 to M 7.5) determined in the inversions of the empirical attenuation relation (Chapter 6, Table 6.1). Based on these results, a reasonable value for a magnitude and mechanism independent stress drop for applications to WNA is 60 bars. The additional WNA parameters, Q(f) and kappa, are listed in Table 4.1 by geologic province or combined provinces for region independent applications. For generic applications a rock kappa value of 0.04 sec is recommended since the Mojave Province (kappa = 0.030 sec) is significantly underrepresented in rock sites (Chapter 5). For soil sites, Chapter 6 will show

that kappa does depend on level of control motion (expected rock outcrop) and an appropriate constant value requires assessment of desired levels of conservatism. In general, a soil kappa of 0.06 sec represents a reasonable value for generic applications. It is important to emphasize, however, that all of these parameters; stress drop, kappa, and Q(f), must be used in a manner consistent with the crustal and soil/rock amplification factors used in the inversions. For example, the kappa of 0.06 sec must be used with soil amplification appropriate for soil sites ranging in depth from 100 ft to 1,000 ft and is most appropriate for deep soils. In all cases, rock or soil sites, crustal amplification must also be included for these parameter values to result in realistic ground motion levels.

Table 5.2 Earthquakes Modeled

Earthquake	Date	M	Fault Distance Ranges(km)	Rock Sites	Soil Sites	Total Sites
San Fernando	1971	6.6	3 - 218	21	18	39
Tabas	1978	7.4	3 - 90	3	1	4
Coyote Lake	1979	5.7	3 - 30	3	7	10
Imperial Valley	1979	6.4	1 - 50	2	33	35
Imperial Valley(AS)	1979	5.3	12 - 52	0	16	16
Morgan Hill	1984	6.2	1 - 70	8	21	29
Nahanni	1985	6.8	6 - 16	3	0	3
North Palm Springs	1986	6.0	1 - 90	9	20	29
Whittier Narrows	1987	6.0	10 - 80	18	70	88
Superstition Hills(B)	1987	6.4* (6.7)	1 - 28	1	11	12
Saguenay	1988	5.8	47 - 460	22	0	22
Loma Prieta	1989	6.9	5 - 90	33	20	53
Little Skull Mtn.	1992	5.7 (4.4,4.2)**	15 - 98	8	0	8
Landers	1992	7.2	1 - 177	5	52	57
Cape Mendocino	1992	6.8	8 - 45	1	4	5
Northridge	1994	6.7	7 - 147	23	71	94
			Total	159	344	503

*Preferred Value (see Chapter 5)
**Aftershocks

Table 5.4 Northridge Earthquake Source, Path, and Site Parameters

M = 6.7
$\Delta\sigma$ bars = 62.9* (point), 39.2 (finite)**
Q_0 = 264, η = 0.60 (Table 4.1)
Point Source Depth = 11 km
Crustal Model: Wald and Heaton (1994)
Rock Site Parameters
Nonlinear Zone: 500 ft
κ = 0.03 sec: rock below nonlinear zone, V_s = 3,281 ft/sec
κ = 0.04 sec: total, small strain
G/G_{max} and Hysteretic Curves: generic soft rock, Chapter 6
Soil Site Parameters
Nonlinear Zone: 500 ft
κ rock = 0.03 sec: below nonlinear zone, V_s = 3,281 ft/sec
κ rock = 0.04 sec: total, small strain
G/G_{max} and Hysteretic Curves: generic deep soil, Chapter 6
Finite Fault Parameters
Fault Length = 18.0 km, Fault Width = 21.9 km (Wald and Heaton, 1994)
M (subevent) = 5.0
Subfault Length = 3.6 km, Subfault Width = 2.6 km
Number of Subfaults = 40
Rise Time = 1.30 sec, Subevent Rise Time = 0.15 sec, Subevent Stress Drop = 30 bars
Slip Model: Wald and Heaton (1994)
Site Distances and Kappa Values, See Table 4.2

*Table 4.2

** $\Delta\sigma = \frac{7}{16} M_0 / (A/\pi)^{\frac{3}{2}}$

Table 5.5 San Fernando Earthquake Source, Path, and Site Parameters

M = 6.6
$\Delta\sigma$ bars = 36.1* (point), 34.3 (finite)**
Q_0 = 264, η = 0.60 (Table 4.1)
Point Source Depth = 8 km
Crustal Model: Wald and Heaton (1994) Northridge
Rock Site Parameters
Nonlinear Zone: 500 ft
κ = 0.03 sec: rock below nonlinear zone, V_s = 3,281 ft/sec
κ = 0.04 sec: total, small strain
G/G_{max} and Hysteretic Curves: generic soft rock, Chapter 6
Soil Site Parameters
Nonlinear Zone: 500 ft
κ rock = 0.03 sec: below nonlinear zone, V_s = 3,281 ft/sec
κ rock = 0.04 sec: total, small strain
G/G_{max} and Hysteretic Curves: generic deep soil, Chapter 6
Finite Fault Parameters
Fault Length = 18.0 km, Fault Width = 19.0 km (Heaton, 1982)
M (subevent) = 5.0
Subfault Length = 3.0 km, Subfault Width = 3.2 km
Number of Subfaults = 36
Rise Time = 1.25 sec, Subevent Rise Time = 0.15 sec, Subevent Stress Drop = 30 bars
Slip Model: Modified Heaton (1982)
Site Distances and Kappa Values, See Table 4.2

*Table 4.2

** $\Delta\sigma = \frac{7}{16} M_0 / (A/\pi)^{\frac{3}{2}}$

Table 5.6 Whittier Narrows Earthquake Source, Path, and Site Parameters

M = 6.0
$\Delta\sigma$ bars = 95.7* (point), 27.3 (finite)**
Q_0 = 264, η = 0.60 (Table 4.1)
Point Source Depth = 15 km
Crustal Model: Wald and Heaton (1994) Northridge
Rock Site Parameters
Nonlinear Zone: 500 ft
κ = 0.03 sec: rock below nonlinear zone, V_s = 3,281 ft/sec
κ = 0.04 sec: total, small strain
G/G_{max} and Hysteretic Curves: generic soft rock, Chapter 6
Soil Site Parameters
Nonlinear Zone: 500 ft
κ rock = 0.03 sec: below nonlinear zone, V_s = 3,281 ft/sec
κ rock = 0.04 sec: total, small strain
G/G_{max} and Hysteretic Curves: generic deep soil, Chapter 6
Finite Fault Parameters
Fault Length = 10.0 km, Fault Width = 10.0 km (Hartzell and Iida, 1990)
M (subevent) = 5.0
Subfault Length = 3.3 km, Subfault Width = 2.5 km
Number of Subfaults = 12
Rise Time = 0.50 sec, Subevent Rise Time = 0.15 sec, Subevent Stress Drop = 30 bars
Slip Model: Hartzell and Iida (1990)
Site Distances and Kappa Values, See Table 4.2

*Table 4.2

** $\Delta\sigma = \frac{7}{16} M_0 / (A/\pi)^{\frac{3}{2}}$

Table 5.8 Loma Prieta Earthquake Source, Path, and Site Parameters

M = 6.9
$\Delta\sigma$ bars = 73.7* (point), 33.0 (finite)**
Q_0 = 176, η = 0.60 (Table 4.1)
Point Source Depth = 12 km
Crustal Model: Wald et al. (1991)
Rock Site Parameters
Nonlinear Zone: 500 ft
κ = 0.03 sec: rock below nonlinear zone, V_s = 3,281 ft/sec
κ = 0.04 sec: total, small strain
G/G_{max} and Hysteretic Curves: generic soft rock, Chapter 6
Soil Site Parameters
Nonlinear Zone: 500 ft
κ rock = 0.03 sec: below nonlinear zone, V_s = 3,281 ft/sec
κ rock = 0.04 sec: total, small strain
G/G_{max} and Hysteretic Curves: EPRI, Chapter 6
Finite Fault Parameters
Fault Length = 40.0 km, Fault Width = 17.5 km (Wald et al., 1991)
M (subevent) = 5.0
Subfault Length = 3.3 km, Subfault Width = 2.5 km
Number of Subfaults = 84
Rise Time = 1.60 sec, Subevent Rise Time = 0.15 sec, Subevent Stress Drop = 30 bars
Slip Model: Wald et al. (1991)
Site Distances and Kappa Values, See Table 4.3

*Table 4.3

** $\Delta\sigma = \frac{7}{16} M_0/(A/\pi)^{\frac{3}{2}}$

Table 5.10 Coyote Lake Earthquake Source, Path, and Site Parameters

M = 5.7
$\Delta\sigma$ bars = 70.1* (point), 14.6 (finite)**
Q_0 = 176, η = 0.60 (Table 4.1)
Point Source Depth = 8 km
Crustal Model: Liu and Helmberger (1983)
Rock Site Parameters
Nonlinear Zone: 500 ft
κ = 0.03 sec: rock below nonlinear zone, V_s = 4,900 ft/sec
κ = 0.04 sec: total, small strain
G/G_{max} and Hysteretic Curves: generic soft rock, Chapter 6
Soil Site Parameters
Nonlinear Zone: 500 ft
κ rock = 0.03 sec: below nonlinear zone, V_s = 4,900 ft/sec
κ rock = 0.04 sec: total, small strain
G/G_{max} and Hysteretic Curves: EPRI, Chapter 6
Finite Fault Parameters
Fault Length = 10.0 km, Fault Width = 7.6 km Liu and Helmberger (1983)
M (subevent) = 5.0
Subfault Length = 3.3 km, Subfault Width = 2.5 km
Number of Subfaults = 9
Rise Time = 0.36 sec, Subevent Rise Time = 0.15 sec, Subevent Stress Drop = 30 bars
Slip Model: Liu and Helmberger (1983)
Site Distances and Kappa Values, See Table 4.2

*Table 4.3

** $\Delta\sigma = \frac{7}{16} M_0 / (A/\pi)^{\frac{3}{2}}$

Table 5.12 Morgan Hill Earthquake Source, Path, and Site Parameters

M = 6.2
$\Delta\sigma$ bars = 49.0* (point), 10.0 (finite)**
Q_0 = 176, η = 0.60 (Table 4.1)
Point Source Depth = 8 km
Crustal Model: Hartzell and Heaton (1986)
Rock Site Parameters
Nonlinear Zone: 500 ft
κ = 0.03 sec: rock below nonlinear zone, V_s = 5,086 ft/sec
κ = 0.04 sec: total, small strain
G/G_{max} and Hysteretic Curves: generic soft rock, Chapter 6
Soil Site Parameters
Nonlinear Zone: 500 ft
κ rock = 0.03 sec: below nonlinear zone, V_s = 5,086 ft/sec
κ rock = 0.04 sec: total, small strain
G/G_{max} and Hysteretic Curves: EPRI, Chapter 6
Finite Fault Parameters
Fault Length = 27.0 km, Fault Width = 11.5 km (Hartzell and Heaton, 1986)
M (subevent) = 5.0
Subfault Length = 3.4 km, Subfault Width = 2.9 km
Number of Subfaults = 32
Rise Time = 0.70 sec, Subevent Rise Time = 0.15 sec, Subevent Stress Drop = 30 bars
Slip Model: Hartzell and Heaton (1986)
Site Distances and Kappa Values, See Table 4.3

*Table 4.3

** $\Delta\sigma = \frac{7}{16} M_0 / (A/\pi)^{\frac{3}{2}}$

Table 5.14 Landers Earthquake Source, Path, and Site Parameters

M = 7.2
$\Delta\sigma$ bars = 40.7* (point), 15.4 (finite)**
Q_o = 371, η = 0.60 (Table 4.1)
Point Source Depth = 8 km
Crustal Model: Wald and Heaton (1994b) Landers
Rock Site Parameters
Nonlinear Zone: 500 ft
κ = 0.02 sec: rock below nonlinear zone, V_s = 6,496 ft/sec
κ = 0.03 sec: total, small strain
G/G_{max} and Hysteretic Curves: generic soft rock, Chapter 6
Soil Site Parameters
Nonlinear Zone: 500 ft
κ rock = 0.02*** sec: below nonlinear zone, V_s = 6,496 ft/sec
κ rock = 0.03 sec: total, small strain
G/G_{max} and Hysteretic Curves: EPRI, Mojave soil, generic deep soil, Peninsular Range soil, Chapter 6
Finite Fault Parameters
Fault Length = 78.0 km, Fault Width = 15.0 km
M (subevent) = 5.0
Subfault Length = 3.1 km, Subfault Width = 3.0 km
Number of Subfaults = 125
Rise Time = 1.80 sec, Subevent Rise Time = 0.15 sec, Subevent Stress Drop = 5 bars
Slip Model: Wald and Heaton (1994b)
Site Distances and Kappa Values*

*Table 4.4

** $\Delta\sigma = \frac{7}{16} M_0 / (A/\pi)^{\frac{3}{2}}$

***For sites located in the Peninsular Range a kappa value of 0.03 sec is used

Table 5.16 North Palm Springs Earthquake Source, Path, and Site Parameters

M = 6.0
$\Delta\sigma$ bars = 62.8* (point), 4.5 (finite)**
Q_0 = 371, η = 0.60 (Table 4.1)
Point Source Depth = 10 km
Crustal Model: Hartzell (1989)
Rock Site Parameters
Nonlinear Zone: 500 ft
κ = 0.02 sec: rock below nonlinear zone, V_s = 5,778 ft/sec
κ = 0.03 sec: total, small strain
G/G_{max} and Hysteretic Curves: generic soft rock, Chapter 6
Soil Site Parameters
Nonlinear Zone: 500 ft
κ rock = 0.02 sec: below nonlinear zone, V_s = 5,778 ft/sec
κ rock = 0.03 sec: total, small strain
G/G_{max} and Hysteretic Curves: EPRI, Chapter 6
Finite Fault Parameters
Fault Length = 22.0 km, Fault Width = 15.2 km (Hartzell, 1989)
M (subevent) = 5.0
Subfault Length = 3.1 km, Subfault Width = 3.0 km
Number of Subfaults = 35
Rise Time = 0.45 sec, Subevent Rise Time = 0.15 sec, Subevent Stress Drop = 30 bars
Slip Model: Hartzell (1989)
Site Distances and Kappa Values*

*Table 4.4

** $\Delta\sigma = \frac{7}{16} M_0 / (A/\pi)^{\frac{3}{2}}$

Table 5.19 Tabas Earthquake Source, Path, and Site Parameters

M = 7.4
$\Delta\sigma$ bars = 21.5* (point), 12.3 (finite)**
Q_0 = 291,. η = 0.60 (Table 4.1, Combined Provinces)
Point Source Depth = 8 km
Crustal Model: Hartzell and Mendoza (1991)
Rock Site Parameters
Nonlinear Zone: 500 ft
κ = 0.03 sec: rock below nonlinear zone, V_s = 5,414 ft/sec
κ = 0.04 sec: total, small strain
G/G_{max} and Hysteretic Curves: generic soft rock, Chapter 6
Soil Site Parameters
Nonlinear Zone: 500 ft
κ rock = 0.03 sec: below nonlinear zone, V_s = 5,414 ft/sec
κ rock = 0.04 sec: total, small strain
G/G_{max} and Hysteretic Curves: EPRI, Chapter 6
Finite Fault Parameters
Fault Length = 95.0 km, Fault Width = 45.0 km (Hartzell and Mendoza, 1991)
M (subevent) = 5.0
Subfault Length = 3.2 km, Subfault Width = 3.0 km
Number of Subfaults = 450
Rise Time = 3.53 sec, Subevent Rise Time = 0.15 sec, Subevent Stress Drop = 5 bars
Slip Model: Hartzell and Mendoza (1991)
Site Distances and Kappa Values*

*Table 5.18

** $\Delta\sigma = \frac{7}{16}\,\pi\, M_0/(A/\pi)^{\frac{3}{2}}$

Table 5.21 Imperial Valley Earthquakes Source, Path, and Site Parameters

M = 6.4 (5.3 Aftershock)
$\Delta\sigma$ bars = 23.2* (point), 12.6 (finite)** (28.7*, Aftershock)
Q_0 = 264, η = 0.60 (Table 4.1, Peninsular Range)
Point Source Depth = 8 km (9.6 km, Aftershock)
Crustal Model: Liu and Helmberger (1985)
Rock Site Parameters
Nonlinear Zone: 500 ft
κ = 0.02 sec: material below nonlinear zone, V_s = 1,312 ft/sec
κ = 0.03 sec: total, small strain
G/G_{max} and Hysteretic Curves: generic soft rock, Chapter 6
Soil Site Parameters
Nonlinear Zone: 500 ft
κ rock = 0.02 sec: below nonlinear zone, V_s = 3,773 ft/sec
κ rock = 0.03 sec: total, small strain
G/G_{max} and Hysteretic Curves: Imperial Valley
Finite Fault Parameters
Fault Length = 42.0 km, Fault Width = 10.0 km (Hartzell and Heaton, 1983)
M (subevent) = 5.0
Subfault Length = 3.0 km, Subfault Width = 2.5 km
Number of Subfaults = 56
Rise Time = 0.73 sec, Subevent Rise Time = 0.15 sec, Subevent Stress Drop = 5 bars
Slip Model: Hartzell and Heaton (1983)
Site Distances and Kappa Values*

*Table 5.22 (5.23, Aftershock)

** $\Delta\sigma = \frac{7}{16} M_0 / (A/\pi)^{\frac{3}{2}}$

Table 5.25 Nahanni Earthquake Source, Path, and Site Parameters

M = 6.8
$\Delta\sigma$ bars = 13.4* (point), 13.5 (finite)**
Q_0 = 317, η = 0.86 (Table 5.31, Saguenay)
Point Source Depth = 4 km
Crustal Model: Hartzell et al. (1994)
Rock Site Parameters
Nonlinear Zone: Hard Rock, Linear Analysis
κ = Site Specific From Inversion (Table 5.26), V_s = 8,531 ft/sec
Soil Site Parameters
No soil sites
Finite Fault Parameters
Fault Length = 48.0 km, Fault Width = 21.0 km, (Hartzell et al., 1994)
M (subevent) = 5.0
Subfault Length = 2.8 km, Subfault Width = 3.5 km
Number of Subfaults = 102
Rise Time = 1.15 sec, Subevent Rise Time = 0.15 sec, Subevent Stress Drop = 5 bars
Slip Model: Hartzell et al. (1994)
Site Distances and Kappa Values*

*Table 5.26

** $\Delta\sigma = \frac{7}{16} M_0 / (A/\pi)^{\frac{3}{2}}$

Table 5.27 Superstition Hills (B) Earthquakes Source, Path, and Site Parameters

M = 6.4
$\Delta\sigma$ bars = 43.4* (point), 31.2 (finite)**
Q_0 = 264*, η = 0.06* (Table 4.1, Peninsular Range)
Point Source Depth = 9 km
Crustal Model: Imperial Valley (Table 5.20)
Rock Site Parameters
Nonlinear Zone: 500 ft
κ = 0.02 sec: material below nonlinear zone, V_s = 1,312 ft/sec
κ = 0.03 sec: total, small strain
G/G_{max} and Hysteretic Curves: generic soft rock, Chapter 6
Soil Site Parameters
Nonlinear Zone: 500 ft
κ rock = 0.02 sec: below nonlinear zone, V_s = 3,773 ft/sec
κ rock = 0.03 sec: total, small strain
G/G_{max} and Hysteretic Curves: Imperial Valley
Finite Fault Parameters
Fault Length = 20.0 km, Fault Width = 11.5 km (Wald et al., 1990)
M (subevent) = 5.0
Subfault Length = 3.3 km, Subfault Width = 2.9 km
Number of Subfaults = 24
Rise Time = 0.74 sec, Subevent Rise Time = 0.15 sec, Subevent Stress Drop = 5 bars
Slip Model: Wald et al. (1990)
Site Distances and Kappa Values*

*Table 5.28

** $\Delta\sigma = \frac{7}{16} M_0 / (A/\pi)^{\frac{3}{2}}$

Table 5.30 Saguenay Earthquake Source, Path, and Site Parameters

M = 5.8
$\Delta\sigma$ bars = 572.2* (point), 13.7 (finite)**
Q_o = 317, η = 0.86 (Table 5.31)
Point Source Depth = 25.7 km
Crustal Model: Hartzell et al. (1994)
Rock Site Parameters
Nonlinear Zone: Hard Rock, Linear Analysis
κ = Site Specific From Inversion (Table 5.31), V_s = 8,531 ft/sec
Soil Site Parameters
No soil sites
Finite Fault Parameters
Fault Length = 10.0 km, Fault Width = 10.0 km, (Hartzell et al., 1994)
M (subevent) = 5.0
Subfault Length = 3.3 km, Subfault Width = 2.5 km
Number of Subfaults = 12
Rise Time = 0.46 sec, Subevent Rise Time = 0.15 sec, Subevent Stress Drop = 200 bars
Slip Model: Hartzell et al. (1994)
Site Distances and Kappa Values*

*Table 5.31

** $\Delta\sigma = \frac{7}{16} M_o / (A/\pi)^{\frac{3}{2}}$

Table 5.32 Little Skull Mountain Crustal Model

Thickness (km)	V_s (km/sec)	Density (cgs)
0.040	0.6	1.70
0.040	1.2	2.00
0.140	1.5	2.30
0.600	2.1	2.40
0.780	1.9	2.40
1.500	2.9	2.40
2.200	3.4	2.50
10.700	3.5	2.75
16.000	3.8	2.90
	4.6	3.30

Table 5.33 Little Skull Mountain Earthquake Source, Path, and Site Parameters

M = 5.6
$\Delta\sigma$ bars = 63.7* (point), 21.9 (finite)**
Q_o = 256*, η = 0.47*
Point Source Depth = 12 km
Crustal Model: Modified Regional
Rock Site Parameters
Nonlinear Zone: Rock, Linear Analysis (Low Levels of Motion $\leq$ 20%g)
κ = Site Specific From Inversion (Table 5.34), V_s = 1,969 ft/sec
Soil Site Parameters
No soil sites
Finite Fault Parameters
Fault Length = 7.0 km, Fault Width = 6.6 km, (Aftershock zone)
M (subevent) = 5.0
Subfault Length = 2.3 km, Subfault Width = 3.3 km
Number of Subfaults = 6
Rise Time = 0.38 sec, Subevent Rise Time = 0.15 sec, Subevent Stress Drop = 30 bars
Slip Model: Derived
Site Distances and Kappa Values*

*Table 5.34

** $\Delta\sigma = \frac{7}{16} M_o/(A/\pi)^{\frac{3}{2}}$

Table 5.34 Single Earthquake Inversion Little Skull Mountain

Regional Q_o, η = 256, 0.47

M^* = 5.7, 4.4, 4.2

$\Delta\sigma$ (bars) = 63.7, 33.7, 45.6 ± 1.9, 1.2, 2.0

Site	Name	Number	κ (sec)	Category	R (km)
1	LAT		0.036		17.5, 17.5,17.5
2	NTS		0.031		26.8, 26.8, —
3	BEA		0.004		46.8, 46.8,98.8
4	PA2		0.031		58.5, —, —
5	PA1		0.031		63.9, —, —
6	LVC		0.017		98.7, —, —
7	LVA		0.028		98.2, 98.2, —
8	DVS		0.032		98.8, 98.8,98.8

AVG = 0.023

*Parameters held fixed

Starting values: $\Delta\sigma$ = 100 bars, κ = 0.040 sec

Shear-wave velocity = 3.5 km/sec, density = 2.7 cgs, crossover distance = 64 km

Table 5.36 Cape Mendocino Earthquake Source, Path, and Site Parameters

M = 6.8
$\Delta\sigma$ bars = 27.2* (point), 13.2 (finite)**
Q_o = 176*, η = 0.06 (Table 4.1, North Coast)
Point Source Depth = 9.6 km
Crustal Model: Graves (1994)
Rock Site Parameters
Nonlinear Zone: 500 ft
κ = 0.03 sec: rock below nonlinear zone, V_s = 4,922 ft/sec
κ = 0.04 sec: total, small strain
G/G_{max} and Hysteretic Curves: generic soft rock, Chapter 6
Soil Site Parameters
Nonlinear Zone: 500 ft
κ rock = 0.03 sec: below nonlinear zone, V_s = 4,922 ft/sec
κ rock = 0.04 sec: total, small strain
G/G_{max} and Hysteretic Curves: generic deep soil, Chapter 6
Finite Fault Parameters
Fault Length = 32.0 km, Fault Width = 32.0 km (Graves, 1994)
M (subevent) = 5.0
Subfault Length = 3.2 km, Subfault Width = 2.9 km
Number of Subfaults = 110
Rise Time = 1.40 sec, Subevent Rise Time = 0.15 sec, Subevent Stress Drop = 30 bars
Slip Model: Graves (1994)
Site Distances and Kappa Values, See Table 5.35

*Table 4.1

** $\Delta\sigma = \frac{7}{16} M_0 / (A/\pi)^{\frac{3}{2}}$

Table 5.39 Stress Drop Summary

Earthquake	Date	M	Stress Drop Inversion (bars)	Stress Drop SE (bars)	N
San Fernando	1971	6.6	36.1	1	39
Tabas, Iran	1978	7.4	21.5	1	4
Coyote Lake	1979	5.7	70.1	2	10
Imperial Valley	1979	6.4	23.2	1	35
Imperial Valley(AS)	1979	5.3	28.7	1	16
Morgan Hill	1984	6.2	49.0	1	29
Nahanni	1985	6.8	13.4	1	3
North Palm Springs	1986	6.0	62.8	1	29
Whittier Narrows	1987	6.0	95.7	1	88
Superstition Hills(B)	1987	6.4.(6.7)	43.4 (26.6)	1	12
Saguenay	1988	5.8	572.2	22	22
Loma Prieta	1989	6.9	73.7	1	53
Little Skull Mtn.	1992	5.7	63.7	2	8
A		4.4	340	1	5
B		4.2	46.0	2	3
Landers	1992	7.2	40.7	1	57
Cape Mendocino	1992	6.8	27.2	1	5
Northridge	1994	6.7	62.9	1	94

WNA AVG* = 46.9

Excludes* Saguenay, Nahanni, and aftershocks

Figure 5.137. Comparison of average horizontal component 5% damped pseudo relative absolute response spectra: recorded motions (solid lines), finite-source simulations (dashed lines).

Figure 5.138. Site location map for the Little Skull Mountain earthquake.

Figure 5.139. Slip model for the Little Skull Mountain earthquake. Best fit model from a random suite of slip distributions.

Figure set 5.140. Comparison of Fourier amplitude spectra for the Little Skull Mountain earthquake. Solid lines: recorded motion horizontal components vector sum divided by $\sqrt{2}$ (2 Hz wide triangular smoothing window). Dashed lines: initial model calculations. Dash-dotted lines: final model calculations.

Figure 5.141. Model bias and variability estimates for the Little Skull Mountain earthquake computed over all 8 sites for the point-source model.

Figure 5.142. Comparison of average horizontal component 5% damped pseudo relative absolute response spectra: recorded motions (solid lines), point-source simulations (dashed lines).

Figure 5.143. Model bias and variability estimates for the Little Skull Mountain earthquake computed over all 8 sites for the finite-source model.

Figure 5.144. Comparison of average horizontal component 5% damped pseudo relative absolute response spectra: recorded motions (solid lines), finite-source simulations (dashed lines).

Figure 5.145. Site location map for the Cape Mendocino earthquake.

Figure 5.146. Slip model for the Cape Mendocino earthquake (from Graves, 1994).

Figure 5.147. Comparison of Fourier amplitude spectra for the Cape Mendocino earthquake. Solid lines: recorded motion horizontal components vector sum divided by $\sqrt{2}$ (2 Hz wide triangular smoothing window). Dashed lines: initial model calculations. Dash-dotted lines: final model calculations.

Figure 5.148. Model bias and variability estimates for the Cape Mendocino earthquake computed over all 5 sites for the point-source model.

Figure 5.149. Comparison of average horizontal component 5% damped pseudo relative absolute response spectra: recorded motions (solid lines), point-source simulations (dashed lines).

Figure 5.150. Model bias and variability estimates for the Cape Mendocino earthquake computed over all 5 sites for the finite-source model.

Figure 5.151. Comparison of average horizontal component 5% damped pseudo relative absolute response spectra: recorded motions (solid lines), finite-source simulations (dashed lines).

Figure 5.152. Model bias and variability estimates for all earthquakes computed over all 503 sites for the point-source model.

Figure 5.153. Model bias and variability estimates for all earthquakes computed over all 344 soil sites for the point-source model.

Figure 5.154. Model bias and variability estimates for all earthquakes computed over all 159 rock sites for the point-source model.

Figure 5.155. Model bias and variability estimates for all earthquakes computed over all 487 sites for the finite-source model.

Figure 5.156. Model bias and variability estimates for all earthquakes computed over all 328 soil sites for the finite-source model.

Figure 5.157. Model bias and variability estimates for all earthquakes computed over all 159 rock sites for the finite-source model.

Figure 5.158. Model bias and variability estimates for all earthquakes computed over all 481 sites for the empirical model.

Figure 5.159. Model bias and variability estimates for all earthquakes computed over all 344 soil sites for the empirical model.

Figure 5.160. Model bias and variability estimates for all earthquakes computed over all 137 rock sites for the empirical model.

Figure 5.161. Best fitting rise times for the 15 earthquakes modeled using the stochastic finite-source ground motion model.

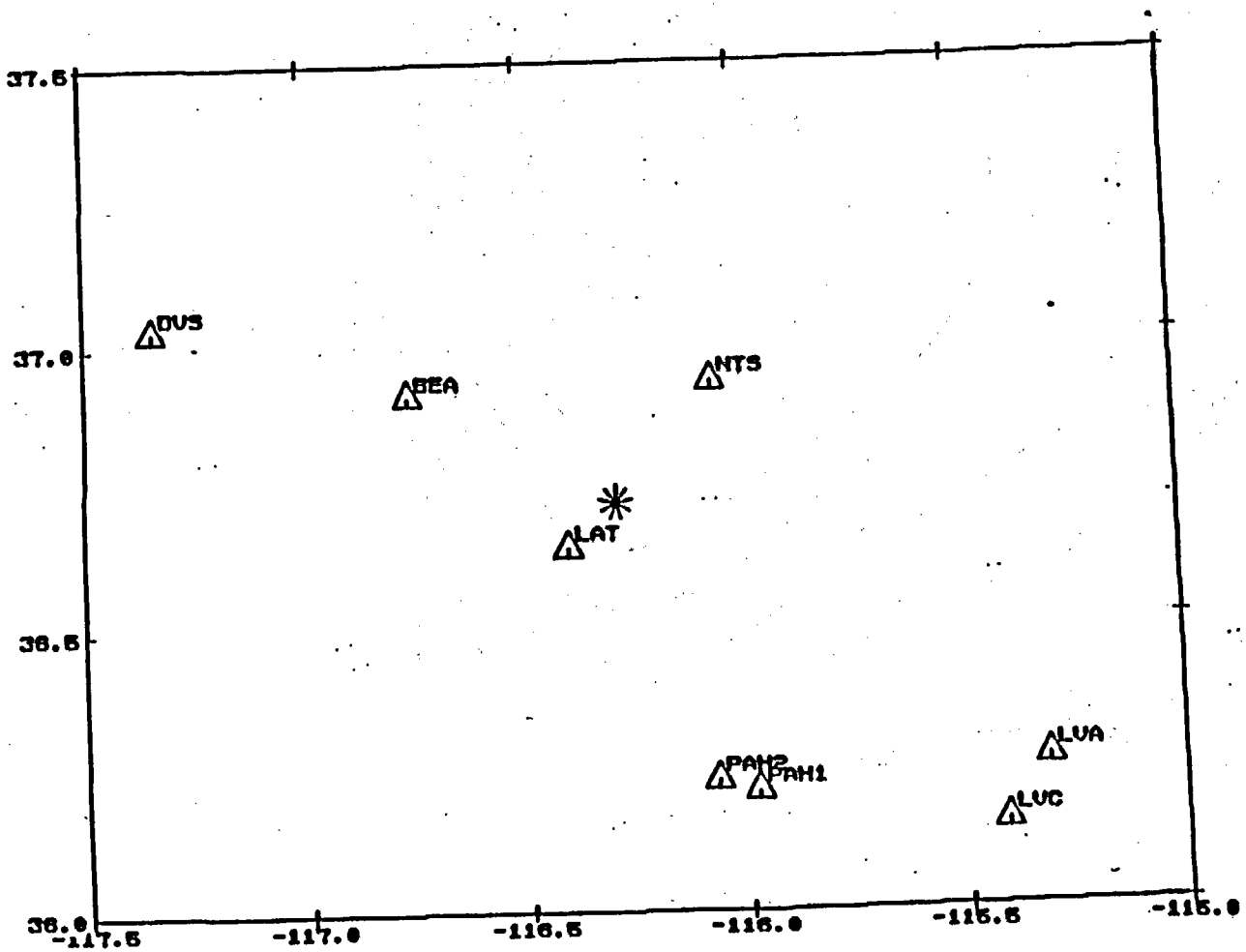

Figure 5.138

EQHD-V4.00:FILE: SITES:HP2 EPICENT.HP2
.SCA:1000000 MFAC:1.0 XFAC:1.0 Nm=0 Nx=0

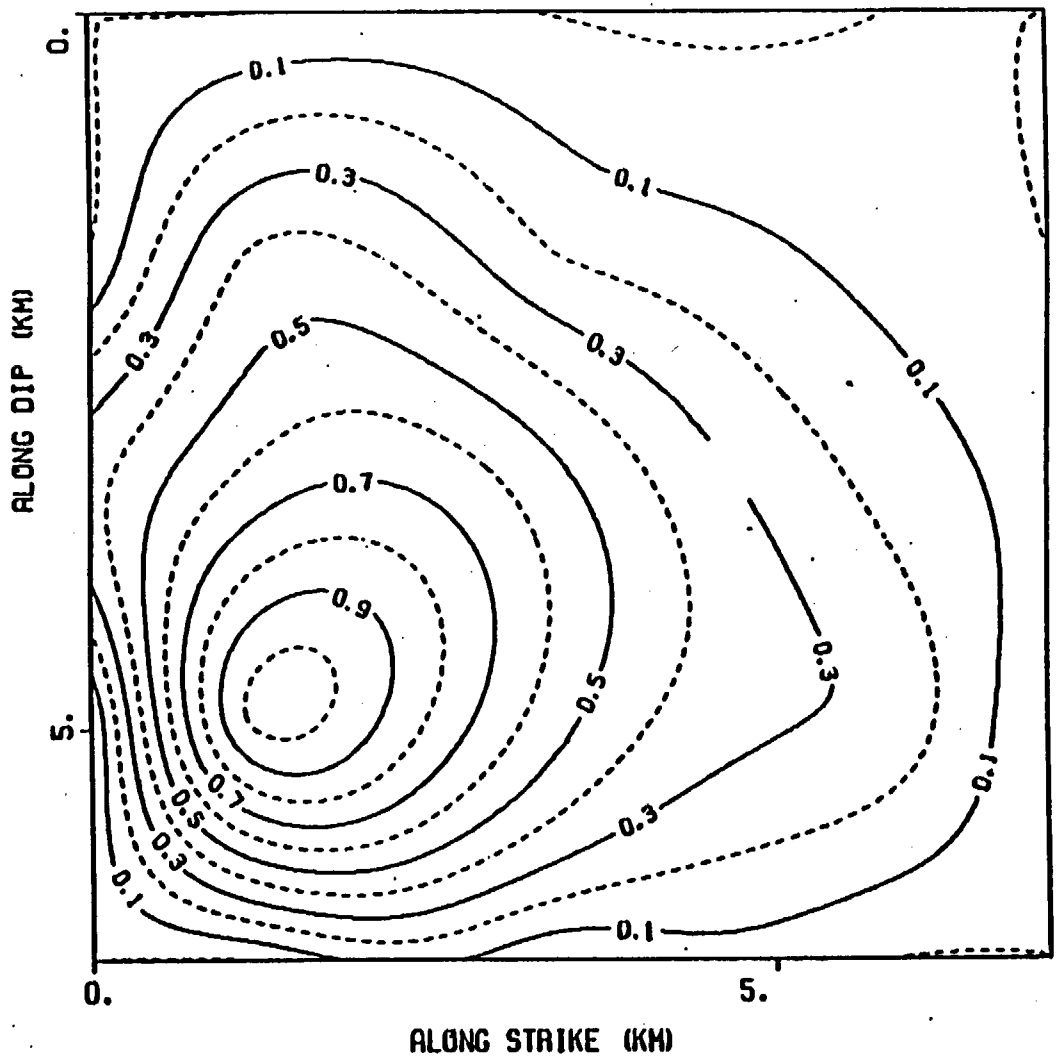

LITTLE SKULL MOUNTAIN

Figure 5.139

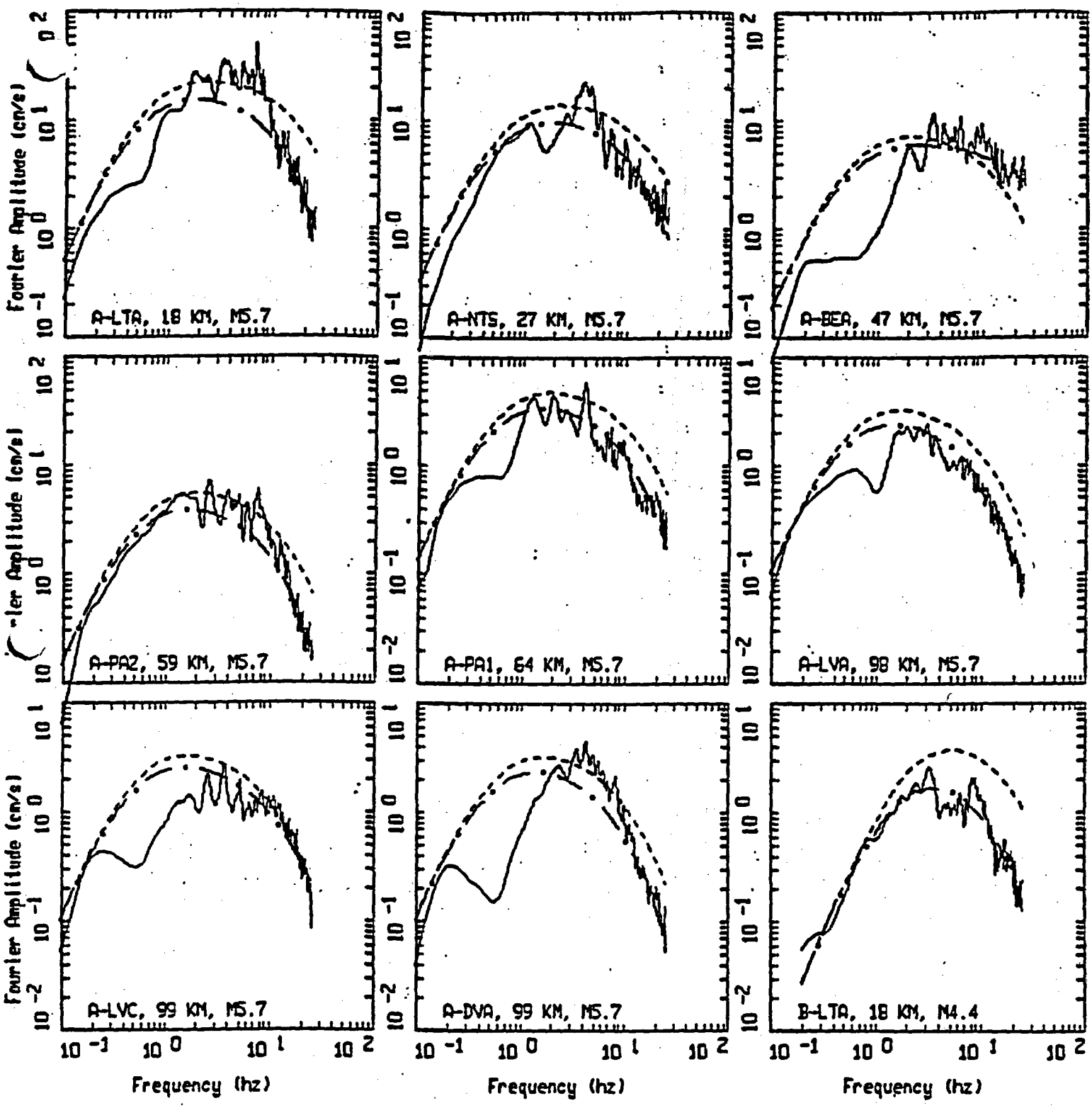

LITTLE SKULL MTN EARTHQUAKES, PAGE 1 OF 2.

Figure Set 5.140

LEGEND

——— DATA

- - - - - INITIAL MODEL

— • — FINAL MODEL

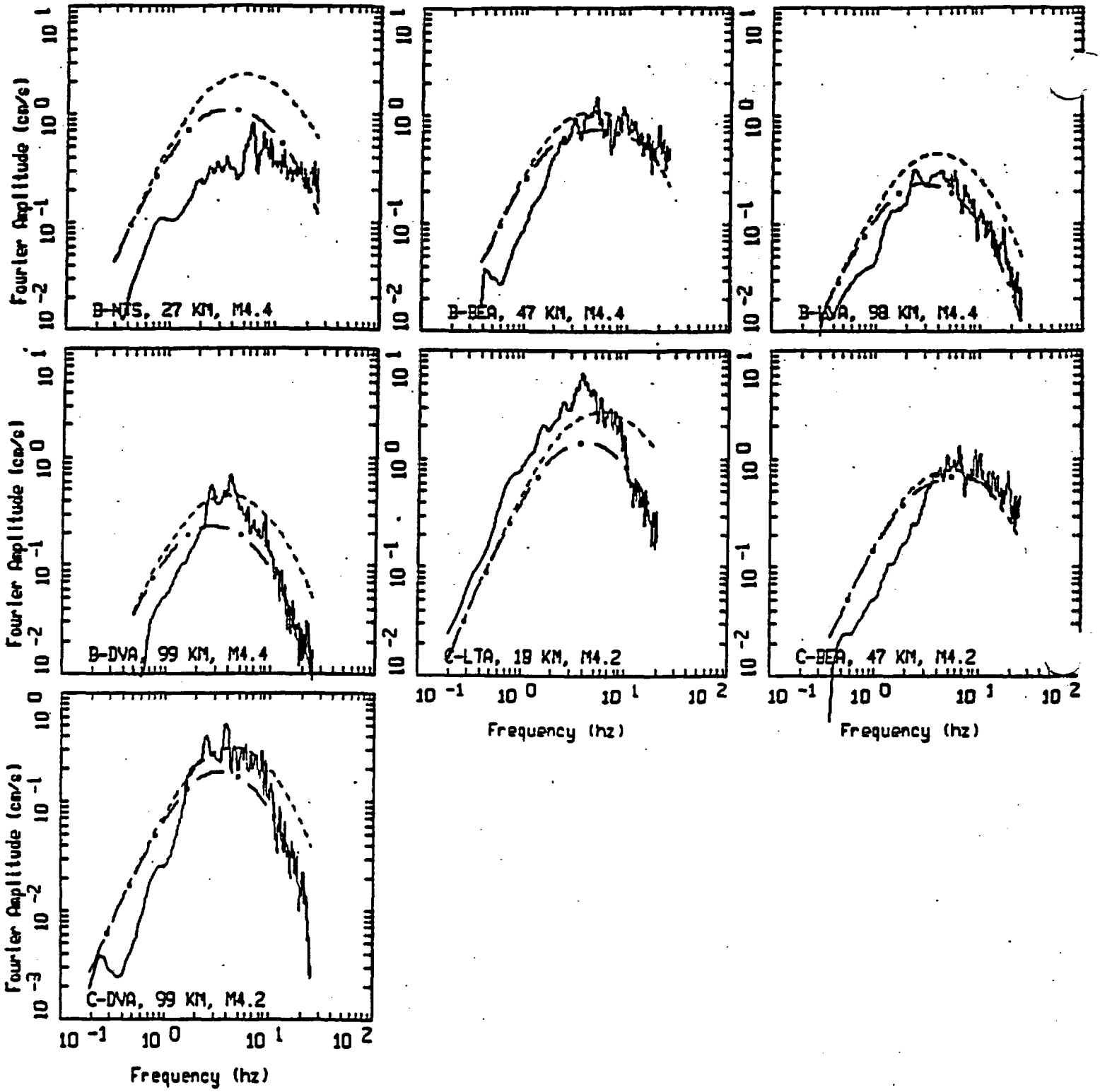

LITTLE SKULL MTN EARTHQUAKES, PAGE 2 OF 2.

LEGEND

——— DATA

- - - - - INITIAL MODEL

— • — FINAL MODEL

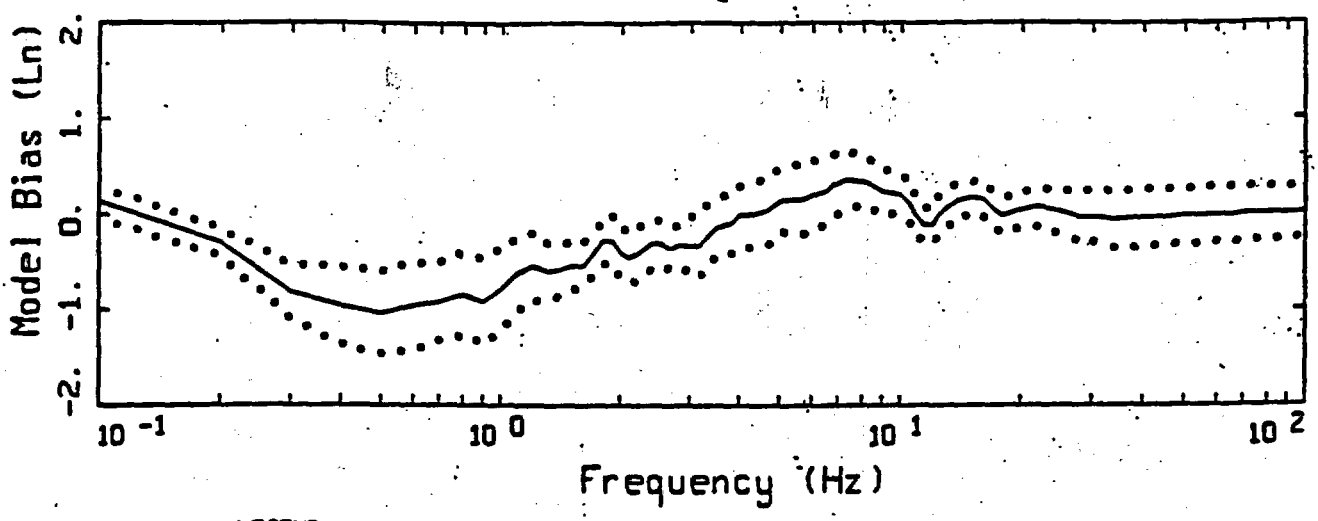

LEGEND
MODELING BIAS
90% CONFIDENCE INTERVAL OF MODELING BIAS
90% CONFIDENCE, INTERVAL OF MODELING BIAS

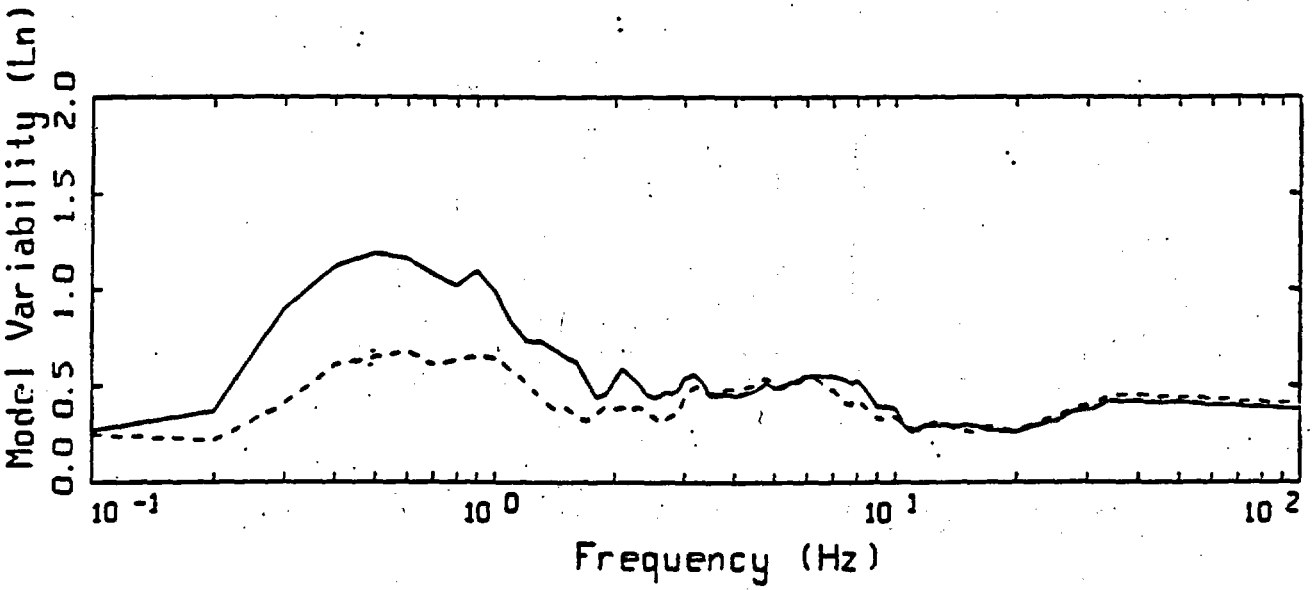

LEGEND
MEAN=0.0
BIAS CORRECTED

LITTLE SKULL MTN POINT-SOURCE
NONLINEAR, ALL 8 SITES

Figure 5.141

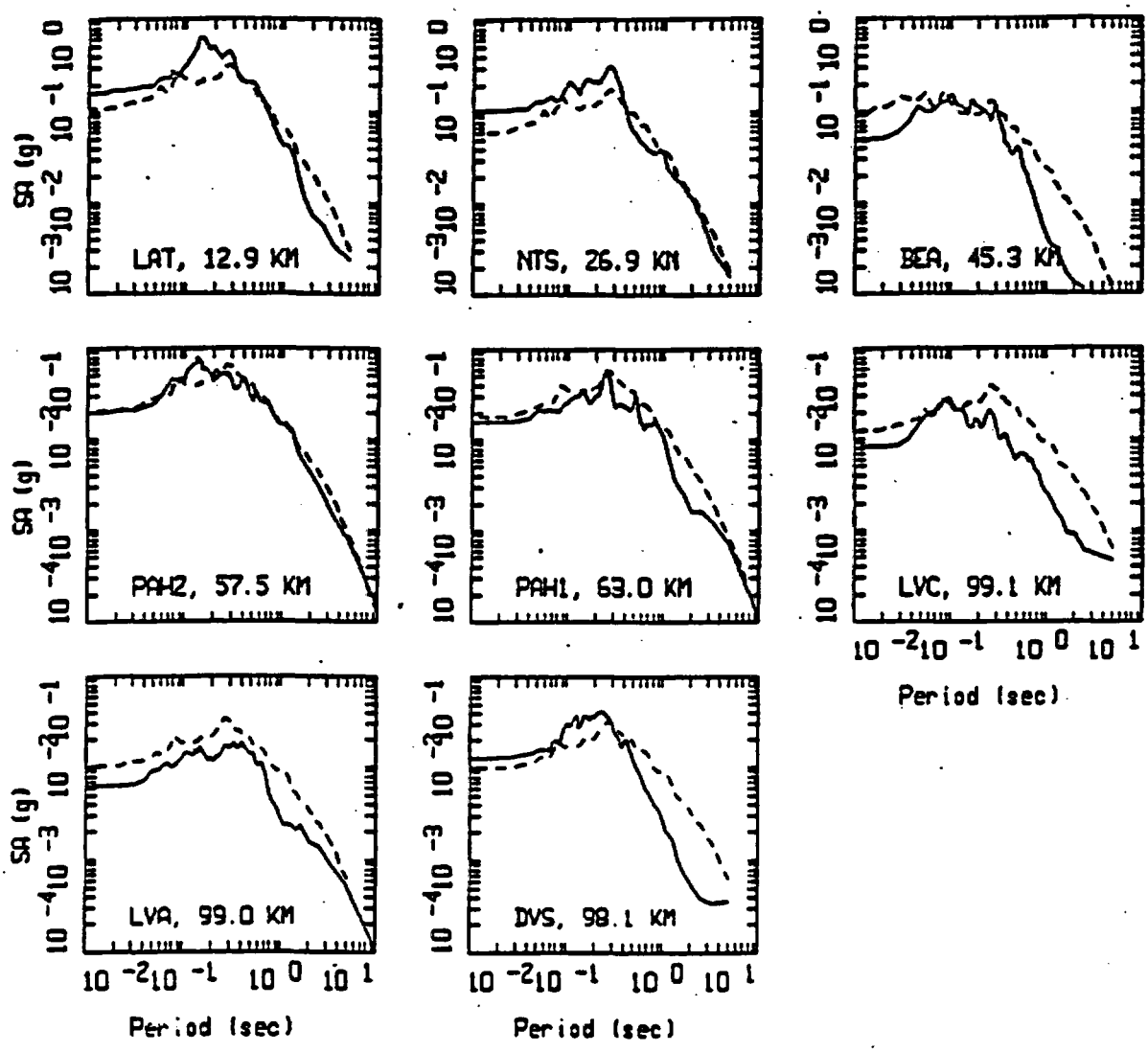

LITTLE SKULL MTN, POINT SOURCE MODELING, PAGE 1 OF 1.
NONLINEAR.

LEGEND
——— DATA
----- MODEL

Figure 5.142

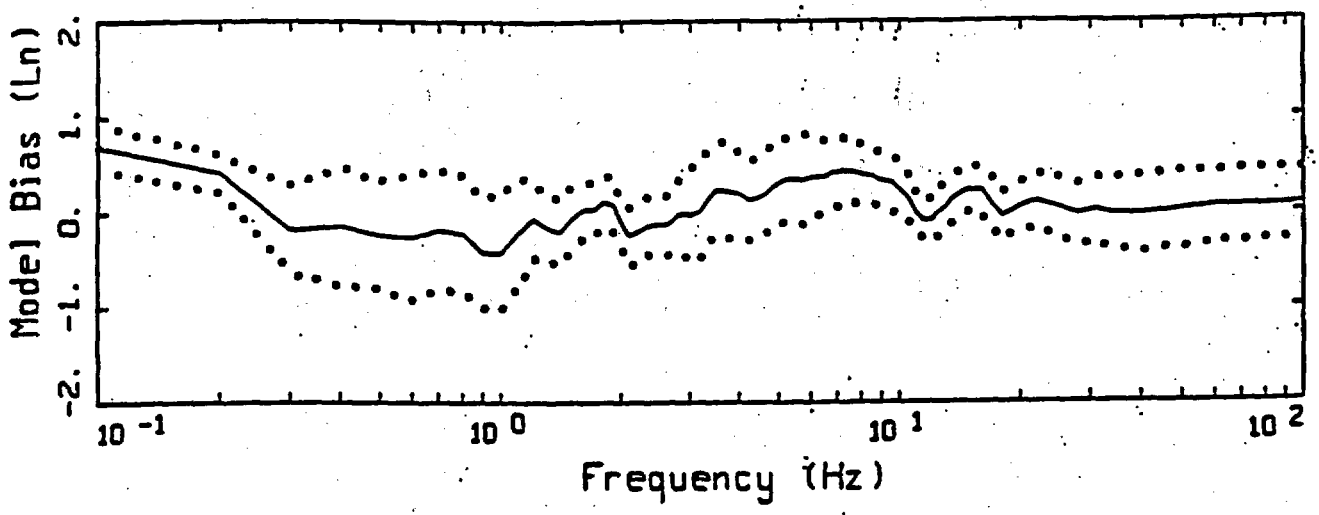

LEGEND
MODELING BIAS
90% CONFIDENCE INTERVAL OF MODELING BIAS
90% CONFIDENCE INTERVAL OF MODELING BIAS

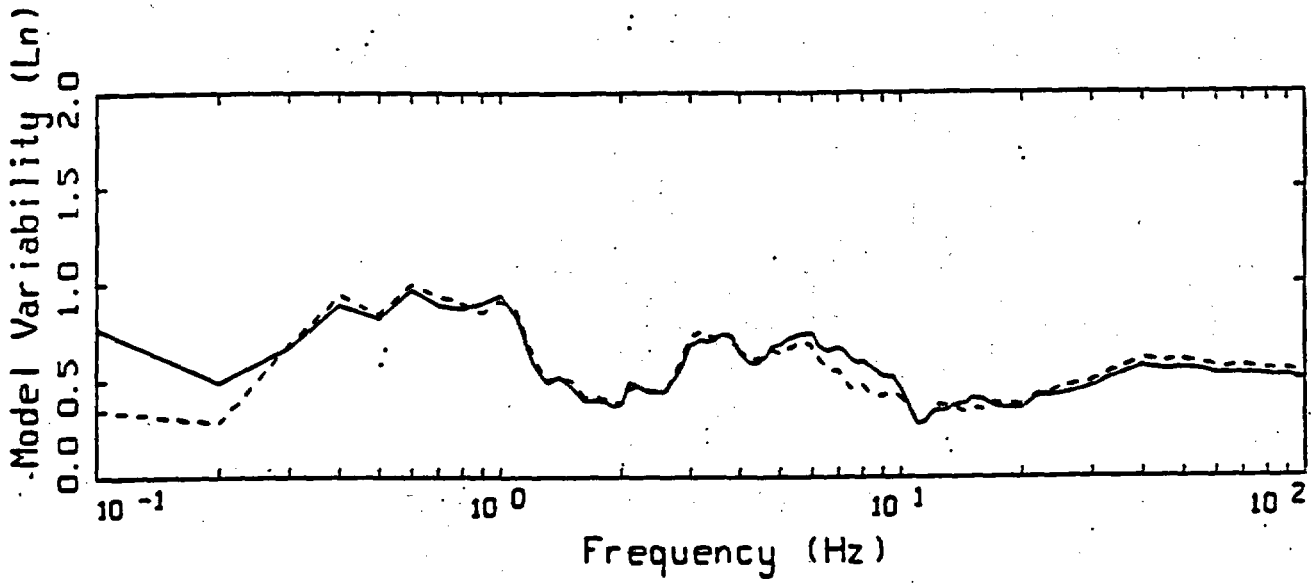

LEGEND
MEAN=0.0
BIAS CORRECTED

LITTLE SKULL MTN FINITE-SOURCE
NONLINEAR, ALL 8 SITES

Figure 5.143

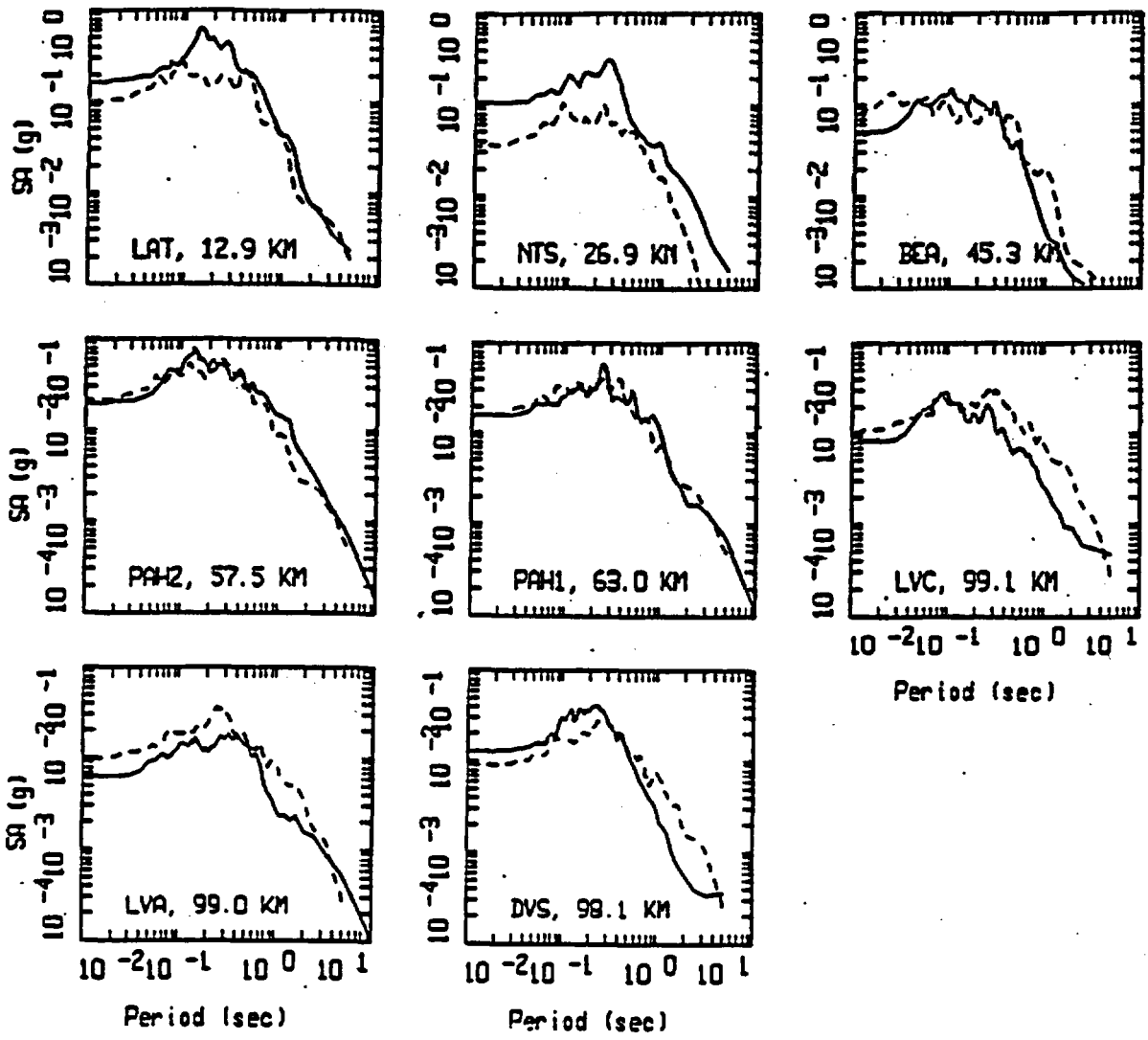

LITTLE SKULL MTN, FINITE SOURCE MODELING, PAGE 1 OF 1.
NONLINEAR.

LEGEND
——— DATA
----- MODEL

Figure 5.144

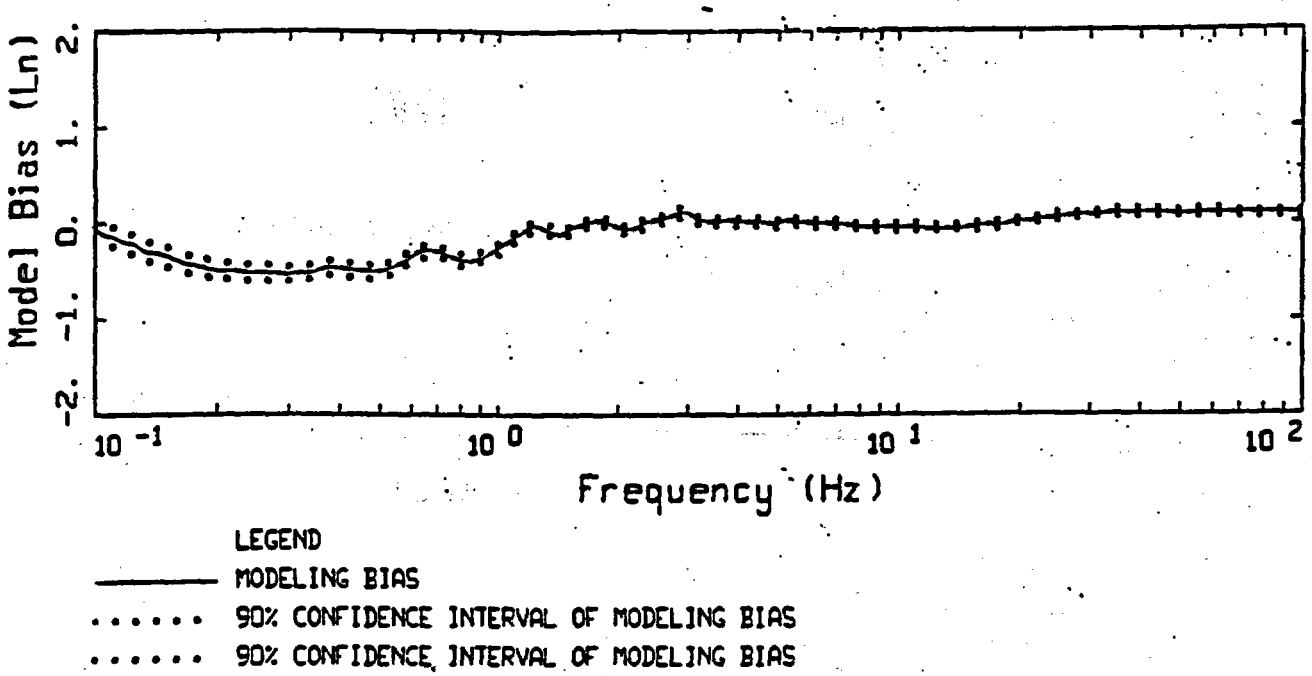

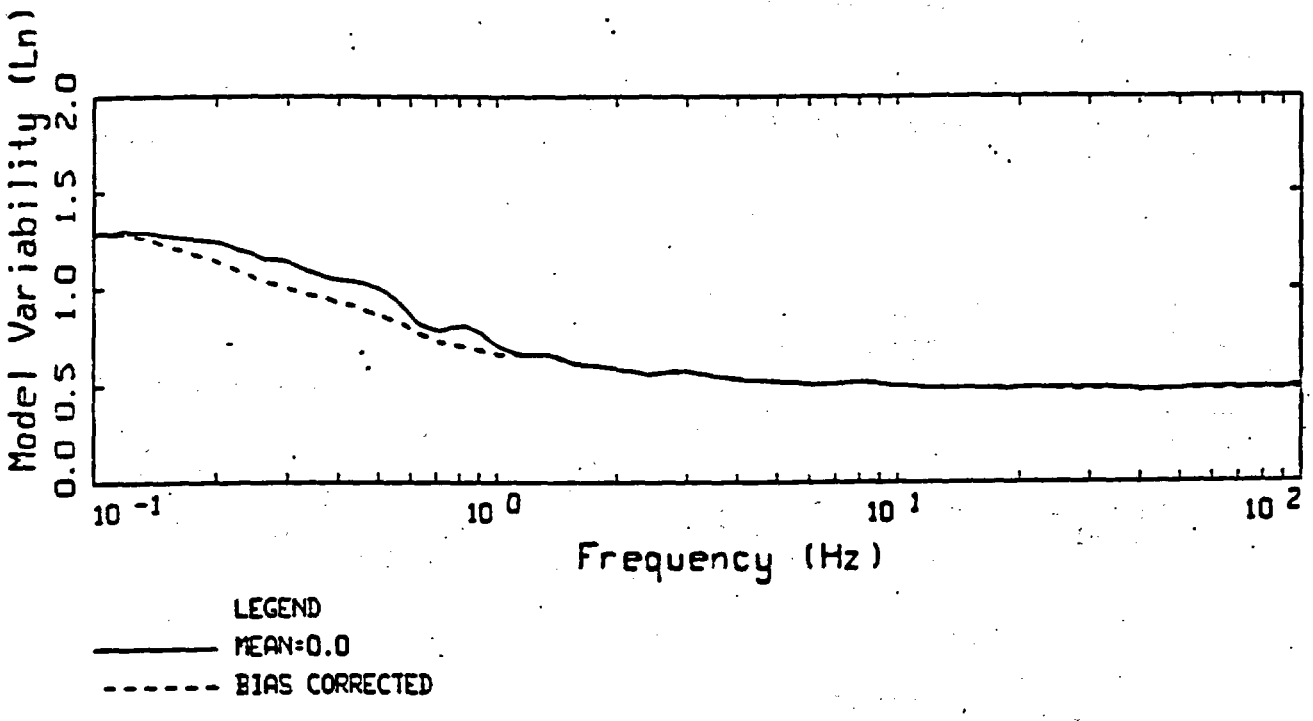

16 EARTHQUAKES POINT-SOURCE
NONLINEAR, ALL 503 SITES

Figure 5.152

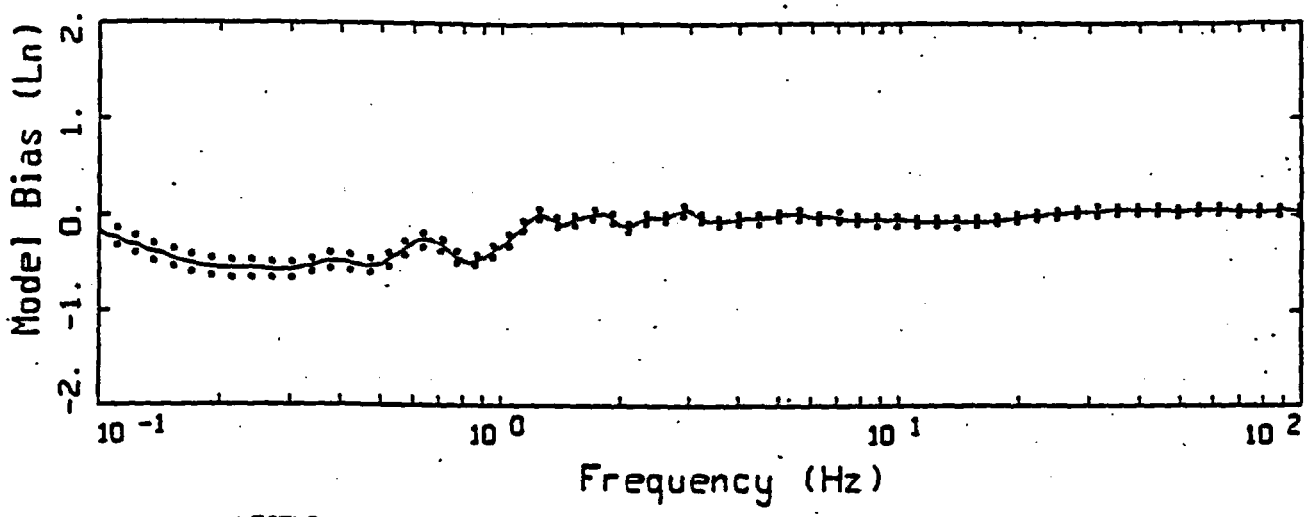

LEGEND
MODELING BIAS
90% CONFIDENCE INTERVAL OF MODELING BIAS
90% CONFIDENCE INTERVAL OF MODELING BIAS

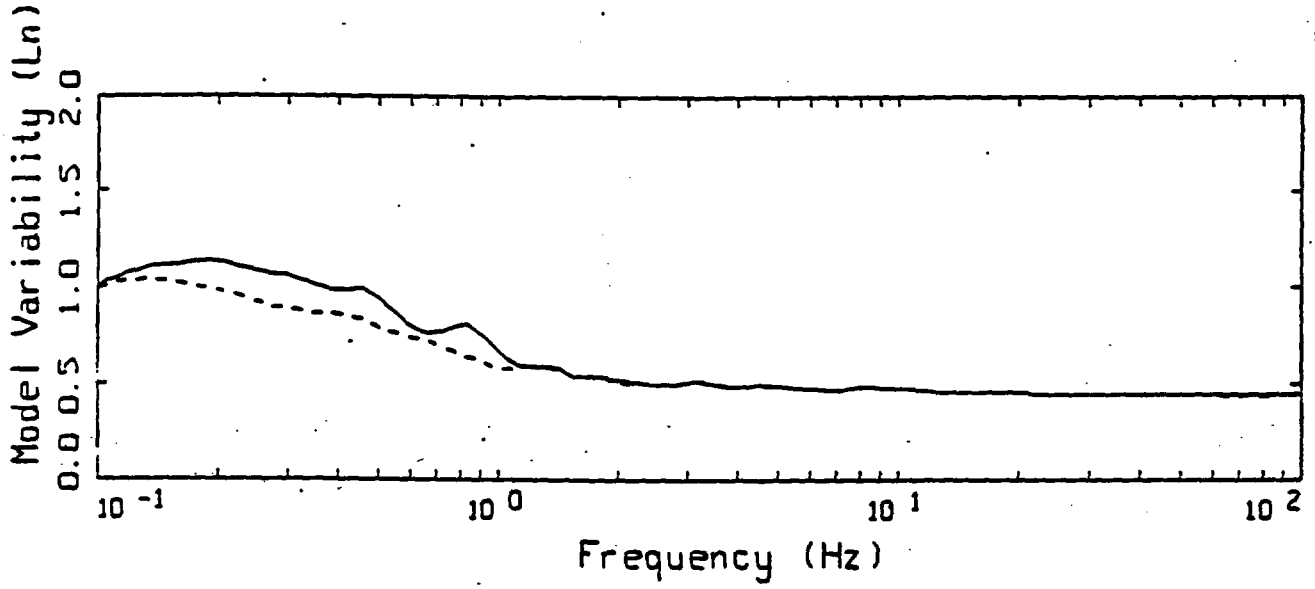

LEGEND
MEAN=0.0
BIAS CORRECTED

16 EARTHQUAKES POINT-SOURCE
NONLINEAR, ALL 344 SOIL SITES

Figure 5.153

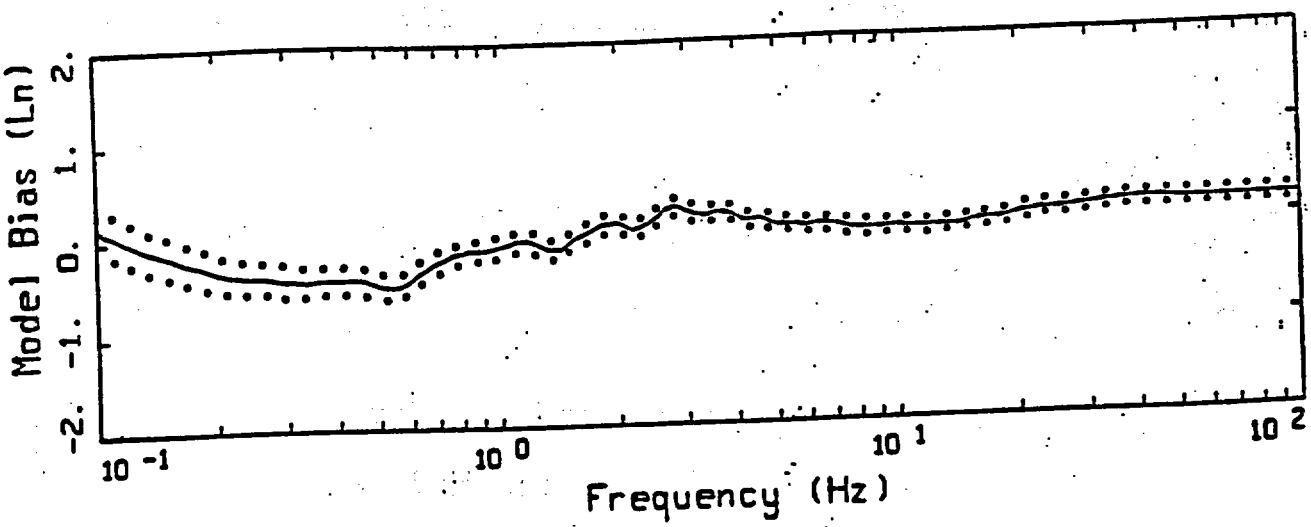

LEGEND
MODELING BIAS
90% CONFIDENCE INTERVAL OF MODELING BIAS
90% CONFIDENCE INTERVAL OF MODELING BIAS

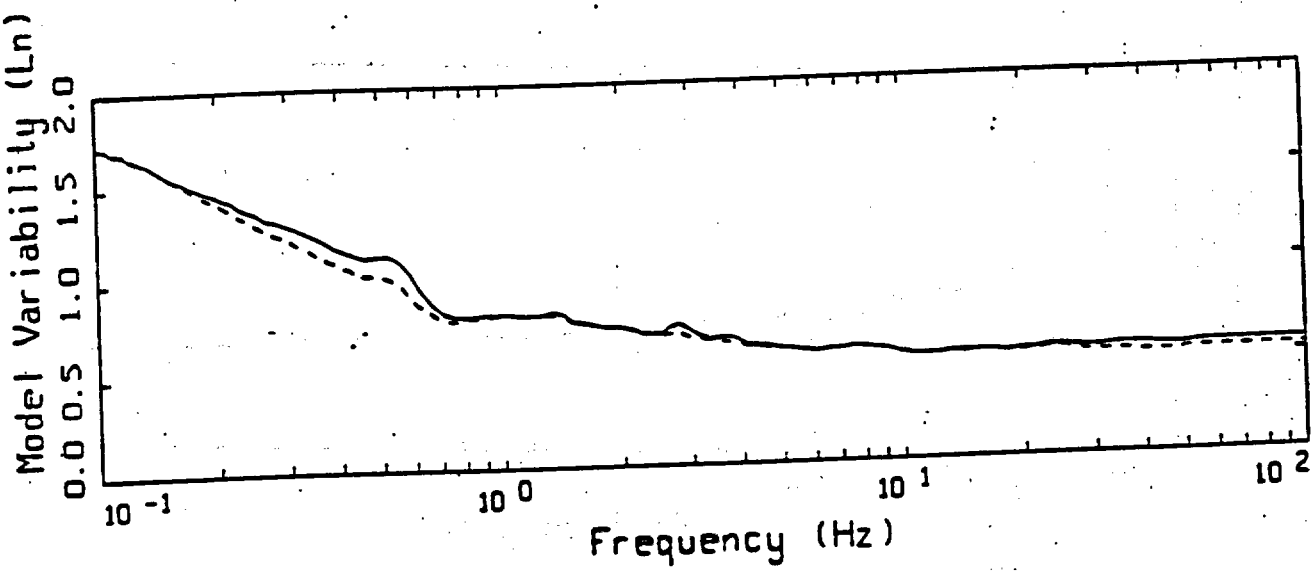

LEGEND
MEAN=0.0
BIAS CORRECTED

16 EARTHQUAKES POINT-SOURCE
NONLINEAR, ALL 159 ROCK SITES

Figure 5.154

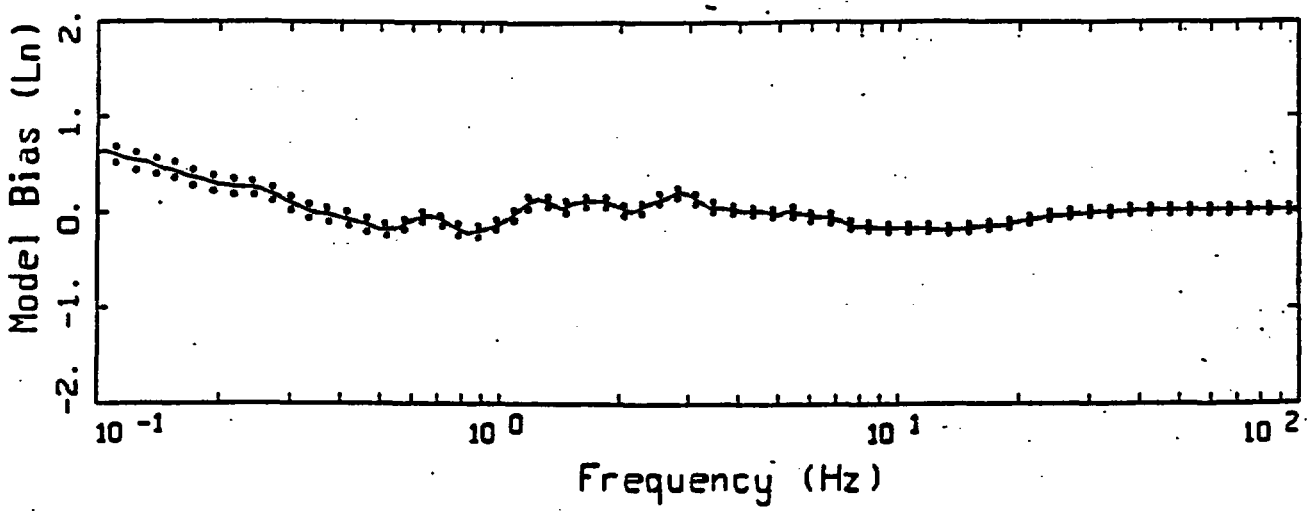

LEGEND
MODELING BIAS
90% CONFIDENCE INTERVAL OF MODELING BIAS
90% CONFIDENCE INTERVAL OF MODELING BIAS

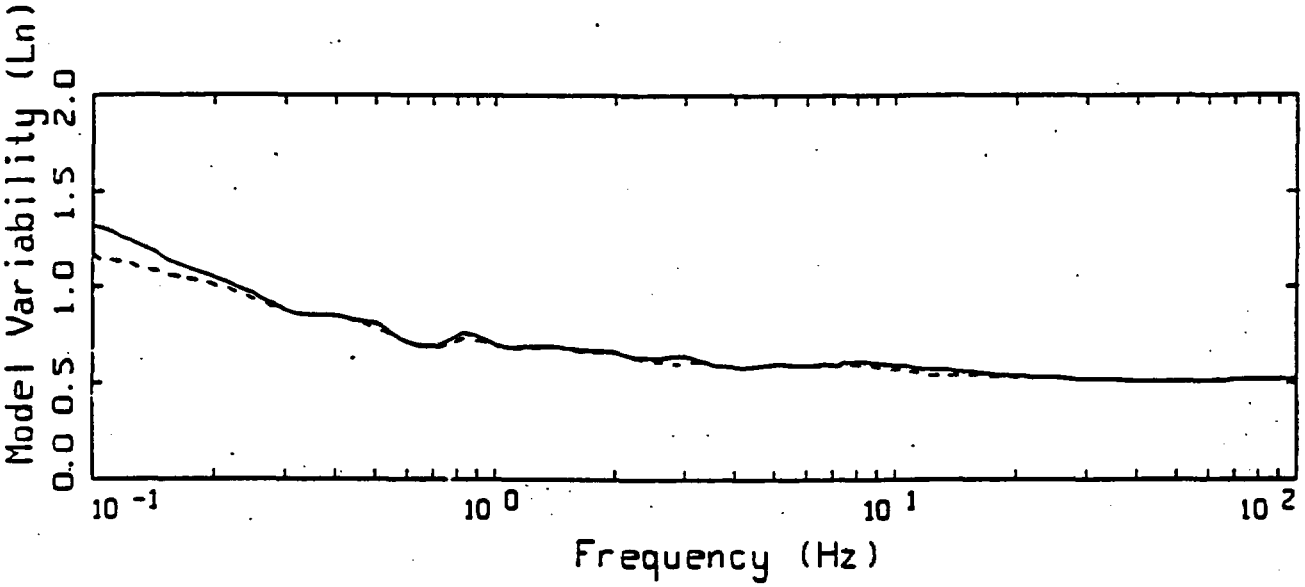

LEGEND
MEAN=0.0
BIAS CORRECTED

15 EARTHQUAKES FINITE-SOURCE
NONLINEAR, ALL 487 SITES

Figure 5.155

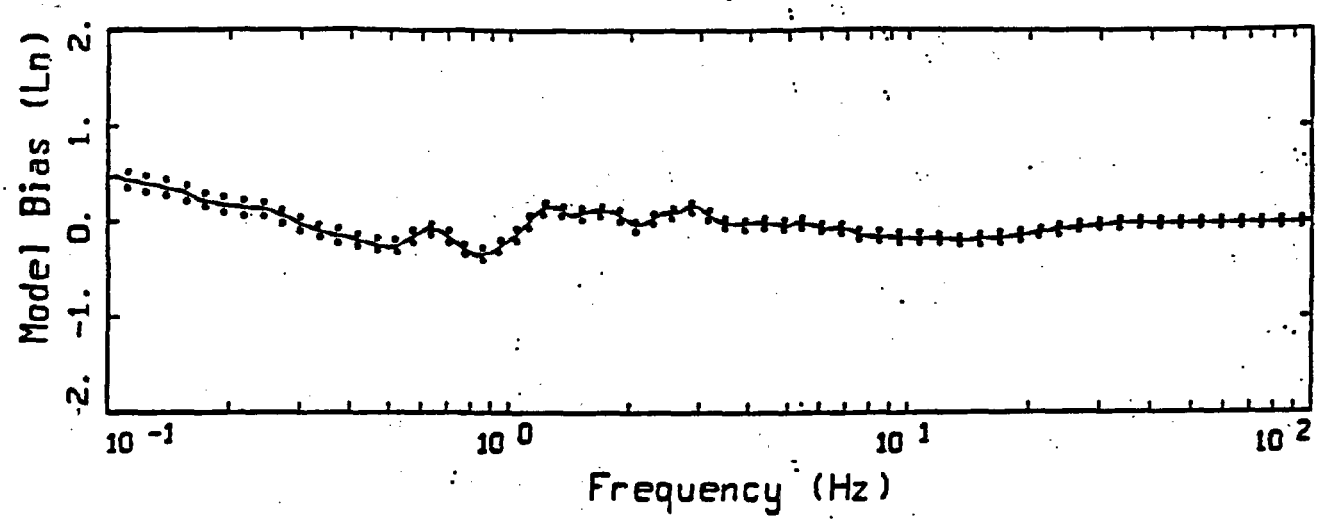

LEGEND
MODELING BIAS
90% CONFIDENCE INTERVAL OF MODELING BIAS
90% CONFIDENCE INTERVAL OF MODELING BIAS

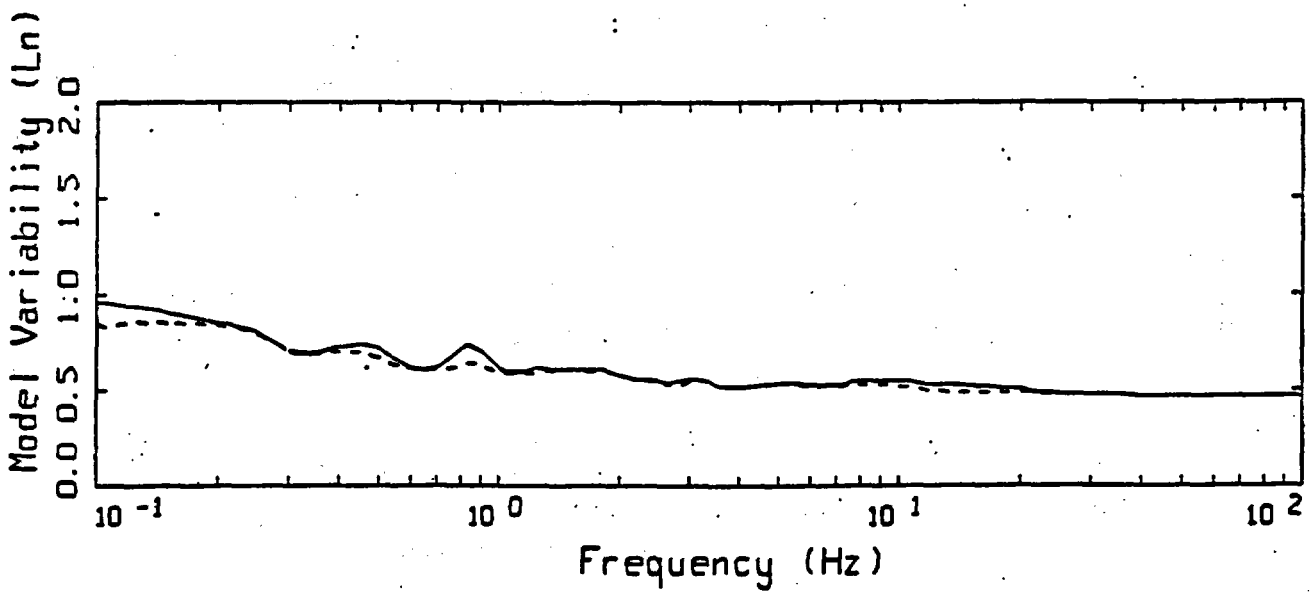

LEGEND
MEAN=0.0
BIAS CORRECTED

15 EARTHQUAKES FINITE-SOURCE
NONLINEAR, ALL 328 SOIL SITES

Figure 5.156

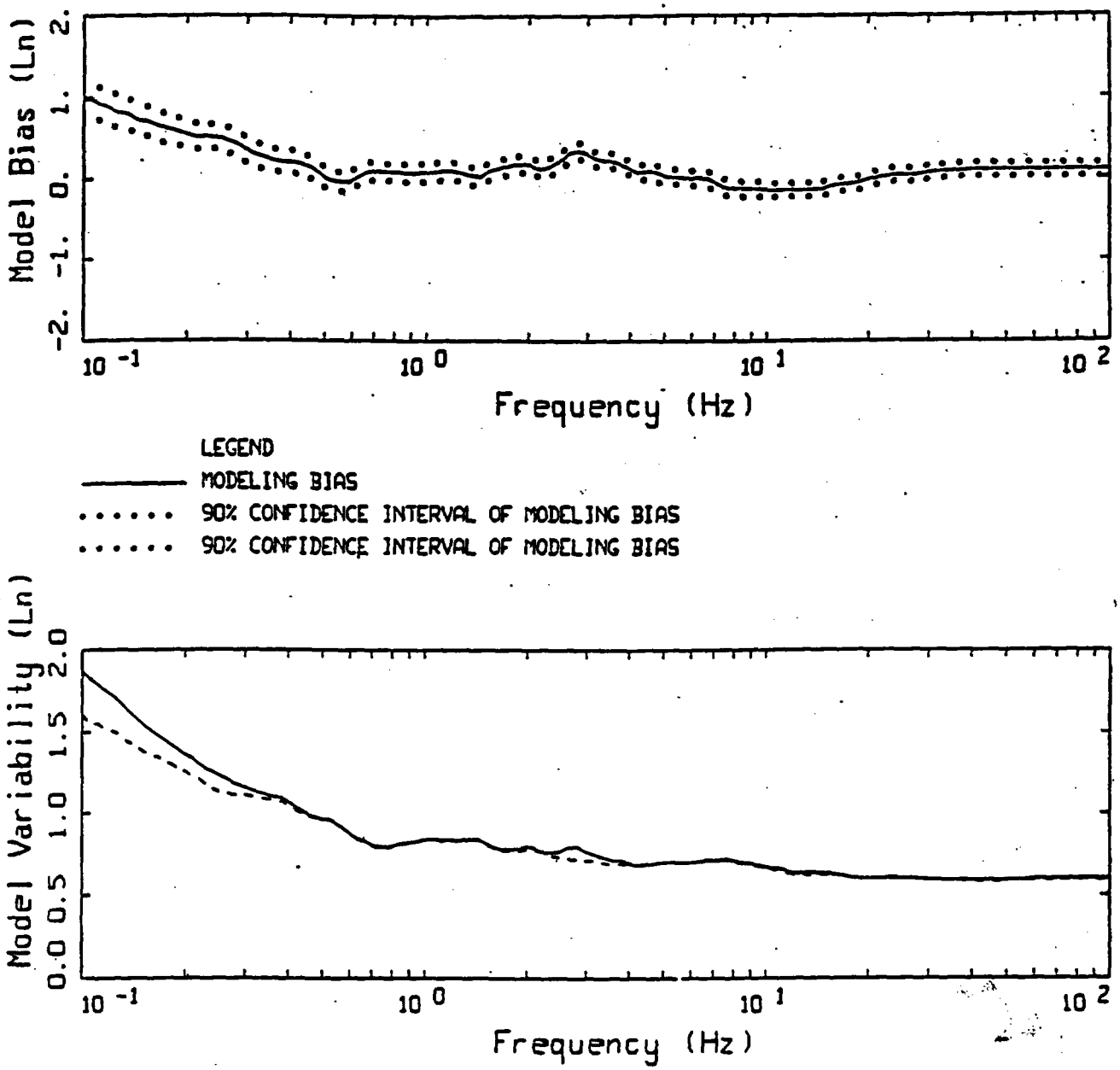

15 EARTHQUAKES FINITE-SOURCE
NONLINEAR, ALL 159 ROCK SITES

Figure 5.157

THIS PAGE IS AN OVERSIZED DRAWING OR FIGURE,

THAT CAN BE VIEWED AT THE RECORD TITLED:

Yucca Mountain Project
Project Summary Schedule
Baseline Thru CR 97/012
Sheet 1 of 3

WITHIN THIS PACKAGE

NOTE: Because of this page's large file size, it may be more convenient to copy the file to a local drive and use the Imaging (Wang) viewer, which can be accessed from the Programs/Accessories menu.

THIS PAGE IS AN OVERSIZED DRAWING OR FIGURE,

THAT CAN BE VIEWED AT THE RECORD TITLED:

Yucca Mountain Project
Project Summary Schedule
Baseline Thru CR 97/012
Sheet 2 of 3

WITHIN THIS PACKAGE

NOTE: Because of this page's large file size, it may be more convenient to copy the file to a local drive and use the Imaging (Wang) viewer, which can be accessed from the Programs/Accessories menu.

THIS PAGE IS AN OVERSIZED DRAWING OR FIGURE,

THAT CAN BE VIEWED AT THE RECORD TITLED:

Yucca Mountain Project
Project Summary Schedule
Baseline Thru CR 97/012
Sheet 3 of 3

WITHIN THIS PACKAGE

NOTE: Because of this page's large file size, it may be more convenient to copy the file to a local drive and use the Imaging (Wang) viewer, which can be accessed from the Programs/Accessories menu.